Ex-situ and *In-situ* Soft X-Ray Spectro-Microscopy Studies of Manganese Oxide Electrodes for Energy Storage Applications

By

Haytham Bassyouny Abdelsalam Elsayed Eraky, M.Sc.

A Thesis

Submitted to the School of Graduate Studies

in Partial Fulfillment of the Requirements

for the Degree of

Doctor of Philosophy

McMaster University

DOCTOR OF PHILOSOPHY (2024)   McMaster University
(Chemistry)   Hamilton, Ontario

TITLE: *Ex-situ* and *in-situ* soft X-ray spectro-microscopy studies of manganese oxide electrodes for energy storage applications

AUTHOR: Haytham Eraky, M.Sc. (Alexandria University)

SUPERVISOR: Professor A. P. Hitchcock

NUMBER OF PAGES: 299

ABSTRACT

Energy storage systems such as batteries and supercapacitors store electrical energy in the form of chemical energy and release it when required. Among the various electrode materials, manganese oxides (MnOx) are promising electrode materials for these devices. Despite its outstanding theoretical capacitance, Mn-based oxide electrodes have several limitations that impede their electrochemical performance. Understanding how the charges are efficiently stored in the electrodes or across the electrode/electrolyte interface is crucial for developing advanced electrode material in the field of energy storage applications.

The goal of my thesis is to develop and apply synchrotron-based scanning transmission X-ray microscopy (STXM) to investigate changes in the oxidation state of Mn and their spatial distributions in MnOx electrodes in the context of energy storage and release. To achieve high-precision qualitative and quantitative STXM identification and mapping of different MnOx species, calibrated and high-quality reference Mn 2p and O 1s NEXAFS (near edge X-ray absorption fine structure) spectra were measured. In collaboration with Wenjuan Yang and her PhD supervisor, Prof. Igor Zhitomirsky, I performed *ex-situ* STXM studies on Mn_3O_4-based supercapacitor electrode materials to investigate the influence of different synthesis methods and activation protocols on the charging behavior and capacitance performance. In collaboration with Pablo Ingino and his supervisor, Prof. Martin Obst (Bayreuth University), and my colleague, Dr. Chunyang Zhang, I helped develop a three-electrode, microfluidic-based flow electrochemical device for *in-situ* STXM. This device was used to electrodeposit MnO_2 on the working electrode (WE) and track the oxidation state and morphological changes by STXM while scanning the potential of the cell in different electrolyte pH. The *in-situ* STXM studies showed a spontaneous reduction of the initially deposited MnO_2 resulting from the local pH change at the WE. Additionally, a significant change from a quasi-uniform MnO_2 film to a dendritic MnO_2 structure was observed at oxidative potential. This dendritic growth resulted from dissolution/redeposition of MnO_2 during charging/discharging processes, indicating a partial reversibility of dissoluble Mn species. The *ex-situ* and *in-situ* STXM studies I performed provide mechanistic insights that will help further improve Mn oxides-based electrodes and their applications as energy storage devices.

ACKNOWLEDEGMENTS

TABLE OF CONTENT

LIST OF FIGURES

LIST OF TABLES

LIST OF ABBREVIATIONS AND SYMBOLS

A	Electrode surface Area
A^-	Electrolyte Anion.
α	Incidence Angle
AD	Anode Surface
AEY	Auger Electron Yield,
ALS	Advanced Light Source
B	Concentration of Active Species
b	Tafel slope
B_{bulk}	Concentration of Active Species in the Bulk
$B_{surface}$	Concentration of Active Species at the Surface
c	Speed of Light.
C	Capacitance
C^+	Electrolyte Cation
CA	Chronoamperometry
CAD	Computer Aided Design
CALM	Center of Advanced Light Microscopy
CCD	Charge-Coupled Device
CD	Cathode Surface
CDI	Coherent Diffraction Imaging
C_{dl}	Electric Double Layer Capacitance
CE	Counter Electrode
CGO	Conjugate Gradient Optimization
CLS	Canadian Light Source
CMOS	Complementary Metal-oxide Semiconductor
CNC	Computerized Numerical Control (Machine)
CNTs	Carbon Nanotubes
CO_2	Carbon Dioxide
CF	ConFlat (flange)

CP	Chronopotentiometry
C_S	Specific Capacitance
C_S max	Maximum Specific Capacitance
C_{sp}	Pseudocapacitance
C_{th}	Theoretical Capacitance
CV	Cyclic Voltammetry
D	Diameter of Zone Plate
d	Lattice spacing.
DBA	Double Bend Achromat
D_c	Diffusion coefficient of the reacting species
DI	Deionized Water
d_s	Charge Separation Distance
E	Energy
E°	Standard Potential
E_0	Potential Amplitude
$E_{Ag/AgCl}$	V vs Silver/Silver Chloride Electrode
E_{Au}	V vs Gold
E_{cell}	Cell Potential
ED	Energy density
EDL	Electric Double Layer
EELS	Electron Energy Loss Spectroscopy
EES	Electrochemical Energy Storage
E_i	Incident Photon Energy
EIS	Electrochemical Impedance Spectroscopy
E_{pa}	Anodic Peak Potential
E_{pc}	Cathodic Peak Potential
EPU	Elliptically Polarizing Undulator
E_{RHE}	V vs Reversible Hydrogen Electrode
E_{SHE}	V vs reversible Standard Hydrogen Electrode
EVs	Electric Vehicles

EXP	Experiment
EY	Electron Yield
F	Faraday's constant
f	Focal Length
FBs	Flow Batteries
FF	Fossil Fuels
F_{ph}	photon flux
FY	Fluorescence Yield
GCD	Galvanostatic Charge-Discharge Cycling
GUI	Graphical User Interface
HEBM	High Energy Ball Milling
HEG	High energy Spherical Grating
HEVs	Hybrid Electric Vehicles
I	Transmitted photon flux
I_0	Incident photon flux
i	Current
i_0	Current Amplitude
i_{cap}	Current required for the formation of EDL and Pseudocapacitance
i_{diff}	Current Related to Slow Diffusion-Controlled Processes
IdV	Area Under the Curve in Cyclic Voltammogram.
i_p	Peak Current
i_{pa}	Anodic Peak Current
i_{pc}	Cathodic Peak Current
IRAS	Infrared Reflection Absorption Spectroscopy
J	Current Density
J_0	Exchange current density
JCPDS	Joint Committee on Powder Diffraction Standards
K	Equilibrium Constant
$K_3[Fe(CN)_6]$	Potassium ferricyanide
$K_4[Fe(CN)_6]$	Potassium ferrocyanide

KB	Ellipsoidal Kirkpatrick-Baez Mirrors
$KMnO_4$	Potassium Permanganate
L	Sampling Depth
LEG	Low energy Spherical Grating
Li–SBs	Lithium–Sulfur Batteries
LIBs	Lithium-ion Batteries
m	Diffraction Order
M	Mass of Electroactive Material
MABs	Metal-air Batteries
MEG	Medium energy Spherical Grating
MIBs	Metal-ion Batteries
Mn_2O_3	Dimanganese Trioxide
Mn_3O_4	Trimanganese Tetraoxide
MnO	Manganese Monoxide
MnOx	Manganese Oxides
$MnSO_4$	Manganese Sulfate
MSE	Mercury Sulfate Electrode
MW	Molecular weight
n	Number of Electrons; Zone-number of Zone Plate
NA	Numerical Aperture
Na_2SO_4	Sodium Sulfate
NCM	Nickel Cobalt Manganese Batteries
NEXAFS	Near Edge X-ray Absorption Fine Structure
NMR	Nuclear Magnetic Resonance
NSLS	National Synchrotron Light Source
OCP	Open Circuit Potential
OD	Optical Density
OER	Oxygen Evolution Reaction
ORR	Oxygen Reduction Reaction
OSA	Order Selecting Aperture
PCB	Printed Circuit Board

PD	Power Density
PDMS	Polydimethylsiloxane
PEY	Photoelectron Yield
PFY	Partial fluorescence yield
PGM	Plane Grating Monochromator
$P_{if}(E)$	Probability of Electron Transition from an Initial state to Final state
PMMA	Poly(methyl methacrylate)
PMT	Photomultiplier Tube (Detector)
POE	Primary Optical Enclosure
PPY	polypyrrole
PTH	polythiophene
PANI	polyaniline
PA	polyacetylene
Q	Reaction Quotient
q	Charge
QC	Quercetin
R	Ohmic Resistance; Universal Gas Constant
RE	Reference Electrode
Res	Spatial resolution
r_n	Width of the nth Zone of the Zone Plate
SCs	Supercapacitors
SEY	Secondary Electron Yield
SF	Stack Fit
SF_6	Sulphur Hexafluoride
SGM	Spherical Grating Monochromator
Si_3N_4	Silicon nitride
SIBs	Sodium-ion Batteries
SM	Spectro-Microscopy beamline
SOH	Battery's State of Health
SPEM	Scanning Photoelectron Microscopy

SDD	Silicon Drift Detector
STXM	Scanning Transmission X-ray Microscopy
SVD	Singular Value Decomposition
T	Absolute Temperature
t	Time
TFY	Total Fluorescence Yield
TH	Testable Hypothesis
TMOs	Transition Metal Oxides
TXM	Transmission X-ray Microscopy
UV-vis	Ultraviolet–visible Spectroscopy
V_2O_5	Vanadium pentoxide
V	Voltage
WE	Working Electrode
X- PEEM	X-ray Photoemission Electron Microscopy
XAS	X-ray Absorption Spectroscopy
XANES	X-ray absorption near edge structure
XPS	X-ray Photoelectron Spectroscopy
XRD	X-ray Diffraction
Z	System Impedance
Z_0	Warburg Coefficient
ZIBs	Zinc-ion Batteries
Z_{img}	imaginary Impedance
$ZnSO_4$	Zinc Sulfate
ZP	Fresnel zone plate
Z_r	Real Impedance
α-MnO_2	Alpha-Manganese Dioxide
β	Emission Incidence Angle
β-MnO_2	Beta-Manganese Dioxide
3D	Three-dimensional
$\langle\Psi_f|$	Final state

$\lvert \Psi_i \rangle$	Initial state
η	Overpotential
[Ox]	Concentration of Oxidized Chemical Species
[Red]	Concentration of Reduced Chemical Species
$\lvert Z \rvert$	Absolute Value of The Impedance Vector.
$\propto v$	Surface Charge Contribution in Cyclic voltammetry
$\propto v^{1/2}$	Bulk Charge Contribution in Cyclic voltammetry
ε_0	Dielectric Constant of Vacuum
ε_r	Electrolyte Dielectric Constant
p	Probability of fluorescence
δ	Diffusion layer Thickness
ΔG	Gibbs Free Energy
$\Delta G°$	Standard Gibbs Free Energy
ΔH	Enthalpy
$\Delta H°$	Standard Enthalpy
ΔS	Entropy
$\Delta S°$	Standard Entropy
ΔV	Potential Window
$\eta(Ef)$	Detector efficiency
θ	X-ray Incidence Angle
λ	Wavelength
μ	Absorption coefficient
ρ	Material density
$\rho_f(E)$	Energy density of the Final States.
σ_x	X-ray Absorption Cross Section
υ	Cyclic Voltammetry Scan Rate
ϕ	Phase Angle
ω	Angular Frequency
Ω	Solid Angle Emission of the Electron

Chapter 1

Introduction

The world is undergoing a transition from polluting fossil fuels to sustainable, non-polluting power sources. Improved technologies for electrochemical energy conversion and storage systems are needed. Analytical methods which can give insights into such systems can help better understand, and thus optimize systems such as supercapacitors and batteries. This thesis describes how I have used soft X-ray spectroscopy and spectromicroscopy to study Mn oxide-based electrochemical systems. It includes development of a device for in-situ studies and several examples of its use. In this chapter the applications of this work to energy storage systems are presented and the significance of my contributions is discussed. The chapter concludes with an outline of the whole thesis.

1.1   Motivation of thesis

World energy consumption has significantly increased in recent decades, primarily using fossil fuels (FF). It is clear from many studies (Edenhofer et al., 2013; Ghosh & Ghosh, 2020) that the CO_2 generated by fossil fuel combustion and other FF-related emissions, such as methane from flared natural gas, and nitrogen oxides from combustion, have a significant negative impact on the environment and are leading to global warming. There is a broad consensus that the world is currently facing an extremely perilous situation that can only be mitigated by (i) reducing power use; (ii) replacing fossil fuel-based systems with electricity-based systems; (iii) powering the electrical grid with sustainable, non-FF sources. To address these challenges, it is crucial to develop sustainable and efficient energy systems based on renewable energy sources such as wind, solar, hydropower, geothermal and biomass energies. However, some of these sources, in particular wind and solar, are not always available. Therefore, development of efficient, cost-effective, energy storage systems is necessary to ensure a consistent and reliable supply of electrical energy (Shin et al., 2020).

Among different energy storage systems, electrochemical technologies are widely used in both stationary and mobile energy storage applications (Pires et al., 2014). Stationary electrochemical energy storage (EES) systems, such as Li-ion (W. Wang et al., 2013) and flow

batteries (Xie et al., 2019), are designed to store electricity in large quantities for long periods of time, typically for grid-scale applications. EES powered by the grid or by solar energy are used for peak-shaving in the industrial sector to avoid power consumption spikes during high demand times (Belmonte et al., 2017; Chua et al., 2020). Mobile electrochemical energy storage systems such as nickel metal hydride, nickel cobalt manganese (NCM) Li-ion batteries (Yoon et al., 2017), or hybrid battery/supercapacitor energy storage systems (Kouchachvili et al., 2018) are designed to be used in small scale applications, such as electric vehicles (EVs), hybrid EVs (HEVs) (Verma et al., 2021), and to power electronic devices (Hosseini et al., 2014).

EES systems can be differentiated based on their energy storage mechanisms. Batteries (regardless of their type) store energy in the form of a change in the oxidation state of chemical species and release the stored energy by a reversible oxidation-reduction (redox) process. Conventional capacitors store energy through the accumulation of electric charges between its plates. Supercapacitors can store electric charge electrostatically through the formation of electric double layer (EDL), redox process, or a combination of EDL charge storage and battery-like redox processes for energy storage and release. (Abruña et al., 2008; Minakshi et al., 2020).

The efficiency and performance of battery and supercapacitor devices are greatly affected by the type and properties of the active electrode materials employed (Parveen et al., 2022). Many different transition metal oxides (TMOs), such as Fe_3O_4 (Liu et al., 2013), Co_3O_4 (Hu et al., 2016), V_2O_5 (Foo et al., 2014; N. Zhang et al., 2018), NiO (Mhaisalkar et al., 2010) and MnO_2 (Xue et al., 2011), have been investigated as possible electrode materials for batteries and supercapacitors. Among TMOs, manganese-based oxides (Mn_xO_y) have attracted much attention as potential electrode materials due to their high theoretical capacitance (1380 Fg^{-1}), wide potential range, high natural abundance, low cost and environmental friendliness (Parveen et al., 2022; Yu et al., 2011). Despite the outstanding theoretical capacitance, Mn-based oxide electrodes have many drawbacks that hinder achieving high performance. These include low actual specific capacitance (capacitance per unit of mass), low electronic conductivity, poor ionic diffusion, and low cycling stability resulting from dissolution of MnO_2 material at acidic pHs (Wei et al., 2011), (Z. Wang et al., 2021).

Mn$_3$O$_4$ is a highly promising cathode material used in energy storage applications (Beknalkar et al., 2022). Various methods have been used to improve the electrochemical performance of those electrodes, such as enhancing the electrical conductivity of the Mn$_3$O$_4$-based electrode material through the development of nanostructure composites of Mn$_3$O$_4$, and highly conductive carbonaceous compounds (such as graphene, carbon nanotubes (CNTs) and activated carbon) (Low et al., 2019). Another common approach is to involve a capping agent, such as quinone or quercetin, during the synthesis procedure. This approach helps reduce the size of the nanoparticles and restrict particle growth, increasing the surface area of the electrode material and consequently enhancing its capacitance performance (Awad & Zhitomirsky, 2023; Yang & Zhitomirsky, 2023). The charge storage mechanism of the Mn$_3$O$_4$-based electrode in Na$_2$SO$_4$ electrolyte involves two steps, solvation (**Eq. 1.1**) followed by redox reaction (**Eq. 1.2**) as follows (Suktha et al., 2017; Yang & Zhitomirsky, 2023):

$$Na_2\,SO_4\,(aq) + \ Mn_3O_4\,(s)\ +\ H_2O\ \rightarrow$$

$$[Na_yMn_3O_4\,.\,H_2O]^{y+} + (2-y)Na^+(aq) + \ SO_4^-(aq) \qquad \textbf{Eq. 1.1}$$

$$Na_yMnO_x\,.\,H_2O \rightarrow \ MnO_x\,.\,H_2O + \ yNa^+ + \ ye^- \qquad\qquad \textbf{Eq. 1.2}$$
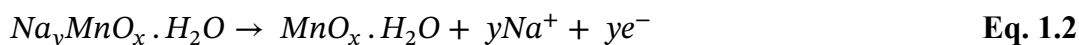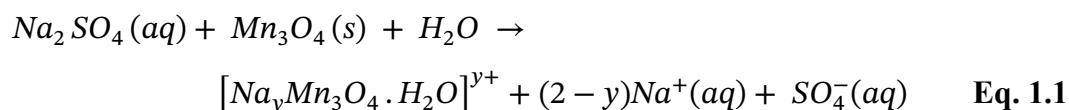
Nevertheless, the behavior of charging/discharging processes of the Mn$_3$O$_4$ electrodes is not well understood (Wu et al., 2015). The challenges to understand the charging mechanism arises from the activation phenomena of the electrode (Liu et al., 2019; Sayyed et al., 2021; Wu et al., 2015). In this context, two different studies (presented in **Chapter 7** and **Chapter 8**) were performed on Mn$_3$O$_4$ supercapacitor electrodes subjected to different preparation methods and different activation procedures to investigate the activation behavior and charging mechanism.

On the other hand, MnO$_2$ is also an attractive and extensively studied electrode material in different energy storage applications. However, the actual capacitance of practical devices is considerably lower than the theoretical capacitance value. The redox reactions in MnO$_2$ systems are known to occur between Mn^{4+} and Mn^{3+} species. In aqueous electrolyte, the redox reaction primarily takes place through the adsorption/desorption (formation of EDL) or intercalation/deintercalation of protons [H$^+$] or electrolyte cations [C$^+$] at the surface or into the bulk of the MnO$_2$(IV) electrode material (pseudocapacitive behavior), resulting in the

formation of reduced $MnOOH^+$ and/or $MnOOC^+$(III) species, as described in **Eq. 1.3**, followed by disproportionation reduction of Mn^{3+} to Mn^{2+}, as described in **Eq. 1.4** (Devaraj & Munichandraiah, 2009; Rodrigues et al., 1998):

$$MnO_2 + H^+ + e^- \rightarrow MnOOH \qquad \textbf{Eq. 1.3}$$

$$MnOOH + 3H^+ + e^- \rightarrow Mn^{2+} + 2H_2O \qquad \textbf{Eq. 1.4}$$
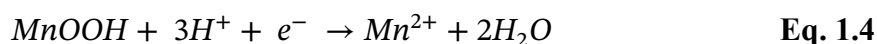
However, there is still ongoing debate regarding the reversibility of Mn dissoluble species (Li et al., 2012; Sopčić et al., 2013). The dissolution of MnO_2 into an electrolyte, poor cycling performance, and morphological changes can significantly impede the electrochemical performance of MnO_2 electrode materials. Therefore, understanding chemical and morphological changes during charging/discharging processes and how charge is efficiently stored in the electrodes or across the electrolyte/electrode interface will help further improvement of MnO_2 electrodes in energy storage application. For this reasons, various *in-situ* STXM studies (presented in **Chapter 9)** were conducted to investigate the morphological changes and track the oxidation state changes during the oxidation and reduction processes using the custom *in-situ* flow electrochemical device described in **Chapter 4**.

The significance of understanding Mn redox reactions is broader than energy storage applications. Manganese oxides are highly reactive minerals found abundantly in nature, they play a crucial role as redox centers in different elemental cycles within biotic and abiotic systems (Ghosh, 2020; Jung et al., 2020). Manganese oxides are involved in different environmental redox reactions. For instance, birnessite (δ-MnO_2) can directly convert Se(IV) to Se(VI), Cr(III) to Cr(VI), and As(III) to As(V) (Borch et al., 2010). Despite the ability to cycle many redox elements, the reactivity of Mn oxides under different environmental conditions is still unexplored (Fischel et al., 2015).

The research reported in this thesis developed scanning transmission X-ray microscopy (STXM) as a tool for better understanding of electrochemical reactions of Mn-based oxides. STXM (Ade, 1998) is a synchrotron-based technique that provides imaging with sub-50 nm spatial resolution and chemical speciation through spatially resolved near edge X-ray absorption fine structure (NEXAFS) spectroscopy (Stöhr, 1992). The spectro-microscopic capabilities of STXM enable quantitative mapping of different chemical species. In addition,

STXM can overcome the limitations of some characterization techniques such as X-ray diffraction (XRD) or X-ray absorption spectroscopy (XAS) which provide only bulk-averaged spectral information without any morphological insights, STXM also has advantages over purely imaging methods, such as optical and electron microscopy that provide mainly morphological characterization with limited insight into local chemical structure (Fan et al., 2019; Huang et al., 2020).

Since manganese oxides (MnOx) are used as electrode materials in various energy storage applications, high-quality reference Mn 2p and O 1s NEXAFS spectra are necessary for qualitative identification and quantitative mapping of MnOx species. As discussed in **Chapter 6**, since there were some discrepancies in the literature, part of my thesis involved measuring accurate, quantitative, high-statistical precision O 1s and Mn 2p NEXAFS spectra of a range of Mn compounds in the common oxidation states, using both STXM and non-spatially resolved NEXAFS.

Ex-situ measurements require removing samples from their operational context. *Ex-situ* characterizations can provide valuable information on product distributions and sometimes on reaction mechanisms. However, a much more powerful approach is to investigate chemical and morphological properties of an electrode material under actual operating conditions. Such *in-situ* or *operando* studies can lead to important insights into electrode processes, in particular, charge/discharge reaction mechanisms. *In-situ* studies are those where the sample is under the same physical condition (temperature, pressure, electrolyte) and electrochemical environment as the material experiences in its active state. *Operando* studies involve measurements under real operating conditions with cell components identical or very similar to an actual device. *In-situ* and *operando* measurements provide detailed information (chemical composition, phase, and morphology) about the species present at the electrode/electrolyte interface which can give insights into chemical and morphological changes that cannot be obtained through pre- and post-reaction *ex-situ* studies. In order to perform *in-situ* STXM studies, a three-electrode based, *in-situ* flow electrochemical device was developed and used in several *in-situ* studies of redox reactions of manganese oxides electro-deposited on Au electrodes (**Chapter 9**). This microfluidic-based *in-situ* device was based on a design developed by Pablo Ingino and Martin Obst at the University of Bayreuth (Ingino et al., 2024; Obst et al., 2018; Zhang et al., 2023b;

Zhang et al., 2023a). The optimization of methods to fabricate the *in-situ* flow electrochemical device and develop effective and safe operating procedures was a major component of the experimental work for this PhD thesis. The details of the design, fabrication and operation of the *in-situ* device are presented in **Chapter 4**.

1.2   Fundamentals of electrochemical energy storage

Electrochemical energy storage (EES) and conversion principles were first discovered by Alessandro Volta, who invented the first battery ("voltaic pile") in 1799 (Haas & Cairns, 1999). EES systems play a crucial role in our daily lives due to their widespread use in many applications including mobile electronic devices, EVs, and large-scale power grids. Metal-ion batteries (MIBs) and supercapacitors (SCs) are the most important types of EES (B. Wang et al., 2020). Energy storage devices are rated based on their power and energy density. Power density (PD) is the rate of energy transferred per unit time; it is typically measured in Watt per kilogram (W/kg). Energy density (ED) is the amount of energy stored per unit mass of a system; it is measured in Watt hour per kilogram (Wh/kg) (Fan et al., 2011).

The Ragone plot presented in **Fig. 1.1** (Libich et al., 2018) illustrates PD and ED of different energy storage systems (conventional capacitors, supercapacitors, batteries and fuel cells). Conventional capacitors have significantly higher power density than batteries and fuel cells due to their physical adsorption/desorption charge storage mechanism. On the contrary, batteries and fuel cells have high energy densities compared to capacitors, but they suffer from low power density due to their sluggish faradic (oxidation/reduction) reaction kinetics. Supercapacitors are energy storage devices that bridge the PD and ED functionality gap between conventional capacitors and batteries (Cui & Meng, 2020; Goodenough et al., 2007). **Table 1.1** presents a performance parameters comparison between capacitors, batteries and supercapacitors (Divyashree & Hegde, 2015).

The theoretical energy density and power density of SCs can be calculated using the following equation (Fan et al., 2011; Ling & Jose, 2021):

$$ED = \frac{1}{2} (C_s \; x \; \Delta V^2) \qquad\qquad \textbf{Eq. 1.5}$$

$$PD = \frac{ED}{\Delta t} \qquad\qquad \textbf{Eq. 1.6}$$

where ED is energy density, PD is power density, C_s is specific capacitance, ΔV is the potential window during the measurement, and Δt is the discharge time. The gravimetric energy density of batteries is related to their weight and can be calculated as follows (J.-S. Kim et al., 2020):

$$ED = \frac{1}{M} \int_0^t iV \, dt \qquad \textbf{Eq. 1.7}$$

where M is the Mass of cell, i is the current density, and t is the discharge time.
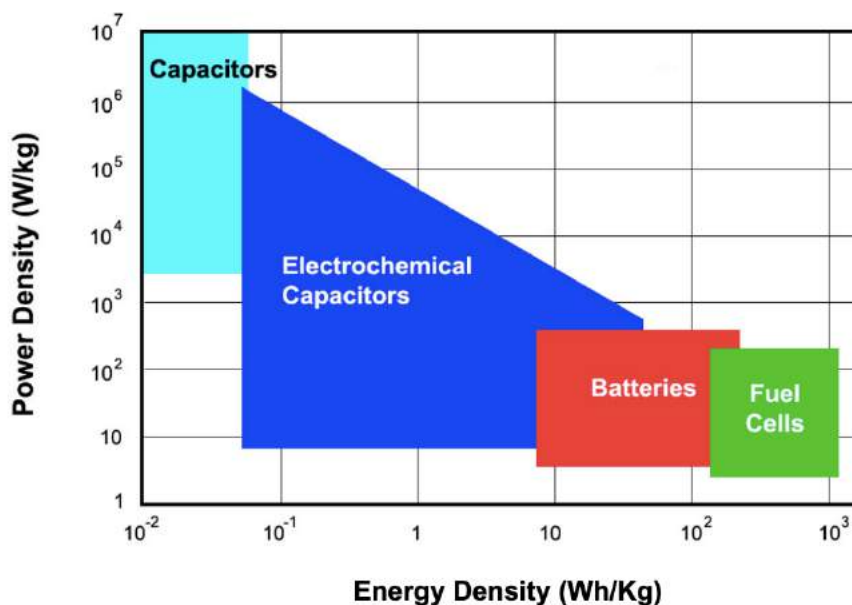
Figure 1.1 Ragone chart: power density as a function of energy density for different electrochemical energy storage systems. Reprinted from (Libich et al., 2018). With permission from Elsevier.

Table 1.1 Comparison of properties of capacitors, batteries, and supercapacitors. Adapted from (Divyashree & Hegde, 2015).

Function	Capacitor	Battery	Supercapacitor
Charge time	ms - ms	Hours	ms - m
Discharge time	ms - ms	1 - 900 min	ms - d
Energy density	<0.01 Wh/L	50 - 300 Wh/L	0.5 - 5 Wh/L
Power density	>10^4 W/L	<500 W/L	$10^3 – 3 \times 10^3$
Cycle life	$10^6 - 10^8$	200 - 1000	$10^6 - 10^8$

1.2.1   Batteries

Batteries are the most common power sources used in both industrial and consumer electronics applications. They are composed of electrochemical cells that consist of a positively charged electrode (cathode) and a negatively charged electrode (anode) that are electrically connected by an ionic conductive electrolyte. Different electrodes and electrolytes used in batteries exhibit different chemical reactions. The specific chemical species used significantly impact the electrochemical performance, voltage window, energy storage capacity, and lifetime of a battery (Dell & Rand, 2001). There are two types of batteries based on their charging processes:

i.   **Primary batteries** involve irreversible chemical reactions and can only be used once (**Fig. 1.2A**). This category includes zinc/manganese dioxide (Zn/MnO_2) batteries, Zinc-carbon batteries and alkaline batteries (Cairns, 2004).

ii. **Secondary batteries** involve reversable chemical reactions and can be discharged and recharged repeatedly (**Fig. 1.2B**). This category includes lithium-ion batteries (LIBs), lithium–sulfur batteries (Li–SBs), sodium-ion batteries (SIBs), zinc-ion batteries (ZIBs), lead-acid batteries, and flow batteries (FBs) (Lu et al., 2017).
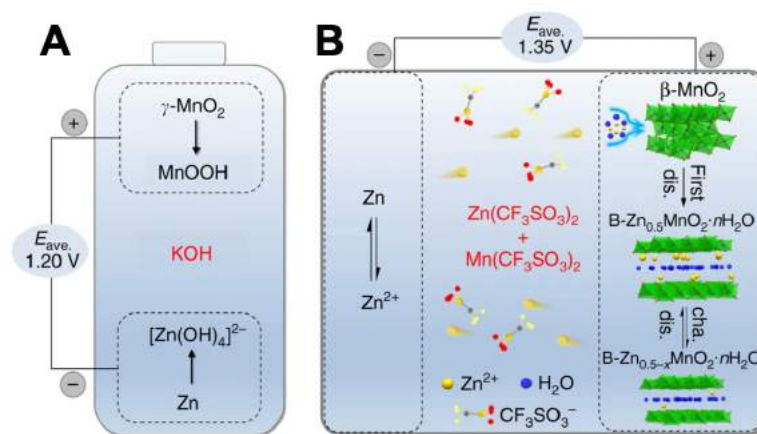
Figure 1.2 Schematic illustration of Zn-MnO₂ battery chemistry. (A) primary alkaline Zn-MnO₂ battery using γ-MnO₂ as cathode, Zn as anode, and KOH as electrolyte. **(B)** rechargeable (secondary) Zn-MnO₂ battery using β-MnO₂ as cathode, Zn as anode and Zn/Mn(CF₃SO₃)₂ as electrolyte. Reprinted from (Zhang et al., 2017). With permission from Springer Nature.

1.2.2   Supercapacitors

Supercapacitors (SCs) (also called electrochemical capacitors) have attracted wide attention as energy storage devices owing to their high-power density, long cyclic life and fast charging/discharging processes (Chen et al., 2020). Similar to batteries, SCs consist of two electrode materials deposited onto current collectors and separated by an electrolyte and a separator. With a combination of high-power density and relatively high-energy density, SCs are widely used in many different applications as energy storage devices, such as portable electronics, memory back-up systems, automotives, industrial power and energy systems. SCs can be classified into two main categories based on the energy storage mechanism: electric double-layer (EDL) capacitors and pseudocapacitors (**Fig. 1.3**). These are described in detail in **Section 2.2**. Asymmetric hybrid capacitors also can be obtained by a combination of EDL and pseudocapacitance electrode materials. **Table 1.2** present typical electrode materials used in each type of SCs with a comparison of capacitance performance and cycling stability (Lin Li et al., 2014).

Table 1.2 Types of electrode materials used in SCs.

	Material	**Capacitance**	**Cycling stability**
EDL capacitors	Carbon based materials	Moderate	Excellent
Pseudocapacitors	TMOs and conducting polymer	High	Poor
Hybrid SCs	Carbon-TMOs /conducting polymer	High	Moderate
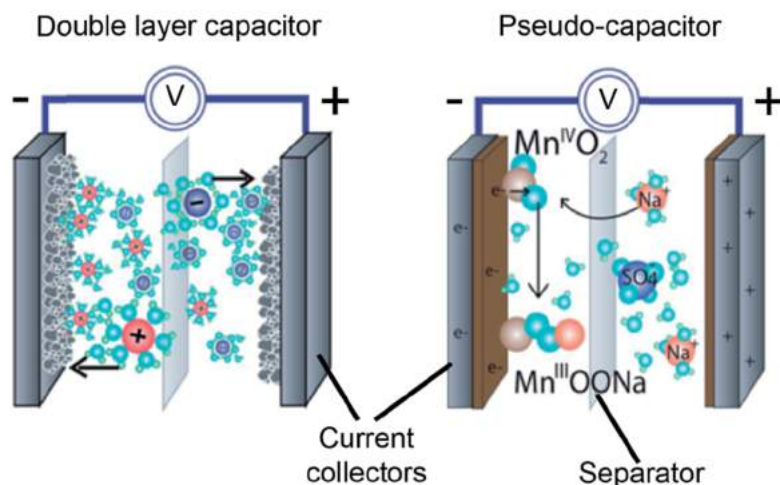
Figure 1.3 Schematics diagram of (A) carbon based electric double layer capacitors. **(B)** pseudocapacitor (using MnO_2 as active electrode material). Reprinted from (Gulzar et al., 2016). With permission from Springer Nature.

1.3   Significance of my thesis to electrochemical energy storage applications

The electrochemical performance of batteries and supercapacitors as energy storage systems are closely related to the type and properties of the active electrode materials (Yan et al., 2020), which can undergo structural and chemical changes during charge/discharge processes. A better understanding of the charge and discharge mechanisms that take place at the electrode/electrolyte interface will help further improvement of electrode materials used in this field. In my thesis, I made *ex-situ* and *in-situ* studies of a variety of Mn oxide-based electrochemical systems to help understand the chemical and morphological changes of MnOx electrode materials used in energy storage systems. Through these studies, I have made the following contributions to this field:

A. I generated reliable Mn 2p and O 1s NEXAFS reference spectra that can be used in STXM and/or NEXAFS studies of Mn species in different scientific areas, including electrochemical conversion, environmental studies, biogeochemistry, and more.

B. I clarified the active MnOx species initially present, and after extensive cycling of Mn_3O_4-based SCs (in collaboration with Zhitomirsky's group). This helped identify the optimum electrochemical activation procedure and fabrication method associated with the enhanced capacitance performance.

C. In collaboration with Chunyang Zhang, Pablo Ingino, Martin Obst and Hooman Hosseinkhannazer, I developed procedures at McMaster to fabricate a novel, microfluidic-based flow electrochemical *in-situ* cell compatible with several types of soft X-ray STXMs. The safe operating procedures to use these devices were developed by carrying out experiments in collaboration with Chunyang at 6 different STXMs at 5 synchrotron facilities (CLS, Soleil, MaxIV, Bessy and Solaris).

D. I discovered an un-expected, 'spontaneous' reduction of electrodeposited MnO_2 to MnO through the *in-situ* change of electrolyte from 0.1 M $MnSO_4$ to 0.1 M Na_2SO_4. While initially a surprise, I hypothesized that the reduction was pH-driven and fully consistent with the Pourbaix diagram of this system, I verified this through pH dependent *in-situ* STXM studies.

E. The goal of the *in-situ* STXM studies of the electrodeposited MnO_2 layer was to measure the relative contributions of EDL and redox processes in MnO_2-based supercapacitors. While this goal was not explicitly achieved, I showed that redox cycling is a major contributor. I also performed an unsuccessful search for direct evidence of the EDL process by monitoring spatial location and amounts of Na^+ ions. Nevertheless, the Upper limits of the EDL contribution were estimated from these unsuccessful results.

1.4 Outline of the thesis

Chapter 2 describes the fundamentals of the energy storage mechanisms, including thermodynamic and kinetic principles. It then gives an overview of manganese oxides as promising electrode materials for energy storage applications. This is followed by an introduction to *ex-situ* and *in-situ/operando* electrochemical spectroscopic and microscopic techniques, as well as a literature review of *in-situ* spectromicroscopic characterization.

Chapter 3 describes the principles of X-ray absorption spectroscopy, including transmission, total electron yield and fluorescence yield detection methods. The fundamentals of STXM including principles and instrumentation are outlined. This chapter concludes with details of STXM data acquisition and data analysis procedures.

Chapter 4 presents a detailed description of the design, fabrication process, operation procedures and challenges of the *in-situ* flow STXM electrochemical device. In addition to my *in- situ* studies of redox cycling of electrodeposited MnOx materials, this device was also used extensively by Chunyang Zhang to investigate Cu-based CO_2 electro-reduction catalysts under potentials where CO_2 reduction was occurring (Zhang et al., 2023b; Zhang et al., 2023a).

Chapter 5 presents experimental details including lab-based electrochemical techniques and methods. This is followed by sample preparation for (*ex-situ*) STXM and complementary characterization techniques used in the thesis.

Chapter 6 presents high quality and calibrated O 1s and Mn 2p reference spectra of different manganese oxidation states (MnO, $MnSO_4$, Mn_3O_4, Mn_2O_3, α-MnO_2, β-$MnO_2,$ and $KMnO_4$) measured by STXM and TEY. The result of this study formed the basis for accurate STXM quantitative chemical mapping of different complex Mn oxide systems throughout this thesis.

Chapter 7 presents results of an *ex-situ* STXM study of Mn_3O_4-based supercapacitor electrode material. This study was performed on samples subjected to different electrochemical procedures to investigate the activation behavior and charging mechanism(s) of Mn_3O_4-MWCNT supercapacitor electrode material using quercetin as a dispersant. The results obtained from the studies revealed that the charge storage mechanism involved redox Mn^{3+}/Mn^{4+} reactions on the particle surface and in the bulk. Subsequent capacitance increases during the activation procedures resulted from gradual oxidation of the as-prepared Mn_3O_4 electrode to MnO_2. This chapter is presented in the published format (Yang, W., Eraky, H., Zhang, C., Hitchcock, A.P. and Zhitomirsky, I., 2022. Scanning transmission X-ray microscopy studies of electrochemical activation and capacitive behavior of Mn_3O_4 supercapacitor electrodes. *Journal of Materials Chemistry A*, 10(35), pp.18267-18277).

Chapter 8 presents results of an *ex-situ* STXM study of Mn_3O_4-based supercapacitor electrode material synthesized by two different methods involved using high energy ball milling (HEBM) and quercetin (as capping agent) in the electrode material synthesis. This study was performed to investigate the influence of fabrication method and electrochemical activation on charge storage. Partial oxidation of the as-prepared Mn_3O_4 during activation was detected and related to the higher electrochemical performance of Mn_3O_4 prepared using

quercetin in the synthesis. This chapter is presented in the published format (Yang, W., Eraky, H., Zhang, C., Hitchcock, A.P. and Zhitomirsky, I., 2024. Electrochemical and scanning transmission X-ray microscopy studies of MnO_2 and Mn_3O_4 for supercapacitor cathodes: Influence of fabrication method and electrochemical activation on charge storage. *Chemical Engineering Journal*, p.149391).

Chapter 9 present results of *in-situ* STXM studies of MnO_2-based electrode for energy storage applications. These studies were performed to investigate charge storage/degradation mechanisms of MnO_2-based electrode material for SCs and batteries. Spatially resolved NEXAFS spectra of as-deposited MnO_2 and after the MnO_2 deposit was subjected to different electrochemical processes were measured at Mn 2p and O 1s -edges on both the working electrode (WE) and the counter electrode (CE). In this study, I observed a spontaneous reduction of the initially electro-deposited MnO_2 film to a mixture of Mn^{2+} and Mn^{3+} after changing electrolyte from $MnSO_4$ to Na_2SO_4 at the open circuit potential (OCP). This reduction occurs as result of local pH change, which is confirmed through performing *in-situ* experiments at different electrolyte pH (pH=4 and pH=8). The obtained results indicate that the pseudocapacitive behavior occurs through a $Mn^{4+} \leftrightarrow Mn^{3+}/Mn^{2+}$ redox reaction. Additionally, a considerable deposition of the dissoluble MnO species was observed on the counter electrode (CE), which was associated with degradation of the initially deposited MnO_2 electrode on the WE. At high positive potential, there was a significant change in the morphology of the deposited MnO_2 during charging process (extensive, irreversible dendrite formation). Furthermore, the results from the *in-situ* study of the MnO_2 system indicate a partially reversible $MnO \leftrightarrow MnO_2$ redox reaction during oxidation and reduction processes. These studies provide better understanding of the overall morphological and chemical changes that occur at both WE and CE during charging and discharging processes.

Chapter 10 summarizes the results and highlights the contributions my thesis has made to fundamental understanding and instrument development. Future experiments in which *in-situ* STXM could be used to learn more about supercapacitor and battery electrode materials are described.

The Appendix contains (1) list of my publications and presentations. (2) list of software used in the studies. (3) Supplementary information sections from Chapters 6, 7 and 8.

Chapter 2

Electrochemical Energy Storage and Analytical Electrochemistry

This chapter describes the fundamentals of the analytical electrochemical methods used in this work. It then gives an overview of energy storage mechanisms for supercapacitors and batteries. Basic concepts of thermodynamics and kinetics of energy storage are described. This is followed by an overview of manganese oxides as promising electrode materials and their challenges. For better understanding of manganese oxide-based energy storage systems and to address some of their challenges, experimental hypotheses related to the research performed in this work are presented.

2.1 Fundamentals of Electrochemistry

Electrochemistry is a branch of science that deals with electrical energy and chemical reactions, in which the electrochemical reactions involve the generation or input of electric currents. Electrochemistry is involved in various applications that we meet everywhere in our daily lives, such as energy storage and conversion (Elliott et al., 2019; Rajagopalan et al., 2022; Wei et al., 2011), corrosion prevention (Perez & Perez, 2016), electroplating (Rajoria et al., 2021) and biosensors (Grieshaber et al., 2008). In any electrochemical system, such as batteries and supercapacitors, two electrodes separated by an electrolyte and connected by an external electrical conductor are essential to allow the movement of ions from one electrode to the other through the electrolyte, while electrons simultaneously flow through the external circuit (Newman & Balsara, 2021).

Batteries and supercapacitors utilize electrochemical processes, with distinct mechanisms determining their energy and power density. The electrochemical reactions in batteries and supercapacitors result in unique charge-storage characteristics. For instance, in lithium ion (Li^+) batteries, the diffusion-controlled insertion of Li^+ ions facilitate redox reactions in bulk electrode materials, which can be slow. On the other hand, EDL supercapacitors store charge through the adsorption of electrolyte ions onto electrode material surfaces without the need for redox reactions, allowing for rapid response to potential changes and high-power output. Despite the high power density, the energy density of EDL is lower

than that of batteries due to the surface confinement of charge. On the other hand, pseudocapacitance EDL involves reversible redox reactions near the electrode surface, leading to enhanced charge storage capacity. This pseudocapacitance behavior serves as an additional mechanism for capacitive energy storage. Pseudocapacitive materials offer the potential to achieve energy density comparable to batteries while maintaining the cycle life and power density of EDL supercapacitors (Simon et al., 2014).

Electrochemical characterization techniques are essential tools to assess the electrochemical behavior of any electroactive materials under different electrochemical conditions. In any electrochemical cell, there are three types of electrode systems that can be used: two-electrode system, three-electrode system, and four-electrode system. All lab-based electrochemical characterizations and *in-situ* STXM measurements reported in this thesis are performed using a three-electrode system: working electrode (WE), counter electrode (CE), and reference electrode (RE) **(Fig. 2.1)**. The WE is the electrode where the reaction of interest takes place, while the CE allows electrons to flow through the cell and closes the electrical circuit. The WE potential is measured using the RE, which maintains a constant electrochemical potential although no current passes through it (Choudhary et al., 2017). In order to minimize the solution resistance, it is important to place the working electrode as close as possible to the reference electrode (Zoski, 2006).
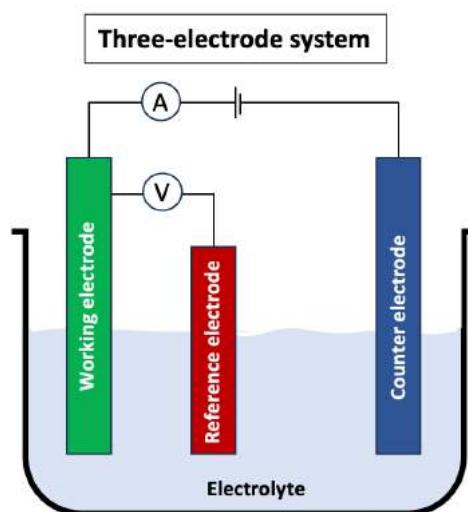
Figure 2.1 Schematic of three-electrode system configuration.

Neither the WE nor the CE are explicitly designed to be anode or cathode. Electrolytic cells involve non-spontaneous reactions that require an external electron source. During the discharge, the anode at which oxidation takes place is the negative electrode that releases electrons to the external circuit, while the cathode, at which reduction occurs, is the positive electrode that acquires electrons from the external circuit. The negative and positive electrodes are reversed during a charging process (Nguyen & Savinell, 2010; Winter & Brodd, 2004). On the other hand, in a galvanic cell in which a spontaneous redox reaction occurs, the electrons flow from the anode to the cathode through the external circuit. Thus, the anode is always the negative electrode and the cathode is always the positive electrode (Biesheuvel et al., 2009).

Electrochemical characterization of any electrochemical system depends on different factors, including WE and CE conditions, electrolyte ions, charge, current, and voltage. These factors directly or indirectly affect the redox reactions and play a crucial role in determining the electrochemical properties of the electrode materials. The following equation explains how the current depends on different parameters (Choudhary et al., 2017):

$$i = \frac{nFAD_c\,(B_{bulk} - B_{surface})}{\delta} \qquad\qquad \textbf{Eq. 2.1}$$

where i is the measured current, n is the number of electrons in the redox reaction, D_c is the diffusion coefficient of the reacting species, A is the electrode area, F is Faraday's constant, B_{bulk} is the concentration of the species in the bulk solution, $B_{surface}$ is the concentration of the species at the electrode surface, and δ is the diffusion layer thickness.

Different electrochemical characterization techniques can be used to investigate the electrochemical performance of different electrode materials, including cyclic voltammetry (CV), chronoamperometry (CA), chronopotentiometry (CP), galvanostatic charge-discharge cycling (GCD), and electrochemical impedance spectroscopy (EIS), A detailed description of each technique is given below:

2.1.1 Cyclic voltammetry (CV)

CV is a widely used technique in electrochemistry to study the behavior of electrode materials. It involves applying a linear voltage ramp and measuring the resulting current within a specific potential range. The CV cycle consists of positive or negative potential ramping in

the first half-cycle, followed by an opposite direction ramping in the second half-cycle. This technique can be performed with a single or multiple potential cycles. The shape of the CV curve provides valuable information about the redox reaction, capacitive properties, mass transport, and system reversibility.

The scanning speed (slope of the ramp signal) can be expressed as scan rate, which is measured in volts per unit of time. A fast scan rate decreases the size of the diffusion layer, and thus, increases the current response. For reversible electron transfer processes, the peak current increases linearly with the square root of the scan rate, as described by the Randles-Sevcik equation (Bard et al., 2022; Savéant, 2006):

$$i_p = 0.446\ nFAB_{bulk}\left(\frac{nFvD}{RT}\right)^{1/2} \qquad \textbf{Eq. 2.2}$$

where i_p is the peak current, v is the scan rate (V s^{-1}), n is the number of electrons transferred in the redox system, A is the electrode surface area (cm^2), D is the diffusion coefficient (cm^2 s^{-1}), B_{bulk} is the analyte bulk concentration (mol cm^{-3}), F is Faraday's constant, R is the universal gas constant, and T is the absolute temperature. In the context of a reversible CV, these terms are defined in **Fig. 2.2A**

Evaluation of the reversibility of an electrochemical system (reversible, quasi-reversible, and irreversible) can be performed by extracting parameters from the cyclic voltammogram. These parameters include anodic peak current (i_{pa}), cathodic peak current (i_{pc}), anodic peak potential (E_{pa}), cathodic potential (E_{pc}), and the potential difference between E_{pa} and E_{pc}. If the system is electrochemically reversible, the ratio between the anodic and cathodic peak currents (i_{pa}/i_{pc}) is equal to 1, and the difference between E_{pa} and E_{pc} (ΔE_p) (also called peak-to-peak separation) is ~57 mV for a 1-electron transfer at 25 °C based on the following equation (Scholz, 2010):

$$\Delta E_p = 2.22\ \frac{RT}{nF} = \sim 57\ \text{mV} \qquad \textbf{Eq. 2.3}$$

On the contrary, if the ratio of i_{pa}/i_{pc} is not equal to 1, and $\Delta E_p > 57$ mV, then the electrochemical system is quasi-reversible, indicating a slow redox reaction. On the other hand, the cyclic voltammogram of irreversible chemical species shows only one anodic or cathodic peak. These three situations are outlined in Figure **2.2B** (T. Kim et al., 2020).
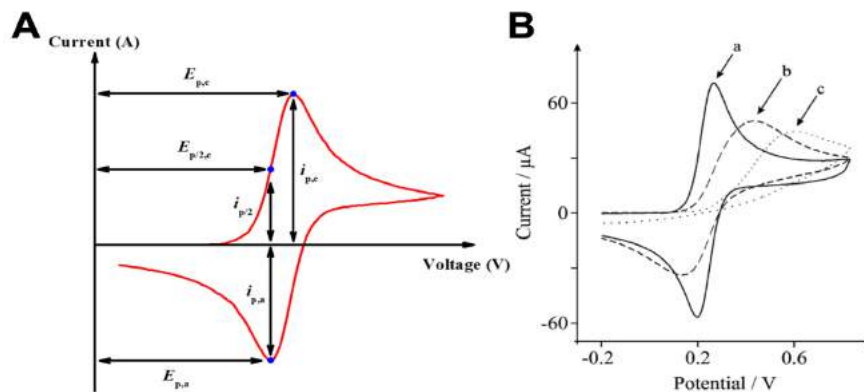
Figure 2.2 **(A)** example of cyclic voltammogram. **(B)** Comparison of CV shape in different electrochemical systems: a) reversible, b) quasi-reversible, and c) irreversible. Reprinted from (T. Kim et al., 2020). With permission from Journal of Electrochemical Science and Technology.

Cyclic voltammograms also provide information about the capacitance behavior at different scan rates. The specific capacitance of an electrode material can be calculated from the CV based on the following equation (Choudhary et al., 2017):

$$C_s = \frac{\int IdV}{v.M.\Delta V}$$ **Eq. 2.4**

where C_s is the specific capacitance (F/g), ΔV is the potential window (V), M is the mass of electroactive material (g), v is the scan rate (mV s^{-1}), and IdV is the area under the CV curve.

2.1.2   Chronopotentiometry (CP)

The term "Chronopotentiometry" is derived from the words "chrono" which stands for time (or function of time), and "poten" which refers to the potential (Monk, 2008). CP is a technique in which a single or step current is applied (also called a galvanostat), and the potential response is measured as a function of time (Bard et al., 2022). Prior to applying current, the analyte concentration is similar at the electrode surface and in the bulk solution. This equilibrium state establishes the open circuit potential (OCP), which refers to the potential difference between WE and RE when no current flows between the electrodes. Once the current is applied, the amount of analyte is reduced at the electrode surface. Therefore, the concentration of the analyte at the electrode surface decreases, leading to the formation of an analyte concentration gradient between the bulk solution and the electrode surface. This change

in the analyte concentrations leads to a change in the potential response (Choudhary et al., 2017). The CP technique can be conducted in different ways: by applying constant current, linearly rising current, current reversal, and cyclic current, as presented in **Fig. 2.3** (Pyun et al., 2012).
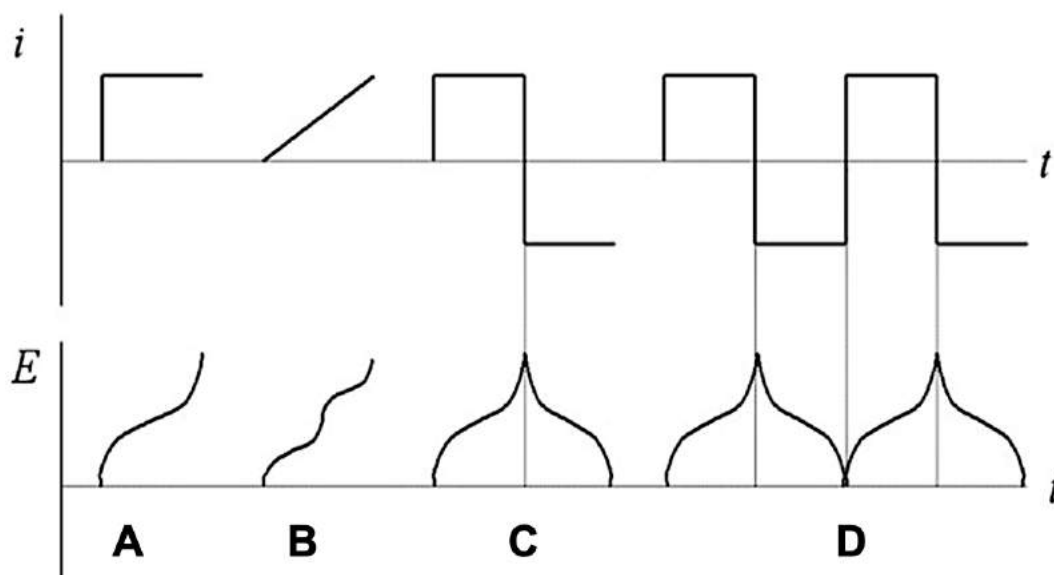
Figure 2.3   Different types of CP techniques. (A) constant current. **(B)** linearly rising current. **(C)** current reversal. **(D)** cyclic current. Reprinted from (Pyun et al., 2012). With permission from Springer.

In constant current CP, an anodic (or cathodic) current is applied to the electrode, causing the electroactive species to undergo oxidation (or reduction) at a constant rate. When the concentration of the reactant reaches zero at the electrode surface, the electrode potential will shift towards more anodic (or cathodic) values. Thus, the CP shape is related to the reversibility of the electrode reaction (Pyun et al., 2012). In the *in-situ* STXM study (**Chapter 9**), I used this technique (constant current CP) to electrochemically deposit MnO_2 on the microchip gold electrode from an electrolyte solution containing $MnSO_4$ as a precursor.

2.1.3   Chronoamperometry (CA)

CA is an electrochemical technique used to study the electrode redox reaction. In this method, single or multiple step potentials are applied while monitoring the current produced at the working electrode as a function of time and constant overpotential. After applying a constant potential to the working electrode, the potential steps immediately from the point where no faradaic reaction exists to the point where the oxidation or reduction reaction occurs (**Fig. 2.4A**). Over time, the concentration of the electroactive species at the electrode surface reaches zero, resulting in formation of a concentration gradient. As long as the working electrode maintains a constant potential, the diffusion layer formed due to the concentration gradient expands away from the electrode surface, causing a decrease in the slope of the concentration gradient, which consequently leads to the decay of the generated current (**Fig. 2.4B** and **C**). CA is described by the standard Cottrell equation, which identifies the decay of electrode current over time (Pyun et al., 2012; Scholz, 2010):

$$i(t) = nFAB\sqrt{\frac{D}{\pi.t}} \qquad \textbf{Eq. 2.5}$$

where i is the current, n is the number of electrons transferred per reaction step, A is the electrode surface area (cm^2), D is the diffusion coefficient (cm^2 s^{-1}), B is the concentration of active species (mol cm^{-3}), F is Faraday's constant and t is the time.
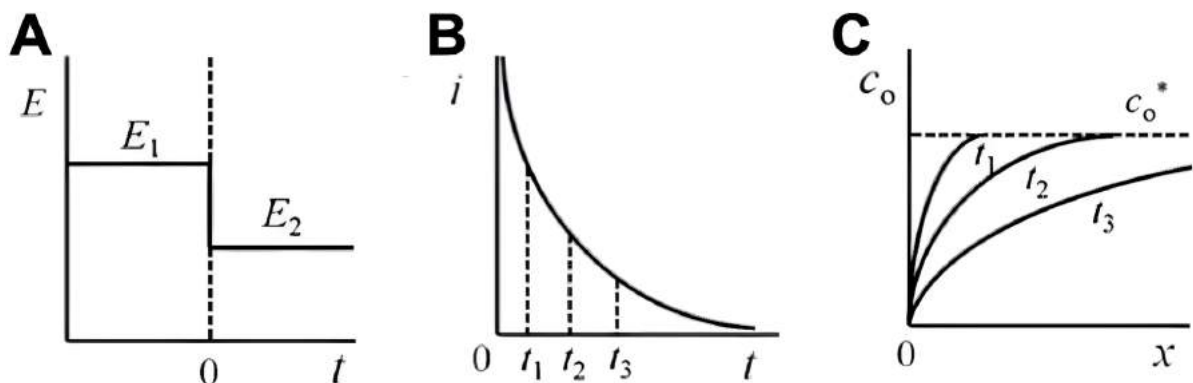
Figure 2.4   Schematic of CA experiment. (A) step potential. **(B)** generated current as a function of time. **(C)** expected diffusion layer profile of the active species during CA measurement. Reprinted from (Pyun et al., 2012). With permission from Springer.

2.1.4   Electrochemical impedance spectroscopy (EIS)

EIS is an important technique that is widely used to determine the impedance of an electrochemical cell. EIS is used in the characterization of energy storage devices. An electrochemical cell with a high impedance may have considerable over-potential, low-rate capabilities, and low energy efficiency (Pyun et al., 2012). Therefore, it is crucial to understand the changes in the impedance that occur during charging and discharging processes and over a large number of cycles. EIS measures the impedance of an electrochemical cell by applying a low-amplitude sinusoidal AC voltage or AC current on the measured electrode while measuring the amplitude and phase angle of the sinusoidal response as a function of frequency (Pyun et al., 2012). A Nyquist plot (**Fig. 2.5**) is usually used to analyze EIS data by plotting the real part of the impedance against the negative of the imaginary part of the impedance. The applied voltage can be calculated from the following equation (Pyun et al., 2012):

$$E(t) = E_0 \, \cos(\omega t) \qquad\qquad \textbf{Eq. 2.6}$$

where $E(t)$ is the applied potential as a function of time (t), E_0 is the potential amplitude, and ω is the angular frequency (rad/s), defined as the number of oscillations per unit time multiplied by 2π. Subsequently, the generated current can be expressed as (Pyun et al., 2012):

$$i(t) = i_0 \, \cos(\omega t - \varnothing) \qquad\qquad \textbf{Eq. 2.7}$$

where $i(t)$ is the generated current as a function of time, i_0 is the current amplitude, and $\varnothing$ is the phase angle. Based on **Eq. 2.6** and **Eq. 2.7**, the system impedance $Z(t)$ can be calculated from the time dependent version of Ohm's law as follows (Pyun et al., 2012):

$$Z(\omega) = \frac{E(t)}{i(t)} = Z_0 \, \frac{\cos(\omega t)}{\cos(\omega t - \varnothing)} \qquad\qquad \textbf{Eq. 2.8}$$

where Z_0 is the Warburg coefficient (defined as a constant phase element with a 45° constant phase shift). Further, the impedance and the absolute value of the impedance vector can be represented using complex algebra as (dos Santos et al., 2023):

$$Z = Z_r + Z_{img} \qquad\qquad \textbf{Eq. 2.9}$$

$$|Z| = \sqrt{Z_r^2 + Z_{img}^2} \qquad\qquad \textbf{Eq. 2.10}$$

where Z_r is the real impedance, Z_{img} is the imaginary impedance, and $|Z|$ is the absolute value of the impedance vector.
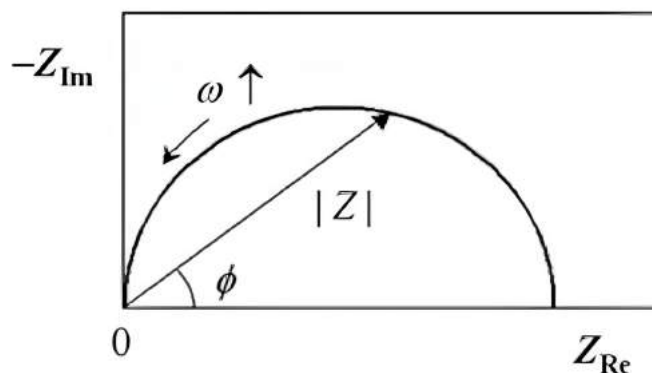
Figure 2.5 Schematic of Nyquist plot showing the phase angle (ϕ), angular frequency (ω), and the absolute value of the impedance vector. Reprinted from (Pyun et al., 2012). With permission from Springer.

2.2   Energy storage mechanisms

2.2.1   Electrical double-layer energy storage

Electrical double-layer (EDL) energy storage occurs through a reversible adsorption/desorption of electrolyte cations at the electrode/electrolyte interface. In EDL energy storage energy is stored physically (electrostatically) without any faradaic reactions. During charging processes, negative and positive charges (anions and cations) of the electrolyte are polarized toward the anode and cathode, respectively, and accumulate on the surface of the solid electrode material to form an EDL (also called Helmholtz Double Layer) (Bard et al., 2022). EDL capacitors can deliver electrical energy quickly because the charges only move small distances. However, the amount of stored energy is limited, resulting in a much lower energy storage capacity compared to other energy storage systems (Liu et al., 2018). Ideally, carbon-based materials (such as activated carbon, graphite, and carbon nanotubes) are used as electrode materials (Chen et al., 2014) owing to their high surface area and excellent electrical conductivity, which consequently reduces the resistivity and provides a short ion diffusion pathway (Marichi et al., 2017).

In EDL capacitors, the current responds linearly with the scan rate, and the cyclic voltammogram has a rectangular shape (Liu et al., 2018), as presented in **Fig. 2.6A**. The charging and discharging processes at the surface of the cathode and anode can be described as follows (Kour et al., 2022; Zheng et al., 1997):

- At the cathode (negative electrode):

  Charging: $\quad CD + C^+ + e^- \rightarrow (CD^-C^+)_{surface}$ **Eq. 2.11**

  Discharging: $(CD^-C^+)_{surface} \rightarrow CD + C^+ + e^-$ **Eq. 2.12**
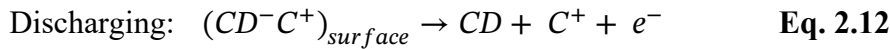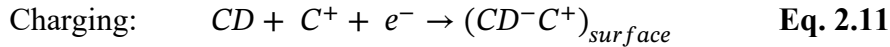
- At the anode (positive electrode):

  Charging: $\quad AD + A^- \rightarrow ((AD)^+A^-)_{surface} + e^-$ **Eq. 2.13**

  Discharging: $(AD^+A^-)_{surface} + e^- \rightarrow AD + A^-$ **Eq. 2.14**
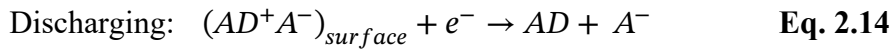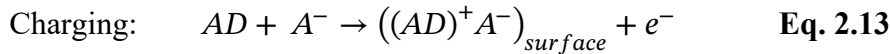
where CD is the cathode surface, C^+ is the electrolyte cation, AD is the anode surface, and A^- is the electrolyte anion.

The EDL capacitance can be calculated from the following equation (Bilal et al., 2022; Huang et al., 2021; Liu et al., 2018):

$$C_{dl} = \frac{q}{V} = \frac{\varepsilon_r\, \varepsilon_0\, A}{d_s} \qquad \textbf{Eq. 2.15}$$

where C_{dl} is the EDL capacitance, q is the total charge transferred at potential V, ε_r is the electrolyte dielectric constant, ε_0 is the dielectric constant of vacuum, d_s is the charge separation distance, and A is the electrode surface area.

2.2.2 Pseudocapacitance

Pseudocapacitance is an energy storage mechanism that involves adsorption/desorption and rapid redox reactions on/near the electrode surface. This process involves charge transfer without any significant changes in the bulk phase. During charging/discharging processes, the electrode materials undergo reversible redox reactions, resulting in a flow of faradaic current through the supercapacitor cells (Augustyn et al., 2014). Intercalation pseudocapacitance (battery-like) is another type of faradaic process, in which the electrolyte cation intercalates into the crystal structure of the active electrode material. Unlike batteries, this process occurs

without phase transformation during the charge transfer processes (Liu et al., 2018). The faradaic redox reaction can be presented as follows:

$$MO_x + yA^+ + xe^- \leftrightarrow MO_xA_y \qquad \textbf{Eq. 2.16}$$
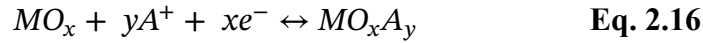
Similar to EDL, pseudocapacitance (C_{sp}) can be calculated as:

$$C_{sp} = \frac{q}{V} \qquad \textbf{Eq. 2.17}$$

An ideal capacitive system exhibits symmetric cyclic voltammograms **(Fig. 2.1B)** with minimal or no potential shifts between the anodic and cathodic peaks, especially at slow scan rates (Gogotsi & Penner, 2018).

2.2.3   Intercalation and deintercalation

Rechargeable batteries, such as lithium-ion batteries, store charge by intercalation or deintercalation of electrolyte cations into the cathode, driven by an electrical potential. During the discharge process, the electroactive species of the cathode material is reduced, and electrolyte cations are intercalated into the available sites in the crystal lattice of the cathode material. To maintain electroneutrality of the system, electrons flow from the negatively charged anode to the positively charged cathode through the external circuit. In contrast, during the charging process, the flow of ions and electrons is reversed, so that the electrolyte cations are deintercalated from the cathode lattice structure, and the electrons flow back to the negatively charged anode (Massé et al., 2017; Yan et al., 2023). The total energy (E) discharged from a battery is the integral of its voltage (V) with respect to its capacity (C_s) as described below (Massé et al., 2017):

$$E = \int V(C)\, dC_s \qquad \textbf{Eq. 2.18}$$

The maximum specific capacity of the active electrode is determined by the number of electrons injected or removed during cycling process (Massé et al., 2017):

$$C_{s\,max} = \frac{nF}{3.6\,MW} \qquad \textbf{Eq. 2.19}$$

where $C_{S\,max}$ is the maximum specific capacity (mAh/g), n is number of electrons inserted per unit of reaction, F is Faraday's constant, and MW is the molecular weight of reactant. In

contrast to EDL capacitors, the cyclic voltammogram of supercapacitors that use a redox active electrode material exhibits oxidation and reduction peaks (Shin et al., 2020). **Figure 2.6(A-D)** presents schematic cyclic voltammograms of supercapacitors and batteries (Gogotsi & Penner, 2018). **Figure 2.7(A-E)** illustrates different energy storage mechanisms and identifies the electrode active materials used in each type (Wang et al., 2019).
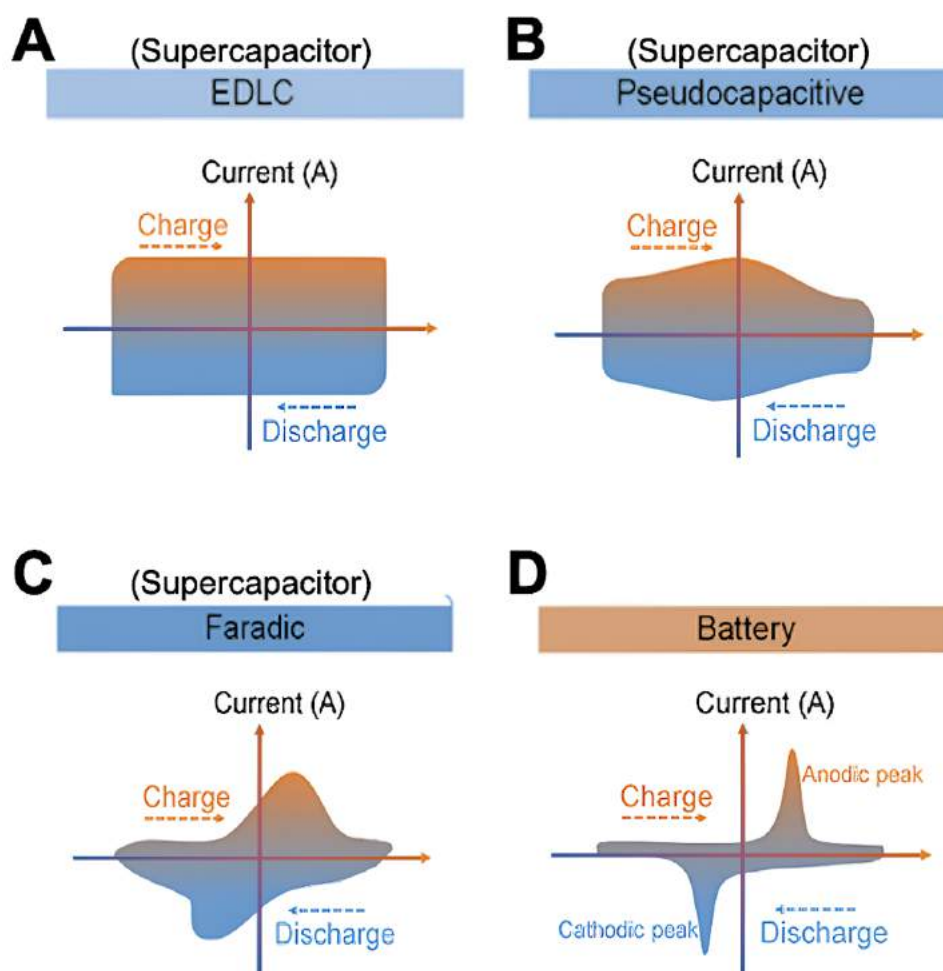
Figure 2.6 Schematic cyclic voltammograms of: (A) EDL capacitors. **(B)** pseudocapacitive material (combination of surface redox and intercalation). **(C)** faradaic (dominated by redox reaction, battery-like CV). **(D)** typical battery CV. Reprinted from (Huang et al., 2022). With permission from WILEY.
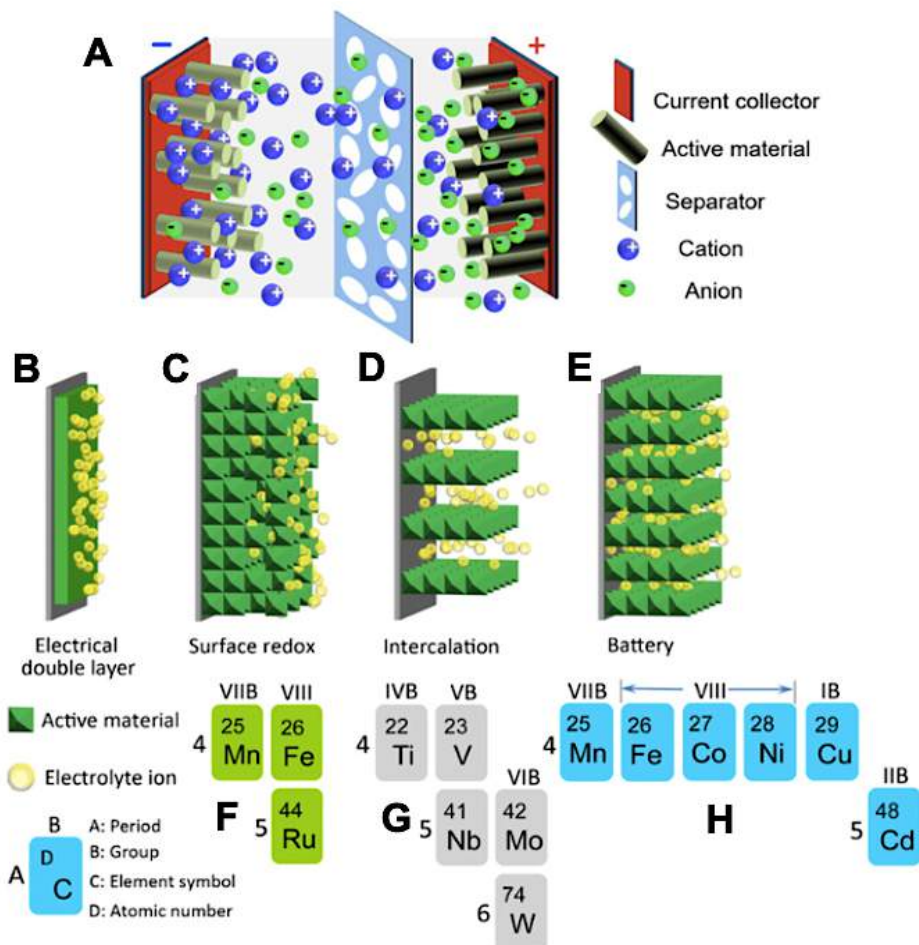
Figure 2.7 **(A)** The schematic illustration of the supercapacitor structure. **B)** electrical double layer capacitance**. (C)** surface redox capacitance. **(D)** intercalation capacitance. **E)** battery behavior. **(F-H)** electrode active materials used in each type. Reprinted from (Wang et al., 2019). With permission from Elsevier.

Energy storage mechanisms can be deduced from the CV shape as presented in **Fig. 2.6**. In general, the CV of supercapacitors has a rectangular shape. EDL-based materials, such as carbonaceous materials, have an ideal rectangular CV shape (**Fig. 2.6A**). In pseudocapacitive-based electrode materials, such as Mn oxides, faradaic electron transfer (redox) and non-faradaic charge storage (EDL) occur, the CV shape for such systems have a non-ideal rectangular shape (**Fig. 2.6B**). Some supercapacitor electrode materials, such as nickel and cobalt oxides or hydroxides, are dominated by redox mechanisms, and thus, the CV

shape has widely separated peaks (**Fig. 2.6C**). On the other hand, the CV of battery electrode materials always has sharp, well separated oxidation and reduction peaks, as shown in **Fig. 2.6D**. All studies in this thesis were performed on manganese oxide-based electrode materials. These oxides exhibit surface redox reactions, as presented in **Fig. 2.7**, and the CV have a non-ideal rectangular shape, as illustrated by the experimental CV measurements presented in **Chapter 5**, **Fig. 5.6B**.

2.3   Thermodynamics and kinetics of energy storage

The electrochemical energy storage properties are primarily determined by the thermodynamics and kinetics of one or more specific electrochemical reactions. The basic thermodynamic equation for a reversible electrochemical reaction is (Frackowiak & Béguin, 2013; Winter & Brodd, 2004).

$$\Delta G^{\circ} = \Delta H^{\circ} - T\Delta S^{\circ} \qquad \text{Eq. 2.20}$$

where ΔG is the Gibbs free energy, ΔH is the enthalpy, ΔS is the entropy, and T is the absolute temperature. The terms ΔG, ΔH, and ΔS are state functions and depend only on the identity of the materials and the initial and final states of the reaction. The degree symbol (°) is used to indicate a standard condition (1 M concentration, 1 bar, and 25 °C).

The net available electrical energy from a certain reaction is determined by ΔG, which is the difference in free energy of products and reactants. By calculating ΔG, we can determine the maximum amount of electrical energy obtained from the reaction. The relation between ΔG and the cell potential is (Frackowiak & Béguin, 2013; Winter & Brodd, 2004):

$$\Delta G = -nFE_{cell} \qquad \text{Eq. 2.21}$$

or

$$\Delta G^{\circ} = -nFE^{\circ} \qquad \text{Eq. 2.22}$$

where ΔG° is the standard Gibbs free energy, n is the number of electrons transferred in a reaction, F is the Faraday's constant (96485 C/mol e⁻), E° is the standard potential, and E_{cell} is the cell potential (not necessarily under standard conditions).

Spontaneous reactions are characterized by a negative ΔG and positive E_{cell} values. Positive ΔG and negative E_{cell} values correspond to a non-spontaneous reaction. Standard Gibbs free energy is related to the equilibrium constant as follows (Hem, 1963):

$$\Delta G° = -RT \ ln \ K \qquad \qquad \textbf{Eq. 2.23}$$

where $\Delta G°$ is the standard Gibbs free energy, R is the gas constant, T is the absolute temperature, and K is the equilibrium constant of the reaction. K represents the relationship between the reactants and products when the chemical reaction (aA+bB $\leftrightarrow$ cC+dD) reaches the equilibrium and can be defined for that reaction as follows (Langmuir, 1997):

$$K = \frac{[C]^c[D]^d}{[A]^a[B]^b} \qquad \qquad \textbf{Eq. 2.24}$$

For reactions that are not at a state of equilibrium, reaction quotient (Q) is used instead of K. Q is equivalent to the relative amounts of products and reactants present during a chemical reaction and can be expressed as $\frac{[Red]}{[Ox]}$, in which [Red] and [Ox] is the concentration of the reduced and oxidized chemical species, respectively. At the state of equilibrium, Q is equal to K, and ΔG = zero. When Q < K, the reaction will move in the forward direction (reaction will be shifted toward the products). In contrast, when Q > K, the reaction will proceed in the reverse direction (toward reactants) (Langmuir, 1997; Petrovic, 2021).

From **Eq. 2.22** and **2.23**, the relation between standard potential (E°) and equilibrium constant (K) can be expressed as (Hem, 1963):

$$E° = \frac{RT}{nF} \ ln \ K \qquad \qquad \textbf{Eq. 2.25}$$

The relation between E_{cell} and standard cell potentials can be expressed by the Nernst equation (Frackowiak & Béguin, 2013):

$$E_{cell} = E° - \frac{RT}{nF} \ ln \ Q \qquad \qquad \textbf{Eq. 2.26}$$

where $E°$ is the standard potential for the net electrochemical reaction, R is the gas constant, T is the absolute temperature, n is the number of electrons transferred per mole of reaction, F is the Faraday's constant (96485 C/mol e-), and Q is the reaction quotient. For example, the

electrodeposition of MnO_2 using $MnSO_4(aq)$ as a precursor can be described as follows (Hem, 1963):

$$Mn^{2+}SO_4^{2-}(aq) + 2H_2O \leftrightarrow MnO_2(s) + 4H^+(aq) + 2e^- + SO_4^{2-}(aq) \quad \textbf{Eq. 2.27}$$
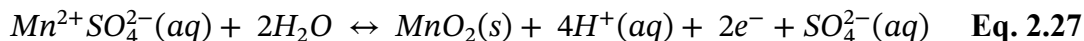
The standard potential (E°) of this two-electron transfer reaction is 1.23V vs SHE. When the concentration of $MnSO_4$ is 0.1M, the measured pH is 5.2. Since pH = -log[H$^+$], the concentration of H$^+$ is this case will be 10$^{-5.2}$. The reaction quotient (Q) $= \frac{[Red]}{[Ox]} = \frac{Mn^{2+}}{[H^+]^4}$. Thus, the actual cell potential (E$_{cell}$) can be calculated from the Nernst equation (**Eq. 2.26**) as follows:

$$E_{cell} = 1.23 - \frac{8.314 \ x \ 298.15}{2 \ x \ 96485} \ In \ \frac{0.1}{[10^{-5.2}]^4} = \ +0.66V \ vs \ SHE \qquad \textbf{Eq. 2.28}$$

Overall, the relations between the thermodynamic functions of Gibbs free energy (ΔG°), cell potential (E°), and equilibrium constant (K) (**Eq. 2.22**, **Eq. 2.23,** and **Eq. 2.25**) are used to predict the spontaneous direction of the reaction and the possibility of occurrence (spontaneous or non-spontaneous). Note that, thermodynamically spontaneous reactions may not occur due to kinetic limitations.

Since my research is focused on manganese-oxide materials, the half-reactions of the manganese and water system, with their corresponding ΔG° and standard potential (E°), are listed in **Table 2.1**. The Pourbaix diagram presented in **Fig. 2.8** (Crapnell & Banks, 2022) plots the equilibrium potential (E) between manganese and its various oxidized species as a function of pH. This diagram provides information about the thermodynamic stability of different MnOx species as a function of pH and applied potential in an aqueous solution. The dashed lines give the potential stability boundaries of water, in which the upper and lower dashed lines represent the equilibrium potential for oxygen and hydrogen evolution reactions. A horizontal line represents a pure redox reaction (pH-independent), while a vertical line represents a pure acid-base reaction (potential-independent). The positive or negative solid diagonal lines represent redox reactions that occur in an acid or alkaline medium (Verink, 2011; Yi & Majid, 2018).

Table 2.1   Half reactions of the manganese and water system with their corresponding $\Delta G°$ and standard potential (E°)

Half-reaction	$\Delta G°$ (kJ mol^{-1})	E°(V)
$Mn^{2+} + 2e^- \leftrightarrow Mn$	228	-1.181
$MnO + 2H^+ + 2e^- \leftrightarrow Mn + H_2O$	126	-0.653
$Mn_3O_4 + 2H^+ + 2e^- \leftrightarrow 3MnO + H_2O$	-43	0.223
$3Mn_2O_3 + 2H^+ + 2e^- \leftrightarrow 2Mn_3O_4 + H_2O$	-160	0.829
$2MnO_2 + 2H^+ + 2e^- \leftrightarrow Mn_2O_3 + H_2O$	-188	0.974
$MnO_4 + 4H^+ + 3e^- \leftrightarrow MnO_2 + 2H_2O$	-492	1.700
$Mn_3O_4 + 8H^+ + 2e^- \leftrightarrow 3Mn^{2+} + 4H_2O$	-349	1.809
$Mn_2O_3 + 6H^+ + 2e^- \leftrightarrow 2Mn^{2+} + 3H_2O$	-286	1.482
$MnO_2 + 4H^+ + 2e^- \leftrightarrow Mn^{2+} + 2H_2O$	-237	1.228
$O_2 + 4H^+ + 4e^- \leftrightarrow 2H_2O$	-474	1.228
$2H^+ + 2e^- \leftrightarrow H_2$	0	0.000
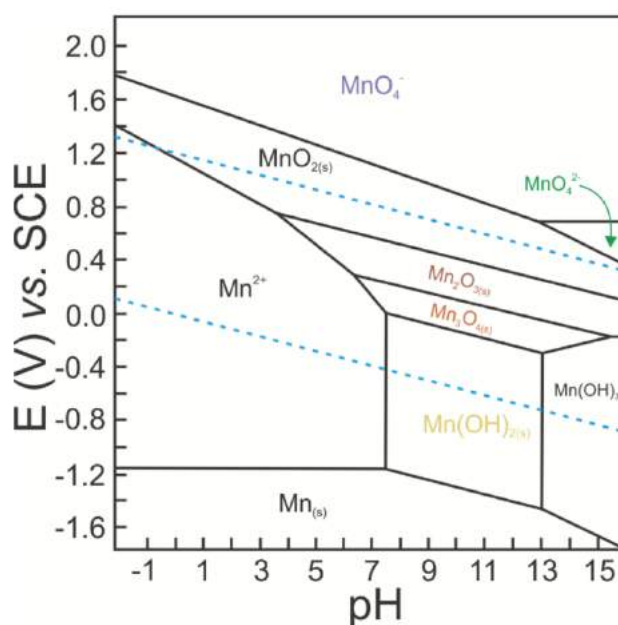
Figure 2.8   Pourbaix diagram of the Mn/H$_2$O system at 25 °C. Reprinted from (Crapnell & Banks, 2022). With permission from Elsevier.

Various experimental techniques are used to investigate the electrochemical behavior of battery reactions. Measurement of the current-voltage characteristics on the discharge curve (polarization curve) is the most common technique used to determine the relationship among discharge/charge rate, capacity, and battery's state of health (SOH). The conceptual polarization curve presented in **Fig. 2.9** can be divided into three potential regions related to the kinetics of the redox system: (1) Activation polarization (corresponding to charge transfer reactions), (2) ohmic polarization (due to ionic and contact resistances) and (3) concentration polarization (corresponding to mass transportation limitation) (Geyer et al., 2009; H. Wang et al., 2020).
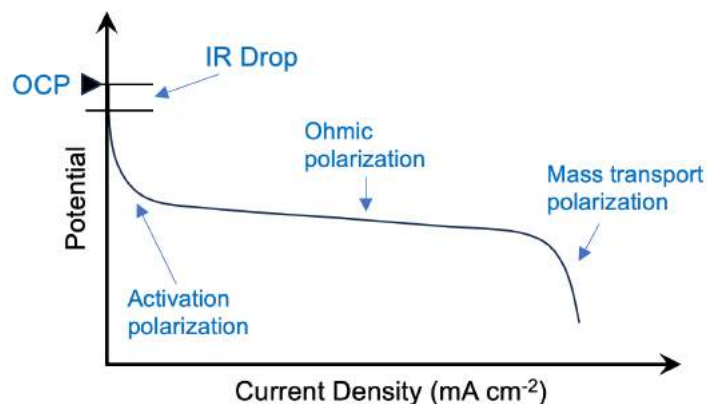
Figure 2.9 Schematic of typical polarization curve of energy storage systems. Adapted from (Geyer et al., 2009).

The difference between the experimental potential (where the redox reaction occurs) and the thermodynamic equilibrium potential can be expressed as overpotential (η) (Petrovic, 2021). From the polarization curve, the activation polarization follows the Tafel equation and can be calculated as follows (Winter & Brodd, 2004):

$$\eta = b \, log_{10} \frac{J}{J_0} \qquad\qquad \textbf{Eq. 2.29}$$

where b is the Tafel slope (mV dec.$^{-1}$), J is the current density (A/m^2), and J_0 is the exchange current density (A/m^2), which is the equal flow of current density in both directions at the

reversible potential (Abderezzak, 2018). The relationship between the overpotential (η), current (i), and ohmic resistance (R) can be expressed by Ohm's Law (Winter & Brodd, 2004):

$$\eta = iR \qquad \textbf{Eq. 2.30}$$

The concentration polarization resulting from mass transportation limitation is correlated to the overpotential as follows (Winter & Brodd, 2004):

$$\eta = \frac{RT}{n}\ln\left(\frac{B_{surface}}{B_{bulk}}\right) \qquad \textbf{Eq. 2.31}$$

where $B_{surface}$ is the concentration at the electrode surface, and B_{bulk} is the concentration in the bulk of the solution. In CV measurements, particularly for supercapacitors which exbibit EDL and pseudocapacitive behavior, the total current measured at a specific potential scan rate $i(v)$ is the sum of the current related to slow diffusion-controlled processes (i_{diff}), the current required for the formation of EDL at the electrode/electrolyte interface, and the current required to initiate fast redox reactions at the electrode surface (i_{cap}). These are related by to the following equation (Liu et al., 2018):

$$i(v) = i_{cap} + i_{diff} = av^b \qquad \textbf{Eq. 2.32}$$

where v is the scan rate, and both a and b are adjustable parameters. The b value, the slope of a linear plot of log (i) versus log (v), is used to obtain kinetic information regarding the electrochemical reactions **(Fig. 2.10A)**. A b value of 1 indicates fast near-surface activities (including surface redox reactions and EDL charging or discharging), In contrast, a b value of 0.5 corresponds to slow diffusion battery-type redox processes that occur in the bulk. The b value between 0.5 to 1.0 indicates a transition between pseudocapacitive and battery-type materials.

For better understanding of reaction mechanisms, quantitatively distinguishing between capacitive processes and diffusion controlled redox processes is crucial. When surface dominant reactions control the process, the response current exhibits a linear relationship with scan rate (v), while in the diffusion controlled redox processes the response current varies linearly with the square root of scan rate ($v^{1/2}$). The total response current can be expressed as follows (Liu et al., 2018; Liu et al., 1998):

$$i(v) = i_{cap} + i_{diff} = k_1 v + k_2 v^{1/2} \qquad \textbf{Eq. 2.33}$$

k_1 and k_2 values can be determined from the slope and intercept, respectively, of a linear fit to plots of $i(V)/v^{1/2}$ versus $v^{1/2}$. Based on that, we can differentiate between capacitive, and diffusion controlled redox processes **(Fig. 2.10 B and C)**.
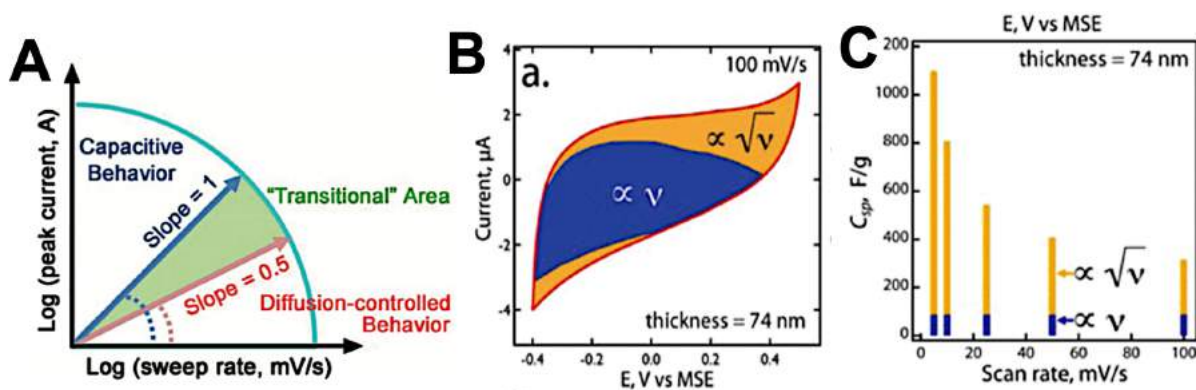
Figure 2.10 (A) Plot of log current vs log scan rate indicates the different b values. **(B)** example of CV differentiates surface ($\propto v$) and bulk ($\propto v^{1/2}$) charge contribution (E vs mercury sulfate electrode (MSE)). **(C)** example of a bar graph showing specific capacitance of surface and bulk material. Reprinted from (Liu et al., 2018). With permission from WILEY.

2.4 Manganese oxides

Various manganese oxides have been studied extensively as electrode materials for energy storage applications since their first use in supercapacitors in 1999 (Lee & Goodenough, 1999). Manganese (Mn) is a transition metal element with five unpaired 3d electrons. This electronic structure allows it to exist in various oxidation states, including Mn(II), Mn(III), Mn(IV), Mn(VII) (the highest oxidation state in the periodic table), and a mixed valence Mn(II/III), each with a variety of crystal structures. Manganese is the 5th most abundant metal in the earth's crust. It is non-toxic, low-cost, and relative to alternatives, the extraction from ores is environmentally friendly (Butt et al., 2023). Moreover, it has a wide positive potential window (1.0 V) compared to other transition metal oxides, such as NiO (0.5 V) (Paulose et al., 2017) and Co_3O_4 (0.5 V) (Liao et al., 2013). The potential window refers to the range of charging and discharging potentials where the chemical and physical changes of the electrodes

are reversible (Dai et al., 2015) (**Table 2.2**). In addition, manganese oxides exhibit high theoretical capacitance, which is 1370 F/g for MnO_2-based electrodes (Han et al., 2016). The theoretical capacitance is calculated from the following equation (Sun et al., 2020):

$$C_{th} = \frac{n \cdot F}{M \cdot V} \qquad\qquad \textbf{Eq. 2.34}$$

where C_{th} is the theoretical capacitance, n is the number of transferred electrons in the redox reaction, F is the Faraday's constant, M is the molar mass of the metal oxide, and V is the potential window.

Due to these physicochemical features, MnOx is used as an electrode material in several different types of EES systems, including lithium-ion batteries (LIBs), Zinc-ion batteries (ZIBs), supercapacitors, and metal-air batteries (MABs). The performance of MnOx-based electrodes is influenced by various parameters, including the specific oxide(s) crystal structures, morphology, electrical conductivity, and loading mass (Hu et al., 2018). The influence of each of these parameters is discussed in the following sections.

Table 2.2   Theoretical capacitance and potential window of different metal oxides.

Metal Oxide	Theoretical capacitance (Fg^{-1})	Potential window (V) vs SHE	Ref.
MnO_2	1370	1.0	(Han et al., 2016; Ke et al., 2023)
NiO	2584	0.5	(Paulose et al., 2017; Sung & Shin, 2020)
V_2O_5	2120	2.0	(Huang et al., 2019; Sung & Shin, 2020)
Co_3O_4	3560	0.5	(Liao et al., 2013)
RuO_2, xH_2O	1200-2200	1.2	(Chodankar et al., 2020; Sung & Shin, 2020)
Fe_2O_3	984	-0.9	(Chodankar et al., 2020; Sung & Shin, 2020)

2.4.1   Crystal Structures

The capacitance of MnOx is significantly influenced by the crystal structure, as cation transport and intercalation through the crystal structure are highly dependent on the tunnel size. For instance, MnO_2 has various crystallographic structures, including α-MnO_2(Hollandite), β-MnO_2 (Pyrolusite), γ-MnO_2 (Intergrowth), λ-MnO_2 (Spinel), δ-MnO_2 (Birnessite), and R-MnO_2 (Ramsdellite) **(Fig. 2.11)**. In α-MnO_2 and the 2D layered δ-MnO_2, the tunnel size is ~0.46 nm and ~0.7 nm, respectively. Larger tunnel sizes result in higher capacitance through more facile intercalation/deintercalation of electrolyte cations. On the contrary, λ-MnO_2 and β-MnO_2 have a lower capacitance due to a smaller tunnel size (< 0.3 nm) (Hu et al., 2018; Hu et al., 2017; Kitchaev et al., 2017).
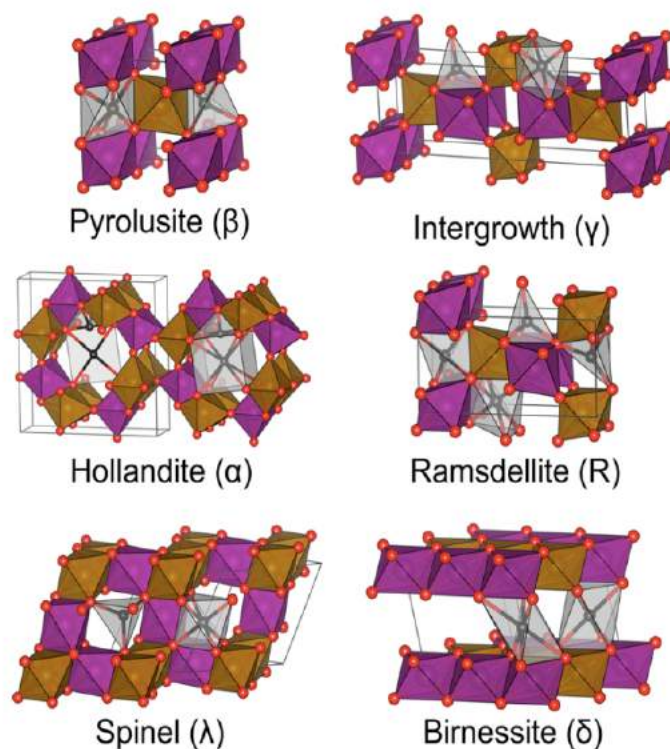
Figure 2.11 Different crystallographic structures of MnO$_2$ and predicted sites for cations intercalation. The purple spheres present spin-up and spin-down Mn atoms, brown spheres denote MnO_6 octahedra, and black spheres with the surrounding gray polyhedral displays predicted electrolyte cations intercalation sites. Reprinted from (Kitchaev et al., 2017). With permission from American Chemical Society.

2.4.2   Electrical Conductivity

Both electronic and ionic conductivity are crucial for efficient charge transfer and electrolyte ion diffusion during redox reactions in supercapacitor and battery electrodes. However, the poor electrical conductivity of MnOx-based materials has hindered their ability to achieve high capacitance. Therefore, extensive effort has been devoted to improve the electrical conductivity by either growing the MnOx electrode materials on conducting substrates such as carbon-based compounds (Ganguly et al., 2016; Yan et al., 2010) or metal foams (G. Wang et al., 2013)), or by doping MnOx with other transition metals (such as nickel (Ni) (G. Wang et al., 2013), cobalt (Co) (Tang et al., 2015), zinc (Zn) (Poonguzhali et al., 2015) and copper (Cu) (Hashem et al., 2011). **Figure 2.12A** presents a scanning electron microscope (SEM) image of MnO_2 and carbon nanotubes (CNTs) composites, while **Fig. 2.12B** and **2.12C** compare the electrochemical performance of MnO_2/CNTs in comparison to that of pristine CNTs and MnO_2 electrodes (Li Li et al., 2014).
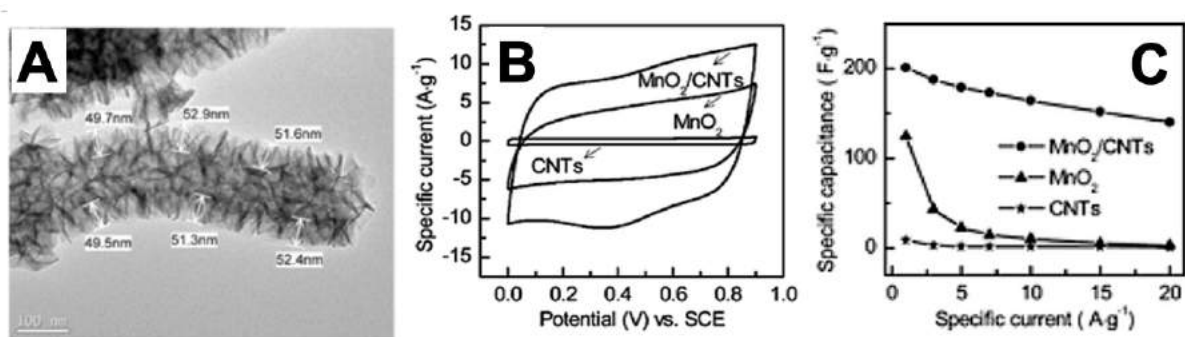
Figure 2.12 (A) SEM images of MnO_2/CNTs composite. **(B)** CVs of MnO_2/CNTs, MnO_2, and CNTs at the scan rate of 50 mV s^{-1}. **(C)** capacitance of pristine CNTs, MnO_2, and MnO_2/CNTs at different current densities (Li Li et al., 2014). With permission from American Chemical Society.

2.4.3   Morphology

The morphology of MnOx nanomaterials significantly impacts their electrochemical performance (including specific capacitance) due to its impact on the accessible surface area and redox-active sites (Wei et al., 2011). MnOx catalysts can be found in different shapes, such as nanowires, nanoflowers, nanorods, nanospheres, nanocubes, and nanobelts (see **Fig. 2.13**), depending on the preparation methods and precursors used (Dey & Kumar, 2020). Taking manganese dioxide as an example, MnO_2 nanowires with a diameter of 8-16 nm exhibit a higher capacitance (350 F/g) than nanorods with a diameter of 15-35 nm (243 F/g), owing to the availability of more redox-active sites for charge transfer and fast diffusion pathways (Wu, 2005). Recently, three-dimensional (3D) MnO_2 materials attracted attention as promising catalytic materials for supercapacitors (Yu et al., 2009) and batteries (Bi et al., 2019) applications. These materials have a significantly higher surface area compared to their bulk forms, providing more sites/unit mass for redox reactions.
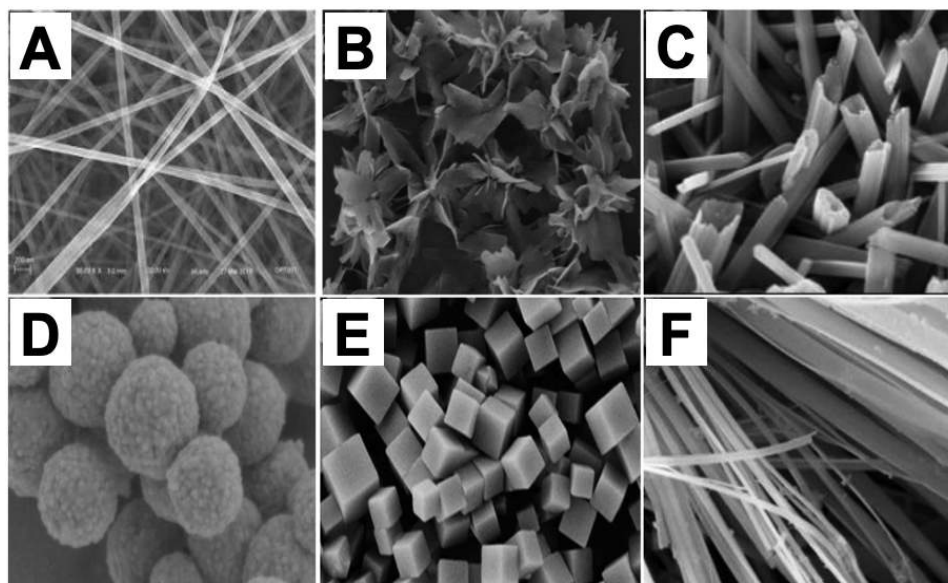
Figure 2.13 Manganese nanoparticles in various shapes. (A) nanowires **(B)** nanoflowers. **(C)** nanorods. **(D)** nanospheres. **(E)** nanocubes and **(F)** nanobelt (Dey & Kumar, 2020). With permission from ELSVIER.

2.4.4   Loading mass

Since pseudocapacitance mostly occurs at the surface or sub-surface of the electrode material (Eftekhari & Mohamedi, 2017), the gravimetric capacitance of MnOx-based electrodes decreases as the loading mass increases, especially for MnOx thin films (Kang et al., 2013; Vijayakumar et al., 2018). Increasing the electrode thickness may reduce the number of redox-active sites, resulting in a decrease in pseudocapacitance contribution. Therefore, high gravimetric capacitances for MnOx-based electrodes tend to correspond to low loading masses (> 1 mg/cm^2) (Hu et al., 2018; Kang et al., 2013). To achieve a high capacitance with high loading mass, the morphology of the electrode nanomaterial, as well as the substrate structure need to be optimized (Hu & Wang, 2015; Huang et al., 2015).

2.4.5   Challenges of Mn oxides-based electrodes

   I.   Electrochemical performance of manganese oxides-based electrodes is limited by their poor electrical conductivity ($10^{-5} – 10^{-6}$ S cm^{-1}) (Huang et al., 2014; Yu et al., 2016).

  II.   The practical applications of manganese oxides-based electrodes are hindered by their significantly lower actual capacitance value compared to the theoretical value (1380 F g^{-1}) (Guo et al., 2019).

 III.   Poor morphological stability during charging/discharging processes.(Guo et al., 2019; Han et al., 2020).

  IV.   Irreversible phase transformation (Jing et al., 2022; Wu et al., 2020).

   V.   Irreversible reduction and dissolution of Mn^{4+} to Mn^{2+} owing to the high oxidation overpotential from divalent manganese to tetravalent manganese (Jing et al., 2022; Li et al., 2012; Sopčić et al., 2013), which is still under debate.

  VI.   Microstructure changes in MnO$_2$-based electrodes during charge storage (Chen et al., 2015; Iamprasertkun et al., 2017).

2.4.6   Hypothesis and experimental design of my studies of MnOx-based electrodes

For better understanding of chemical and physical changes that take place during charging and discharging processes, and to address specific challenges of MnO$_2$-based

electrodes, different testable hypotheses (TH) and associated experimental designs are listed
below:

I. MnO_2 electrode will be reduced to both Mn^{3+} and Mn^{2+} species during reduction process.

   ▪ Experimental tests: Investigate MnOx oxidation state change at Mn 2p and O K
      edges while applying a reduction potential.

   ▪ Predicted outcomes:

   ⇒ If: MnO_2 didn't reduce, then TH is FALSE.

   ⇒ If: MnO_2 reduced to Mn^{3+} only, then TH is FALSE.

   ⇒ If: MnO_2 reduced to Mn^{3+} and Mn^{2+}, then TH is TRUE.

II. Formation of EDL on the surface of the MnO_2 electrode in Na_2SO_4 electrolyte during
    charging process can be detected by spectroscopic measurements.

   ▪ Experimental tests: Compare the intensity of Na signals (at Na K edge) at the edge
      of the MnO_2 electrode and in the electrolyte region during a reduction process.

   ▪ Predicted outcomes:

   ⇒ If: Intensity of Na signals at the edge of the electrode > electrolyte, then TH is
      TRUE.

   ⇒ If: Intensity of Na signals at the edge of the electrode = electrolyte, then TH is
      FALSE.

   ⇒ If: Intensity of Na signals at the edge of the electrode < electrolyte, then TH is
      FALSE.

III. The morphology change of MnO_2 is due to the redeposition of dissoluble Mn^{2+} species to
    MnO_2 during the oxidation process.

   ▪ Experimental tests: Measure the Mn oxidation state of the (MnOx) growth formed
      on WE after the oxidation process.

   ▪ Predicted outcomes:

   ⇒ If: the oxidation state of the Mn growth is Mn^{4+}, then TH is TRUE.

   ⇒ If: the oxidation state of the Mn growth is Mn^{2+} or Mn^{3+}, then TH is FALSE.

   ⇒ If: the growth is not MnOx species, then TH is FALSE.

IV. Mn^{2+}(aq) species can be reversibly oxidized to MnO_2 during the oxidative phase of oxidation/reduction processes.

- <u>Experimental tests:</u> Investigate the oxidation state change of Mn species on WE and CE at Mn 2p edges.

- <u>Predicted outcomes:</u>

$\Rightarrow$ If: Mn^{2+} is oxidized to Mn^{4+} after repeated oxidation processes, then TH is TRUE.

$\Rightarrow$ If: Mn^{2+} is oxidized to Mn^{3+} after repeated oxidation processes, then TH is FALSE.

$\Rightarrow$ If: Mn^{2+} didn't oxidize and the oxidation state remains as it is, then TH is FALSE.

V. Local pH changes to a more acidic value can reduce MnO_2 electrode material without an applied potential.

- <u>Experimental tests:</u> Investigate the oxidation state of Mn species at OCP in different electrolyte pH.

- <u>Predicted outcomes:</u>

$\Rightarrow$ If: MnO_2 reduced at acidic pH and not at alkaline pH, then TH is TRUE.

$\Rightarrow$ If: MnO_2 is not reduced at acidic pH, then TH is FALSE.

$\Rightarrow$ If: MnO_2 reduced at both acidic and alkaline pH, then TH is FALSE.

VI. High capacitance of Mn_3O_4 supercapacitor electrodes is due to conversion of Mn_3O_4 to MnO_2 during activation cycles.

- <u>Experimental tests:</u> Investigate the oxidation state of as-prepared Mn_3O_4 after different activation cycles.

- <u>Predicted outcomes:</u>

$\Rightarrow$ If: Mn_3O_4 converted or partially converted to MnO_2, then TH is TRUE.

$\Rightarrow$ If: Mn_3O_4 didn't convert to MnO_2, then TH is FALSE.

VII. Using quercetin (as capping agent) in preparation of Mn_3O_4 supercapacitor electrodes will induce the oxidation of Mn_3O_4 to MnO_2 more than using high energy ball milling (HEBM) method.

- <u>Experimental tests:</u> Compare oxidation state changes of the as-prepared Mn_3O_4 electrode using quercetin as capping agent with HEBM method after different activation cycles.

- <u>Predicted outcomes:</u>

$\Rightarrow$ If: Mn_3O_4 prepared by quercetin oxidized to MnO_2 > electrodes prepared by HEBM method, then TH is TRUE.

$\Rightarrow$ If: Mn_3O_4 prepared by quercetin oxidized to MnO_2 = electrodes prepared by HEBM method, then TH is FALSE.

$\Rightarrow$ If: Mn_3O_4 prepared by quercetin oxidized to MnO_2 < electrodes prepared by HEBM method, then TH is FALSE.

In order to achieve these goals, it is necessary to use an analytical method that can measure the oxidation state of Mn oxides as a function of the charge state of the electrode, current/potential response, and microstructure changes under controlled electrolyte and electrochemical conditions. In the next chapter, the methodology of scanning transmission X-ray microscopy (STXM) is described. STXM was used to test the hypotheses outlined above.

Chapter 3
Techniques and Principles

This chapter describes the fundamental principles of X-ray absorption spectroscopy (XAS) including Transmission, Fluorescence yield (FY) and Electron yield (EY) detection modes. The use of accelerator-based synchrotron light sources is discussed. The principles and instrumentation for scanning transmission X-ray microscopy (STXM) are then presented. This is followed by an introduction of ex-situ and in-situ studies using STXM as spectromicroscopic technique compared to stand-alone spectroscopy and microscopy techniques.

3.1   Principles of X-ray absorption spectroscopy

Since the first discovery of the X-ray by Wilhelm Röntgen in 1895 (Röntgen, 1896), X-ray have been used in many ways to study matter. In the early 20th century, Charles Barkla discovered that, when sufficiently excited (typically using a high energy electron beam), each element of the periodic table emits characteristic X-rays (Barkla, 1903). Between 1912 and 1915, Max von Laue discovered X-ray diffraction (von Laue, 1915) and William Bragg and his son developed the first x-ray diffractometer (Bragg & Bragg, 1913). Henry Moseley plotted the frequencies of emitted X-rays versus atomic number and discovered that the square root of the frequency of the emitted x-ray is proportional to the atomic number. (Moseley, 1914; Moseley, 1913). These pioneer efforts, along with Niels Bohr's development of the atomic structure model (Bohr, 1913), have fundamentally advanced our understanding of matter.

X-ray absorption spectroscopy (XAS) measures photo-absorption processes in which a core (inner-shell) electron is excited into unoccupied energy levels, thereby promoting a system from its ground state to a high energy excited state. Because the energies of core electrons have discrete values, the response of each system is a specific function of the energy of the incident photon beam. An X-ray absorption spectrum is a plot of the probability of creating a core excited or ionized state as a function of X-ray energy. **Figure 3.1A** presents the X-ray absorption spectrum of α-MnO$_2$ in the region of O 1s and Mn 2p excitation and ionization. **Figure 3.1B** is an energy level sketch identifying schematically the origin of the spectral

features. The spectrum, its features and the underlying electronic transitions are discussed in greater detail in **chapter 6**. In brief, the O 1s spectrum shows 2 sharp peaks in the pre-edge region (529 – 535 eV) corresponding to excitation from O 1s to empty 3d valence levels. The Mn 2p spectrum exhibits 2 peaks in the 630 – 650 eV region corresponding to Mn $2p_{3/2} \rightarrow 3d$ excitation (L$_3$), and broad peaks in the 650 – 660 eV region corresponding to Mn $2p_{1/2} \rightarrow 3d$ excitation (L$_2$).
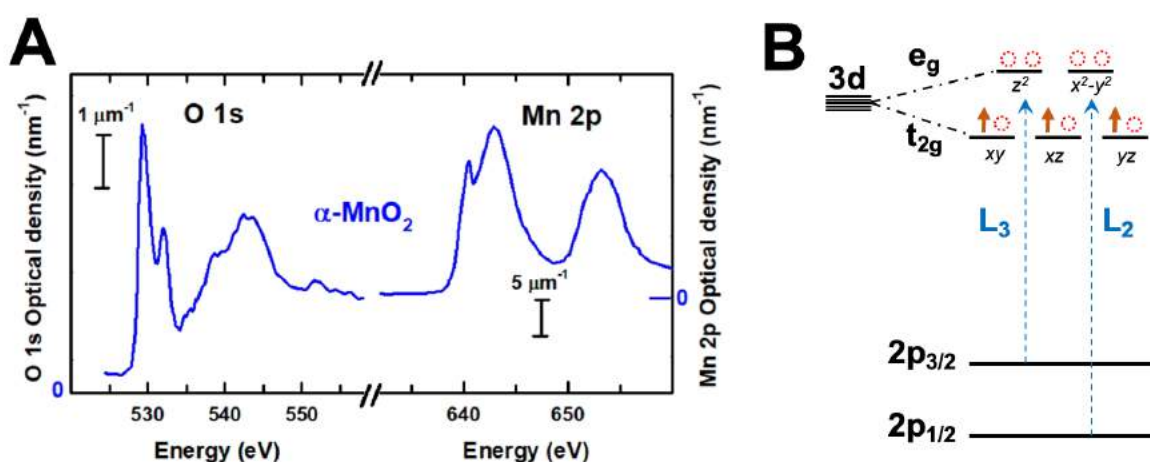
Figure 3.1 (A) Mn 2p and O 1s X-ray absorption spectra of α-MnO$_2$. **(B)** schematic diagram of Mn 2p → 3d transitions (dashed circles indicate 3d holes).

The X-ray absorption cross section (σ_x) is given by the number of electrons excited per unit time divided by the photon flux (number of incident photons per unit time per unit area) as follows (Stöhr, 1992):

$$\sigma_x = \frac{P_{if}(E)}{F_{ph}(E)} \qquad\qquad \textbf{Eq. 3.1}$$

where $F_{ph}(E)$ is the incident photon flux and $P_{if}(E)$ is the probability of a transition from an initial state $|\Psi_i\rangle$ to a final state $\langle\Psi_f|$ resulted from the time dependent electric field perturbation (V(E,t)) created by the incident X-ray. $P_{if}(E)$ can be expressed as follows (Stöhr, 1992):

$$P_{if}(\underline{E}) = \frac{2\pi}{\hbar} \left| \langle \Psi_f | V(\underline{E}, t) | \Psi_i \rangle \right|^2 \sigma_f(\underline{E}) \qquad \textbf{Eq. 3.2}$$

where $\sigma_f(\underline{E})$ is the energy density of the final states, and $\hbar$ is reduced Planck's constant. $F_{ph}(\underline{E})$ can be obtained by dividing the energy flux of the electromagnetic radiation by the photon energy as follows (Stöhr, 1992):

$$F_{ph}(\underline{E}) = \frac{\omega\, V_0(\underline{E})^2}{8\pi\hbar c} \qquad \textbf{Eq. 3.3}$$

where ω is the electromagnetic wave angular frequency, $V_0(\underline{E})$ is the potential vector amplitude of the electric field, and c is the speed of light.

Based on the incident photon energy XAS can be classified into the soft X-ray regime (40 - 2000 eV) and the hard X-ray regime (>5000 eV), while the intermediate range (1000 – 5000 eV) is labelled the tender X-ray regime. In the soft X-ray regime, the XAS in the ~60 eV region around the threshold of a core level excitation is often called the near edge x-ray absorption fine structure (NEXAFS). In the hard X-ray regime, the XAS spectrum is typically split into two regions, the X-ray absorption near edge structure (XANES) (again, ~60 eV around the core level threshold, analogous to NEXAFS) and the extended X-ray absorption fine structure (EXAFS) (typically 20 eV above threshold to 1000 – 2000 eV above threshold) (Liu & Weng, 2016). All XAS measurements reported in this thesis were performed in the soft X-ray regime and thus are labelled NEXAFS.

XAS spectra can be measured in many ways since any phenomenon which involves the initial creation of a core excited /ionized state will reflect the XAS process in some way.   The three most common detection modes are transmission (Parratt et al., 1957), electron yield (EY,) and fluorescence yield (FY) mode (Stöhr, 1992) are presented in **Fig. 3.2** (Watts et al., 2006). Transmission mode detection is related to XAS by the Beer-Lambert law **(Eq. 3.4)**. The EY and FY signals are linearly proportional to the XAS. In FY mode, the intensity of the X-ray photons emitted as the core hole decays are measured as a function of the incident X-ray energy. In the EY mode, the flux of electrons ejected from the sample as a function of the incident X-ray energy are measured, either directly using a current collector or electron spectrometer, or indirectly through the drain current from the X-ray ionized sample. Each of these modes have further subtleties, which are discussed briefly in the following sections.
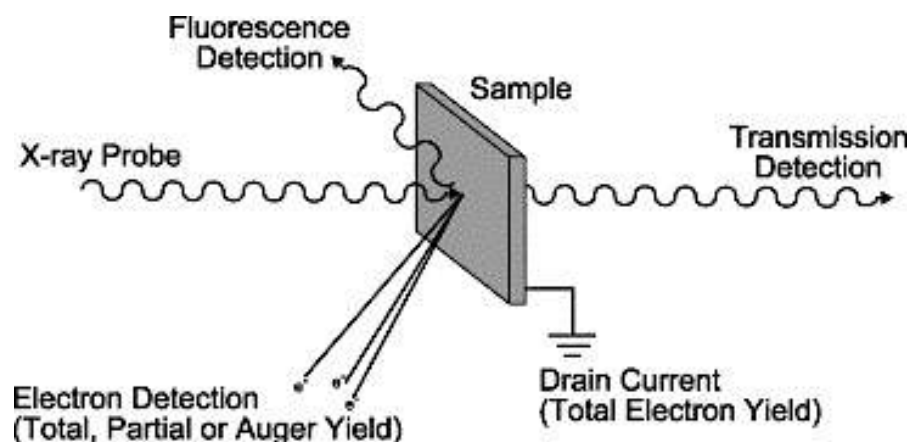
Figure 3.2   Schematic of the three main detection modes (Transmission, EY and FY) of NEXAFS spectroscopy (Watts et al., 2006). With permission from Elsevier.

3.1.1   Transmission mode

In transmission mode, when the X-ray penetration depth is greater than the sample thickness at all energies of interest, the XAS is derived from the transmitted and incident X-ray intensities by the Beer-Lambert law (Lambert, 1760). The optical density (OD), also known as absorbance (*A*), is related to the transmitted X-ray intensity by (Hitchcock, 2012):

$$OD(E) = \ln\left(\frac{I_0(E)}{I(E)}\right) \qquad \textbf{Eq. 3.4}$$

where I_0 is the incident X-ray photon flux, while I is the transmitted photon flux. The OD can be related to the sample thickness and density as:

$$OD(E) = \mu(E).\rho.l \qquad \textbf{Eq. 3.5}$$

where ρ is the material density (g/cm^3), μ is the energy dependent mass absorption coefficient (cm^2/g), and *l* is the sample thickness (cm, nm or μm). More generally, the OD spectrum for an n-component system is the linear combination of the OD of each species, and can be described as:

$$OD(E) = \sum_i^n \sigma_i(E).\rho_i(E).l_i \qquad \textbf{Eq. 3.6}$$

45

where σ_i (E) is the spectral response, ρ_i (E) is the density and l_i is the thickness of component *i*. In order to obtain valid XAS using soft X-ray transmission detection, the sample must be thin enough that a significant fraction of the incident X-rays penetrate the sample. If not, and only a small fraction of the X-rays passes through, absorption saturation will lead to spectral distortion. Absorption saturation, which depends strongly on the nature of the spectrum (intense, sharp features saturate more readily), the photon energy, and the absorption edge, was a major challenge in this thesis research, as is discussed elsewhere in the thesis (see **Section 4.2.9** and **Section 6.4.2**). To allow transmission detection for all *ex-situ* measurements performed in the thesis, typically sample thicknesses of less than 200 nm were required to avoid spectral distortion.

3.1.2 Fluorescence yield (FY) mode

When an atom is excited by absorbing an X-ray photon, it creates a core (inner shell) hole. This highly excited state will decay rapidly in a time of $\sim 10^{-15}$ s by emitting a fluorescence photon or ejecting one or more Auger electrons (De Groot & Kotani, 2008). The intensity of these emitted X-ray fluorescence photons as a function of incident photon energy is the fluorescence yield (FY) spectrum since the number of fluorescence photons is correlated to the number of core holes created. The X-ray photons have a mean free path that is the same order of magnitude as the incident X-rays. As a result, the FY mode is suitable for investigating bulk electronic structures because it has a relatively high probing depth in the soft X-ray region (>100 nm). At the same time, for samples >1 µm (at Mn 2p edge), the FY signals can be affected by absorption saturation.

FY can be measured in several different modes, including partial fluorescence yield (PFY) and total fluorescence yield (TFY) (Wadati et al., 2012). In PFY mode, an energy-sensitive X-ray detector (usually a silicon drift detector, SDD (Nakanishi & Ohta, 2012) is used to measure the spectrum of the emitted X-rays, which have specific energies depending on the energy of the electron which fills the core hole (Deslattes et al., 2003). **Figure 3.3** shows the Mn 2p spectrum of α-MnO$_2$ measured at the CLS-SGM beamline in PFY mode using an SSD (Note that the spectral features are distorted due to absorption saturation (see **Fig. 6.3B** for the unsaturated spectrum)).
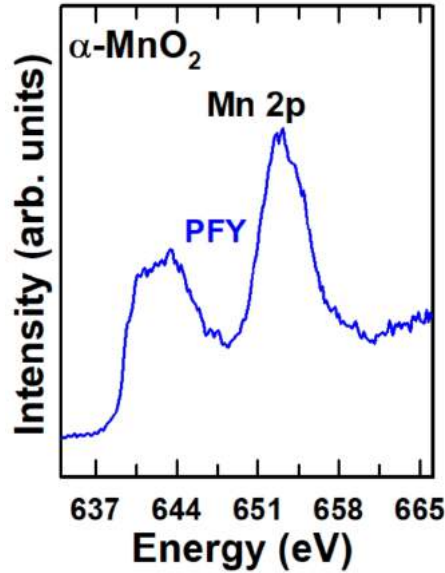
Figure 3.3   Mn 2p spectra of α-MnO$_2$ measured in PFY mode (using SSD).

In contrast, all X-rays that are emitted from the sample with any energy contribute to the TFY mode signal, which is measured by integrating all of the emitted X-ray spectrum detected by an SDD, or by using an X-ray detector without energy resolution such as a microchannel plate (Wiza, 1979). Taking Mn as an example, TFY and PFY can be described by the following equation (Wadati et al., 2012):

$$TFY = PFY_{Mn} + \sum\nolimits_x PFY_{other} \qquad \textbf{Eq. 3.7}$$

$$TFY = \eta(Ef)\frac{\Omega}{4\pi} * \frac{p_{Mn}(E_i,E_{Mn})\mu_{Mn}(E_i)}{\mu_T(E_i)+\mu_T(E_x)\frac{\sin\alpha}{\sin\beta}} + \sum\nolimits_x \eta(Ef)\frac{\Omega}{4\pi} * \frac{p_x(E_i,E_x)\mu_x(E_i)}{\mu_T(E_i)+\mu_T(E_x)\frac{\sin\alpha'}{\sin\beta}} \qquad \textbf{Eq. 3.8}$$

Where, $\eta(E_f)$ is the detector efficiency, Ω is a solid angle of the detector, α is the incidence angle, β is the emission exit angle, E_i is the incident photon energy, p_{Mn} and p_x is the probability of fluorescence at energy E_{Mn} and E_x, respectively. μ_{Mn} and μ_x are the X-ray absorption coefficient resulting from electrons filling the Mn and x core hole, respectively. μ_T is the total X-ray absorption coefficient which can be calculated for a pure compounds from the following equation (Wadati et al., 2012):

$$\mu_T = \mu_{Mn} + \sum\nolimits_x \mu_x \qquad \textbf{Eq. 3.9}$$

3.1.3   Electron yield (EY) mode

When the photon energy exceeds the core level ionization energy, an electron can be ejected directly (called a photoelectron), or the core hole can decay by the emission of an Auger electron. The core excited states can decay non-radiatively by emitting electrons through a 2-electron process, in which one electron fills the core hole, and the other is ejected from the sample at a specific photon energy. The initially ejected Auger electron (and the photo electron) can interact with other atoms and cause a cascade of lower energy electrons, some of which eventually escape from the sample. XAS can be measured in total electron yield (TEY) mode, where all escaping electrons are counted. If an electron energy analyzer is used, then various partial electron yield detection modes (PEY – photoelectron yield, AEY – Auger electron yield, SEY – secondary (low energy) electron yield) can be used to provide some control of sampling depth.   Primary electrons are those that escape the sample directly without energy loss. Secondary electrons are those which have suffered inelastic collisions with other atoms before reaching the surface, resulting in the ejection of additional low-energy electrons. In general, the detection of electrons escaping a surface depends on their kinetic energy and trajectory regardless of their source (primary or secondary electrons). In TEY, in soft X-ray region, the effective sampling depth in most materials is < 5 nm (Stöhr, 1992) In this work only TEY was used. The intensity of TEY can be expressed as follows (Stöhr, 1992):

$$I_{TEY} = \frac{\Omega}{4\pi} I_0 \varphi + \frac{\mu.\rho.L}{\mu.\rho.L + sin\theta} \qquad\qquad \textbf{Eq. 3.10}$$

where Ω is the solid angle of emission of the electron, I_0 is the incident photon flux (photons/s), φ is a constant, ρ is the material density (g/cm^3), μ is the energy dependent mass absorption coefficient (cm^2/g), θ is the X-ray incidence angle and L is the sampling depth (cm or nm). In the soft X-ray region, it is accepted that $\mu.\rho.L << \sin\theta$ (when the incidence angles (θ) is > 10º). Thus, $\mu.\rho.L + \sin\theta \approx \sin\theta$, and **Eq 3.10** can be reduced to:

$$I_{TEY} = \frac{\Omega}{4\pi} I_0 \varphi + \frac{\mu.\rho.L}{sin\theta} \qquad\qquad \textbf{Eq. 3.11}$$

3.2   XAS instrumentation

3.2.1   11ID-1 SGM beamline at the CLS

The non-spatially resolved XAS of Mn compounds (**chapter 6**) were measured at the Spherical Grating Monochromator (SGM) 11ID-1 beamline of the Canadian Light Source (CLS). The X-ray source at the SGM beamline is an elliptically polarizing undulator (EPU) (Cutler et al., 2018). A spherical grating monochromator provides monochromatic photons in the range of 240 eV - 2000 eV with a photon flux of 4 x 10^{12} (photons/s/0.1%BW at 250 eV) into a spot size of 50 μm × 50 μm and >5000 resolving power (Cutler et al., 2018)

Figure 3.4 shows the layout of the SGM beamline at the CLS (Regier, Paulsen, et al., 2007). The soft X-ray beam is deflected horizontally by M1 and M2 plane mirrors. Then, the deflected light is directed to one of the spherical gratings through the cylindrical M3 mirror and a liquid cooled entrance slit. Inside the monochromator, one of the low energy (LEG), medium energy (MEG) or high energy (HEG) spherical gratings disperses the X-rays coming from the entrance slit. By adjusting the grating angle, the photon energy of the beam can be precisely controlled. The 3 spherical gratings are used to cover photon energies up to 2000 eV through different line spacings (600, 1100 and 1700 lines/mm). The movable exit slit after the monochromator is designed to track changes in the gratings to optimize the X-ray photon flux and resolution (Regier, Paulsen, et al., 2007). The monochromatic beam is then refocused by the M4 toroidal mirror to the first endstation (X-ray photoemission, XPS), while the M5 mirror refocuses the beam to the second endstation (XAS). The first XPS endstation operates at ultra-high vacuum and is used mainly to perform X-ray photoemission. The second XAS endstation operates at pressure of 10^{-6}-10^{-9} Torr and is equipped for transmission, TEY, TFY and PFY measurements (**Fig. 3.4** and **3.5A**) (Cutler et al., 2017; https://sgm.lightsource.ca, 2023 Nov. 19; Regier, Paulsen, et al., 2007) . The SGM beamline is equipped with a set of ellipsoidal Kirkpatrick-Baez (KB) mirrors (Dynes et al., 2018) used to focus the beam down to a 10 μm x 10 μm spot prior to the XAS end station. The KB system is composed of 2 mirrors (vertical and horizontal) with elliptical shapes, which allows focusing the X-ray beam to an adjustable spot, as illustrated in **Fig. 3.5B** (Wang et al., 2023).
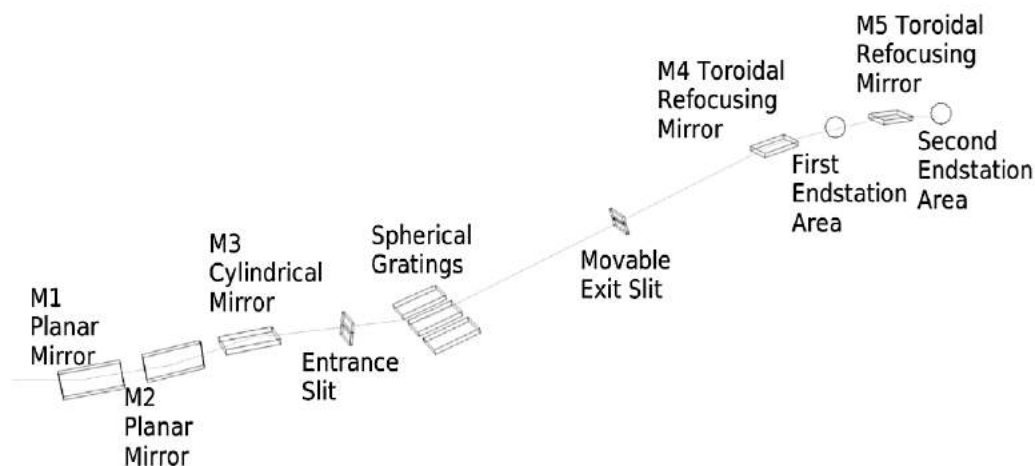
Figure 3.4 Optical layout of SGM, 11ID-1 beamline at the CLS (Regier, Paulsen, et al., 2007). With permission from AIP Publishing.
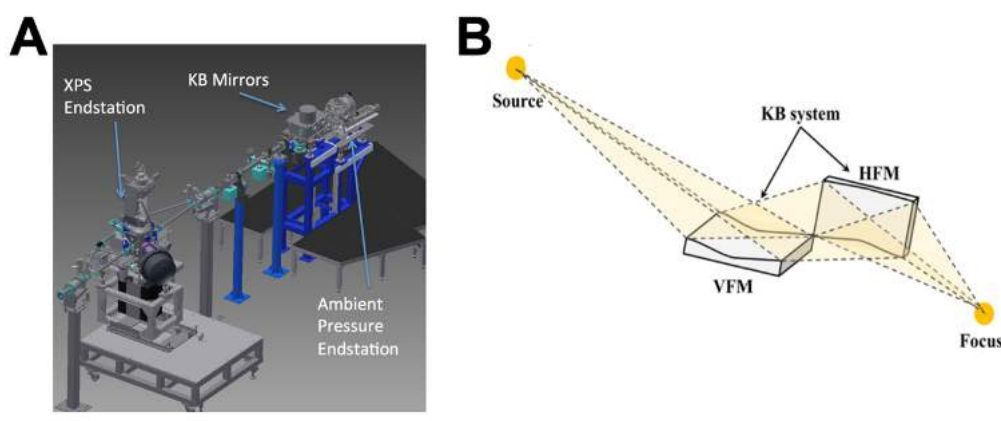
Figure 3.5 **(A)** Endstation-1(XPS) and Endstation-2 (XAS) at SGM, CLS (https://sgm.lightsource.ca, 2023 Nov. 19). **(B)** Reprinted from (Wang et al., 2023). With permission from Springer.

All soft XAS measurements in the thesis were performed in the second endstation using simultaneous detection by TEY, PFY and TFY. The measurements were conducted at room temperature under high vacuum (~10^{-6} Torr). The storage ring was operated in top-off mode with a stable current of 220 ± 1 mA. During my measurements, the X-ray beam was focused to a 25 μm diameter spot. More details about the experimental measurements are provided in **chapter 6**.

3.3   X-ray imaging

Over the past decade, a significant development in X-ray sources and detector technology and increased complexity of X-ray imaging tools led to significant improvements in spatial and temporal resolution in both synchrotron and laboratory-based experimental techniques. Therefore, X-ray imaging has become increasingly valuable in various applications, particularly in studying energy conversion and storage materials (Lou et al., 2021). The high-resolution of the X-ray imaging bridges the gap between optical and electron imaging and combines the advantages of both techniques. Moreover, the remarkable penetration capability of X-rays enables non-destructive characterization and facilitates *in-situ/operando* experiments (Cao et al., 2020).

There are two main categories of X-ray nano/micro-imaging using synchrotron X-ray sources: full-field imaging methods and scanning imaging methods. Full-field imaging methods (**Fig. 3.6A, B, D and E)** use an area detector to record a complete image in a single shot. These methods are fast and ideal for studying dynamic processes that require high temporal resolution. On the other hand, scanning imaging methods (**Fig. 3.6C** and **F**) construct an image pixel-by-pixel through mechanical raster scanning of the sample (or by x-y scanning the focusing optics, as in the cryo-STXM). While these methods are slower due to the mechanical scan, they offer high sensitivity to different properties of the sample and can utilize multiple detectors as presented in **Fig. 3.6C**. Another way to categorize X-ray imaging methods is based on the imaging systems and the principles of information extraction. When data is acquired as a real space image, it is known as a real space imaging method (**Fig. 3.6A, B and C)**. Conversely, if the sample's structural information is encoded in a diffraction pattern, it is referred to as a reciprocal space imaging method (**Fig. 3.6D, E** and **F**) (Lin et al., 2017; Zan et al., 2021).
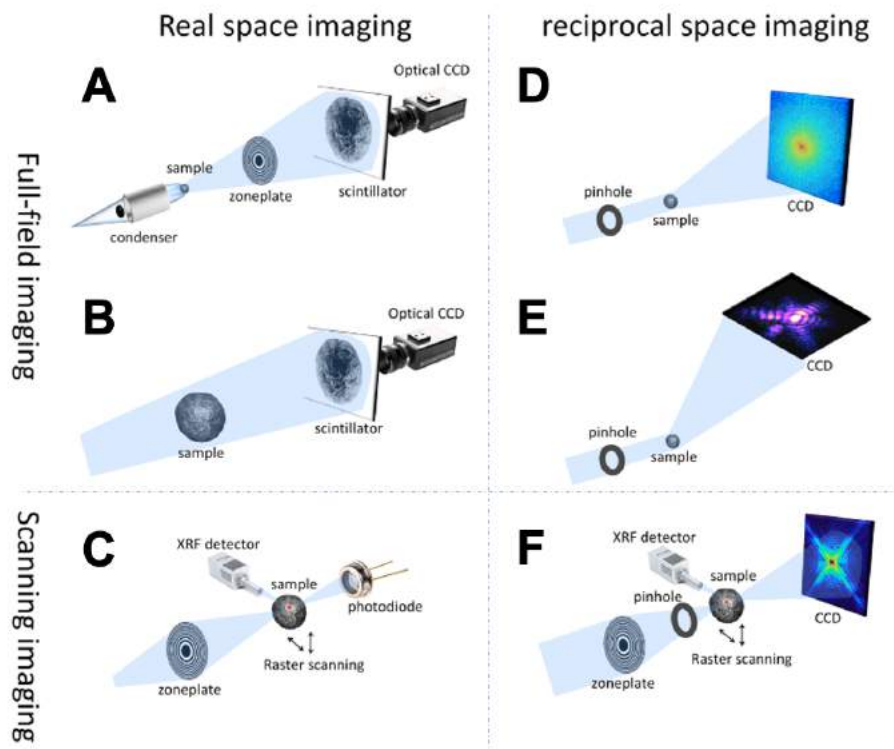
Figure 3.6 Schematic of different X-ray imaging techniques. **(A** and **B)** are the nanoscale and microscale full-field transmission X-ray microscopy, respectively. **(C)** scanning microscopes (in transmission and florescence modes). **(D)** coherent diffraction imaging. **(E)** Bragg coherent diffraction imaging. **(F)** Ptychography (scanning coherent diffraction imaging) (Lin et al., 2017). With permission from American Chemical Society.

X-ray imaging can be conducted using both soft X-rays (< 2 keV) and hard X-rays (> 5 keV). Hard X-rays possess a shorter wavelength (< 0.2 nm) and remarkable penetrating capability (Cao et al., 2020). The common techniques used for hard X-ray imaging include X-ray projection imaging, coherent diffraction imaging (CDI) and X-ray transmission microscopy (TXM). X-ray projection is a type of imaging where a sample is positioned between an X-ray source and an area detector (such as a charge-coupled device (CCD) or complementary metal-oxide semiconductor (CMOS) camera) coupled to a scintillator with an optical objective lens. The X-rays pass through the sample and project directly onto the detector, in which the imaging depends on the contrast between different parts of the measured sample

(Cao et al., 2020). On the other hand, CDI is a lensless imaging technique in which the imaging is performed by illuminating the sample by a coherent X-ray beam and the X-ray detectors typically measure speckled diffracted X-ray patterns in the far-field (Wen et al., 2019). TXM is a full-field imaging technique in which the X-ray beam is focused on the sample, and the transmitted X-ray beam is then projected onto the detector after being amplified by a Fresnel zone plate acting as the objective lens. The spatial resolution is determined by the width of the outermost zone of the zone plate (typically 20–30 nm), while the size of the focused X-ray beam determines the field of view (Cao et al., 2020; Zan et al., 2021).

Synchrotron-based soft X-ray imaging includes four main techniques: scanning transmission X-ray microscopy (STXM), full-field transmission X-ray microscopy (TXM), scanning photoelectron microscopy (SPEM), and X-ray photoemission electron microscopy (X-PEEM) (**Fig. 3.7**) (Hitchcock, 2015). In STXM, images are measured by (x,y) raster scanning the sample while recording the transmitted X-ray intensity by a detector behind the sample. Details of STXM principles and instrumentation are presented in **Sections 3.5** and **3.6**. Like STXM, SPEM imaging is performed by (x,y) scanning the sample. The X-ray beam is focused onto a sample using a zone plate, resulting in the generation of photoelectrons, which are then detected by a dispersive electron spectrometer (Lou et al., 2021). TXM can also be utilized in the soft X-ray range, similar to hard X-ray imaging. TXM spectromicroscopy is mainly used for water window (<520 eV) imaging of biological samples and magnetically sensitive imaging and magnetic dynamics. Tomography and cryo-tomography are commonly measured by TXM. Despite recent improvements to overcome uneven illumination and image drift issues, the TXM technique requires a much higher dose than STXM (Hitchcock, 2015). XPEEM is a full-field microscopy technique that used the monochromatic X-ray beam to illuminate the sample. Electrons near the surface are ejected and accelerated by an electric field (<1 kV/mm) into an electrostatic or magnetic electron microscope column, resulting in a highly magnified image. The image is then recorded by a detector (e.g. channel plate) (Hitchcock, 2022). In all imaging modes (STXM, TXM, SPEM, and XPEEM), NEXAFS spectroscopy and spectro-microscopy is acquired by measuring images at a sequence of incident photon energies at the core edge of the element of interest.
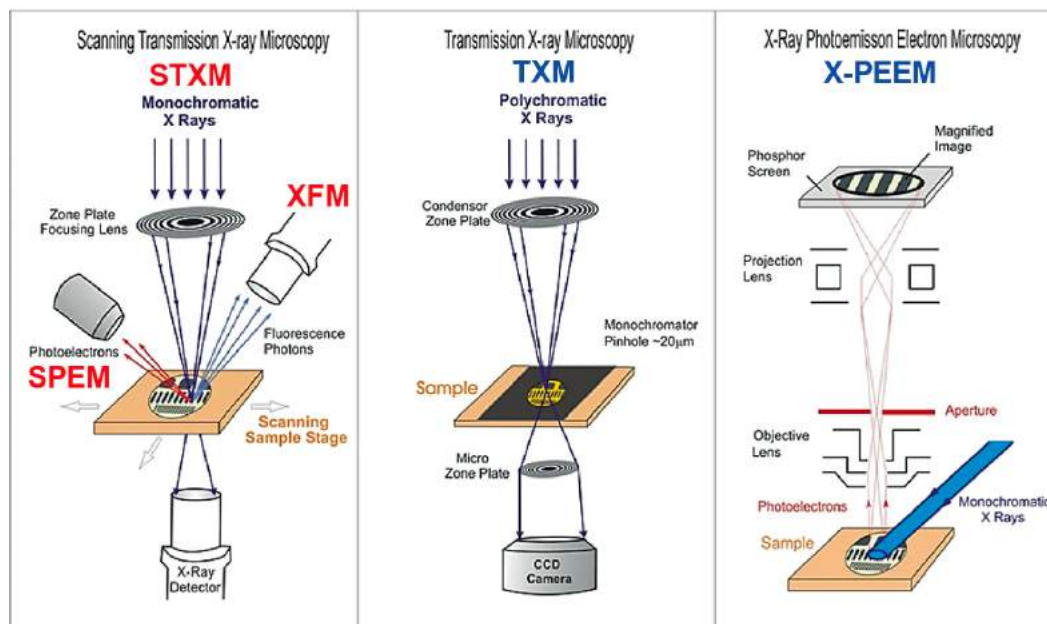
Figure 3.7 Schematic of the four common types of soft X-ray imaging techniques: transmission X-ray microscopy (STXM), scanning photoelectron microscopy (SPEM), full-field transmission X-ray microscopy (TXM), and full-field X-ray photoemission electron microscopy (X-PEEM). Reprinted from (Hitchcock, 2015). With permission from Elsevier.

3.4 Introduction to STXM

STXM is an advanced synchrotron-based technique which integrates both X-ray microscopy and X-ray spectroscopy to provide chemically sensitive imaging at a high spatial resolution with detailed information about chemical speciation, electronic properties and elemental composition through near-edge x-ray absorption fine structure (NEXAFS) contrast (Hitchcock, 2015; Hitchcock & Toney, 2014). STXM has a number of advantages over other microscopies, spectroscopies and spectromicroscopies including relatively high spatial resolution (20-30 nm), high chemical and structural sensitivity (speciation) and high energy resolution. In addition, compared to electron microscopies and core level electron energy loss (TEM-EELS), STXM is much less limited by radiation damage (A. P. Hitchcock et al., 2008), although it does occur. These features make STXM an ideal tool for studying electrode materials used in energy storage/conversion applications, especially when it is combined with an *in-situ* capability (Arul et al., 2021; Dong & Vayssieres, 2018).

All of the ~24 existing STXMs are illuminated by grating monochromator beamlines and operate in the soft X-ray range, typically from 200 eV to 2000 eV (although there has been one STXM study of Li battery material at the 55 eV Li K-edge (Ohigashi et al., 2020)), and several STXMs are on beamlines with usable photon flux to ∼3000 eV. This energy range includes K edges from carbon (280 eV) to phosphorus (2150 eV) and L-edges from potassium (290 eV) to strontium (2000 eV) (Arul et al., 2021). Most of the STXM measurements I performed during my PhD studies were at the Mn 2p edge (630 - 670 eV) and O K edge (524 – 570 eV). **Table 3.1** presents a comparison of STXM beamlines at different synchrotron facilities which I used during my PhD research.

Table 3.1   STXM properties in different Synchrotron Facilities

Synchrotron Facility	Location	Beamline	Ring E (GeV)	E (eV)	References
CLS (3rd generation)	Saskatoon, Canada	10ID-1	2.9	250-3000	(Cutler et al., 2007; Ellis & Hallin, 2011)
MaxIV (4th generation)	Lund, Sweden	SoftiMAX	3.0	275-2500	(Schwenke et al., 2018; Tavares et al., 2018)
Bessy II (3rd generation)	Berlin, Germany	Mystic	1.7	250-750	(Beckhoff et al., 2000; A. P. Hitchcock et al., 2008; Nolle et al., 2012)
		Maxymus	1.7	150 – 1900	
Solaris (4th generation)	Kraków, Poland	DEMETER	1.5	100-2000	(Kowalski et al., 2021; Wawrzyniak et al., 2021)
ALS (3rd generation)	Berkeley, CA, USA	11.0.2	1.9	200-2000	(Feggeler et al., 2023; Nichols et al., 2022)

3.5   STXM principles

Figure 3.8 presents a schematic diagram of STXM (Hitchcock et al., 2014). In STXM, a monochromated X-ray beam at a specific photon energy is focused by a Fresnel zone plate (ZP) to a 20-50 nm spot. Through a focusing procedure, the sample is placed at the focal spot. The order selecting aperture OSA (typically 50-90 μm diameter) eliminates zero order (the 80-90 % of the X-rays that are not focused by the ZP), and partially blocks higher order diffraction X-rays from the ZP (Jacobsen, 2019). Images are measured by (x,y) raster scanning the sample

while recording the intensity of the transmitted X-rays detected by a phosphor/photomultiplier tube (PMT) detector located behind the sample.
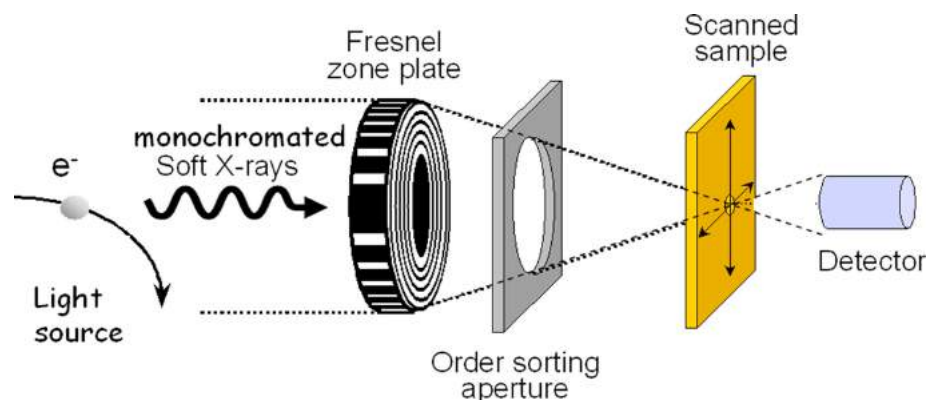
Figure 3.8 Schematic diagram of STXM components (Hitchcock et al., 2014). With permission from Elsevier.

The ZP, a circular diffraction grating nano-focusing optic, is a key component of STXM. The signal intensity, focal length and spatial resolution depend on the diameter (120–300 μm) of the ZP and the width of the outermost zone (20 – 100 nm) of the ZP (Obst & Schmid, 2014). ZPs consist of a series of concentric rings (made from nickel or gold) which are opaque to soft X-rays alternated with circular slots of silicon nitride (Si_3N_4) substrate between the metal zones that are transparent to X-rays (see **Fig. 3.9**) (Wang, 2011). The interference condition of a zone plate is described by (Howells et al., 2007):

$$f^2 + r_n^2 = \left(f + \frac{mn\lambda}{2}\right)^2 \qquad \textbf{Eq. 3.12}$$

where f is the focal length (presents the distance between the ZP and the focused spot), r_n is the radius of the nth zone, λ is the wavelength of the incident X-rays, m is the diffraction order (m = 0, ±1, ±2, ±3, ...) and n is the zone number. The first order light (m = ±1) is the most intense diffracted light that typically used in STXM measurements. For first order light, **Eqn. 3.12** can be expressed as (Howells et al., 2007):

$$r_n^2 = n\lambda f + \frac{n^2\lambda^2}{4} \qquad \textbf{Eq. 3.13}$$
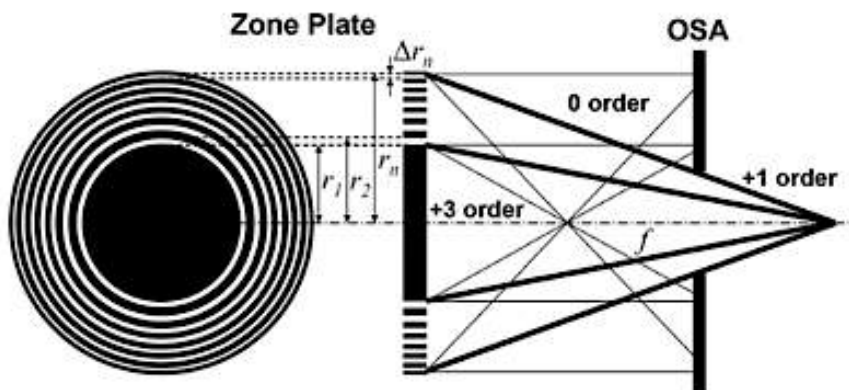
Figure 3.9   Schematic geometry of a zone plate and X-ray focusing scheme of STXM (Wang, 2011).

Since The focal length, $f \gg n\lambda$ (f is in mm scale, while λ is < 10 nm scale), f can be expressed as (Howells et al., 2007):

$$f \approx \frac{r_n^2}{n\lambda} \qquad\qquad \textbf{Eq. 3.14}$$

Due to the equal area of each zone in the ZP, the number of zones (n) and the outmost zone width (Δr_n) can be calculated by (Howells et al., 2007):

$$n = \frac{\pi r_n^2}{2\pi r_n \cdot \Delta r_n} = \frac{r_n}{2\Delta r_n} \qquad\qquad \textbf{Eq. 3.15}$$

$$\Delta r_n = r_n - r_{n-1} \qquad\qquad \textbf{Eq. 3.16}$$

Then, the focal length (f) in **equation 3.14** can be converted to (Howells et al., 2007):

$$f = \frac{2r_n\,\Delta r_n}{\lambda} = \frac{D\,\Delta r_n\,E}{1240} \qquad\qquad \textbf{Eq. 3.17}$$

where D ($=2r_n$) is the ZP diameter. The photon energy is related to the wavelength (λ) by E (eV) = hc/λ, where h is Planck's constant (6.626×10^{-34} J.s) and c is the speed of light in vacuum (2.998×10^{-8} m/s) (Attwood, 2000; Thompson et al., 2001). Thus, the focal length is linearly proportional to the photon energy, and the ZP must move upstream as the photon

energy increases in a spectral scan in order for the image to be in focus. The numerical aperture (NA) of the ZP is defined as (Falcone et al., 2011):

$$NA = \frac{r_n}{f} = \frac{\lambda}{2\Delta r_n} \qquad \textbf{Eq. 3.18}$$

The diffraction-limited spatial resolution of the ZP (Res) according to the Rayleigh criterion is (Attwood, 2000; Thompson et al., 2001):

$$Res = 0.61\frac{\lambda}{NA} = 1.22 \ \Delta r_n \qquad \textbf{Eq. 3.19}$$

The spatial resolution (Res) of the STXM is largely determined by the width of the outer zone of the ZP. Alignment of the ZP relative to the X-ray beam, zone plate quality and the diffraction order are also factors affecting STXM spatial resolution. During my PhD studies, STXM experiments were performed using ZPs with outer zone widths of 25-50 nm. Therefore, the predicted spatial resolution of the STXM images was 30-60 nm.

3.6   STXM instrumentation

The development of soft X-ray STXM started at the National Synchrotron Light Source (NSLS-1) in NY, USA in 1985 (Kirz & Rarback, 1985). This STXM used a 1 μm diameter pinhole as a scanning probe to record images of wet biological samples. The use of synchrotron radiation (generated by an undulator) and ZP based STXM was introduced in the late 1980s at the NSLS-1 (Buckley et al., 1989; Rarback et al., 1988). An interferometer controlled STXM was then developed at a bend magnet beamline (5.3.2 polymer STXM) at the Advanced Light Source (ALS) in 2001 (Kilcoyne et al., 2003; Warwick et al., 2002). Most of the STXM measurements reported in this thesis were performed at the 10ID-1 Spectro-Microscopy (SM) beamline at the Canadian Light Source (CLS), This instrument is described in detail.

3.6.1   10ID-1 SM ambient STXM beamline at the CLS

The CLS on the campus of the University of Saskatchewan in Saskatoon is the only synchrotron facility in Canada. CLS is a third-generation 2.9 GeV facility which consists of a 250 MeV electron linac, booster ring and a 12-cell Double Bend Achromat (DBA) storage ring with a circumference of 171 m (Cutler et al., 2007; Ellis & Hallin, 2011). While initially operated in decay mode, since 2021, CLS operates in a top-up mode at 220 mA current. The

bend magnets of the storage ring generate synchrotron radiation in the infrared to hard X-ray range. The CLS has 18 beamlines including the 10ID-1 Spectromicroscopy (SM) beamline. The Apple type II undulator, which is the source point of the SM beamline, generates soft X-rays with high brightness. The SM beamline has two branches. The first is the STXM branch line which illuminates two in-house constructed STXM microscopes: the ambient-STXM (Kaznatcheev et al., 2007; Kilcoyne et al., 2003) and the cryo-STXM (Leontowich et al., 2018). The second branch line is equipped with a commercial (Elmitech) photoemission electron microscope (X-PEEM).

Figure 3.10 presents photos of the10ID Spectromicroscopy (SM) beamline at the CLS. The SM beamline is designed to combine both spectroscopy and microscopy with a resolving power of 3000 in the energy range from 130 to 2700 eV and with a spatial resolution of ~30 nm (Kaznatcheev et al., 2007). X-rays are generated by the 2.9 GeV electron beam passing through an elliptically polarized undulator (EPU). The EPU consists of magnet arrays with alternating magnetic orientations. By adjusting the phase of the four arrays of magnets (by displacing the girders on which they are mounted) the EPU can produce linearly polarized X-rays with an arbitrary orientation of the E-vector from -90° to +90° (0º is horizontal). In addition, the EPU has the capability of producing left and right circularly polarized X-rays in the first harmonic, at energies below 900 eV. For the studies carried out for this thesis, the EPU was used in left circularly polarization. The first mirror (M1) is a gold coated sagittal cylinder inside the primary optical enclosure (POE) of the 10ID which deflects and focuses the X-rays in the vertical direction. The beamline is equipped with a plane grating monochromator (PGM) (Kaznatcheev et al., 2007), in which a plane pre-mirror (M2) deflects the beam vertically onto the grating. The PGM works with collimated light to disperse the X-rays in the vertical direction from which a single photon energy is selected by an exit slit. There are two sets of baffles (comprising a 4-jaw adjustable aperture) located before and after the monochromator. The 4-jaw aperture before the monochromator prevents unwanted X-rays from the bent magnet upstream of the 10ID1 EPU from entering the monochromator, while the 4-jaw aperture after the monochromator is used to minimize higher order light entering the M4 refocusing mirrors.

The monochromated X-ray beam can be switched between the STXM and the PEEM branch lines by a mirror (M3). When the M3 is displaced in-board, it redirects the X-ray

beam to the PEEM branch line. If M3 is retracted by moving it out-board, the X-ray beam goes straight into the STXM branch line. To remove second-order X-rays at the carbon K-edge, a Ti foil is used as a transmission filter after the exit slit (Kaznatcheev et al., 2007).

Figure 3.10 10ID SM beam line at the CLS: (A) STXM. **(B)** SM beamline. **(C)** Elliptically polarizing undulator (EPU) (Kaznatcheev et al., 2007). With permission from Elsevier.

The ambient-STXM chamber is designed to achieve a vacuum pressure of ~ 10^{-6} Torr. During the *ex-situ* STXM measurements reported in the thesis, the STXM is initially pumped to a rough vacuum of 0.1 mbar before introducing helium (He) gas into the chamber at a pressure ranging from 1/3 - 1/6 bar. Helium gas has very low X-ray absorption which allows use of all the photon flux. He is also a good thermal conductor (~20x that of air) which stabilizes the chamber temperature and minimizes drifts of the area measured (Kilcoyne et al., 2003). An interferometer system is used to control the position of the beam on the sample. For *in-situ* STXM measurements, using the custom device, there is a high probability of fluid leaks if the chamber is pumped. Therefore, almost all *in-situ* measurements used a slight overpressure (~1.1 bar) of He gas to displace the air in the STXM chamber. Typically, at the CLS, ~10 % of a 200 bar He gas cylinder is used during this process which takes approximately 10-15 min (at Solaris, with a much smaller vacuum, the He consumption is negligible). While this procedure is used routinely at the ambient-STXM at CLS, it caused many problems at other synchrotrons, including MaxIV and Bessy. At MAXIV sparking due to the long discharge length in He, especially at ~ 1 mbar, damaged several stepper motor drivers.

Figure 3.11A presents a schematic of the STXM components at the SM 10ID1 beamline (CLS). **Figure 3.11B** shows a photo of the ZP, OSA, sample holder and detector inside the ambient STXM chamber at CLS. During STXM measurements, adjustment of the

positions of some STXM components are limited to specific directions. The ZP moves only in the z direction (along the length of the beamline), while the OSA can move only in the (x, y) directions. The z-position of the OSA defines the origin of the z-scale. The sample can be moved in (x, y, z) either by stepping motor coarse stages (25 mm in x, 12 mm in y) or by an integrated (x,y,z) piezo stage (the motion range is limited to (60 x 60 μm in (x,y)). The detector can be moved in the (x, y, z) directions and is mounted on the same z-coarse stage as the sample so a fixed sample-detector distance is maintained. Adjustments of STXM components need to be performed carefully to achieve best resolution and performance. A ZP with 35 nm outer zone width, outer diameter of 155 μm, and 80 μm central stop is mostly used during both *ex-situ* and *in-situ* STXM measurements. However, a lower resolution ZP (50 nm outer zone width, 300 μm outer diameter and 90 μm central stop) was also used and was preferred for *in-situ* STXM measurements since there was a longer OSA-sample distance. The OSA is fabricated from a molybdenum (Mo) sheet with laser drilled circular apertures that are (x,y) aligned with the center of the ZP to allow only the 1st order diffraction light for STXM measurements. The detector used in the ambient STXM is a high-performance photomultiplier (PMT) detector coupled to a Lucite pipe coated with a thin polycrystalline phosphor film to convert soft X-rays to visible light (**Fig. 3.12**) (Hitchcock, 2012; Kilcoyne et al., 2003).
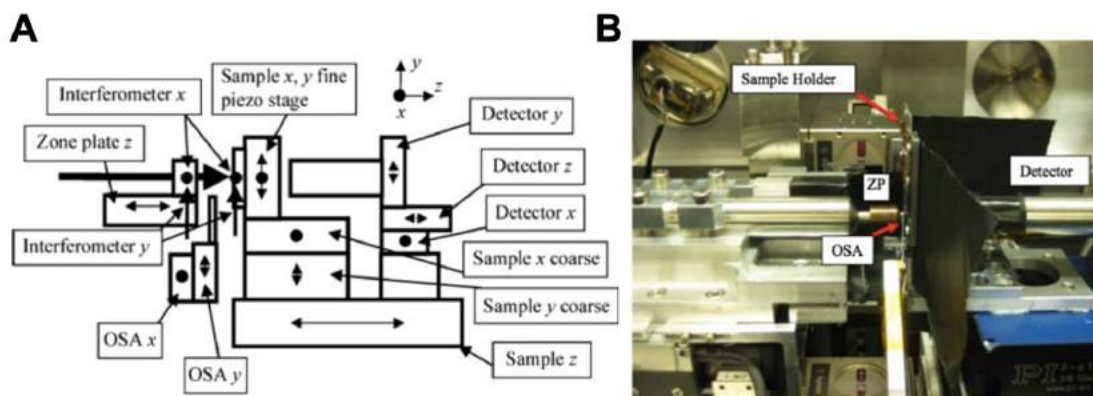
Figure 3.11 STXM microscope components at SM 10ID1 beamline (CLS). (A) schematic of STXM components (Kilcoyne et al., 2003). With permission from IUCr Journals. **(B)** photo of ZP, OSA, sample holder, and detector inside STXM chamber (Zhu, 2016).
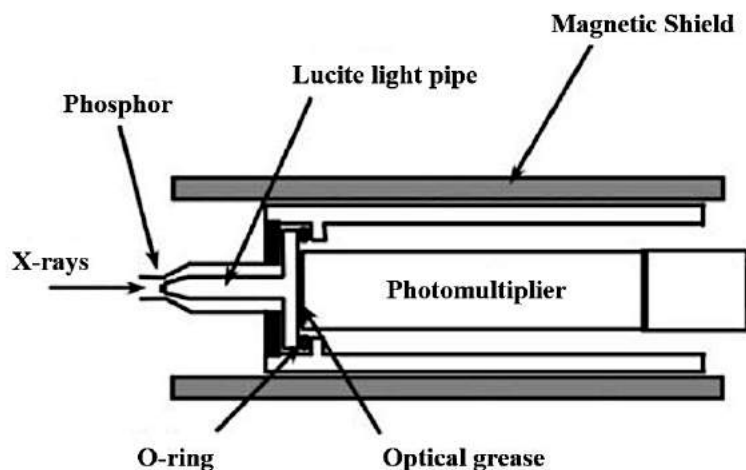
Figure 3.12 Schematic of PMT X-ray detector and the phosphor coated pipe (Kilcoyne et al., 2003). With permission from IUCr Journals.

3.7 *Ex-situ* and *in-situ* characterization of MnOx-based electrode material

Ex-situ techniques refer to measurements that take place outside the natural environment of the sample and analyzed under controlled laboratory conditions. *In-situ* characterization refers to investigations that take place in the natural environment of a sample. Understanding reaction mechanisms involved in the charging/discharging processes of supercapacitors or batteries are crucial for enhancing and optimizing the performance of active electrode materials (MnOx in this case). Therefore, a variety of experimental techniques have been used to investigate the MnOx charge-storage behavior of batteries and supercapacitors electrodes including: electron energy-loss spectroscopy in transmission electron microscopy (TEM-EELS) (Lee et al., 2019), energy dispersive X-ray spectroscopy in transmission electron microscopy (TEM-EDX) (Guo et al., 2020), X-ray diffraction (S. Wang et al., 2021), Raman spectroscopy (Hardwick et al., 2008), nuclear magnetic resonance (NMR) spectroscopy (H. Wang et al., 2013), X-ray absorption spectroscopy (XAS) (Mansour et al., 2022; Patra et al., 2021) and scanning transmission electron microscopy (STEM) (Hynek et al., 2019; Yang et al., 2022). Most of those techniques have been used under *ex-situ* conditions to understand behavior/mechanisms of MnOx based electrode materials in its initial state and after different electrochemical processes.

Nevertheless, the electrochemical processes in real batteries and supercapacitors occur in a liquid electrolyte. Although, *ex-situ* characterizations can provide valuable chemical and morphological information, it only allows to study sample materials before and/or after electrochemical operations or reactions. Therefore, the mechanism of morphological and chemical changes caused by (electro)chemical reactions in electrochemical systems can be only inferred indirectly by *ex-situ* techniques (Hwang et al., 2020; van der Wal et al., 2021). Typically, after the electrochemical reaction, the sample (electrode material in this case) is removed from the liquid electrolyte and stored for subsequent *ex-situ* characterization. In some cases, the samples are ground or embedded in resin and microtomed to a specific thickness. During the preparation, transportation or storage, the chemical properties of the sample can be changed as results of exposure to air and absence of electrolyte. To gain a deeper understanding of electrochemical reaction mechanisms involving manganese oxides and to provide insights into some of challenges discussed in **Section 2.4.5**, it is necessary to perform experimental studies under *in-situ* conditions.

Different *in-situ* studies have been developed to understand electrochemical behavior of manganese oxide-based electrode materials in different energy storage applications of batteries and supercapacitors. Yuan et al. (Yuan et al., 2015) used *in-situ* STEM to study lithiation behavior in single crystalline α-MnO$_2$ nanowire in Li-ion batteries. Bhatia et al. (Bhatia et al., 2022) presented the first *in-situ* TEM study of LiMn$_{1.5}$Ni$_{0.5}$O$_4$ (LMNO) cathode material used in micro batteries to analyze the local morphological and structural changes during cycling in liquid electrolyte. Chang et al. (Chang et al., 2007) presents an *in-situ* X-ray absorption spectroscopy (XAS) study to investigation the energy storage mechanism of the Mn oxide in KCl aqueous solution at different applied potentials. The results indicate that the pseudocapacitive performance of the MnO$_2$ electrode resulted from redox reaction of manganese oxide species with an oxidation state of +3.23 and +3.95, in addition to incomplete recovery of the Mn oxidation state (from +3.23 to +3.27) after the electrochemical redox cycle (as a reason for capacity fading).

3.7.1 *In-situ* soft X-ray spectro-microscopic techniques

There are several *in-situ* techniques that can be used to study the chemical and morphological properties of different electrochemical systems. These *in-situ* techniques can be broadly classified into three main categories:

i. Microscopic techniques, such as *in-situ* SEM and TEM (Velasco-Velez et al., 2020; Z. Zhang et al., 2018)

ii. Spectroscopies techniques, such as *in-situ* XAS (Chang et al., 2007), and *in-situ* infrared reflection absorption spectroscopy (IRAS) (Aastrup et al., 1998),

iii. Spectro-microscopies techniques, such as *in-situ* UV-vis (Takashima et al., 2014), Raman microscopy (Dokko et al., 2003) and *in-situ* STXM (Prabu et al., 2018) which is the technique mostly used in the thesis and introduced in detail.

Spectro-microscopies are advanced techniques that integrate principles of both spectroscopy and microscopy. Spectro-microscopy has significant advantages over *in-situ* spectroscopy or *in-situ* microscopy. This technique provides both spectroscopic data and high-resolution microscopic images simultaneously, which allow a correlation of spectroscopic information with the spatial distribution of chemical species in a specific region of the measured samples. This correlation provides deep understanding of local variations and heterogeneities of active material. Additionally, *in-situ* spectro-microscopy allows for real-time observation of morphological and spectroscopical changes during different electrochemical processes. By combining both microscopic and spectroscopic information, spectro-microscopy can provide a better understanding of catalytic materials. *In-situ* spectro-microscopy provides a comprehensive insight into the behavior and properties of catalytic materials. under realistic operating conditions.

STXM provides identification and quantitative mapping of different chemical species. Despite its advantages, the application of STXM in supercapacitor and battery research is still in its infancy. **Table 3.2** presents some of *in-situ* STXM studies on electrochemical reactions, applications, or phenomenon. The *in-situ* study presented in the thesis is the first *in-situ* STXM experiment designed to study MnO_2 based electrode material for energy storage applications.

Table 3.2 List of *in-situ* STXM studies of electrochemical reactions.

In-situ STXM studies	Reference
In-situ spatial and time-resolved studies of electrochemical reactions by scanning transmission X-ray microscopy	(Guay et al., 2005)
In-situ soft X-ray dynamic microscopy of electrochemical processes	(Bozzini et al., 2008)
An *in-situ* synchrotron-based soft X-ray microscopy investigation of Ni electrodeposition in a thin-layer cell	(Bozzini et al., 2009b)
Synchrotron-based *in-situ* soft X-ray microscopy of Ag corrosion in aqueous chloride solution	(Bozzini et al., 2009a)
Corrosion of Ni in 1-butyl-1-methyl-pyrrolidinium bis (trifluoromethylsulfonyl) amide room-temperature ionic liquid: an *in-situ* X-ray imaging and spectromicroscopy study	(Bozzini et al., 2011a)
In-situ X-ray spectromicroscopy study of bipolar plate material stability for nano-fuel-cells with ionic-liquid electrolyte	(Bozzini et al., 2011b)
Fabrication of a Sealed Electrochemical Microcell for *in-situ* Soft X-ray Microspectroscopy and Testing within Situ Co-Polypyrrole Composite Electrodeposition for Pt-Free Oxygen Electrocatalysis	(Bozzini et al., 2014)
Electrodeposition of manganese oxide from eutectic urea/choline chloride ionic liquid: An *in-situ* study based on soft X-ray spectromicroscopy and visible reflectivity	(Bozzini et al., 2012b)
Electro-deposition of Cu studied with *in-situ* electrochemical scanning transmission x-ray microscopy	(Hitchcock et al., 2016)
Origin and hysteresis of lithium compositional spatiodynamics within battery primary particles	(Lim et al., 2016)
CO_2 Reduction: From the Electrochemical to Photochemical Approach	(Wu et al., 2017)
Instrumentation for *in-situ* flow electrochemical Scanning Transmission X-ray Microscopy (STXM)	(Prabu et al., 2018)

3.7.2   Development of *in-situ* STXM technique

In-situ soft X-ray STXM microscopy to investigate various electrochemical systems with high spatial resolution and chemical sensitivity requires a suitable *in-situ* device that can provide control and exchange of liquid electrolyte, provision of potential control in at least a 3-electrode configuration (ideally, with a true reference electrode, and thus, a four-electrode device), and the device must be compatible with the spatial and other constraints of soft X-ray STXMs. Development of an *in-situ* device with robust electrical and fluid connections, including a reference electrode, and with the ability to quickly change electrolyte would provide significant advantages in investigation of different electrochemical systems.

In 2005, Daniel Guay et al. (Guay et al., 2005) reported the first *in-situ* STXM study of electrochemical reactions in a liquid cell. The electrochemical cell used in this study was designed to contain electrodeposited polyaniline on a thin Au film covered with a thin electrolyte layer of 1 M HCl, sandwiched between two X-ray transparent silicon nitride windows and subjected to different electrochemical processes. After that, Benedetto Bozzini and his group (Brindisi Fuel Cell Durability Laboratory, Italy) extended the *in-situ* STXM studies to a series of electrochemical reactions and phenomenon including electrodeposition of transition metals (Bozzini et al., 2009a; Bozzini et al., 2009b), Galvanic coupling (Bozzini et al., 2011b) and fuel cells (Bozzini et al., 2011a). Recently, Prabu et al. (Prabu et al., 2018) presented results of an *in-situ* STXM study of Cu oxidation and reduction using a 3D printed *in-situ* flow electrochemical device equipped with 3-electrodes micro-chips. Examples of different STXM *in-situ* cells presented in **Fig. 3.13**.
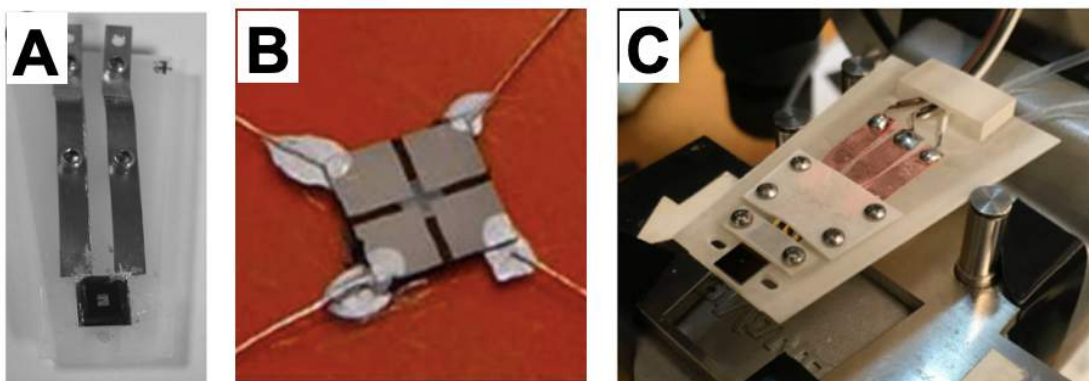
Figure 3.13 Examples of STXM *in-situ* cells used in different electrochemical systems. **(A)** *in-situ* cell designed by Guay et al. to study electrochemical reactions of polyaniline (Guay et al., 2005). With permission from American Chemical Society. **(B)** *in-situ* cell designed by Bozzini et al. to study behavior of Ag in neutral electrolyte (Bozzini et al., 2008). With permission from Elsevier. **(C)** *in-situ* flow cell designed by Parbu et al. to study Cu oxidation and reduction mechanisms (Prabu et al., 2018). With permission from AIP Publishing.

In the next chapter (4) I describe in detail the design, fabrication and optimization of the flow electrochemical device that I helped develop and used in my thesis research.

Chapter 4

In-situ Flow Electrochemical Device for Soft X-ray Scanning Transmission X-ray Microscopy

This chapter describes the in-situ flow electrochemical STXM device that was developed and used as part of the research reported in this thesis. The basic design and first implementation of the microfluidic based device was achieved by Pablo Ingino, a PhD student in the group of Martin Obst at the University of Bayreuth, Germany. In collaboration with my group colleague Chunyang Zhang, I optimized the fabrication at McMaster University and the operational procedures for its use at synchrotron STXMs. This chapter describes in detail the fabrication procedure and gives a step-by-step operational guide. It highlights how various challenges were overcome and identifies remaining deficiencies that require improvement. The chapter concludes by giving examples of STXM experiments performed using the in-situ flow electrochemical device: solution electrochemistry (ferri/ferrocyanide); manganese oxide redox cycling; electrodeposition of Cu nanoparticles; and investigation of Cu nanoparticles for CO_2 electroreduction catalysis.

4.1 Overview

As described in detail in **Chapter 3**, STXM is a NEXAFS based spectromicroscopy that provides quantitative chemical mapping. In order to use STXM for *in-situ* or *operando* studies of electrochemical processes involving liquid electrolytes (see **Section 3.7.2**), it is necessary to have a device that provides electrical connections and the ability to change the electrolyte while at the same time have a structure that is compatible with the severe spatial constraints of soft X-ray STXMs.

Recently, various commercial STXM *in-situ* devices have been developed, such as the liquid electrochemical cell from Hummingbird Scientific (https://hummingbirdscientific.com) with continuous electrolyte flow and advanced sealing technology. The Hummingbird device has external leak-checking capabilities, a full Ag/AgCl reference electrode and can be equipped with different electrode designs optimized for specific electrochemical systems (Zhou & Wang, 2021). Another commercial STXM *in-situ* flow device is provided by Norcada

Inc. (https://www.norcada.com). This device has the advantage of an *in-situ* heating setup that provides information about thermal modification of different materials (Kim et al., 2022).

Nagaska et al. (Nagasaka et al., 2010) developed a design for *in-situ* STXM measurements, and evaluated the efficiency of the reported cell by measuring bulk liquid water at the O K-edge region. The Hitchcock group has presented two different devices for *in-situ* soft X-ray STXM electrochemical studies. In 2005, Guay et al. (Guay et al., 2005) reported *in-situ* spatial and time-resolved STXM studies of electro-transformation of polyaniline using a sealed liquid cell. Further, extensive studies were presented by Bozzini et al. (Bozzini et al., 2008; Bozzini et al., 2014; Bozzini et al., 2017). In 2018 Prabu et al. (Prabu et al., 2018) reported a 3D printed *in-situ* flow electrochemical device equipped with an earlier version of the 3-electrode micro-chip (Norcada Inc, https://www.norcada.com) system and demonstrated its capabilities by monitoring electrodeposition and electro-stripping of copper from the working electrode. While the Prabu et al. (Prabu et al., 2018) device did work, it was very prone to leaking, was not vacuum compatible, and took a long time to change the electrolyte since it had only a single inlet and outlet.

The goal of the technical developments described in this chapter was to develop an *in-situ* flow electrochemical STXM platform that can be used to study different aqueous electrochemical systems under a variety of experimental conditions and has the ability to work at X-ray energies below 500 eV (the limit for the Hummingbird and Norcada devices), in particular at the C 1s edge (280-320 eV).

As described in detail below, the *in-situ* STXM flow electrochemical device has a robust structure, reliable electrical connections, and the ability of rapid fluid exchange. The *in-situ* device has four microfluidic channels and is based on a three-electrode system. The design of the *in-situ* device is compatible with the common STXM 3-pin kinematic sample holders (Hitchcock et al., 2021). In order to demonstrate its capabilities and versatility, results of *in-situ* STXM studies of different electrochemical systems using the current device are presented. These include solution based redox cycling (ferri/ferrocyanide) (Ingino et al., 2024) Cu-based electrocatalysis of CO_2 reduction (Zhang et al., 2023b; Zhang et al., 2023a) and Mn oxide electrodeposition and redox cycling (**Chapter 9**).

4.2   Detailed description of the *in-situ* flow electrochemical device

The *in-situ* flow electrochemical device features three electrodes, all of which are accessible for STXM study, and a dual inlet, dual outlet microfluidic flow system that facilitates rapid exchange of electrolyte. The device is compatible with STXM trapezoidal plate sample holders (Kilcoyne et al., 2003). **Figure 4.1** presents images of the device from upstream (**Fig. 4.1A**) and downstream (**Fig. 4.1B**) inside the ambient STXM (Kaznatcheev et al., 2007) at the Canadian Light Source (CLS, Saskatoon, Canada). The device consists of three main parts: (I) a machined printed circuit board (PCB), (II) polydimethylsiloxane (PDMS)/cover glass composite with four microfluidic channels (2 inlet and 2 outlet) connected to silicone tubes and (III) a poly(methyl methacrylate) (PMMA) plate as a backplate. The PDMS/glass cell is sandwiched between the PCB and the PMMA plate. **Figure 4.1C** shows the device under an optical microscope prior to mounting the cell in the STXM chamber. **Figure 4.1D** is a photograph of the soft X-ray translucent silicon nitride (Si_3N_x) window area (240 μm x100 μm) showing the three gold electrodes - working electrode (WE), counter electrode (CE), and reference electrode (RE). Newton interference rings, sometimes visible in the cell (**Fig. 4.1D**), can be used to estimate the fluid thickness. Details of the design, fabrication, assembly and operational procedures are given in the following sections.
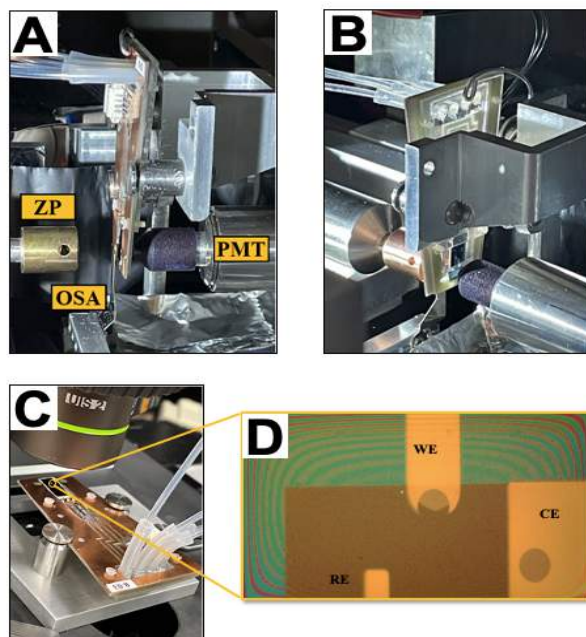
Figure 4.1   Photos of the *in-situ* flow electrochemical cell. (A) Upstream and **(B)** downstream views of *in-situ* Flow electrochemical mounted in the ambient STXM at the CLS. **(C)** image of the *in-situ* device being set-up under and optical microscope. **(D)** the working area of the cell showing the 3 electrodes (Reflection, 20x). Newton rings are seen because the cell is filled with electrolyte.

4.2.1   Design and fabrication of the mold to prepare the microfluidic channels

Prior to preparing the PDMS polymer mixture and to sustain a specific structure and shape of the microfluidic cell, a process for fabricating a casting mold was developed using Xurography (Graphtec ROBO Pro, CE500 Irvine, CA) as presented in **Fig. 4.2A** The pattern cut into a self-adhesive vinyl film (100 μm thickness, FDC-4300, FDC graphic films, South Bend, IN) was designed using computer aided design (CAD) software (Autodesk, Fusion 360, USA - version 2.0.12160) and patterned using a Graphtec blade (CB09UB, Graphtec ROBO Pro, CE500 Irvine, CA) (**Fig. 4.2B**). The vinyl mask was then lifted off and stuck to a clean polystyrene Petri-dish (100 mm diameter) as shown in **Fig. 4.2C**. A pair of sharp tweezers was used to carefully remove the rest of the vinyl film around the designed mold structure. **Fig. 4.2D** shows the 2 inlet and 2 outlet channels templated in the vinyl mold with each channel being 0.2 mm wide and 100 μm high. Each channel ends with a 0.4 mm x 0.4 mm port that provides a microfluidic pathway to flow electrolyte through the microchips.

4.2.2   PDMS microfluidic cell fabrication

PDMS pre-polymer and curing agent (Sylgard 184 silicone elastomer kit, Dow Corning, Midland, MI) were mixed thoroughly in a 10:1 (wt/wt) ratio in a polystyrene weighing boat (25 mm) for 5 min. The pre-polymer mixture was placed into a vacuum desiccator and degassed for 15 min at low pressure (~20–30 Torr) to remove air bubbles formed during the mixing process. 5 mL of this degassed mixture was flowed over the vinyl mold in a 100 mm polystyrene Petri dish, which provided a 0.8-1.0 mm thick PDMS layer. The mold was allowed to partially dry overnight at room temperature on a flat level surface. The PDMS polymer was then cured at 60 °C for 1 h, using a laboratory oven in air. After curing, the PDMS layer was carefully peeled off from the vinyl mask and placed over a clean cover glass (1.2 mm thickness, 76 x 52 mm, Tedpella). The outer structure of the microfluidic cell was cut off using a sharp scalpel blade. Holes were punched at the top of each microfluidic channel and at the inlet/outlet ports using a 0.75 mm biopsy puncher (EMS-core, 69039-07, USA) as presented in **Fig. 4.2E**. Further, a cover glass with thickness of 0.17 mm (#1.5 thickness, 64 x 50 mm, Tedpella) was rinsed with a mixture of Methanol and Mili-Q water in a ratio of 50:50 then with isopropanol (Sigma Aldrich, 99.8%) and allowed to dry in a clean place.

After complete drying, the mold could be left for up to one day before making the PDMS/glass assembly, which was prepared as follows. First, the cover glass was treated with an air plasma for 90 s. (600 mTorr air pressure and the high-power setting (30 W) in an expanded plasma cleaner (PDC-001, Harrick, Ithaca, NY, USA)). The PDMS layer was peeled off the cover glass and immediately treated with the same plasma conditions, but for only 30 s. Immediately, the PDMS layer was bonded to the cover glass by applying gentle and even pressure over the PDMS layer. It was then cured at 60 °C for 1 h in a closed oven to fully cure (**Fig. 4.2F**). Afterwards, the PDMS/cover glass composite was cut to precisely the same structure as the PDMS layer using a diamond tip scriber (70036, EMS) as shown in **Fig. 4.2G**. Subsequently, a section of silicone tube (0.8 – 1.2cm) with 3.0 mm OD and 1.0 mm ID (Uxcell silicone) was placed on the punched holes at the top of each microfluidic channel, glued using silicone adhesive (Dow Corning 3140) and allowed to cure overnight at room temperature. **Figure 4.2H** shows the complete microfluidic cell.
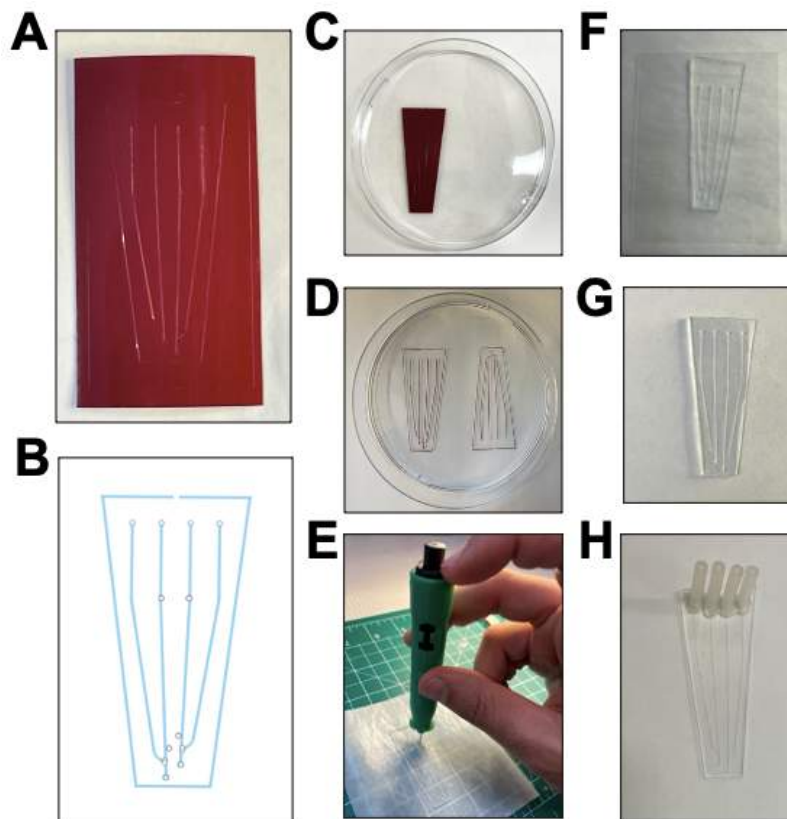
Figure 4.2 Design and fabrication of microfluidic cell. (A) Vinyl casting mold was developed using xurography technique. **(B)** CAD drawing of the casting mold. **(C)** CAD vinyl mask adhered to polystyrene Petri-dish. **(D)** Final structure of the microfluidic vinyl mold. **(E)** punching holes at the top of each microfluidic channel and at the inlet/outlet ports. **(F)** PDMS layer bonded to the cover glass. **(G)** PDMS/glass cell with the same structure. **(H)** microfluidic cell after adhering the silicon tubes to the PDMS.

4.2.3   Design and assembly of electrochemical microchips

Custom electrochemical microchips (referred to as chip "E" and chip "F"), designed in collaboration with, and fabricated by Norcada Inc. (www.Norcada.com), are used in the electrochemical part of the device. Chip 'E' was fabricated with 3 electrodes, while chip 'F' was fabricated with a spacer layer channel defining the electrolyte thickness channel. The electrodes design of chip E (**Fig. 4.3A**) are different from other designs (Bozzini et al., 2014; Lim et al., 2016), Hummingbird scientific cell (https://hummingbirdscientific.com), and Norcada cell (https://www.norcada.com), which typically have the counter electrode

symmetrically surrounding the working electrode. The current design of chip E was chosen to minimize the possibility of counter and working electrodes shorting during multiple deposition and stripping cycles when conditions lead to electrodeposited dendrite formation. The window area of chip E is coated with a hydrophilic layer, while the rest of the chip is coated with a hydrophobic layer (except the contact pad of the electrodes). This coating facilitates the electrolyte flow and helps fill the electrolyte.

Figure 4.3A-a and 4.3A-b present the design of the electrochemical microchips E and F. Figure 4.3A, part c-e is a cartoon of the silicon chips. Figure 4.3B presents an expanded view of the windows and the two assembled microchips (E and F chips). The downstream microchip (chip E), which is equipped with three gold electrodes (see Fig. 4.1D), is a 200 μm thick, 12 mm (V) × 5 mm (H) piece of single crystal Si, with a 100 nm thick silicon nitride (SiN$_x$) X-ray translucent film, on top of which 3 Au electrodes are located. The gold layer is 50 nm thick, except in two regions, a circle in the CE and a semi-circle in the WE, where the Au is only 15 nm thick to increase X-ray transparency. The upstream microchip (chip F) is a 200 μm thick, 7 mm (V) × 5 mm (H) piece of single crystal Si, with a 50 nm thick silicon nitride (SiN$_x$) coating. The shorter vertical size allows a 5 mm space for contact to the Au electrodes on chip E. Chip F encloses the electrolyte and is equipped with a SiO$_x$-spacer layer of a defined thickness. In the studies described in this work chip F's with spacer layers of 0.5 or 1.0 μm were used, but other thicknesses can be provided by Norcada. To allow liquid electrolyte flow into the gap between the two chips, vertically offset (0.8 mm x 0.8 mm) inlet and outlet ports are etched through electrode chip E (see Fig. 4.3Ac). Chip Es are etched to remove the Si in an area of 200 μm x 80 μm (± 30μm) so as to generate a 100 ± 5 nm thick SiNx window. Chip Fs are also etched in the corresponding area (see Fig. 4.3Ab) so as to generate a 50 ± 5 nm thick SiNx window. To ensure that almost all of the electrical signal derives from the electrode area inside the SiNx windows, the surface of chip "E" (except for the window area and the contact pad of the electrodes) is coated with an electrically insulating passivation layer.

The chips are assembled as follows. Just prior to assembly, the "E" and "F" chips are plasma treated for 90 s (600 mTorr air pressure and the high-power setting (30 W) in an expanded plasma cleaner (PDC-001, Harrick, Ithaca, NY, USA). to increase the hydrophilicity

of the spacer and the electrode chip. Directly after plasma treatment, the two chips are positioned under an optical microscope to align the two silicon nitride (SiN_x) windows. They are then sealed at the junction of the 2-chips using Torr-Seal epoxy resin (Varian, Ideal Vacuum, USA). The top and bottom are first sealed while applying pressure to keep the chips as close as possible using the 3D printed sample holder of our previously published *in-situ* device (Prabu et al., 2018). After this, the partial chip assembly is placed in a clean covered petri dish and allowed to complete curing for 72 hrs.

Subsequently, the PDMS surface and the backside of the sealed chips are treated in plasma cleaner for 30 s and 90 s respectively. Immediately, the sealed chips are bonded to the PDMS/glass cell by applying gentle pressure using a flat tweezer. Bonding the chips to the PDMS layer was performed very carefully, so that the (0.8 mm x 0.8 mm) inlet and outlet ports of the microchips are aligned precisely with the (0.4 mm x 0.4 mm) ports of the microfluidic channels. Finally, the two chips are sealed along both sides under a stereo microscope using Torr-Seal epoxy resin as presented in **Fig. 4.3B**. We wait 72 h prior to using the device in order to allow the Torr-Seal to completely cure. The sealing around the chips is investigated carefully to confirm complete sealing and to avoid any possible leakage. The transmission window of the two chips "E" and "F" allows alignment with an accuracy margin of ~20 μm, while bonding the partially sealed chips with the PDMS/glass cell can occur with an accuracy margin of ~100 μm.
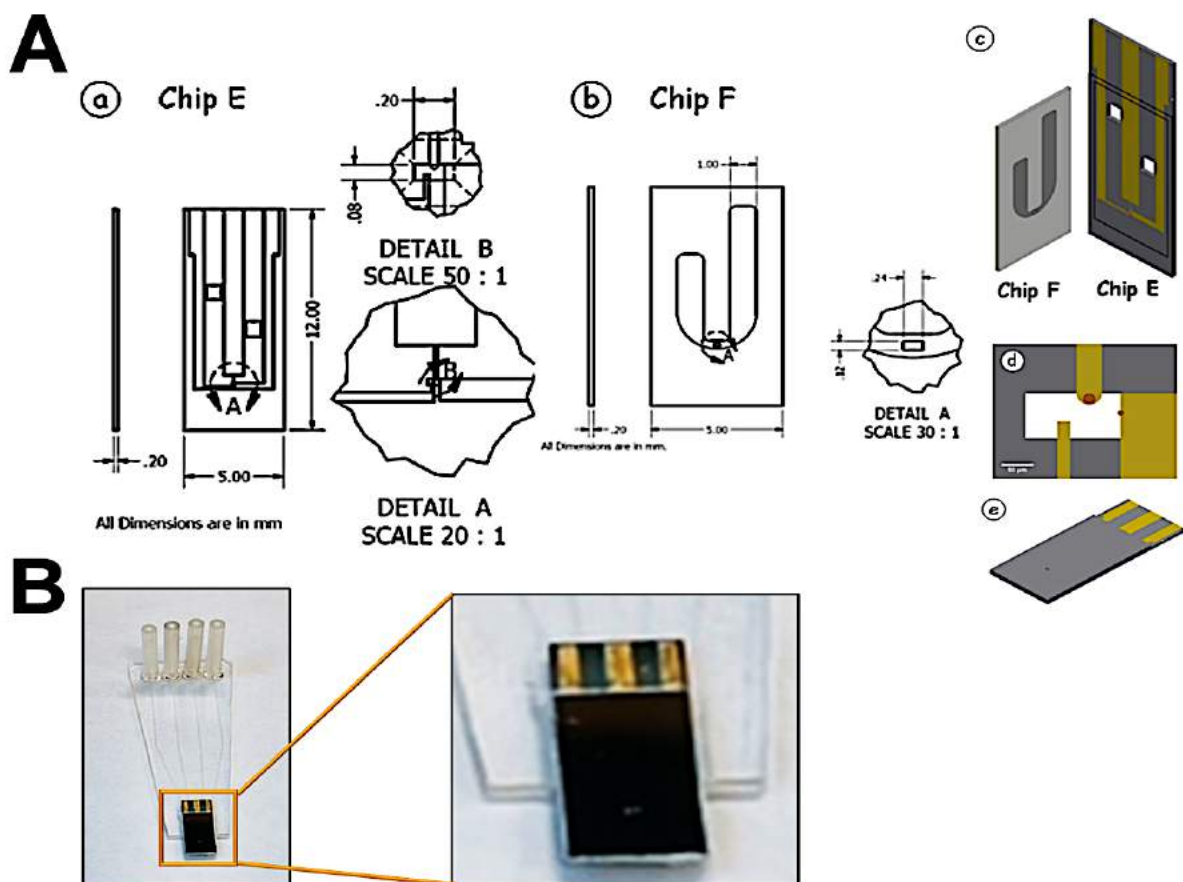
Figure 4.3   Design of electrochemical microchips. (A) Design of silicon nitride chips for used in the fabrication of the *in-situ* flow electrochemical device, **a)** and **b)** describe the design of silicon nitride chips "E" and "F", respectively, **c)** cartoon drawing of the silicon chips used for STXM measurements, **d)** and **e)** expanded cartoon view of the STXM transparent silicon nitride window and the two assembled microchips (E and F chips). Reprinted from (Prabu et al., 2018). With permission from AIP Publishing. **(B)** Microchips (E and F) sealed together (The magnification shows how the uniformity of Torr-Seal epoxy resin around the two chips is inspected).

4.2.4   Printed Circuit Board Frame: design and fabrication

The printed circuit board **(**PCB) was designed using computer-aided design (CAD) software (Autodesk fusion 360, USA - version 2.0.12160), exported in "ipt" format and then used to generate a G-code (geometric code) file used as input to a computer-aided manufacturing (CAM) system which milled the PCB to the desired shape. **Figure 4.4A** and **4.4B** present CAD drawings of the front and back sides of the machined PCB. Copper clad

laminate sheet with a thickness of 2.0 mm (FR4, LAM 093 1/0 9X12X5, Midwest Circuit Technology, USA) was used as the PCB material. It was milled from both the front side (Copper) and the back side (the flame retardant coated, FR4 epoxy) using a computerized numerical control (CNC) machine (Tormach 770M, WI, USA) operated by Paul Gatt in the Department of Chemical Engineering. Details of the front and back sides of the PCB are presented in **Fig. 4.4C** and **4.4D**, respectively. The top side of the PCB has an opening (4 cm x 1 cm) for mounting the 4 silicone tubes (Uxcell, 1mm ID x 3 mm OD, A15121600ux1004, Amazon.ca) into the PDMS/glass composite. The window (0.6 cm x 1.2 cm) has a 300 μm step edge at the bottom of the PCB which supports the bonded chips of the microfluidic cell. This edge allows the chips to remain flat and flush with the PCB surface and helps ensure an even and secure fit. The PCB is designed with 3 copper traces (1 mm wide) for connecting to the three electrodes (see **Fig. 4.4C**). The remainder of the Cu clad layer is used as a ground surface. All four electrodes are soldered to a 4-pin connector plug (MOLEX, 53261-0471, Newark, Canada). A trapezoidal pocket was CNC milled into the glass / epoxy composite at the back side of the copper clad laminate PCB to allow the PDMS/glass microfluidic cell to be placed snuggly into the frame structure. The PCB frame has 6 mounting holes (0.1 mm diameter) through which 0-80 flat head screws are used to screw into 0-80 tapped holes, in order to attach the PMMA backplate to the frame. In addition, there are 2 (1 mm high x 3 mm wide) holes, at the same vertical position as the SiNx windows of the device and 5 mm to the right and left of the window area (see **Fig. 4.4C**). These holes are used to measure the incident flux (I_0), in order to estimate electrolyte thickness by measuring the total absorbance of all parts of the device (windows, electrolyte, Au electrodes and sample material) (see **Section 4.2.9**). Finally, after fabricating the PCB, copper or Au-coated Cu springy connector strips (Feuerherdt GmbH, initial samples were kindly supplied by Prof. Martin Obst, University of Bayreuth, Germany) are soldered to the copper traces as indicated in **Fig. 4.4E.** This PCB structure has advantages of easy access of the microfluidic cell through the frame and provides a robust electrical connection between the Au electrodes of the chips and the potentiostat. Additionally, the flat projection of the *in-situ* device allows performing STXM measurements at very low X-ray energy, in principle as low as 200 eV (depending on the zone plate and OSA) (Zhang, 2023), since the position of the electrodes, and thus the focal plane of the microscope, is only 200 um

below the surface of the PCB frame, This is in contrast to many other *in-situ* flow electrochemical devices (e.g. Hummingbird and Norcada), which typically use O-ring seals requiring a larger (up to 1 mm) 'bulk' of material upstream from the position of the electrodes in order to achieve a reliable seal. Many such devices cannot work below 500 eV, whereas our device has been used for *in-situ* measurements at the carbon K-edge (280-320 eV).

4.2.5   PMMA (backplate) design and fabrication

A 1 mm thick polymethylmethacrylate (PMMA) plate was used as the backplate of the PDMS/glass microfluidic cell. The PMMA sheet was cut with a sharp scalpel blade to specific dimensions (**Fig 4.4F**) that allow the left and right edges to sit on the edges of the recessed machined into the back side of the PCB **(Fig. 4.4B)**. 0.046 mm diameter holes were drilled through the PMMA plate at the same positions as the 6 holes in PCB, and tapped using a carbon steel tap (McMaster-Carr, USA) with thread of 3/64" to fit a 0-80 nylon screw (0-80, flat head, 92929A103, Mcmaster-Carr, USA).
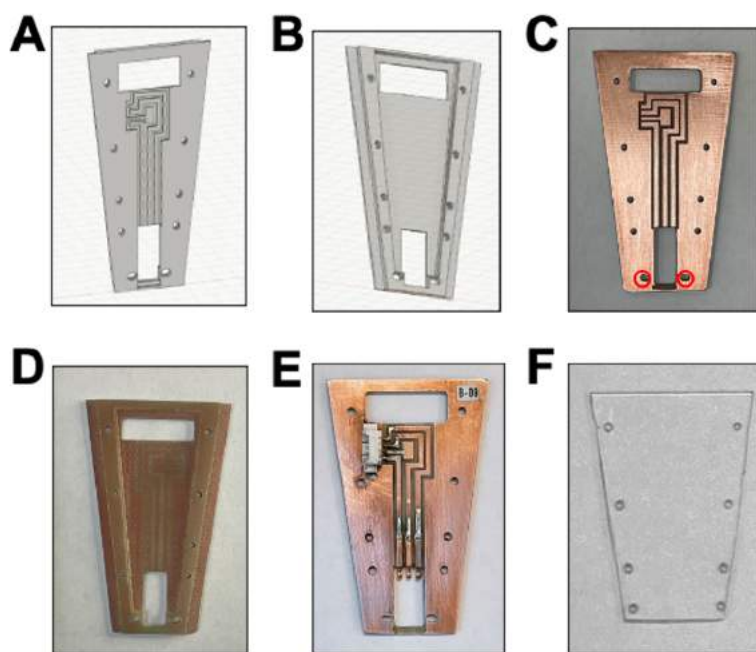
Figure 4.4   Design and photos of the printed circuit board. (A) and **(B)** CAD drawing of front and back side of the designed PCB. **(C)** and **D)** Milled structure of the front and back sides of the PCB used in the *in-situ* electrochemical device. **(E)** 4 pins connector plug, and copper traces are soldiered to the PCB. **(F)** PMMA backplate. The red circles in (C) show the right and left side holes designed to measure the incident flux (I_0).

4.2.6 Assembly of the *in-situ* electrochemical device

The PDMS/glass microfluidic cell is inserted carefully into the PCB frame in the following way. First, the bottom edge of the chips is placed on the 0.3 mm step at the bottom of the PCB window. Second, the silicone tubes are gently maneuvered into the upper PCB window. The springy electrical connection strips should touch each of the electrode contact pads and the PDMS/glass part should be situated into the back side of the PCB frame without any stress points. Third, the PMMA back plate is placed carefully over the glass, and plastic screws are inserted through the PCB holes and screwed gently into the corresponding threaded PMMA holes. The screws should be tightened in alternating sequence with minimal force. After assembly, the device is carefully examined under a stereo microscope (see **Fig. 4.3B**) and then a high magnification optical microscope (e.g. Olympus BX51) to confirm that the glass sheet or the Si_3N_4 window did not crack during the assembly process. **Figure 4.5A(a-c)** shows the PCB, microfluidic cell and PMMA back plate, respectively, used in the fabrication of the *in-situ* device. A cartoon showing an exploded view of the *in-situ* device assembly is presented in **Fig. 4.5Ad.** The *in-situ* device assembly steps are illustrated in **Fig. 4.5B**. All components of the *in-situ* flow electrochemical device, along with specifications and suppliers, are listed in **Table 4.1.**
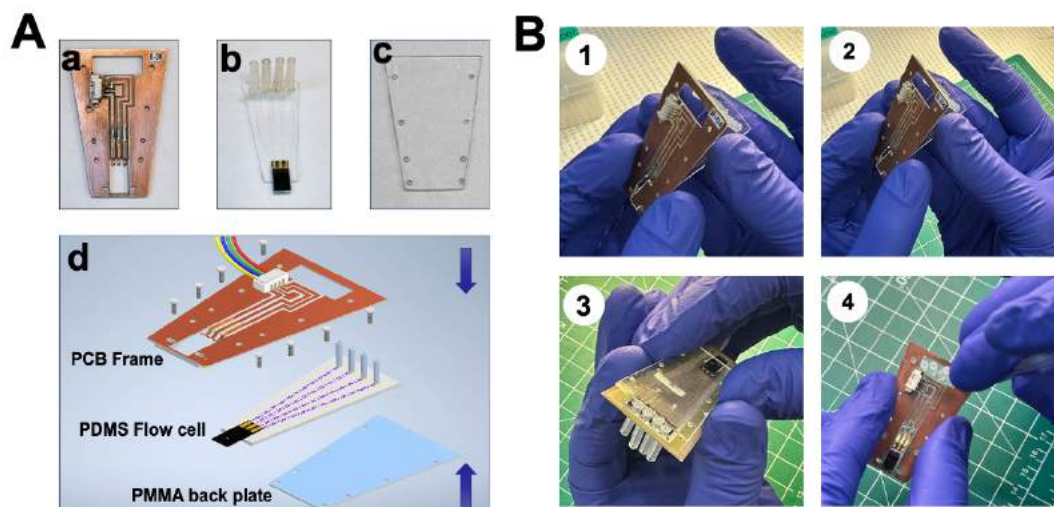
Figure 4.5 **(A)** Components and assembly of the *in-situ* flow electrochemistry device. a) Fabricated PCB, b) Microfluidic cell bonded to microchips (E and F), c) PMMA back plate, and **d)** cartoon drawing of the *in-situ* device assembly. **(B)** Photographs showing the assembly steps of the *in-situ* device.

Table 4.1 List of *in-situ* flow electrochemical device components, specifications, and suppliers

Item	Specification	Part #	Source / supplier
PDMS -Dow Sylgrard 184	0.5 kg kit	119001	McMaster Lab stores
Punch for holes in PDMS	0.75 mm	69039-07	EMS DIASUM
PMMA sheet	1mm thickness, (100L x 150W)	LSK-Arc003	Amazon
T handle tap wrench	1/16 to 5/32 inch	WSW2CYT4	Grainger
Tap (Uncoated High-Speed Steel)	Tap for 0-80 screw, 5/16" Thread Length	2522A751	McMaster-Carr
Drill	3/16" drill for 0-80 screws	SKU 1320.125	McMaster-Carr
Plastic screws (flat head)	0-80, 3/16 long flat head	92929A 102	McMaster-Carr
Uxcell Silicone tube	1mm ID, 3 mm OD	A15121600ux1004	Amazon
Tubing cutter	Perpendicular cuts on polymeric tubing	JR-797	VICI
Tefzel tubing	1/16" OD x .010" ID x 5ft	IDEX 1529	Idex
Cu clad	1-sided FR4 PC boards, (4"x6"), 1.6 mm thick	20X0789	Newark
Cover glass #1.5	Thickness, (64 x 50mm)	260378	Tedpella
Molex 4-pin pico-blade connector header	4-pin connector	53261-0471	Newark
Molex cable assembly	4 positions	15134-0401	Newark
Adapter, pin jack	2mm to 4 mm banana plug	BU-P1809-2	Newark
Banana plug-jack	4 mm (Flange to Potentiostat)	76-118	Newark
Varian Torr Seal Vacuum Equipment	High Vacuum Epoxy, up to 1×10^{-9} Torr	P102144	Ideal vac
Silicone sealant	DOW 732 clear sealant 90ML	65W5700	Newark
DB9 socket cable	Female socket	11.01.6290	Newark
DB9 cable (Female - PEEK, Kapton)	UHV Ribbon Cables (up to 1×10^{-10} Torr)	100880	Accu-Glass
SiNx chips (E and F)	Window Size: 200 m x 80μm F2 (spacer; 500, 1000, 1500 nm)	As per requested	Norcada
DB9 on 2.75"CF Flange	9D-275, 9 Pin Feedthrough on a 2.75" CF Flange	100200	Accu-Glass
USB 3 on 2.75"CF Flange	USB Feedthrough, Double-Ended, 2.75" Conflat Flange, Grounded Shield, UHV Compatible	P1012173	Ideal spectroscopy
Syringe pump	Programmable Single Syringe Pump	NE-1010	pump systems inc.
EMStat4 LR potentiostat	Potential range: ±3 V Current range: 1 nA to 10 mA	EmStat4S Low Range	Palmsense

4.2.7 *In-situ* flow electrochemical device external connections

4.2.7.1 Electrical Connections

In order to perform electrochemical measurements during STXM experiments, the *in-situ* flow electrochemical device can be connected to a potentiostat by two different methods:

(I) Portable potentiostat placed inside STXM chamber. The potentiostat (EmStat4, PalmSens, Houten, Netherlands) cables are connected to the WE, CE, RE and ground electrodes through a male four pin connector cable (MOLEX, 15134-0401, Newark, Canada). The potentiostat inside the STXM chamber is connected to an external computer via a 2.75-inch ConFlat (CF) flange equipped with female USB ports on both the air and vacuum side (11.01.6290, Newark) **(Fig. 4.6C)**. A USB cable inside the STXM chamber connects the potentiostat to the vacuum side of the USB port, while a USB-3 cable is used to connect the air side of the USB port to a computer outside the STXM chamber.

(II) The potentiostat is placed outside the STXM chamber and connected to the electrodes of the microfluidic cell (mounted inside the STXM chamber) through a 4-wire cable from the Molex connector on the PCB board to four pins of a female DB9 connector (UHV Ribbon, 100880, Accu-Glass) which in turn is plugged into a male DB-9 connector (in vacuum) welded into a 2.75-inch CF flange (100200, Accu-Glass). Outside the STXM chamber, the potentiostat signals cable (WE, CE, RE and ground) are connected to the male DB-9 connector on the air-side of the 2.75-inch CF flange through a female DB-9 cable (ROLINE, 11.01.6290, Newark, Canada). This flange is mounted to a 2.75" flange on the STXM tank **(Fig. 4.6D).**
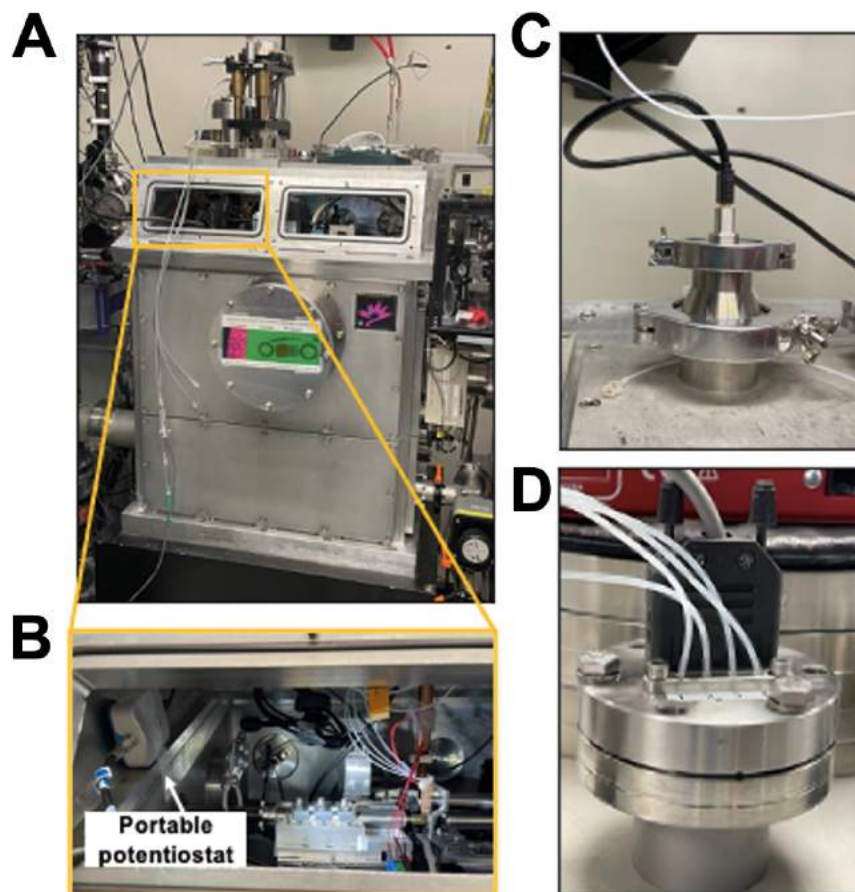
Figure 4.6   Electrical connections between the *in-situ* device and the potentiostat. (A) The CLS ambient STXM chamber after mounting the *in-situ* device inside the tank and connecting to the 2.75-inch CF flange. **(B)** Expanded view of STXM chamber after mounting the *in-situ* device into STXM sample holder, showing the potentiostat placed inside the tank. **(C)** Expanded view of the DB9 flange with the feedthrough tubes while using the potentiostat outside STXM chamber. **(D)** Expanded view of the USB flange while using potentiostat inside STXM chamber.

4.2.7.2 Fluid connections

A syringe pump (New Era, NE-1010, pump systems inc.) outside the STXM chamber is used to control the flow of electrolyte through the cell. The fluid lines of the microfluidic cell inside the STXM chamber are connected to the external syringe pump using Tefzel tubes (1.5 m length with 1.58 mm OD and 0.25 mm ID, SPECO, Canada) which are inserted into the 1 cm long silicone tubes (1.0 mm ID) sealed to the microfluidic cell (Tefzel tubes with larger

ID (1mm) were tried but we found that the lager tube ID increased the electrolyte exchange time and may increase the internal pressure). The four Tefzel tubes are passed through 2 mm holes in the 2.75-inch CF flange. Initially the Tefzel tubes were glued with different adhesive materials to make a vacuum seal into oversized holes. First, we tried Torr-Seal, then 5-min epoxy. However, this approach did not work, probably because of poor contact between the adhesive and the Tefzel tubing. In order to achieve a vacuum seal, a stainless-steel keeper piece with four 1.35 mm holes and four O-rings (ID 1.24mm, OD 2.62 mm) is placed over the holes in the 2.75-inch CF flange through which the Tefzel tubes pass, and the O-rings are compressed between the keeper and the flange as presented in **(Fig. 4.7A and 4.7B)**. **Figure 4.6A** and **4.6B** are photos of the CLS STXM chamber after mounting the *in-situ* device into the tank and connecting the 2.75-inch CF flange while the potentiostat inside the chamber.
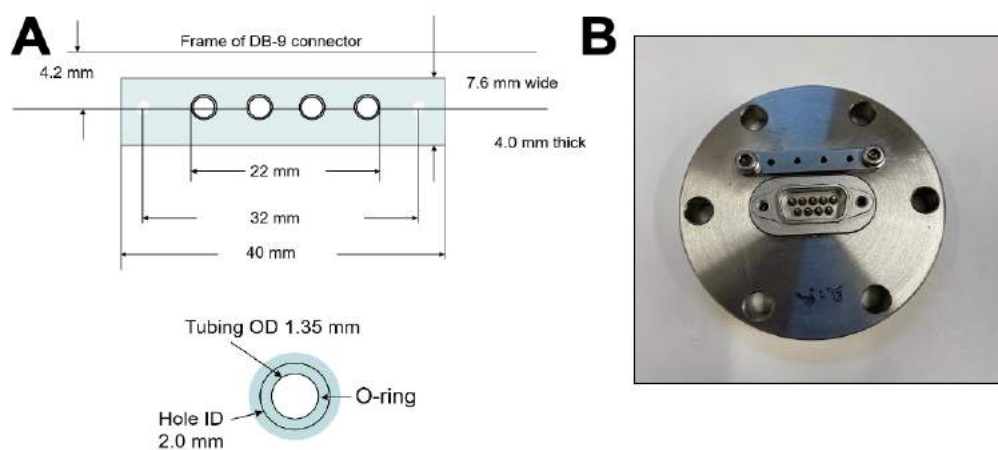
Figure 4.7   Use of a keeper piece for a vacuum tight seal of the Tefzel tubes. (A) detailed design of stainless-steel keeper used to seal the feed through holes in the 2.75-inch flange. **(B)** 2.75-inch flange showing the feed through holes with the keeper piece and the 2-sided DB9 connector, mounted on the same flange.

4.2.8 Operational instructions: Safe Operating Procedure

The following is a systematic step-by-step guide to operate the *in-situ* flow electrochemical device.

4.2.8.1 Filling the cell with electrolyte

1- Prepare the electrolyte solution and fill a 1 mL plastic syringe (839-210-02, Canadawide Scientific).

2- Carefully complete the assembly of the *in-situ* device as described in **Section 4.2.6**.

3- Check the electrical continuity between the exposed gold surface of the WE, CE, RE traces on chip E and the traces on the PCB. A common problem is poor connection at the Au/Cu spring connectors. Also, check the resistance between adjacent Cu traces, which should be greater than 1 GΩ.

4- Place the *in-situ* device into the optical microscope sample holder (this holder has the same design as the holder for the trapezoidal plates in most STXMs).

5- Place the 2.75-inch CF flange with the feedthrough Tefzel tubes into a vice and tighten to hold the flange.

6- Number the tubes as 1,2,3,4. Tubes 1 and 2 are the inlet tubes and tubes 3 and 4 are the outlet tubes.

7- Rinse each tube with deionized water three times.

8- Carefully, insert the four Tefzel tubes one by one into the four silicone tubes of the *in-situ* device (do not apply much force). The Tefzel tubes should be inserted ~1 mm into the silicone tube. Support the silicone tube to minimize force on the tube – PCB joint.

9- Transfer the *in-situ* device in the sample holder to the optical microscope stage.

10- Avoid bending the silicone tubes at the connection point with Tefzel tubes. If needed, use tape to hold the Tefzel tubes to the body of the optical microscope.

11- To minimize the electrolyte dead volume in the system, fill the 2-inlet tubing and the 2-outlet tubing with electrolyte using a 1 mL plastic syringe.

12- Manually, slowly inject the electrolyte from the 1 mL plastic syringe into the first inlet channel. This step typically takes 10 minutes. Watch for the meniscus of the fluid column to disappear into the device, and then appear in the second inlet channel.

13- If an air bubble appears in the Tefzel or silicone tube of the first or second inlet channels, keep pushing the electrolyte to remove the bubble completely from the tubes.

14- Close the second inlet channel by placing a Luer plug (RK-02024-06, Cole-Parmer, Canada) or an empty, closed 1 mL syringe at the end of the Tezfal tubing connected to the silicone tube of the second channel.

15- Place the electrolyte filled 1 mL syringe into the syringe pump (New Era, NE-1010).

16- Turn on the syringe pump, set the flow rate to 50 µl/h in push mode and start the pump.

17- While watching the optical microscope image (through the ocular or on the computer display), monitor the electrolyte entering and filling the microchip window of the *in-situ* device. This process usually takes 15-20 min at a flow rate of 50 µl/h, and more time at slower flow rates.

18- If filling the electrolyte takes more than 30 min, increase the syringe pump flow rate to 100 µl/h.

19- During the filling process, watch carefully for leaks around the chips, from the Torr-sealed joints at the side of the chip assembly, or from the silicone tube - device connection. If a small leak is noticed at the tubing side, try to seal it with 5-min epoxy and check again. If the leak still present, start a new device. If the leak is from the Torr-Seal around the microchips, then directly start a new device (Torr-Seal curing takes 72 h. in room temperature).

20- After confirming that the electrolyte completely fills the window and there are no air bubbles, reduce the pump flow rate to 5-10 µl/h and wait until three or four Newton rings are observed (**Fig. 4.1D**). In some cases, you may need to open the second channel to reduce the pressure inside the flow channels in order to reduce the thickness of the electrolyte to a level where the Newton rings appear (see **Section 4.2.9** for an explanation of the origin of these rings, how to estimate fluid layer thickness, and warnings about possible misinterpretations).

21- Once you confirm the electrolyte has filled the cell and there is no leakage, the device is ready to be used. Typically, with the 5 µl/h flow rate, the cell will be stable for 24 hours and a 70% filled 1 mL syringe will last 140 hrs.

4.2.8.2 Transferring the device to the CLS STXM

1- Retract the detector Z to +5000 μm, the sample Z to +5000 μm and ZP Z to -12000 μm.

2- Remove the 2.75-inch flange at the top of the STXM chamber.

3- Remove the 2.75-inch *in-situ* device CF flange from the vice. Carefully hold the *in-situ* device by the Tefzel tubes, so that there is no stress on the silicone tubes or the body of the device.

4- Slowly and carefully insert the *in-situ* device through the open 2.75-inch flange of the STXM chamber.

5- Once it is inside the chamber, connect the male four pin connector cable to the female Molex connector of the *in-situ* device (see section **4.2.7.1**). Securely hold the PCB board of the device while doing this.

6- Slide the *in-situ* device carefully into the 3-pins of the STXM sample holder, making sure the device descends vertically, without touching the OSA or the detector.

7- The silicone tubes should be coming straight upstream out of the *in-situ* device.

8- Tape the Tefzel tubes to the internal body of the STXM chamber making sure there is no stress on the silicone tubes.

9- If the potentiostat will be used inside the STXM chamber, ensure that it is positioned so there is not spatial conflict with STXM stages or cables, etc.

10- Connect all cables as described in **Section 4.2.7.1**, for either potentiostat inside or potentiostat outside the STXM chamber.

11- Check that the potentiostat software can connect to the potentiostat. (occasionally there are problems with the USB connections).

12- Before closing the STXM chamber, measure OCP for 60 seconds, the OCP should be between -100 and +100 mV, and the fluctuation should be within ± 5 mV.

13- After confirming stability of the electrical connection, position the coarse sample stages such that the window of the *in-situ* device is aligned with the OSA as best as possible. Then bring the sample-Z as close as possible to the desired Z-position (perhaps 500 μm downstream from the A_0 value).

4.2.8.3 Strategies for setting up the STXM and finding the window in the *in-situ* device

1- Close the STXM tank.

2- Follow the protocols for (1) displacing air in tank with He, or (2) pumping and backfill, or (3) running under vacuum, which are described in **Section 4.2.11**).

3- Finding the window – OPTIONS:

  3.1 use the fiducialized optical microscope stage (Note: the software that used to be available to save STXM-compatible images with the optical microscope co-ordinates has not been (& probably never will be) adapted for the new camera but the encoder readout is still there). If the standard position calibration plate (10 um pinhole in center of slot 5, stored in the SM's box of calibration and check samples) is imaged first in the optical microscope and the readout set to zero, and then in the STXM (setting the position of the cursor at the center of the hole to x=0, y=0) , then the encoded readout position of the window of the *in-situ* device (probably accurate to 100 μm) can be used to find the window.

  3.2 Use motor scans to find H_y, the vertical center of left and right holes (**Fig. 4.4C**), and the x-position of the holes closest to the window in the *in-situ* device. H_X, the x-center of the window, should be halfway between these two values. A similar procedure can be used to find V_y, the y-center of the window.

  3.3 Be patient and do large coarse (x,y) imaging (the a-STXM at CLS (prior to the Dec 2023 upgrade) was very slow and inaccurate for these scans).

4- If the window is not found at the photon energy of interest after a reasonable effort (~20 m), it is possible that the electrolyte layer is too thick, and the X-ray transmission at the photon energy you are using is so low. There is effectively no transmitted X-rays. In these cases, it is useful to go to a much higher photon energy, within the limits of the capabilities of the beamline – 1600 eV is typically used at CLS-SM – and search again. As indicated in **Section 4.2.9**, even a 5 mm thick electrolyte layer is easily penetrated at 1600 eV.

5- After finding the window, focusing, imaging and spectroscopy, and spectromicroscopy are performed, as described in **Section 3.5.**

4.2.9   Measuring the electrolyte thickness

Electrolyte thickness is one of the most challenging factors that affect the success of performing *in-situ* STXM measurements. The maximal sample thickness at which STXM can be performed is strongly dependent on the photon energy. For a minimum useable transmission of 5 % (OD = 3), the useable electrolyte thickness (estimated as H_2O) is plotted in **Fig. 4.8**,
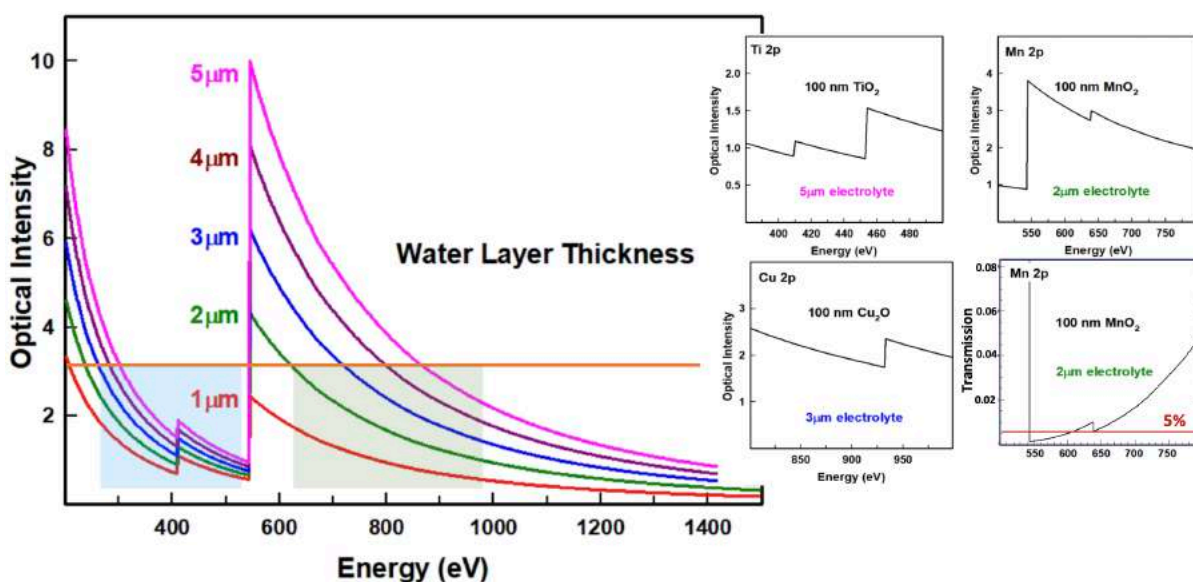
Figure 4.8   Estimating the effect of thickness of the electrolyte layer on the viability of *in-situ* STXM measurements.

which plots the elemental optical density response for the *in-situ* cell (0.15 μm Si_3N_3O plus the indicated thickness (in μm) of water). The blue shaded region is the 'water window' below the O 1s edge. The green shaded area are regions where the elemental response of the water and the windows is below 3 OD (red horizontal line) which is a reasonable upper limit of the OD to avoid absorption saturation. The inserts show the visibility of the Ti 2p, Mn 2p and Cu 2p edges with the indicated sample and electrolyte thickness. Edges below and far above the O K-edge are much more tolerant of thicker electrolyte layers than edges which

are just above the O 1s edge, such as the Mn 2p edge. This was one of the main challenges of my project.

For studies at the Cu edge (930 eV), the upper useable electrolyte thickness is ~3 μm. For studies at the Mn 2p edge (640 eV), the upper electrolyte thickness is 1.5 μm. Thick electrolyte layers (>3-4 μm) can significantly attenuate the transmitted X-rays, hindering measurement of meaningful spectra. The maximum optical density (OD) of a measured sample in STXM should be less than 2.5 (A. Hitchcock et al., 2008; Prabu, 2017). Thicker samples can still be measured. However, absorption saturation distorts spectral shapes due to non-linear absorption (de Groot et al., 2010), and prevents using the observed optical density as a means to measure sample thickness.

The spacer chip (F-chip) supplied by Norcada is designed to have a specific liquid layer thickness (in my *in-situ* STXM measurements we used 500 nm or 1000 nm spacers). However, different parameters can affect the electrolyte thickness during cell preparation and *in-situ* STXM measurements such as: (i) excess sealing material (Torr-Seal) around the two silicon chips (E and F) which sometimes penetrate through the edges of the microchips and increase the gap between the chips; (ii) uneven pressure applied to the top chip (F) during sealing which can resulted in different electrolyte thickness; (iii) syringe pump flow rate (higher rate results in thicker electrolyte) and flow mode (changing from push mode to pull mode is often effective at reducing the electrolyte thickness). If the cell is used under a partial or full vacuum, there will be bulging of the windows, which is easily observed as a greater transmission at the edges of the window. **Figure 4.9** shows the *in-situ* device window filled with 0.1M MnSO$_4$ solution under the optical microscope. The Newton interference rings can be observed clearly at a low flow rate of 5 µl/hr **(Fig. 4.9A)**. However, after increasing the flow rate to 70 µl/hr, a gradual electrolyte bulging occurred, and the Newton rings disappeared **(Fig 4.9B)**. On the other hand, the number of Newton rings, which originate from the interference of the light reflected from the SiNx-electrolyte and electrolyte-air surfaces, can be used as an early estimate of the electrolyte thickness inside the cell. We found that 3-5 rings are equivalent to 2-3 μm. Nevertheless, the uncertainty associated with this estimation is considerable.
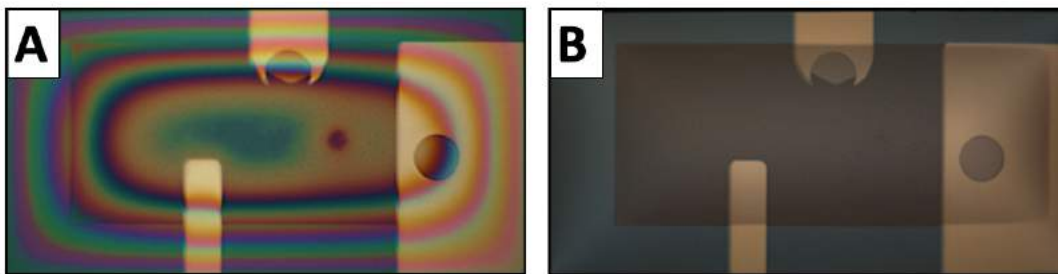
Figure 4.9 Optical images of the *in-situ* device window filled with 0.1M MnSO$_4$ solution under the optical microscope. **(A)** at flow rate of 5 µl/hr. **(B)** at flow rate of 70 µl/hr. (magnification 20x).

During *in-situ* STXM measurements, electrolyte thickness can be estimated from the OD at the photon energy of interest. The solution OD is determined by measuring point spectra at the hole (I$_0$) and at the electrolyte area (I) (see **Fig. 5.12**). After subtracting the contribution of the 150 nm thick SiN$_x$ window, the remaining OD can be divided by the OD of 1 µm of water to estimate the electrolyte thickness. If the measured electrolyte thickness is > 3 µm one or more of the following can be used to decrease the electrolyte layer thickness:

(I)   Release the pressure in the second inlet channel of the *in-situ* device by opening the plug for 30 s. The bulging at the center of the silicon nitrite window should decrease. This method should be performed very carefully. Air bubbles can be generated if the second channel is opened too long (maximum 30 s).

(II)   Change the pump MODE from push mode to pull mode. Measure the electrolyte thickness every ~10 minutes till the electrolyte thickness decreased. This method should be performed carefully to avoid air bubble generation (do not apply too high a flow rate in pull mode (stay < 80 µl/h).

(III)   Decrease the pump flow rate (in push mode), However this method takes a long time to decrease the electrolyte layer thickness (more than one h).

After any of these actions it is a good idea to measure the electrolyte thickness again. If needed, one or more of these methods can be repeated several times.

4.2.10 Challenges of operating the *in-situ* flow electrochemical device.

Many challenges occur either during preparation of the *in-situ* device or during *in-situ* STXM measurements. Detailed description of those challenges is listed below:

(I)   **Cover glass breakage during assembly of the *in-situ* device.** The cell (glass/PDMS part) of the *in-situ* device should be placed inside the PCB frame very carefully (as described in **Section 4.2.6**) since pressure on the cover glass can easily break it.

(II) **Leakage in the silicone tube/ Tefzel tube connection point.** Since the ID of the silicone tube and the OD of the Tefzel tube are similar (1 mm), the Tefzel tube should be tightly connected to the silicone tube. Thus, possibility of leakage at this point is low. However, during filling the electrolyte, if any leakage is observed at the connection point, the Tefzel tube should be inserted more inside the silicone tube.

(III) **Leakage at the Torr-Seal around the micro-chips**. It is essential to perform the sealing under a stereomicroscope and confirm that the Torr-Seal has covered all of the junction between the E and F chips. If a small leakage is observed during filling the electrolyte under the optical microscope, more Torr-Seal can be added on the leak point. We have found that Torr-Seal, left to cure overnight is the most reliable. However, it is also possible to use 5-minute epoxy (preferred brand: Bindullin-Werk H.L. Fuerth, Germany) if the *in-situ* experiments will be performed under atmospheric pressure. On the other hand, if the Torr-Seal has been used for a long time, it may be crystalized and generate leakage even if it covers all the edges of the chips. Fresh Torr-Seal is a good investment (Varian, Ideal Vacuum, USA - USD $100).

(IV) **Poor or faulty electrical connections.** Unstable OCP or unexpected electrochemical behavior (high current/potential or wrong CV shape) can be generated if either there is a short (even 10 MΩ) between the Cu traces of the PCB, or if one of the Au coated Cu spring contacts does not touch one of the three electrodes gold surface of the microchips. It is very important to measure the resistance between the Cu traces as well as the connection between the microchips and the Au/Cu strips after the assembly of the *in-situ* device and before filling the electrolyte.

(V)   **Air bubble generation during STXM measurements.** At high positive or negative applied potential (it is different from one cell to another, but generally $> +0.9V_{Au}$ and $<-$

$0.5V_{Au}$), air bubbles can be produced from the water splitting reaction. Several methods can be used to remove the air bubble (see **Fig. 4.10**): (1) Increase the flow rate to 100-150 µl/h while measuring STXM images of the whole window to confirm that the size of the air bubble is reducing. (2) Change the syringe pump from push to pull mode to withdraw the air bubble. (3) Open the second channel and cautiously push the electrolyte manually using the plastic syringe. **<u>This method is extremely dangerous</u>**. It is critical that the distances from the sample to the OSA and the sample to the detector are increased as much as possible, to reduce the amount of damage that can occur to the STXM, if this action breaks the window. So far, we have had more than 5 accidents in which an *in-situ* cell broke while trying to release an air bubble by manual manipulation of the syringe. Such accidents can damage the OSA, contaminate the ZP and pollute the optics of the interferometer system. Thus, it is very essential to remove the OSA and ZP back by 6 mm and the detector by 6 mm. It is highly recommended to open the STXM chamber and remove the *in-situ* cell from the STXM during this approach to moving an air bubble. Most often it is not successful.
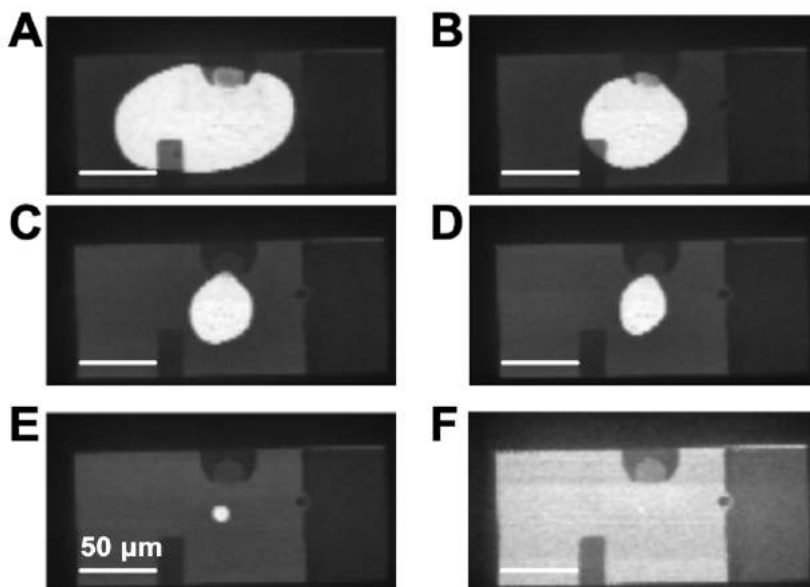
Figure 4.10   Removing an air bubble from the *in-situ* cell inside the STXM. **(A-F)** series of STXM images at 640 eV during air bubble removal by increasing the pump flow rate from 10 µl/h to 80 µl/h in an *in-situ* STXM experiment performed at the CLS.

(VI) **Mounting or demounting the *in-situ* device inside the STXM chamber.** It is very critical to be careful in these procedures. Ideally, two persons, each with prior experience with the cell, should be involved. If the Tefzel tubes twist or the device does not mount correctly in the holder, the ZP and OSA can be damaged. Mounting the device inside the STXM chamber should be performed very carefully and slowly, with good lighting and patience.

(VII) **Pumping the STXM chamber**. The cells made at McMaster have broken almost every time when it has been necessary to pump (Interestingly, cells and devices fabricated by the Obst group at U. Bayreuth have consistently survived similar pumping and being kept under vacuum for more than 24 hours). This is probably because the microchips (bonded to the glass/PDMS cell) are not appropriately set on the thin edge of the PCB, which consequently generates pressure points, causing a cell to leak during the pumping of the STXM tank. Two factors significantly impact this issue: (1) the precision of the PCB inside margins. The microfluidic cell with the microchips should fit precisely inside the PCB. If the PCB milling process (using CNC) does not produce smooth edges, then considerable pressure points will occur. (2) sealing the microchips with Torr-Seal. This sealing should be as thin as possible; too much Torr-Seal around the chips will also generate pressure points. We tried to overcome these issues by increasing the depth of the PCB edges and decreasing the amount of Torr-Seal. Nevertheless, I note that we still have major challenges running the *in-situ* STXM experiments under vacuum.

If it is necessary to pump the STXM chamber: (1) make sure there is maximum possible OSA-sample and sample-detector distances to minimize damage if a leak occurs. (2) ensure that each of the four inlet/outlet tubes are blocked. That way if the cell leaks, there will only be a small local leak (the cell volume is ~0.1 mL) in the *in-situ* device inside the tank. However, if any one of the fluid connection tubes is open, atmospheric pressure will push the full volume of fluid (1-2 mL) into the STXM tank. (3) Start the pumping VERY slowly (try for laminar flow) and pump slowly (~20 m).

4.2.11 *In-situ* STXM measurements under vacuum and at atmospheric pressure

In-situ STXM measurements can be performed under two different conditions:

(I)   Under vacuum by pumping the tank to ∼0.1 mbar and then back filling the chamber with 1/6 - 1/3 bar of He. This is the normal protocol for dry samples at the CLS ambient STXM and some other STXMs, whereas other STXMs only operate in vacuum.

(II)   Displacing the air inside the STXM tank by opening a flange or pumping connection at the lowest level of the tank (air is heavier than He) and slowly increase the He flow rate so that there is a gentle cooling sensation when your hand is placed in the exhaust, but negligible overpressure (the STXM tank pressure should not deviate significantly from 1 bar). We use this approach routinely without cell leakage or other problems at the CLS ambient STXM. It has worked once at the Soleil STXM and several times at the Solaris STXM. However, it could not be used at the ALS or Bessy STXMs due to a radiation safety requirement of a minimum vacuum of 200 mbar. At the MAX IV STXM He was used several times (June 022, October 2023), which unfortunately resulted in large sparks in some of the electrical connections inside the STXM, blowing fuses and damaging stepper motor drivers. These sparks arise because the distance over which an electrical discharge can occur is much longer in He than in air, especially at pressures in the range of 0.1 to 10 mbar (Lech & Węgierek, 2022) Stepper motors are particularly sensitive to shorts because they are current controlled devices.

Almost all of our successful *in-situ* experiments were performed at atmospheric pressure (by replacing the air inside the tank with He gas). Most of the *in-situ* experiments performed under vacuum have failed by breaking the SiNx window. More improvements in the design and execution of the flow electrochemical *in-situ* device are required to make it compatible with vacuum operation. A robust, ideally portable system which could test vacuum compatibility is an absolute requirement. These are provided with the commercial liquid cell *in-situ* devices for electron microscopes and synchrotron use (https://hummingbirdscientific.com; https://www.norcada.com). At the CLS, we have vacuum adaptors which allow us to test the *in-situ* device outside STXM using the test station of the CLS Hummingbird vacuum compatibility system.

4.3 Electrochemical performance of the *in-situ* device

4.3.1 Solution electrochemistry

Cyclic voltammetry (CV) is a common technique used to study the electrochemical properties of different systems (see **Section 2.1.1**). The ferricyanide/ferrocyanide ($K_3[Fe(CN)_6]$/$K_4[Fe(CN)_6]$) redox couple has a CV with well-defined oxidation and reduction peaks that have a nearly ideal Nernstian response (Ferrario et al., 2012; Pajkossy et al., 2021). The electrochemical performance of the *in-situ* device was investigated in a sealed cell under the optical microscope using an equimolar solution of 0.1 M ferricyanide and 0.1 M ferrocyanide. The flow *in-situ* electrochemical device was filled with the ferri/ferrocyanide solution. Three cycles of CV were performed with a scan rate of 20 mVs^{-1} in the potential range of +0.6 to −0.6 V$_{Au}$ with respect to the Au pseudo-reference (V$_{Au}$). The validity, stability and sensitivity of the electrochemical performance of the Au electrodes of the *in-situ* device was confirmed by the repeatable CV shapes of the ($K_3[Fe(CN)_6]$/ $K_4[Fe(CN)_6]$) redox system with typical oxidation and reduction peaks, as presented in **Fig. 4.11.**
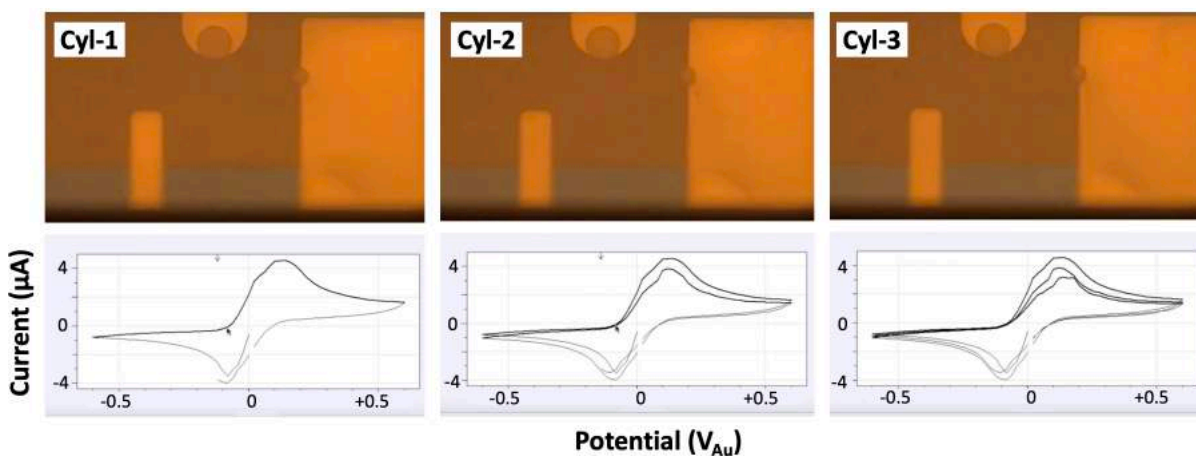
Figure 4.11 Images captured from recorded videos of optical microscope and potentiostat screens during CV measurements performed in the *in-situ* device using 0.1 M ferri/ferrocyanide solution.

4.4 Summary of research performed with the *in-situ* flow electrochemical device

Experiments have been conducted at different synchrotron facilities using the *in-situ* flow device, as outlined in **Table 4.2**.-Here several examples are briefly presented to demonstrate its capabilities.

Table 4.2 List of *in-situ* flow electrochemical STXM experiments.

Date	Synchrotron facility	Experiments (all studies were performed with the *in-situ* device unless indicated otherwise)
2020-02	CLS (Saskatoon, Canada)	Ferri/Ferro cyanide solution redox
2021-09	CLS (Saskatoon, Canada)	Cu CO$_2$R electrocatalyst
		MnOx-redox
2022-03	CLS (Saskatoon, Canada)	Cu CO2R Cuelectrocatalysts
		MnOx-redox
2022-05	MaxIV (Lund, Sweden)	Cu CO2Rcatalysts
		MnOx-redox
2022-06	CLS (Saskatoon, Canada)	*In-situ* STXM studies of Ni-N-C single atom catalysts
		MnOx-redox
		In-situ STXM studies at C 1s edge
2022-07	CLS (Saskatoon, Canada)	*In-situ* STXM/ptychography studies Hummingbird cell
		MnOx-redox
2022-10	Soleil (Saint Aubin, France)	*In-situ* ptychography studies of Cu CO2R catalysts
2023-01	Bessy-II (Berlin, Germany)	Cu CO2R catalysts; *in-situ STXM* chemi-movies
		MnOx-redox
2023-03	ALS (Berkley, USA)	Cu CO2R catalysts; *in-situ STXM* chemi-movies
2023-03	MaxIV (Lund, Sweden)	Ni-N-C single atom catalysts
2023-04	Solaris (Krakow, Poland)	Cu CO2R catalysts; *in-situ STXM* chemi-movies
		MnOx-redox
2023-06	CLS (Saskatoon, Canada)	*In-situ* STXM studies of Ni-N-C single atom catalysts
		In-situ STXM studies at C 1s edge
		MnOx-redox
2023-10	MaxIV (Lund, Sweden)	MnOx-redox

4.4.1 *In-situ* STXM study of the ferri/ferro cyanide system

Imaging, spectroscopy and spectromicroscopy measurements were performed using the ambient STXM at the spectromicroscopy (SM) beamline 10ID1 at the Canadian Light Source (CLS, Saskatoon, Canada) (Kaznatcheev et al., 2007). Initially a 0.1 M ferrocyanide solution $K_4[Fe(CN)_6]$ was introduced. Several Fe L_{23} stacks were measured. Then 4 cycles CV measurement over the potential range of +0.3 to -0.6 V_{Au} at a scan rate of 20 mV/s was performed. Next the ferrocyanide solution was replaced with a 0.1 M potassium ferricyanide $K_3[Fe(CN)_6]$ solution. This process took about 10 min. Once the cell contents were changed, 4 cycles CV measurement was performed using the same parameters as for the ferrocyanide. At the end of the CV measurement, the OCP value was +0.1 V. Several Fe L_{23} stacks were measured on the ferricyanide solution using the same spectroscopic parameters used to measure the ferrocyanide solution. During the spectroscopy stacks of both species, the syringe pump was stopped. The four-cycle CVs took roughly 20 min while each Fe L_{23} stack took 25 minutes to measure.

Figure **4.12A** presents the Fe L_{23} spectra of ferricyanide and ferrocyanide, in comparison to spectra digitized from the literature (Kitajima et al., 2013). The energy scale was set by assigning the position for the first peak in the Fe L_{23} spectrum of $K_3[Fe(CN)_6]$ to 706.2 eV (Kitajima et al., 2013). **Figure 4.12B** presents the cyclic voltammetry (CV) results. In the *in-situ* CV of potassium ferrocyanide ($K_4[Fe(CN)_6]$) the anodic peak occurred at +0.05 V_{Au} and the cathodic peak occurred at –0.01 V_{Au}. For potassium ferricyanide ($K_3[Fe(CN)_6]$) the CV was significant different **(Fig. 4.12D)**, with different peak displacements and a stronger reduction wave and a weaker oxidative wave than in the CV of the ferrocyanide. The anodic and (broad) cathodic peaks of ferricyanide appeared at –0.07 V_{Au} and –0.26 V_{Au} respectively. The –0.12 V shift between the anodic peaks of the two species is much larger than that in CVs of these two species that have been reported in the literature (Frenzel et al., 2017). This may be attributed to increase the electrode polarization resulting in kinetic limitation during the redox reaction.

Despite some small discrepancies, the Fe L_{23} spectra measured in the flow electrochemical cell **(Fig. 4.12C)** are in agreement with literature spectra (Kitajima et al., 2013; Kunnus et al., 2016; Risch et al., 2015). The close similarity of the spectra of the solution

species ($Fe(CN)_6^{n-}$, n = 3, 4) to that of the solid indicates the immediate environment is not changed by dissolution. In each case the Fe ion is coordinated by cyanide ligands (Kunnus et al., 2016). The differences between the spectra of these two species, and in particular the 706 eV peak that is only present in $K_3[Fe(CN)_6]$, easily differentiate these two species.

When scanning the CV of $[Fe(CN)_6]^{4-}$ the anodic potential reached a sufficiently positive potential ($+0.05$ V_{Au}) to oxidize the solution species to $[Fe(CN)_6]^{3-}$. When the scan direction reverses, the $[Fe(CN)_6]^{3-}$ is reduced to $[Fe(CN)_6]^{4-}$ as indicated by the sharp reduction peak at 0 V_{Au}. When the CV of $[Fe(CN)_6]^{4-}$ was scanned in the oxidative direction, starting at 0 V_{Au} there was no oxidation peak in the first cycle, as expected. However, after switching the scan direction and scanning to -0.2 V_{Au} a sharp reduction peak was observed, corresponding to the reduction of $[Fe(CN)_6]^{3-}$ to $[Fe(CN)_6]^{4-}$. On the second, and subsequent cycles, the oxidation peak was observed at $–0.07$ V_{Au}. The peak anodic current in the CV of $[Fe(CN)_6]^{4-}$ was much lower than that in the CV of $[Fe(CN)_6]^{3-}$. This lower current may be due to less migration to the positively charged working electrode of $[Fe(CN)_6]^{3-}$ as compared to $[Fe(CN)_6]^{4-}$ (Rooney et al., 2000).

In general, tracking the oxidation state changes during ferri/ferro redox reaction with a rapid exchange of electrolytes and relatively quick spectroscopic and electrochemical characterization demonstrate the capabilities of the *in-situ* device and its ability to investigate different electrochemical systems.
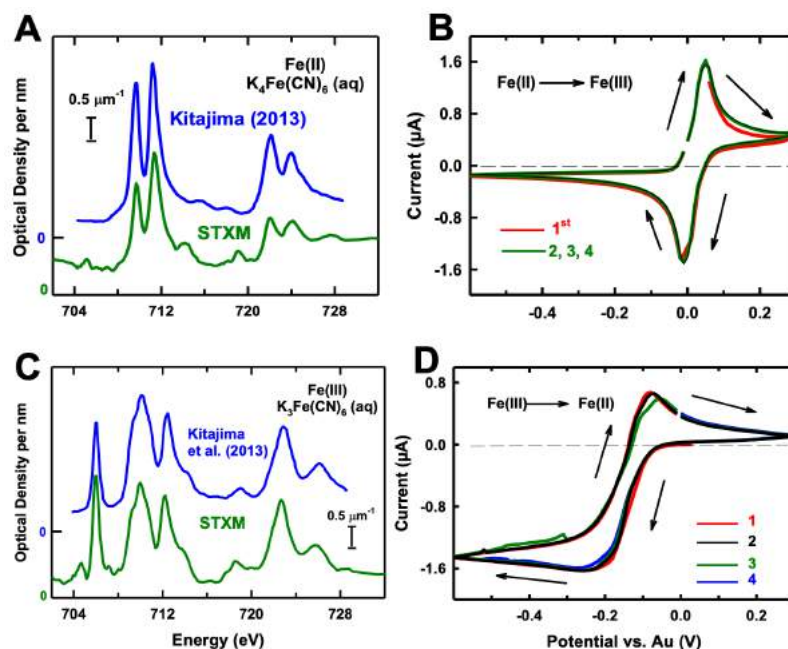
Figure 4.12   STXM spectroscopy and *in-situ* flow electrochemistry of ferricyanide and ferrocyanide. (A) Fe L_{23} X-ray absorption spectrum of 0.1 M potassium ferricyanide solution measured in this study, in comparison to Kitajima et al.(Kitajima et al., 2013). **(B)** Fe L_{23} X-ray absorption spectrum of a potassium ferrocyanide solution, compared to Kitajima et al 2013. **(C)** *In-situ* cyclic voltammetry of 0.1 M potassium ferrocyanide solution measured with a scan rate of 20 mV/s. **(D)** *In-situ* cyclic voltammetry of 0.1 M potassium ferricyanide solution measured with a scan rate of 20 mV/s.

4.5   Summary

The design and capability to fabricate and operate the microfluidic-based *in-situ* device was transferred successfully from Martin Obst's group at the University of Bayreuth to the Hitchcock group at McMaster University. The device has been used at STXMs in different synchrotron facilities (see **Table 4.2**). Our research group has performed *in-situ* STXM experiments on the following electrochemical systems: Fe^{2+}/ Fe^{3+}; redox cycling of MnO_x (see **chapter 9**); electrodeposition of Cu electrocatalysts and monitoring their shape and oxidation state during CO_2 reduction (Zhang et al., 2023b; Zhang et al., 2023a). Additionally, the *in-situ* device has been operated at the C 1s edge (Zhang, 2023). Further enhancements are necessary to ensure the reproducibility of successful *in-situ* experiments under vacuum conditions. Deposition of different electrode materials on the WE has been explored (**Section 10.3.5**) but needs significant improvement to be used routinely.

Chapter 5
Experimental Details

This chapter presents the electrochemical methods used at McMaster University to characterize the MnOx system prior to synchrotron measurements. It describes the sample preparation methods used for ex-situ STXM and other characterizations techniques. An overview of ex-situ and in-situ experiments performed at different synchrotron facilities is provided. Finally, it describes how STXM measurements are performed and how STXM data are analyzed.

5.1   Lab-based electrochemical techniques and methods

Cyclic voltammetry (CV), chronoamperometry (CA) and chronopotentiometry (CP) techniques are used to understand the MnOx electrochemical system and to perform *ex-situ* and *in-situ* studies of electrodeposited MnO_2 electrode material. An EmStat4S LR potentiostat (PalmSens, https://www.palmsens.com) was used in all electrochemical experiments in the lab at McMaster and at synchrotron facilities. This potentiostat is a USB-powered/controlled portable device with a potential range of $\pm$ 3V (0.2%) and a current range of 1 nA - 10 mA (0.2%). It possesses 100 µV potential resolution and <0.1 pA current resolution. It is compatible with Microsoft Windows and controlled by PSTrace software. The device is connected to working (WE), counter (CE), reference (RE) electrodes and ground using a double-shielded cable terminating in banana connectors (2 mm).

For each electrochemical technique, the software method and an associated set of specific parameters are required. For cyclic voltammetry (CV), the initial potential, ending potential, starting potential, scan rate, potential step, current sensitivity, and number of cycles must be defined. For chronoamperometry CA), the applied potential, time interval, and run time are required. For chronopotentiometry (CP), the applied current, time interval, and run time are required. In the open circuit potential (OCP) mode, the potential between working and reference electrodes is monitored using high impedance sampling to monitor the system stability. For electrochemical impedance spectroscopy (EIS), AC potential and frequency

range are required. **Figure 5.1** presents screen shots of the PSTrace Graphical User Interface (GUI) used the set the parameters for each of these modes.
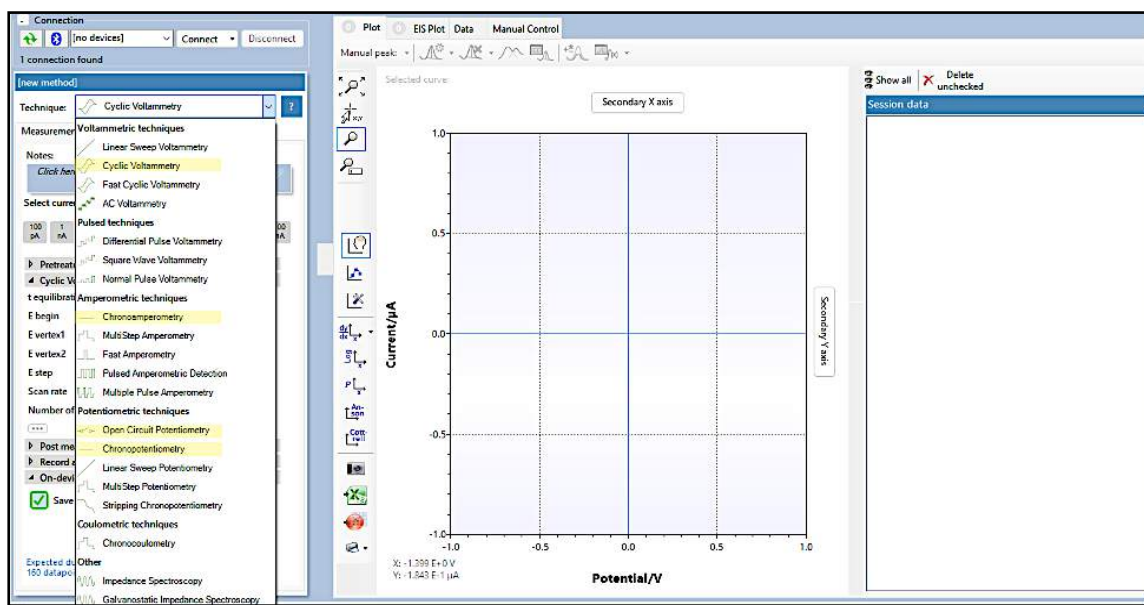
Figure 5.1   Screenshot of the Graphical User Interface (GUI) of the PSTrace software used to control the EmStat4S potentiostat.

5.1.1   Gold electrode fabrication

Au electrodes were fabricated from commercial gold-leaf sheets and polyimide tape (Santos et al., 2018). Gold-leaf sheets (24 Kt) with a thickness of 100 nm, purity of 99.99 % and a size of (79 × 79 mm) were purchased from L.A. gold leaf, USA (1 booklet of 25 sheets costs USD $20). A 25 mm wide polyimide (Kapton) tape with a size of 25 mm (CA-EL-CP-022) was purchased from Amazon, Canada. A sheet of gold leaf was placed on a non-stick paper on a flat surface. Then 10 cm of Kapton tape was placed on the gold leaf, followed by gentle pressing. After that, a razor blade is used to cut the edges of the fabricated electrode to a desired dimension. In most lab experiments, I used Au electrodes with a size of 2x3 cm. After cutting the electrode, 2 pieces (5 mm) of Kapton tape are placed at the top of the Au electrode with a gap of 2 mm to allow electrical connection to the potentiostat cable (**Fig. 5.2**).
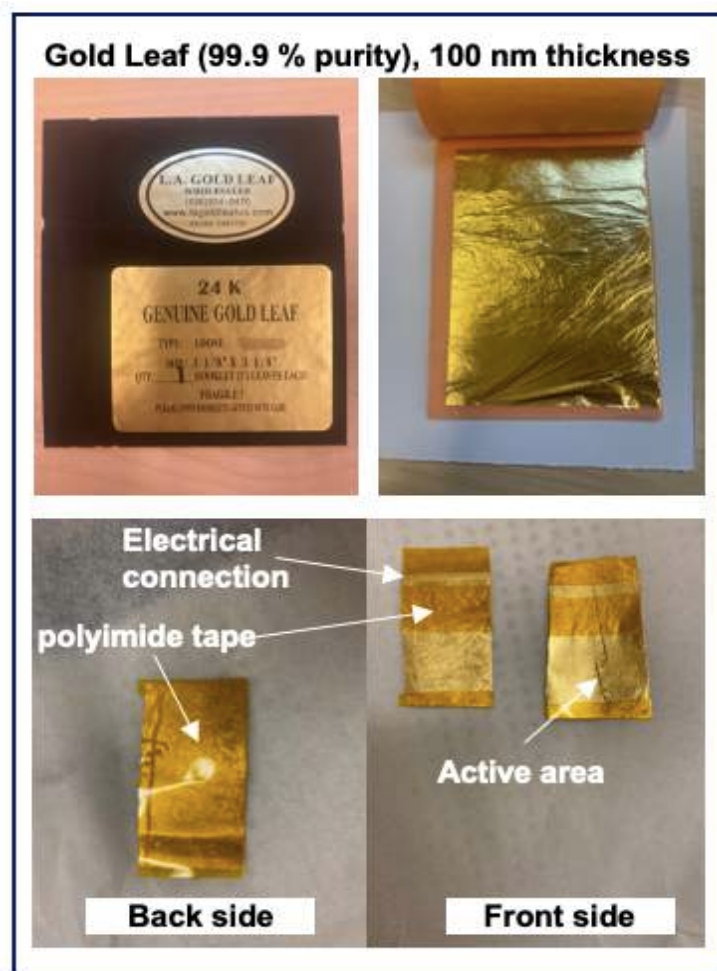
Figure 5.2   Images of the gold-leaf sheets and the fabricated electrode (front and back side).

5.1.2   Comparing Au-leaf and chip E performance using ferri/ferro cyanide CV

Details of the E microchip used in the *in-situ* device are described in **Chapter 4**. In order to compare the electrochemical behavior of the fabricated gold leaf electrodes with that of the Au electrodes of the *in-situ* device microchips, CV measurements (**Fig. 5.4**) were performed using a mixed solution of 0.1 M ferricyanide/ferrocyanide (since its characteristic oxidation and reduction peaks are well-known). One CV measurement using the three Au electrode microchip (in a fully sealed cell) was performed over the potential window of -0.3 V_{Au} to +0.6 V_{Au} and scan rate of 50 mVs^{-1}. Three Au fabricated electrodes (**Section 5.1.1**) were connected as WE, CE and RE to the EmStat4S potentiostat and placed in a 50 mL glass beaker

filled with 25 mL ferri/ferrocyanide solution and subjected to six CV cycles in a potential window of -0.6 V_{Au} to +0.6 V_{Au} and scan rate of 20 mVs^{-1}. **Figure 5.3** presents the experimental setup used to perform both experiments. The fabricated Au electrodes showed a similar CV behavior compared to the microchips CV (see **Fig. 5.4**) indicating a reversible Fe^{2+}/Fe^{3+} couple with anodic peak at +0.33 V_{Au} and cathodic peak at -0.01 V_{Au}. On the other hand, the CV obtained from the Au electrodes of the microchip showed the anodic peak at +0.15 V_{Au} and cathodic peak at +0.09 V_{Au}. The equilibrium potential (the midpoint of the anodic and cathodic peaks) of the fabricated gold leaf electrode and the microchip Au electrodes is +0.16V_{Au} and +0.12V_{Au}, respectively. The deviation in the anodic and cathodic peaks of the fabricated Au electrodes may be related to the gold leaf purity.
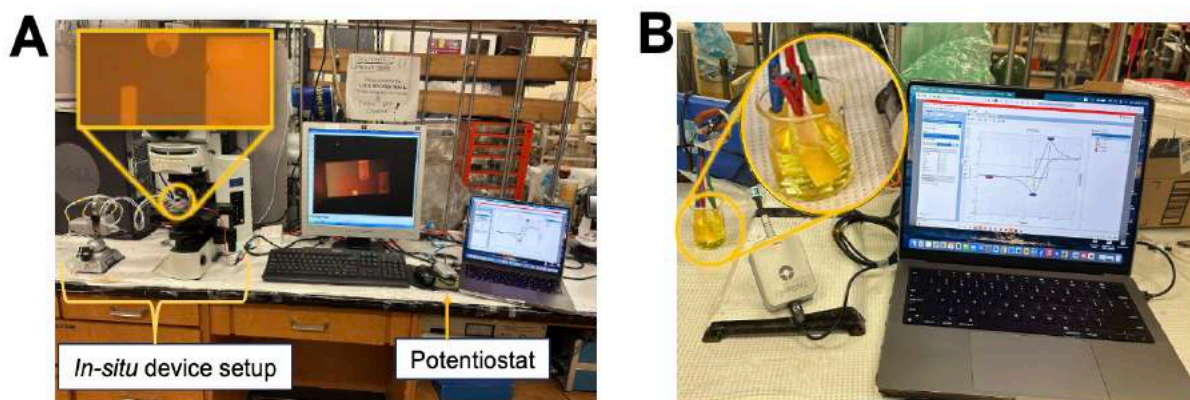
Figure 5.3   Experimental setup of ferri/ferrocyanide system. (A) using the developed *in-situ* device. **(B)** using the gold leaf fabricated electrodes.
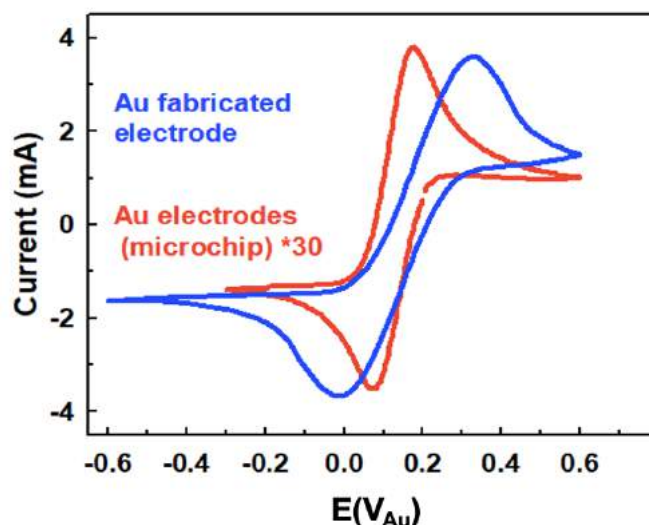
Figure 5.4 Cyclic voltammograms of 0.1M ferri/ferrocyanide solution using 3 Au fabricated electrodes (blue) and 3 Au electrodes of the microchips (red).

5.1.3   MnO$_x$ electro-deposition and redox cycling lab experiments

The electrochemical set up for MnOx lab tests used fabricated gold electrodes (**Section 5.1.1**) as WE, CE and RE, 50 mL beaker and the EmStat4S potentiostat. **Figure 5.5** presents the electrochemical set up used to depositing MnO$_2$ on the Au WE. The three fabricated Au electrodes (2 cm x 2 cm) were inserted into a beaker containing 0.1M MnSO$_4$. A galvanostatic deposition was performed using chronopotentiometry at 2 mA for 2 min (**Fig. 5.6A**). After the electrochemical deposition, the initial Au color of the Au WE (**Fig. 5.5A**) changed to brown in the electrodeposited area (**Fig. 5.5B**). **Figure 5.5C** shows the WE after the MnO$_2$ electrodeposition indicating homogenous deposition over the active area of the Au fabricated WE. After performing the electrodeposition of MnO$_2$ on an Au fabricated electrode, the potentiostat was disconnected and the electrodes removed from the beaker and rinsed with DI water. After that, the electrodes are inserted into a new beaker containing 25 mL of 0.1M Na$_2$SO$_4$ solution. Four CV cycles measurements were performed in the potential window of 0.0 – +0.8 V$_{Au}$ and scan rate of 50 mVs^{-1}(**Fig. 5.6B**) The voltammograms of the 4 cycles are very repeatable showing non-ideal rectangle CV shape (without identified oxidation/reduction peaks), indicating that both surface redox (pseudocapacitance) and non-Faradaic charge storage (EDL) occurred, as illustrated in **Section 2.2.3**.
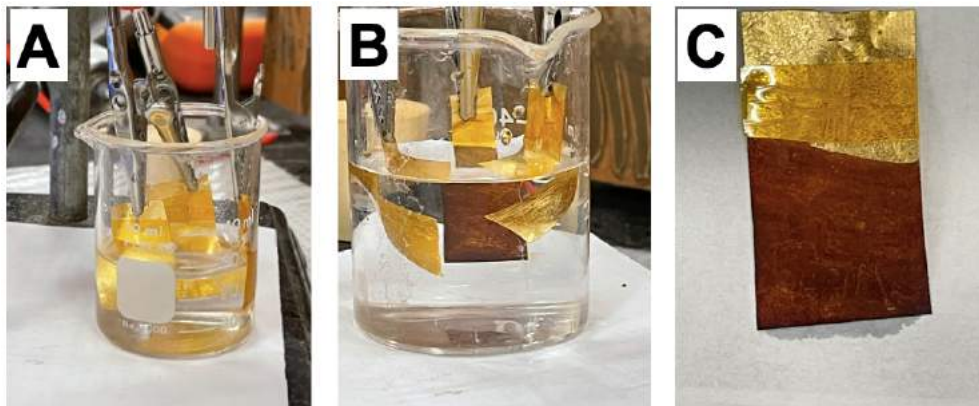
Figure 5.5 Electrochemical set up for MnO_2 electrodeposition. **(A)** Au electrodes before the electrodeposition. **(B)** Au electrodes after the electrodeposition. **(C)** MnO_2 deposition on Au WE.
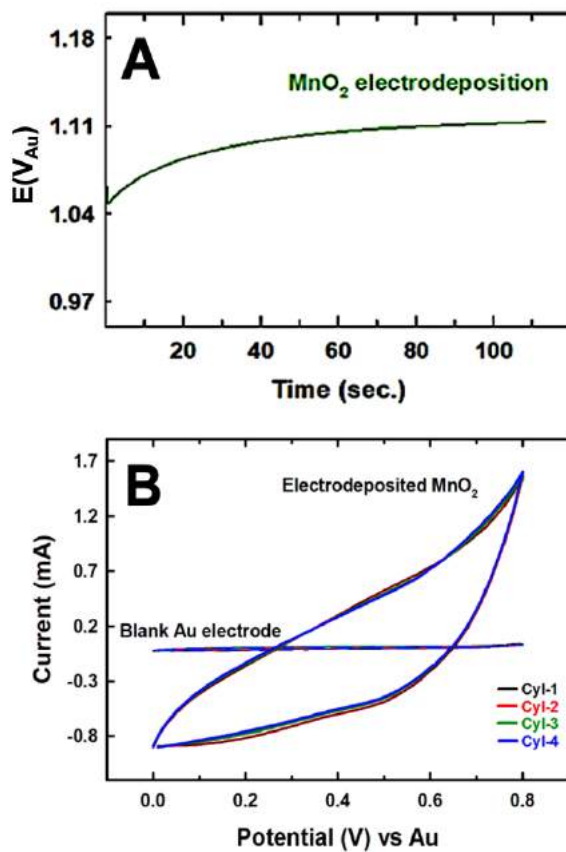
Figure 5.6 **(A)** Galvanostatic deposition of MnO_2 at 2 mA for 2 min. **(B)** CV measurements of electrodeposited MnO_2 in Na_2SO_4, compared to CV of the blank Au electrode.

5.1.4   Relating potentials in the device (V_{Au}) to other standard reference electrodes

In order to compare electrochemical results from the internal pseudo-Au reference and to identify the potential difference between Au and Ag/AgCl reference electrodes, CV results from the *in-situ* cell were compared to the results from CVs measured using a 1 cm^2 pure gold electrode [99.99%, JPGZDJ - LaborXing, China] and a commercial Ag/AgCl (3M KCl) [RREF0021 (Pine Research Instrumentation, USA)] as reference electrodes, platinum wire (Pt) as counter electrode and a glassy carbon disk [ALS Co. Ltd, Japan] as working electrode. The CVs was measured in the potential window of +0.6 to −0.6 V_{Au} (*in-situ* cell) and +0.9 to −0.3 $V_{Ag/AgCl}$ (ex-situ experiment) with a scan rate of 20 mVs^{-1}.

The electrochemical behavior (CV) of the Fe^{2+}/Fe^{3+} cyanide system measured using the pseudo-Au reference electrode and the conventional Ag/AgCl reference electrode are similar **(Fig. 5.7A)**. The CV curves show that the Fe^{2+}/Fe^{3+} couple is nearly reversible at the scan speed used (20 mV/s). The anodic peak occurs at +0.33 V_{Au} and the cathodic peak at -0.01 V_{Au}. The midpoint of the anodic and cathodic peaks was used to define the equilibrium potential of ferri/ferrocyanide system. Its value was +0.16 V_{Au} and +0.42 $V_{Ag/AgCl}$. Considering the Ag/AgCl electrode calibration value (-0.05V), the equilibrium potential of the Ag/AgCl electrode is +0.37 V, indicating a potential difference of +0.21 V between voltages referenced to Ag/AgCl and to the Au pseudo reference. This value is in good agreement with a previously reported result (+0.24 V) (Ferrario et al., 2012). The potential versus Ag/AgCl was then converted to the corresponding potential vs reversible hydrogen electrode (RHE) and standard hydrogen electrode (SHE) based on the Nernst equation (Niu et al., 2020; Rong & Kolpak, 2015):

$$E_{RHE} = E_{Ag/AgCl} + 0.059\, pH + E^0_{Ag/AgCl} \qquad \textbf{(Eq. 5.1)}$$

$$E_{RHE} = E_{SHE} + 0.059\, pH \qquad \textbf{(Eq. 5.2)}$$

The measured pH of 0.1M ferri/ferro cyanide solution was 7.3. Since $E°_{Ag/AgCl} = 0.1976$ V at 25°C and $E_{Ag/AgCl}$ is the experimentally measured potential versus Ag/AgCl reference electrode (L. Wang et al., 2013), the potential vs Ag/AgCl was converted to RHE and SHE using **Eq. 5.1** and **Eq. 5.2**, indicating a potential difference of 0.79 V vs RHE and 0.36 V vs SHE. Therefore, the potential difference between V_{Au} and standard reference electrodes

($V_{Ag/AgCl}$, V_{RHE}, V_{SCE}) in the <u>ferri/ferrocyanide system with pH 7.3</u> (**Fig 5.7B**) can be expressed as:

$$E_{Au} = E_{Ag/AgCl} - 0.21 = E_{RHE} - 0.79 = E_{SHE} - 0.36 \qquad \textbf{(Eq. 5.3)}$$
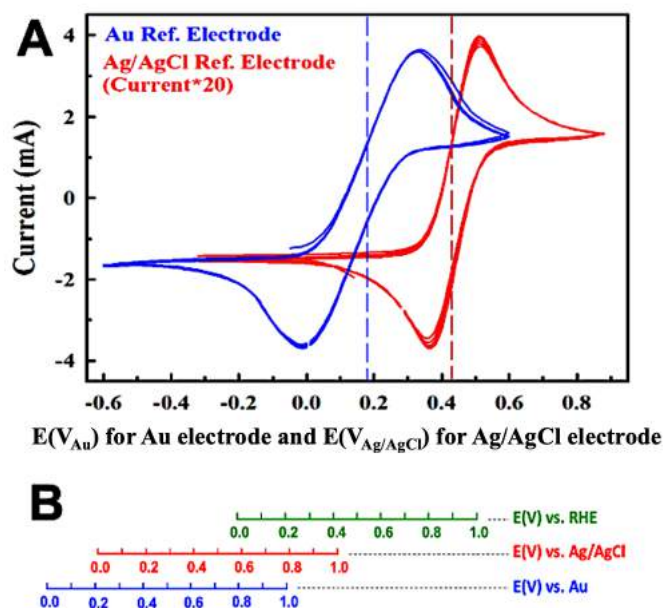
Figure 5.7 Establishing the relationship of V_{Au} and $V_{Ag/AgCl}$. (A) Cyclic Voltammograms (CVs) of 0.1M ferri/ferrocyanide solution using Au and Ag/AgCl as reference electrodes. **(B)** scale diagram of V_{Au} versus $V_{Ag/AgCl}$, V_{RHE} in in the ferri/ferrocyanide system (pH=7.3). Dashed lines are the equilibrium potential of the Au and Ag/AgCl electrodes.

Based on the measured potential different between V_{Au} and $V_{Ag/AgCl}$ ($\Delta E = 0.21$ V, **Eq. 5.3**), and the Nernst equation (**Eq. 5.1** and **5.2**), the relationship between the potentials in the device (V_{Au}) to other standard reference electrodes ($V_{Ag/AgCl}$, V_{RHE}, V_{SCE}) in <u>Na$_2$SO$_4$ electrolyte (pH=6.1)</u> used in the *in-situ* experiments presented in **Chapter 9** is calculated as follows:

$$E_{Au} = E_{Ag/AgCl} - 0.21 = E_{RHE} - 0.77 = E_{SHE} - 0.41 \qquad \textbf{(Eq. 5.4)}$$

Zhang, 2023 measured the potential difference between the Au pseudo-reference electrode of the microchips and the RHE by comparing the CV curves of the Cu redox in a CO_2 saturated 0.1 M $KHCO_3$ system and indicate a -0.43V shift using the Au reference electrode.

5.2   Sample preparation for (*ex-situ*) STXM

5.2.1   Synthesis of Mn_3O_4 and MnO_2 supercapacitor electrodes

A. Mn_3O_4/Quercetin supercapacitor electrodes

This electrode material was used in the research reported in **Chapter 7** and **Chapter 8.** The synthesis of the Mn_3O_4 supercapacitor electrodes was reported elsewhere (Yang et al., 2022). The nanoparticle Mn_3O_4 electrode material was synthesized chemically using chemical precipitation method by dissolving 1.8 g of Manganese nitrate ($Mn(NO_3)_2$) in a 100 mL DI water and slowly adjusting the pH of the solution to pH=10 using 0.01M sodium hydroxide (NaOH) solution. After rinsing the obtained precipitate with water and ethanol, quercetin was added as dispersant in a mass ratio of 13:1 ($Mn(NO_3)_2$: quercetin). The obtained material was centrifuged and then washed with DI water. A Ni foam (95% porosity, 1.6 mm thickness, Vale, Canada) as a current collector was impregnated in a suspension consisting of the as-prepared Mn_3O_4 electrode material, multiwalled carbon nanotubes (MWCNT, ID 4 nm, OD 13 nm, length 1–2 μm, Bayer), and poly(vinyl butyral) (PVB) with a mass ratio of 80:20:3. Further, the suspension was ultrasonicated for 30 min and the resulting porous solid was pressed to 30% of its original thickness.

B. Mn_3O_4 supercapacitor electrodes

This electrode material was used in the study mentioned in **Chapter 8.** The synthesis procedure of these electrodes is the same as the procedure mentioned above (**Section 5.2.1 A**), but without using the dispersant agent (quercetin).

C. Mn_3O_4/High energy ball milling supercapacitor electrodes.

This electrode material was used in the study mentioned in **Chapter 8.** The Mn_3O_4 supercapacitor electrodes were synthesized chemically as described in **Section 5.2.1A**. Consequently, the prepared materials were subjected to high energy ball milling (HEBM) using Mixer Mill MM 500 Nano (Retsch GmbH, Haan, Germany) in aqueous medium at a frequency of 15 Hz for 2 h. QC was used as a dispersant. The mass ratio of manganese oxide : QC was 10:1.

D.   MnO₂ supercapacitor electrodes.

This electrode material was used in the study mentioned in **Chapter 8**. MnO_2 supercapacitor electrodes was synthesized chemically by dissolving 1.6 g of $KMnO_4$ in a 50 mL of water. Subsequently, a 25 mL ethanol was gradually added while continuously stirring the solution for 2 hours. The MnO_2 powder was then obtained by washing and filtering the solution.

E.   MnO₂/High energy ball milling supercapacitor electrodes.

This electrode material was used in the research mentioned in **Chapter 8**. The MnO_2 electrode materials were synthesized chemically as mentioned in **Section 5.2.1 D**, and mixed with quercetin (as dispersant) in a ratio of 10:1 (MnO_2 : quercetin).

5.2.2   Synthesis of α-MnO₂ Zinc Ion Battery (ZIB) electrodes

ex-situ STXM studies were performed on α-MnO_2 ZIBs electrodes subjected to different charging and discharging cycles. Results for α-MnO_2 ZIBs electrode samples after 94 cycles (ending in the charged and discharged state) are briefly described in **Chapter 6**. However, most of the STXM results conducted on these types of electrodes are not mentioned in the thesis. The α-MnO_2 electrode materials were prepared by Thomas Baker and Alejandra Espinoza (Higgins group) using a low temperature solvothermal method. A mixture of 149 mg zinc nitrate hexahydrate ($Zn(NO_3)_2$ $6H_2O$), 251 mg manganese nitrate tetrahydrate ($Mn(NO_3)_2$ $4H_2O$) and 96 mg citric acid are mixed together in 25 mL ethanol and sonicated for 1 h. Further, the solution is filtered and then transferred to a Teflon-lined stainless-steel autoclave and left at 150 °C for 48 h. The obtained product is then washed with ethanol to remove the remaining alkaline salt and then dried under vacuum condition at 100 °C for 12 hours.

5.2.3   Ultra-microtome sample preparation

Different *ex-situ* samples, particularly the α-MnO_2 ZIBs electrode samples, were prepared using ultra-microtoming. All microtome samples were prepared by Marcia Reid at the Electron Microscopy Facility, Faculty of Health Sciences, McMaster University. Ultra-microtoming of different thicknesses allowed STXM measurements of MnOx species without

absorption saturation (as illustrated in **Chapter 6**). For α-MnO$_2$ ZIBs electrode samples, ultra-microtomed sections of 100 nm, 200 nm, 400 nm and 600 nm were placed onto formvar coated TEM grids. Typically, each TEM grid was loaded with samples of 2 different thicknesses. Microtome samples of α-MnO$_2$ ZIBs electrode material on TEM grids are shown in **Fig. 5.8A** and **5.8C**.

5.3   Non-SR characterization of samples

5.3.1   Optical microscopy

Optical microscope with different magnification was an essential tool in preparation of *ex-situ* STXM samples and the *in-situ* device. An Olympus BX51 microscope (at room ABB332, McMaster University) was used to preview *ex-situ* STXM samples that were mounted on grids or SiN$_X$ windows as illustrated in **Fig. 5.8A** and **B**. Prior to performing STXM measurements at synchrotron facilities, visible light microscope (VLM) images were investigated carefully to identify suitable regions of the sample for STXM measurements. **Figure 5.8C** presents an example of optical imaging α-MnO$_2$/Zn ion battery electrode sample mounted on a 3 mm TEM grid at different magnifications to identify potential regions for STXM. The optical microscope was used also in preparation of the *in-situ* device prior to mounting it into STXM chamber. The process of filling the electrolyte is performed under the optical microscope to avoid bubble formation and check for possible leakage. An optical image of filling the *in-situ* device with 0.1M MnSO$_4$ prior to MnOx *in-situ* STXM experiment is presented in **Fig. 4.1**.
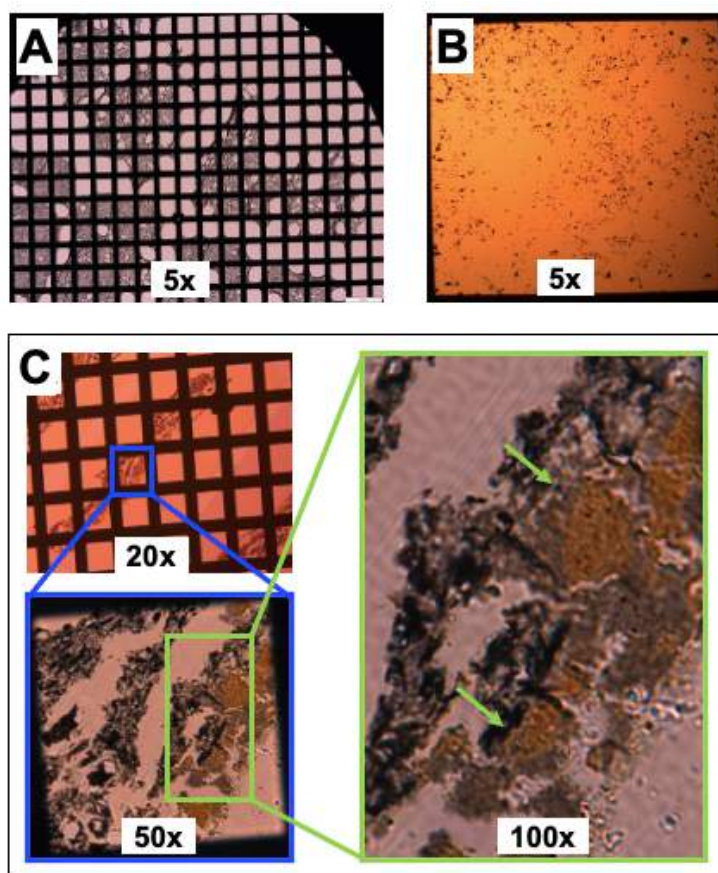
Figure 5.8 Examples of visible light microscope (VLM) images. **(A)** Transmission image of microtomed MnO sample mounted on TEM gride. **(B)** Reflection image of Mn_3O_4 SC-electrode sample mounted on SiN_X windows. **(C)** Example of measuring α-MnO_2/Zn ion battery electrode sample mounted on TEM grid at different magnifications.

5.3.2   Measuring electrolyte thickness using laser fluorescence microscopy

Excessive (> 2 μm) electrolyte thickness is the main factor leading to spectral distortion from absorption saturation during *in-situ* STXM excitements. The upstream microchip (chip F) in the *in-situ* device has a spacer with a defined thickness, typically 500 or 1000 nm. However, the separation of the two chips in the working area typically was 1.5 – 3.5 μm (the E and F microchips in the *in-situ* device are described in detail in **Chapter 4**). For MnOx *in-situ* STXM experiments, the measured spectra are distorted by absorption saturation when the electrolyte is thicker than 2 μm. That distortion blurs the fine features of the Mn 2p spectra, compromising chemical identification. Therefore, prior to some STXM runs, the thickness of

the assembled cell was measured using a laser fluorescence technique at the McMaster Center of Advanced Light Microscopy (CALM, https://calm.mcmaster.ca). A Nikon A1R upright confocal microscope (Nikon Corporation, Japan) was used to acquire a z-stack of images of the assembled *in-situ* cells. A 25x air magnification objective was used with a numerical aperture of 1.10. The imaging sequences (30 images, each 512×512 pixels) measured at a frame rate of 0.5–1 per second with a z - step size of 0.3 μm. The laser power was adjusted to100 mW and a 525 nm fluorescence emission filter was used. ImageJ software (version 1.53, http://imagej.nih.gov/ij) was used to open and process all measured images. **Figure 5.9A** presents an image of the *in-situ* chips measured in fluorescence modes using Nikon A1R upright confocal microscope. Selected images during z-stack measurements are presented in **Fig. 5.9B**.
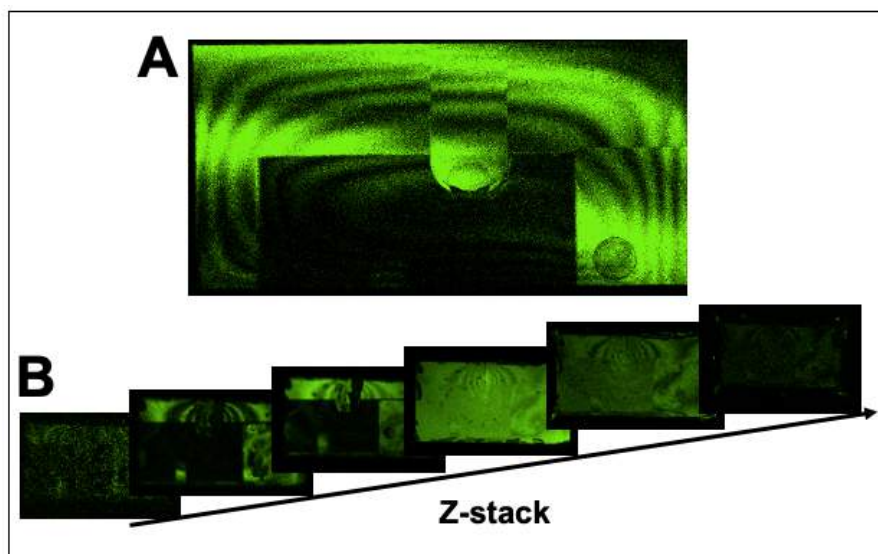
Figure 5.9 **(A)** fluorescence image of the *in-situ* chip (25x magnification). **(B)** Selected images during z-stack measurements (5 images interval).

For this example (*in-situ* cell # 047, measured by STXM at the CLS SM beamline, in Jul. 2022), the thickness measured by laser fluorescence was 2.3 μm ±0.3 μm for the empty cell. The electrolyte thickness (Na_2SO_4) measured from the X-ray absorption was 2.6 μm ± 0.3 μm at a pump flow rate of 5 μl/h (operated in push mode).

5.3.3   X-Ray diffraction (XRD)

Powder X-ray diffraction (XRD), which was used to verify the chemical structure and phase of the samples, provides information about crystal structure and physical properties of crystalline materials. The interaction of the incident monochromatic X-ray beam with the crystalline component of a sample produces interference, which generates unique XRD patterns with sharp Bragg diffraction peaks whose direction depends on the wavelength of X-rays used (Cu K-a, l = 0.15406 nm) and the crystal spacing (d), which can described by Bragg's law (Kaliva & Vamvakaki, 2020):

$$m\,\lambda = 2d\,\sin\theta \qquad\qquad \textbf{Eq. 5.5}$$

where m is the diffraction order, λ is the incident X-ray wavelength, θ is the angle of diffraction and d is the lattice spacing. The XRD measurements of the MnOx compounds studied in the thesis were performed at the McMaster Analytical X-ray Diffraction (MAX) Facility at McMaster University using a Bruker D8 diffractometer. The chemical species and phase were identified by comparing the measured powder patterns to those in the Joint Committee on Powder Diffraction Standards (JCPDS) data base (wanson et al., 1972).

5.4   Experimental details relating to STXM experiments and data analysis

5.4.1   Summary of experimental runs at synchrotron facilities

Table 5.1 presents a list of the *ex-situ* and *in-situ* experimental runs performed during my PhD (2020-2024) at different synchrotron facilities. All runs are listed and are evaluated as successful (S), partially successful (P), or failed (F) in the last column of **Table 5.1**. During my PhD research I used more than 300 hours of beamtime at 6 STXMs at 5 different synchrotrons. Much of the data acquired is not presented in this thesis; it will be the subject of follow-up papers.

Table 5.1   Summary of *ex-situ* and *in-situ* experimental runs at different synchrotron facilities

Date	Synchrotron facility	Experiments	E
2020-02	CLS (Saskatoon, Canada)	*In-situ* study of Ferri/Ferro cyanide redox system	S
2020-09*	CLS (Saskatoon, Canada)	*Ex-situ* study Ferri/Ferro cyanide reference compounds	S
2021-02	CLS (Saskatoon, Canada)	*Ex-situ* study of MnOx samples (electrochemically prepared)	P
2021-08	CLS (Saskatoon, Canada)	*Ex-situ* study of Mn_3O_4 SC electrodes MnOx reference compounds	S P
2021-09	CLS (Saskatoon, Canada)	*Ex-situ* study of Mn_3O_4 SC electrodes *In-situ* study of MnOx system	S P
2021-12	CLS (Saskatoon, Canada)	*Ex-situ* MnOx reference compounds measurements *Ex-situ* study of Mn_3O_4 SC electrodes	S S
2022-03	CLS (Saskatoon, Canada)	*In-situ* study of MnOx system *Ex-situ* MnOx reference compounds measurements	S S
2022-05	MaxIV (Lund, Sweden)	*In-situ* study of MnOx system	F
2022-07	CLS (Saskatoon, Canada)	*In-situ* study of MnOx system *Ex-situ* study of Mn_3O_4 SC electrodes	S S
2022-09	CLS (Saskatoon, Canada)	*In-situ* study of MnOx system *Ex-situ* study of Mn_3O_4 SC electrodes	P S
2023-01	Bessy-II (Berlin, Germany)	*In-situ* study of MnOx system	F
2023-03	MaxIV (Lund, Sweden)	*In-situ* study of MnOx system *Ex-situ* study of MnO_2/Zn-ion battery electrodes	F S
2023-04	Solaris (Krakow, Poland)	*In-situ* study of MnOx system *Ex-situ* study of MnO_2/Zn-ion battery electrodes	F S
2023-06	CLS (Saskatoon, Canada)	*In-situ* study of MnOx system *Ex-situ* study of MnO_2/Zn-ion battery electrodes	S S
2023-08	CLS (Saskatoon, Canada)	*In-situ* study of MnOx system	F
2023-10	MaxIV (Lund, Sweden)	*In-situ* study of MnOx system	F

*Ex-situ experiments were performed remotely due to the Covid-19 lockdown period.

5.4.2 *Ex-situ* STXM sample loading and mounting

Different strategies and techniques were used for loading the dry samples and preparing them for the *ex-situ* STXM measurements presented in the thesis. For Mn_3O_4 and MnO_2 supercapacitor electrodes (**Chapter 7** and **Chapter 8**) the electrode materials were scratched from the Ni foam (current collector) and physically drop-cast on either formvar coated TEM grids (TED Pella Inc.) or SiNx windows (Norcada Inc). For MnOx reference compound samples (**Chapter 7)**, we found that some particles detached from the TEM grids during STXM measurements. To avoid that, the TEM grid with sample particles was covered with another TEM grid, in which the particles were sandwiched between the formvars of the two formvar-coated TEM grids. For MnO and MnO_2 reference compounds, microtome samples with a thickness of 80 nm were prepared as described in **Section 5.2.3**. The α-MnO_2 ZIBs electrode samples were first prepared by scratching the particles from the carbon substrate. However, STXM results indicated different Mn oxidation states in different particles. Therefore, all α-MnO_2 ZIBs electrode samples were then prepared by ultramichrotoming the whole electrode materials with different thicknesses (typically, 100, 200, 400 and 600 nm) after disassembling the electrode from the coin cell and peeling off the glass separators. This technique allows better understanding of oxidation state distribution after different charging/discharging cycles, as illustrated in **Chapter 6**.

After loading, samples were attached to the trapezoidal STXM sample plate using small pieces of single-sided Scotch[TM] tape from the upstream side for TEM grids which are ~40 μm thick, and double-sided tap underneath the ~200 μm SiNx window samples. STXM measurements reported in the thesis were performed at STXM beam lines using a standard trapezoidal STXM plate with 6 holes (2.7 mm diameter) distributed in two rows. In our group, we usually mount a maximum of five samples on the sample plate to leave an empty hole for I_0 measurement.

5.4.3 STXM data acquisition

STXM transmission signals can be recorded in different modes such as single image, point scan and image sequence (stack) (Jacobsen et al., 2000). These modes and their

associated parameters are defined using a pop-up graphical user interface (GUI) which is displayed in **Fig. 5.10.** Each data acquisition mode is described below.
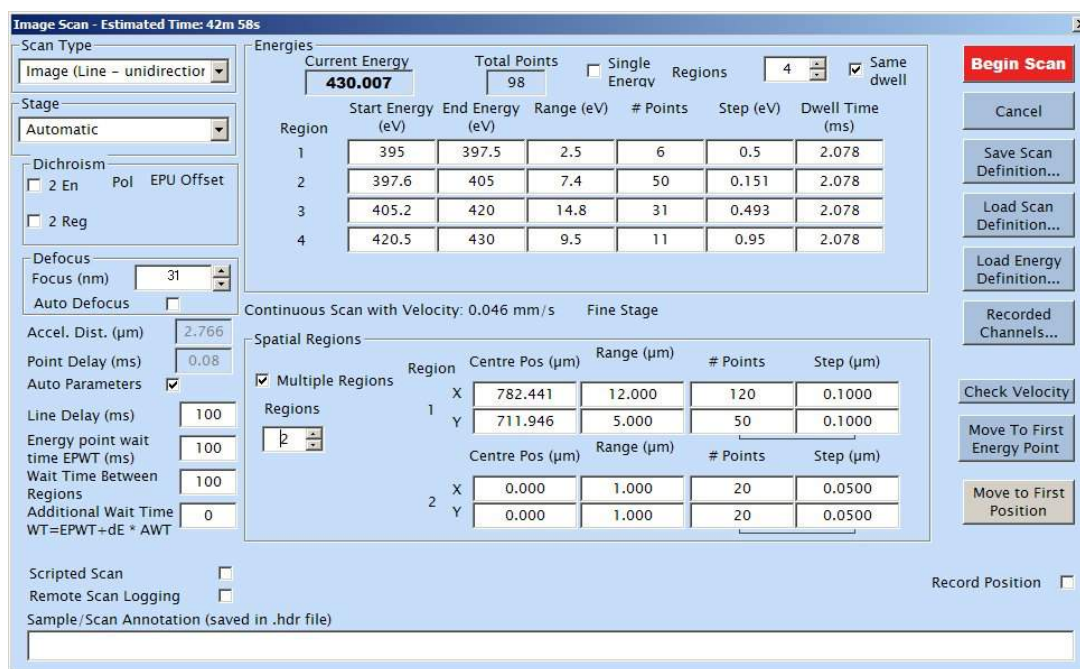
Figure 5.10 Scan GUI for STXM control acquisition software. The choices made indicate this is a 98 energy N 1s stack with 2 spatial regions (region 1 – sample (I), region 2 off-sample (Io)) measured using line-at-a-time, continuous scan mode.

5.4.3.1 Images

In image mode, one or more spatial regions are measured at a single photon energy. To obtain a single energy transmission image, different parameters should be identified, including the photon energy, the (x, y) position of the image center, the (Δx, Δy) dimensions of the image; (δx, δy) point spacing in each dimension and the dwell time at each pixel. Based on the dimensions of the image, different sample moving motors are used. Larger size (coarse) images (> 60 µm) are scanned using the x, y stepper stages. Smaller size (fine) images (< 60 µm in the line scan direction are scanned using piezo stages. The fast (continuous motion) line scan direction is x (horizontal) at CLS and Bessy, but y (vertical) at MaxIV and Solaris. Moreover, multiple spatial regions can be measured in one acquisition.
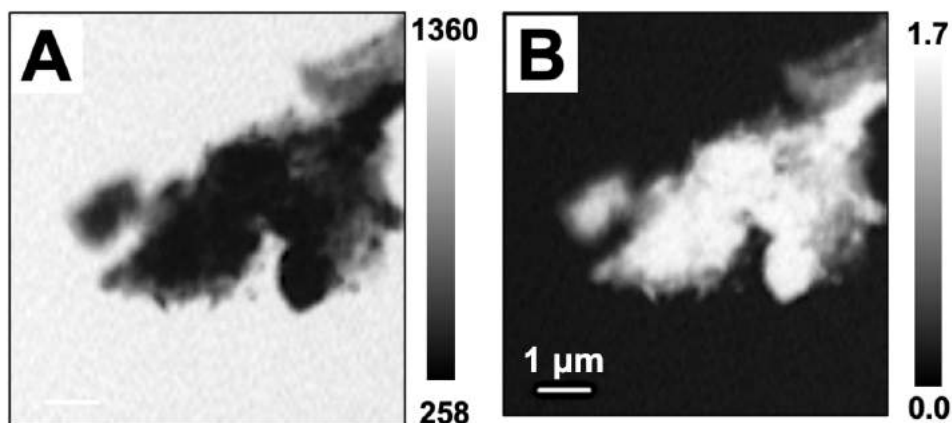
Figure 5.11 STXM images of a Mn_3O_4-based SC electrode material at 642 eV. **(A)** in transmission mode. **(B)** after conversion to optical density. (1 μm × 1 μm, 98 × 98 pixel, 2.0 ms dwell time).

Figure 5.11 presents STXM images at 642 eV in transmission and optical density (OD) modes of Mn_3O_4-based supercapacitor electrode material. In transmission images (**Fig. 5.11A**), dark regions indicate lower transmission and higher absorbance. After a Beers-law conversion of the transmission image to an optical density (OD) image (**Fig. 5.11B**), the contrast is reversed, so that regions of higher OD (stronger absorption) are brighter.

5.4.3.2 Point spectral scan

The transmission spectrum of a sample can be measured using point scan mode at one of more specific points, either in a linear or segmented non-linear energy scan. This method is commonly used in *in-situ* measurements to detect the I_0 and to determine the electrolyte thickness of the *in-situ* cell, as described in **Chapter 4.** The point scan method allows efficient recording of spectra within a short time frame, typically a few minutes. **Figure 5.12** shows an example of a point scan spectrum of a 1.0 M $MnSO_4$ electrolyte (Mn L_3 energy range of 630 eV – 650 eV). The green circle in **Fig. 5.12A** indicates where the spectrum was measured through the electrolyte layer, while the red circle in **Fig. 5.12B** indicates the empty hole of the *in-situ* device where the incident flux (I_0) was recorded. **Figure 5.12C** presents the transmission spectrum at the electrolyte (I, red), at the *in-situ* device hole (I_0, green), and the OD spectrum of the electrolyte (blue), generated using the Beer-Lambert law. This measurement is described in **Chapter 9.**
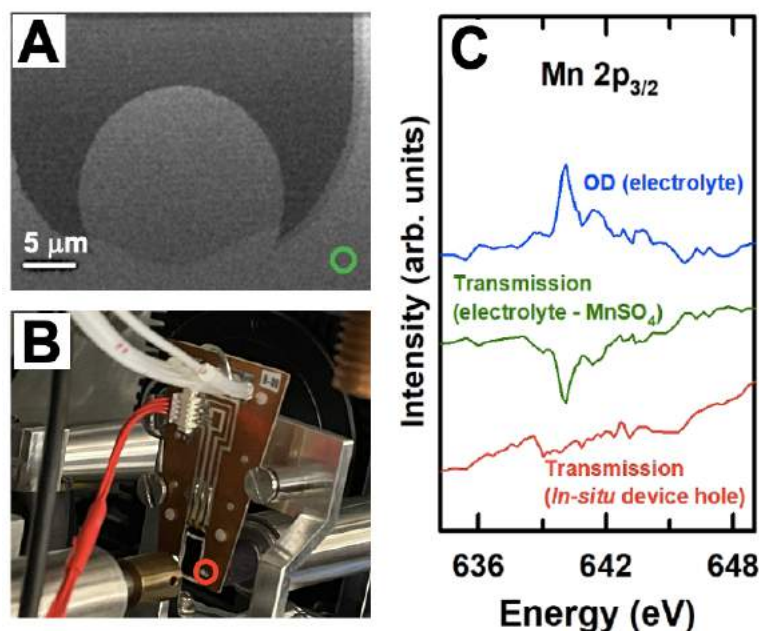
Figure 5.12 Point scan measurement during *in-situ* STXM study of MnOx system. **(A)** STXM transmission image at 640 eV. The green circle indicates where the spectrum through the electrolyte (I) was measured. **(B)** Photo of the *in-situ* device inside the STXM chamber. The red circle indicates the hole of the *in-situ* device where the incident flux (I_0) was measured. **(C)** X-ray signal of the incident X-ray beam (I_0, red), X-ray beam passing through the electrolyte and the SiNx windows (I, green) and the OD spectrum of the electrolyte and the SiNx windows (blue).

5.4.3.3 Image sequence (stack)

Image sequences (also known as stacks (Jacobsen et al., 2000)) are the most powerful method to use STXM for chemical analysis and mapping. In a stack measurement, X-ray transmission images are recorded over a range of photon energies (see **Fig. 5.10** for an example of the definition). Stack measurements can be performed for one or more spatial regions of the measured sample (e.g. a specific region of interest on the sample and an empty area to record the I_0 signal in a quasi-simultaneous manner). Stack measurements with multiple regions were used in most of the MnOx *in-situ* STXM measurements reported in **Chapter 9** to investigate oxidation state changes at both the working and counter electrodes while applying a specific potential. The I_0 signal is measured from a region where the incident X-ray passes off the

sample but through all other components, including the sample support, and the electrolyte in the case of *in-situ* measurements. Despite the continuous position control of the interferometer, stack images often drift over a long acquisition time. Post-alignment processing is necessary to overcome this drift. Three different, automated, Fourier cross-correlation methods alignment methods, as well as several manual alignment procedures are available in the aXis2000 software (Hitchcock, 2023a).

Figure 5.13A(a-e) show selected optical density images from a Mn $2p_{3/2}$ edge (630 eV – 650 eV) stack measured on a α-MnO$_2$/Zn-ion battery electrode. That sample was subjected to 94 charge/discharge cycles (1.8 V at charge and 1.2 V at discharge) and left in the discharged state. **Figure 5.13C** presents spectra extracted from different regions of the sample illustrated in **Fig. 5.13B**.
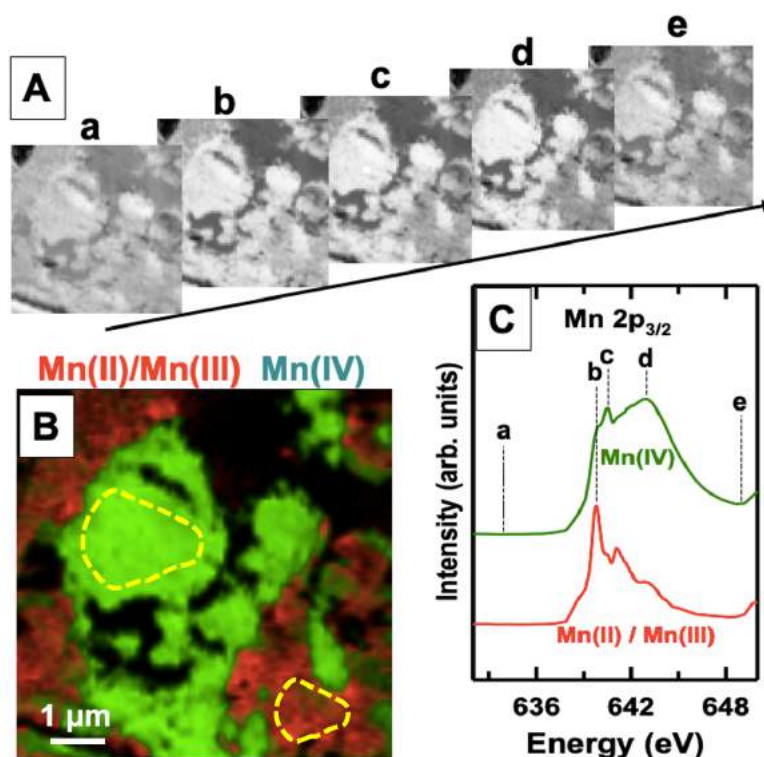
Figure 5.13 Stack measurement of 94 charged/discharged cycles α-MnO$_2$/Zn-ion battery electrode, left in the discharged state. **(A)** selected optical density images recorded from measured stack. **(B)** Internal component map derived from fitting the Mn 2p stack to internal spectra extracted from the samples. **(C)** Mn $2p_{3/2}$ absorption spectra of different region of the sample.

5.5   Data analysis of STXM stacks

5.5.1   Preliminary processing

All *in-situ* and *ex-situ* STXM data reported in this thesis were analyzed using aXis2000 software (Hitchcock, 2023a). Image stacks are stored by STXM control as individual images at each photon energy (and as a single hdf5 file by the pixelator STXM acquisition program used at Soleil). The first step in analyzing a stack is to read all of the transmission images and combine all images as a single object consisting of 2 files (*.dat, *.ncb). The stack is then aligned using either "Jacobsen stack analyze" or the "Zimba" Fourier cross-correlation methods. A suitable I_0 spectrum is then extracted from an off-sample area of the stack, from a second area measured simultaneously, or by a point or stack spectrum from an I_0 region measured either before or after the sample stack was measured. Note that, since the system changes slowly over time, it is best to measure the I_0 in the same region or in a 2-region acquisition if possible. Once the I_0 is obtained the aligned stack is converted to optical density (OD) (as illustrated in **Figure 5.11**), and the OD stack is saved. At this point it is important to calibrate the energy scale, since at most soft X-ray beamlines, the energy scale reported by the beamline software can be in error by values from a few hundred meV, to many eV. The energy scale correction value can be determined in several ways, as described in section **5.5.5**. X-ray absorption spectra can then be extracted from user selected regions of the measured sample.

5.5.2 Conversion of energy-calibrated, aligned OD stacks to component maps by fitting

aXis2000 provides three different methods to generate chemical component maps from energy stacks, two of which were used in my research. Both of these fitting procedures use the Singular Value Decomposition (SVD) matrix method (Koprinarov et al., 2002) to fit the spectrum at each pixel to a linear combination of the user-supplied reference spectra. These two methods are identified as **SVD**, and **stack fit** in the aXis2000 menu. **SVD** provides a set of maps, one for each component, and a map of the residual of the fit averaged over all energies. **Stack fit** is similar, but it also provides a map of a constant component, which has no spectral response. The reference spectra used in stack fitting can be either internal spectra (from the stack itself) or external spectra (from other stacks of related samples, or spectra of well-defined reference compounds). For quantitative analysis, reference spectra with an absolute intensity

scale (optical density per nm (OD1)) are used. This is achieved by rescaling the relative intensity of the reference spectra to match the signal at the pre-edge (-50 to -5 eV from the edge onset) and far-continuum (>30 eV above the edge) to the elemental response for 1 nm thickness of the species with a defined chemical composition and density) (Koprinarov et al., 2002). The elemental X-ray response parameters used in this process are obtained from the Centre for X-ray Optics database. (https://henke.lbl.gov/optical_constants/). Mn 2p and O 1s OD1reference spectra of different MnOx compounds used in the STXM quantitative mapping reported in the thesis are described in detail in **Chapter 6**.

Figure 5.14 presents component maps of a α-MnO$_2$/Zn-ion battery electrode after 94 discharged cycles derived from fitting Mn 2p stack using OD1 reference spectra of MnO, Mn$_2$O$_3$ and α-MnO$_2$ (using the stack fit procedure). The grayscale of each component map represents the thickness (in nm) of each component.
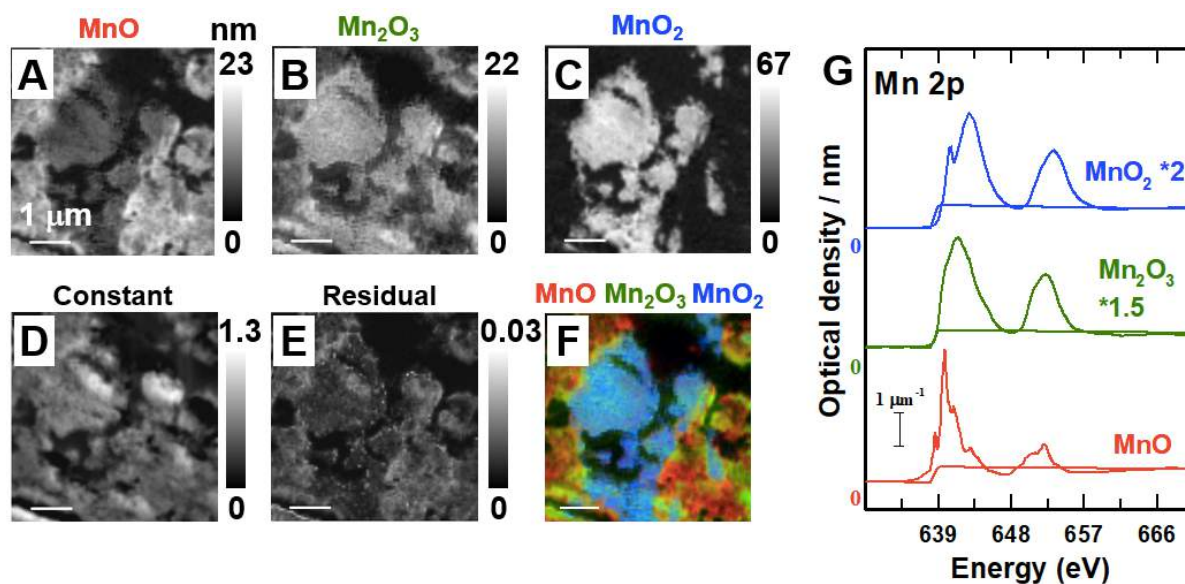
Figure 5.14 Quantitative component mapping of MnOx species in α-MnO$_2$/Zn-ion battery electrode after 94 discharged cycles. **(A)** MnO component map. The gray scale indicates thickness in nm. **(B)** Mn$_2$O$_3$ component map. **(C)** α-MnO$_2$ component map. **(D)** constant map. **(E)** residual of the fit. **(F)** MnO, Mn$_2$O$_3$ and Mn$_3$O$_4$ component map. **(G)** OD1 absorption spectra of MnO (red), Mn$_2$O$_3$ (green) and α-MnO$_2$ (blue) reference compounds used in the stack fit.

5.5.3   Verification of the validity of spectral fitting

The forward fitting SVD or stack fit analyses will always give a set of component maps. In order to build confidence that the fit is valid in the spectral domain, aXis2000 provides methods to examine the quality of the fit in the spectral domain. This can be achieved by extracting internal spectra from region with large amounts of components of interest based on generating a region of interest (ROI) by threshold masking component maps. The quality of the spectral fit can be evaluated by applying spectra curve fitting (linear regression for stack fit and conjugate gradient optimization method (CGO) for SVD) using reference spectra in OD1 intensity scale. Additionally, this method is used to quantitively determine the average thickness of in nm of each individual component (based on the corresponding OD1 reference spectra used) within the area from which the spectra were extracted. Examples of using the curve fit method in quantitative analysis are presented in **Chapter 8** and **Chapter 9**. **Figure 5.15** presents screenshot of the GUI of the SF curve fitting process of a stack measured on electrodeposited MnOx subjected to +0.5 V_{Au} during *in-situ* STXM measurement (**Chapter 9**). The text in the red shaded region to the right of the panel presents the average thickness of MnO (Red), Mn_2O_3 (green) and MnO_2 (blue) in nm scale.
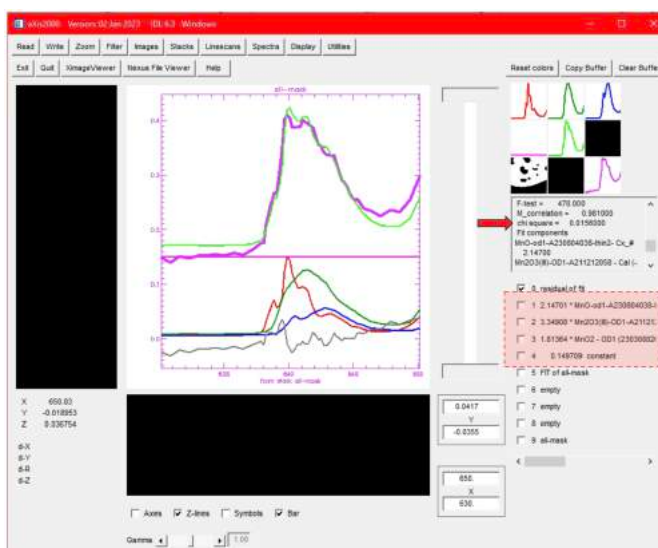
Figure 5.15 Screenshot of the GUI of the SF curve fitting process showing an example of calculating average thickness of MnO (Red), Mn_2O_3 (green) and MnO_2 (blue) in nm scale. The purple spectra presents the average spectra, while light green spectra presents the calculated curve fit. The grey spectra presents the residual of the fit.

5.5.4   Determining absolute area, volume and concentration amounts from stacks

The volume fractions of different species in a measured stack can be determined by threshold masking the average STXM image, followed by calculating the average thickness (in nm) of each individual component using the curve-fitting method as described in **Section 5.5.3**. These values are then combined with the area of each component region to calculate the total volume and volume fractions. To calculate the area of a selected region, the image is multiplied by the masked image, and the average number of pixels (excluding zero values) is counted. aXis2000 provide tools to visualize the combination of area and thickness information through a 3D display as presented in **Fig. 5.16**.
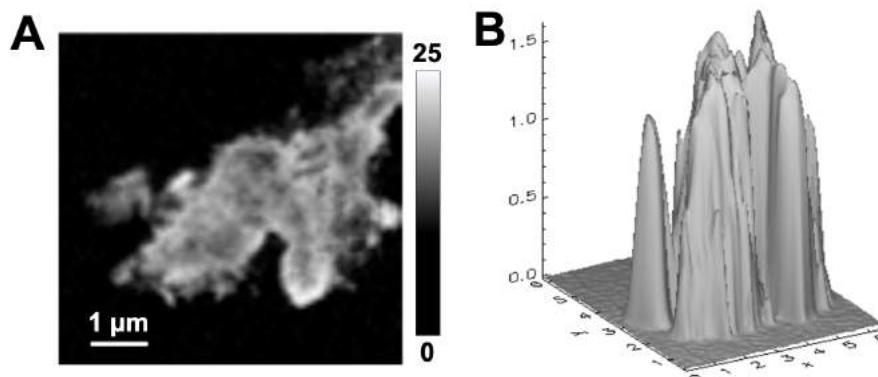
Figure 5.16 (A) MnO_2 region in Mn_3O_4 supercapacitor electrode (Chapter 8). **(B)** 3D display of the MnO_2 region.

5.5.5   Estimating uncertainties in STXM data analysis

(I)   Residual of SVD or SF fitting. The evaluation of the residual stack is crucial in determining the accuracy of the fit. It is expected that the extracted spectra from different regions of the residual stack should be noise only. However, if a chemical component is missed in the fitting process, it is sometimes possible to obtain its spectra from the poorly fit regions of the residuals stack.

(II)   Statistical evaluations of the spectral fit. The residual map image obtained from SVD or SF fitting illustrates the map of the chi-square values for the fit at each pixel. On the other

hand, SF and SVD curve fitting method determine the chi square value illustrated with the red arrow in **Fig. 5.15**. A smaller chi-square value indicates a better fit.

(III) STXM energy scale errors. In order to obtain an accurate fitting (using SVD or SF), the energy scale of spectra extracted from any measured stack should be compared to the energy scale of the corresponding, calibrated, reference spectra. If the deviation value is $> \pm 0.2$ eV, the energy scale of the measured stack should be shifted with this value prior to performing the fitting. It is a common observation that the photon energy scales in most STXMs beamlines are frequently inaccurate, and can undergo changes between runs, and sometimes even change in a single run. Enhancing the accuracy and validity of the measured spectra can be achieved by calibrating the energy scale of soft-X-ray beamlines with appropriate reference gases, such as: SF_6 [F 1s $\rightarrow a_{1g}$, 688.3 eV], CO_2 [(C 1s $\rightarrow$ C 3s, 292.74 eV; (C 1s $\rightarrow$ C 3p, 294.96 eV); (O 1s $\rightarrow$ O 3s, 538.9 eV)], N2 [(N 1s $\rightarrow$ 3s, 406.15 eV); (N 1s $\rightarrow$ 3p, 407.115 eV)], and Ne [1s $\rightarrow$ 3p, 867.05 eV]. Details of spectral calibration performed in the thesis are presented in **Chapter 6**.

(IV) Comparing different models (sets of reference spectra) – In a complex system, different oxidation states can be found, and the accuracy of the fitting is significantly affected by the correct selection of the reference spectral set used in the fitting. For instance, the quantitative mapping of the α-MnO_2 cathodes (used in Zn-ion battery) can vary when using a different set of reference compounds. **Figure 5.17A** presents a quantitative mapping of MnOx species in a discharged Zn/α-MnO_2 electrode after 94 charge/discharge cycles obtained from fitting OD1 reference spectra of MnO, Mn_2O_3, and MnO_2 to the measured stack (**Chapter 6**). **Figure 5.17B** presents quantitative mapping obtained from fitting different set of reference spectra (MnO, Mn_3O_4 (instead of Mn_2O_3), and MnO_2) to the same stack. The MnO_2 thickness in both fittings is nearly identical. However, the thickness of the MnO is changed when Mn_3O_4 is used instead of Mn_2O_3. By comparing the two models using SF curve fitting as illustrated in **Section 5.5.3** and **Section 5.5.5 (II)**, the average spectra is in agreement with the calculated curve fit of both models. However, the chi-square value is slightly lower (=0.019) in the "MnO, Mn_2O_3, MnO_2" model compared to "MnO, Mn_3O_4, MnO_2" model (=0.022) (see **Fig. 5.18**).
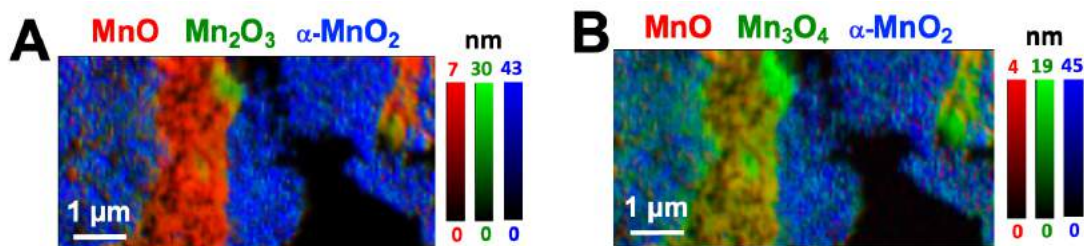
Figure 5.17 Quantitative mapping of MnOx species in a discharged Zn/α-MnO$_2$ electrode after 94 charged/discharged cycles. (A) using OD1 reference spectra of MnO, Mn$_2$O$_3$ and MnO$_2$. (B) using OD1 reference spectra of MnO, Mn$_2$O$_3$ and MnO$_2$.
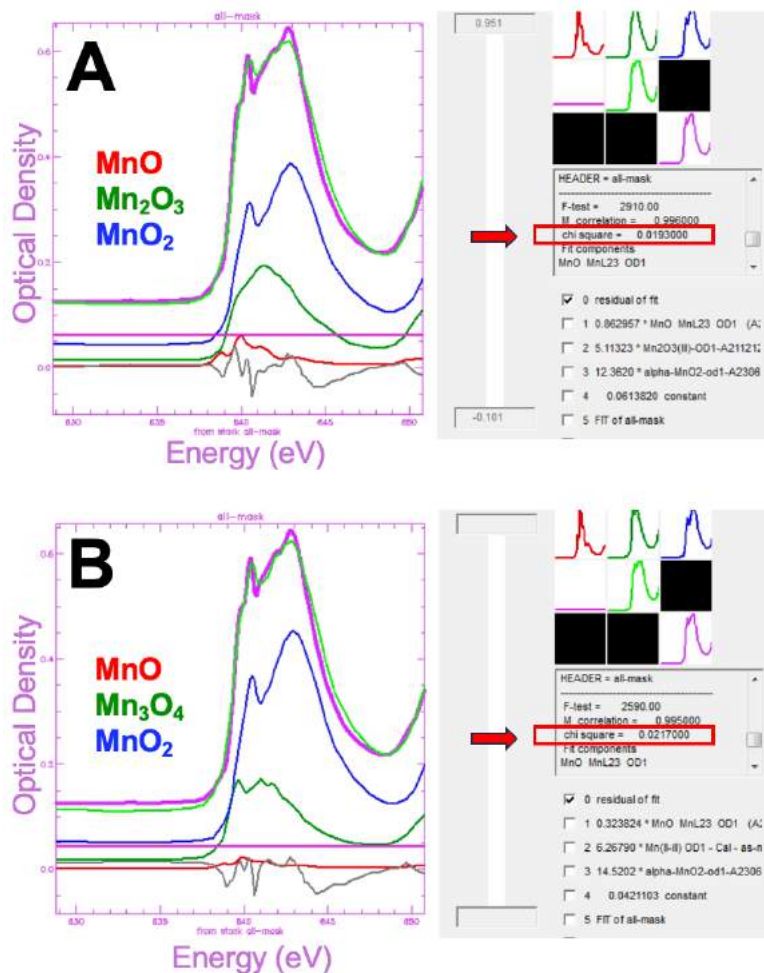
Figure 5.18 Results of the SF curve fitting using different set of reference spectra. **(A)** using OD1 reference spectra of MnO, Mn$_2$O$_3$ and MnO$_2$. **(B)** using OD1 reference spectra of MnO, Mn$_3$O$_4$ and MnO$_2$. The red arrow highlights the chi-square value obtained from the fitting.

Chapter 6

Mn 2p and O 1s X-ray absorption spectroscopy of manganese oxides

This chapter presents experimental measurements of high-quality and accurately calibrated O 1s and Mn 2p reference spectra of different manganese oxidation states measured by STXM and TEY. The results shown in this chapter are foundational for accurate STXM quantitative chemical mapping of MnOx species in subsequent ex-situ and in-situ STXM studies of MnOx complex systems.

This work was submitted to Journal of Electron Spectroscopy and Related Phenomena on Dec 12, 2023. The author list is: Haytham Eraky, James J. Dynes, and Adam P. Hitchcock.

The author of this thesis performed all the STXM and SGM measurements and analyzed all data (in collaboration with Prof. A. P. Hitchcock). The author wrote the publication, with assistance in later stages by Prof. A. P. Hitchcock.

*The supplemental information of this work is presented in **Appendix C**.*

6.1 Introduction

In order to optimize the performance of energy conversion devices based on MnOx chemistry, characterization techniques with quantitative mapping capabilities (i.e. spectromicroscopies) are needed to provide information about the spatial distributions of different Mn species (oxidation state, and possibly phase) and how the species and their spatial distributions might change during electrochemical processes. Such studies can provide mechanistic insights into charge storage and conversion mechanisms in different energy storage applications (Ghosh, 2020; Guo et al., 2022; Khan et al., 2023; Parveen et al., 2022; Rodriguez-Romero et al., 2022; Wang et al., 2018; Zeng et al., 2019), that can lead to enhanced properties of energy materials. As described in **Section 3.4**, STXM is a synchrotron-based, soft X-ray spectromicroscopic technique that uses near edge X-ray absorption spectra (NEXAFS) (Stöhr, 1992) to identify chemical species and provide quantitative chemically selective imaging at sub-30 nm spatial resolution. To fully exploit the capabilities of STXM, it is important to have reliable, accurately calibrated, quantitative NEXAFS spectra of each species of interest. While the Mn 2p (Bourdelle et al., 2021; de Groot et al., 2010; Förster et al., 2021; Galezowski et al., 2020; Garvie & Craven, 1994; Gilbert et al., 2003; Müller et al., 2019; Pecher et al., 2003; Qiao et al., 2013; Risch et al., 2022; Risch et al., 2017; Shi et al., 2022; Toner et al., 2005; Wang et al., 2018) and O 1s (Frati et al., 2020; Gilbert et al., 2003; Müller et al., 2019; Qiao et al., 2013; Risch et al., 2017) NEXAFS spectra of the common MnOx species have been published several times, there are some discrepancies in the literature. Using uncalibrated reference spectra will lead to imprecise quantitative results and will provide inaccurate information about the chemical distribution of MnOx species in a measured sample. Thus, we have carried out, and report here, the results of systematic measurements of the Mn 2p and O 1s NEXAFS spectra of the common manganese oxides using both transmission and total electron yield (TEY) detection. In this work, we provide Mn 2p and O 1s NEXAFS spectra of MnO, MnSO$_4$, Mn$_3$O$_4$, Mn$_2$O$_3$, α-MnO$_2$, β-MnO$_2$, and KMnO$_4$, with spectroscopic assignments of key spectral features.

6.2   Experimental procedures

6.2.1   Materials

Analytical grade manganese oxides were obtained commercially and used without purification: MnO (99.99%, Alfa Aesar), $MnSO_4 \cdot H_2O$ (≥99%, Sigma-Aldrich), Mn_2O_3 (99.9%, Sigma-Aldrich), Mn_3O_4 (synthesized chemically (Yang et al., 2022)), α-MnO_2 (≥99.99%, Alfa Aesar), β-MnO_2 (≥90 %, Sigma-Aldrich) and $KMnO_4$ (99%, Sigma-Aldrich). All chemicals were used as received, without further purification.

6.2.2   Powder X-ray diffraction

X-ray diffraction (XRD) analysis of each compound was performed (Bruker D8, Cu-Kβ radiation) (**Section 5.1.8**). The XRD patterns were recorded from 10° to 80° at a scan rate of 1 degree per min. **Figure S6.1** shows the X-ray diffraction patterns of the MnO, $MnSO_4$, Mn_3O_4, Mn_2O_3, α-MnO_2 and $KMnO_4$ samples studied. Comparison of the observed diffraction patterns with those in the Joint Committee on Powder Diffraction Standards (JCPDS) data base indicates the presence of pure phases for all measured species: manganosite, MnO (JCPDS PDF 04-008-0277); szmikite, $MnSO_4.(H_2O)$ (JCPDS PDF 04-008-9679); bixbyite, Mn_2O_3 (PDF 00-041-1442); hausmannite, Mn_3O_4 (JCPDS PDF 001-1127); pyrolusite, α-MnO_2 (JCPDS PDF 00-044-0141); and potassium permanganate, $KMnO_4$ (JCPDS PDF 04-008-2764).

6.2.3   X-ray Absorption Spectroscopy by STXM

Mn 2p and O 1s X-ray spectra were measured in transmission mode using the ambient STXM at the spectromicroscopy (SM) beamline, 10ID1 (Kaznatcheev et al., 2007) at the Canadian Light Source (CLS, Saskatoon, Canada). STXM samples were prepared as described in **Section 5.1.10**. STXM measurements were performed after pumping the chamber to ~0.1 mbar, then back filling with He to a pressure of ~100 mbar as illustrated in **Section 3.1.5**. All STXM measurements reported in this chapter were performed as descried in **Section 5.13**.

6.2.4   X-ray Absorption Spectroscopy by total electron yield (TEY)

Mn 2p and O 1s X-ray spectra were also measured in TEY mode at the spherical grating monochromator (SGM) beamline 11ID-1 (Regier, Krochak, et al., 2007) at the Canadian Light Source (CLS, Saskatoon, Canada). The samples for total electron yield (TEY) spectroscopy were prepared by grinding the material and pressing the resulting powder into indium foil which was then mounted on a SGM sample support. The TEY measurements were conducted in a high vacuum chamber at room temperature by collecting the total current from the sample as a function of excitation energy. The spectra were measured in both fast scan and conventional, step scan mode with the X-ray beam focused to a 25 μm diameter spot size. In the fast scan mode, the photon energy is scanned continuously while taking time stamped measurements as fast as possible (ms sampling). After the fast scan acquisition, the data is interpolated onto an evenly spaced energy grid. In both modes TEY spectra were measured at 10 different positions of the sample, then averaged. The fast scan mode and multiple, different-area measurements are used to minimize the X-ray dose. We did not observe any changes in the spectra that could indicate radiation damage, even in the higher dose step scan mode.

The incident beam intensity (I_0) was recorded as the current from a gold mesh which was mounted before the final Kirkpatrick-Baez focussing mirrors. While a featureless I_0 was observed at the Mn 2p edge, there was a small O 1s signal from oxide contamination of the surface of the I_0 detector, as shown in **Fig. S6.2**. Fortunately, the O 1s spectral structure in the I_0 signal was small enough that it did not significantly affect the spectral shape. The total fluorescence yield (TFY) and partial fluorescence yield (PFY) spectra were also measured simultaneously with the TEY. However, we found those spectra disagreed significantly from the STXM and TEY spectra, due to absorption saturation. Even using the inverse partial fluorescence yield (IPFY) approach (Achkar et al., 2011), which generally reduces spectral distortion from absorption saturation, did not give correct results. **Figure S6.3** compares α-MnO_2 absorption spectra measured in TEY and PFY modes. The Mn $2p_{3/2}$ characteristic features of αMnO_2 (sharp peak at 640.5 eV and broad peak at 642.9 eV) can be clearly identified from spectra measured with TEY, while these features are significantly distorted by absorption saturation in the TFY and PFY modes.

6.2.5   Comparison of STXM-NEXAFS and TEY-XAS

NEXAFS spectra recorded without spatial resolution gives similar spectroscopy as STXM, often with better statistical precision. TEY is a surface sensitive technique with a sampling depth of a few nanometers (Abbate et al., 1992) whereas STXM is bulk-sensitive in that the NEXAFS spectrum is averaged over the full thickness of the sample, which is typically 50 – 300 nm thick. For samples thicker than ~100 nm absorption saturation can distort the O 1s and Mn 2p NEXAFS spectra when measured in transmission. For TEY-XAS there are concerns that the spectrum may not be of the correct species since surface oxidation can occur during sample preparation or storage of low Mn oxidation state species, particularly for Mn metal (Kawai et al., 2000) and Mn^{2+} compounds (Gorlin et al., 2014). In contrast to STXM, where measurements are performed on individual particles over an area of several μm^2, the TEY measurements performed in this work are ensemble-averaged X-ray absorption spectra (XAS) measured from areas larger than 0.06 mm^2 of sample (Kawai et al., 2000; Wang et al., 2018).

6.2.6   Data analysis

The STXM and TEY data were analyzed using aXis2000 software (Hitchcock, 2023a), as described in **Chapter 5**.

6.2.7   Spectral energy calibration

The energy scale of the SGM beamline was calibrated at the Mn 2p edge using the F 1s $\rightarrow$ a1g peak transition of SF_6 gas at 688.27 eV (Sodhi & Brion, 1984) and at the O 1s edge using the O 1s $\rightarrow$ 3s transition of CO_2 gas at 538.9 eV (Piancastelli et al., 1997; Prince et al., 1999). At the SGM beamline, the gas phase spectra were recorded in transmission by measuring the photodiode signal in the SGM tank with and without SF_6 or CO_2 gas. This calibration was performed in the same run as the TEY measurements since significant (>1 eV) differences in peak positions were noted in different runs. The energy scale of the SM beam line was similarly calibrated using gas phase spectra of SF_6 and CO_2. Supplemental information, **Section S-5** presents examples of the energy scale calibration with these gases.

During measurements of several Cu 2p and Ni 2p compounds at the CLS SGM beamline, differences in the $2p_{3/2} - 2p_{1/2}$ spin orbit splitting of up to 0.5 eV were noted relative to the corresponding spin-orbit splitting measured by STXM at the CLS SM beamline. We attribute the discrepancies to non-linearity of either (or possibly both) of the SM or SGM beamline energy scales. For this work, the Mn $2p_{3/2} - 2p_{1/2}$ spin-orbit splitting in the same compound measured with the SM and SGM beamlines were found to differ by < 0.1 eV. Thus, while flagging this observation as an issue at higher energy edges where the spin-orbit splitting is larger, we are satisfied that a possible non-linearity over the ~15 eV of the Mn $2p_{3/2} - 2p_{1/2}$ spin-orbit splitting is within other uncertainties of our measurements. As shown in the next section, the Mn 2p spectra measured by STXM and TEY mode are very similar in both spectral shape and peak positions.

6.3   Results

6.3.1   Mn 2p spectra of manganese oxides

Mn 2p spectra of different Mn oxides typically consist of one major peak accompanied by several minor, but often sharp, peaks in each of the Mn $2p_{3/2}$ and $2p_{1/2}$ spin-orbit split bands. The overall spectral shape and the energies of the sharp peaks can be used to identify and differentiate each of the Mn oxides species.
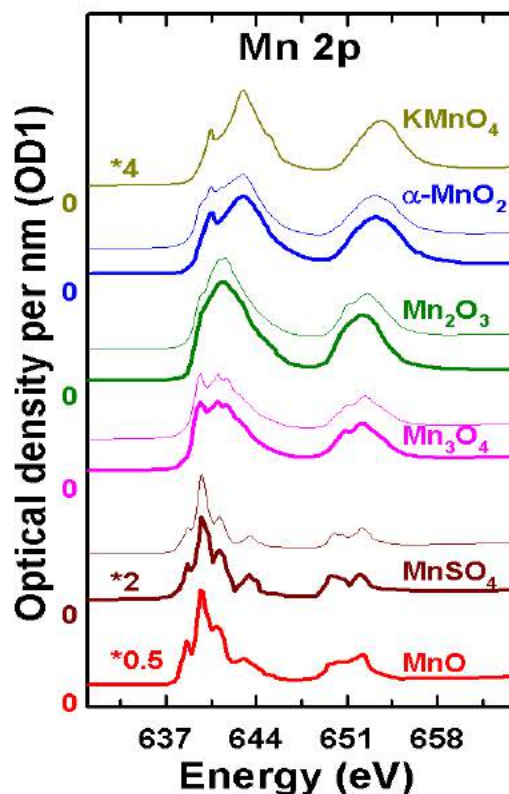
Figure 6.1 Mn 2p spectra of MnO, MnSO$_4$, Mn$_3$O$_4$, Mn$_2$O$_3$, α-MnO$_2$ and KMnO$_4$ measured by STXM (thick solid line) compared to those measured by TEY (thin solid line). The STXM-derived spectra are presented on quantitative OD1 intensity scales, with offsets for clarity. The intensities of the TEY spectra have been scaled and offset to best match the corresponding STXM spectra.

      Figure 6.1 presents the Mn 2p OD1 spectra of MnO, MnSO$_4$, Mn$_3$O$_4$, Mn$_2$O$_3$, α-MnO$_2$ and KMnO$_4$ measured by both STXM (thick solid line) and TEY-XAS (thin solid line). Note that KMnO$_4$ was only measured by TEY-XAS and MnO was only measured by STXM. The energies and proposed assignments of the main spectral features are summarized in **Table 6.1** along with comparison to literature results. The Mn 2p spectra of each species are discussed individually in the following sections.

MnO and MnSO$_4$

      The high-spin ground state of Mn^{2+} (MnO and MnSO$_4$, in this case) has a total of five unpaired electrons in the t$_{2g}$ and e$_g$ orbitals (t$_{2g}^3$, e$_g^2$) (Garvie & Craven, 1994; Held & Bohatý,

2002**)**. The dominant feature of the Mn 2p spectrum of $MnSO_4$ is a very intense peak at 639.8 eV which is accompanied by lower intensity peaks at 638.7 eV, 641.1 eV and 643.4 eV in the $2p_{3/2}$ band, and two broad peaks at 650.0 eV and 652.0 eV in the $2p_{1/2}$ band. The overall shape of the Mn 2p spectrum of $MnSO_4$ is close to that reported in the literature (Pecher et al., 2003; Risch et al., 2022). However, there is considerable variation in the intensity of the finer features**.** The main spectral features match those reported by Risch et al. (Risch et al., 2022), but with 1.2 eV energy scale deviation **(Table 6.1)**.

The Mn 2p spectrum of MnO is very similar to that of $MnSO_4$. It exhibits a very intense L_3 peak at 639.7 eV and lower intensity peaks at 638.6 eV, 640.9 eV and 642.9 eV. The L_2 band exhibits two broad peaks at 650.4 and 652.1 eV with minor peaks at 649.5 and 651.5 eV. Although there is some variation in the intensity of finer features, the overall "triplet-like" shape of the MnO spectrum is in agreement with the spectra reported in the literature **(**Garvie & Craven, 1994**;** Gilbert et al., 2003**;** Risch et al., 2022**;** Toner et al., 2005**)**. It is noteworthy that getting high quality Mn 2p spectra of MnO is very challenging when using transmission detection. The intensity of the main $2p_{3/2}$ peak at 639.7 eV is dramatically affected by absorption saturation even for samples thinner than 30 nm. In order to obtain the spectrum of MnO reported in this work, an embedded and microtomed section with an average thickness of 80 nm was prepared and measured. The Mn 2p spectrum reported here was extracted from a very small particle with only $\sim$10 nm thickness. Adjacent particles which were more than 30 nm thick were distorted by absorption saturation (see **SI section S6.6**). Interestingly the Mn 2p spectrum of MnO reported by Risch et al (Risch et al., 2022) was measured in TEY mode from the surface of a nominally pure metallic Mn sample. This indicates both the ease with which low oxidation states of Mn can oxidize in contact with air, and also the surface sensitivity of TEY detection. **Figure 6.2** compares the Mn $2p_{3/2}$ spectra of MnO and $MnSO_4$. Both spectra exhibit similar $2p_{3/2}$ and $2p_{1/2}$ (see **Fig. 6.1**) spectral features. Nonetheless, the minor $2p_{3/2}$ peaks and the main $2p_{1/2}$ peaks have somewhat different intensities and peak positions (deviation of 0.1- 0.5 eV), indicating that high quality Mn $2p_{3/2}$ spectra can differentiate Mn sulphate and oxide species. Not unexpectedly, there is an even larger difference in the O 1s spectra of these two compounds, as shown below (**Section 6.3.2**).
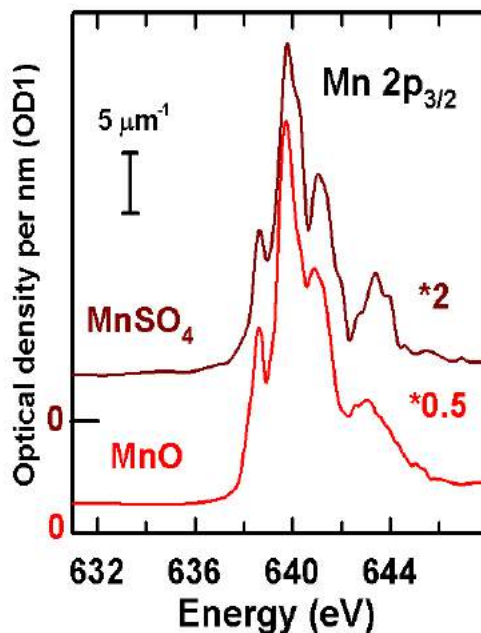
Figure 6.2   Expansion of Mn L_3 spectra of MnO and MnSO$_4$ measured by STXM. The zero-signal level for each spectrum is indicated while the absolute OD1 intensity is given by the combination of the scale bar (5 µm^{-1} = 50^{-3} nm^{-1}) and the gain factor for each species.

Mn$_3$O$_4$

Mn$_3$O$_4$ (Hausmannite) has a complex crystal structure with a 1:2 mixture of Mn^{2+} and Mn^{3+} cations (Garvie & Craven, 1994) and a formal average oxidation state of +2.67. It can be presented by the formula, Mn^{2+}(Mn^{3+})$_2$O$_4$ (Ghosh, 2020). The Mn 2p spectrum of Mn$_3$O$_4$ (**Fig. 6.1**) is in agreement with the literature spectra (Gilbert et al., 2003; Risch et al., 2017). It consists of an initial sharp 2p$_{3/2}$ peak at 639.6 eV, characteristic of Mn^{2+}, followed by two small peaks at 641.0 eV and 641.7 eV which can be related to the Mn^{3+} sites. The STXM and TEY spectra have the same 2p$_{3/2}$ and 2p$_{1/2}$ energy scale and characteristic features, with < 0.1 eV deviation in the position of the two 2p$_{3/2}$ lower intensity peaks. The first 2p$_{3/2}$ peak at 639.6 eV is used to calibrate and compare Mn 2p spectra with reported reference spectra (Gilbert et al., 2003; Risch et al., 2017). The Mn $^{2+}$ and Mn^{3+} ions in Mn$_3$O$_4$ occupy tetrahedral and octahedral sites, respectively. The Mn^{3+} octahedral environment is affected by structural deformation (Jahn-Teller distortion) so that the Hausmannite crystalline structure is distorted to a spinel tetragonal structure (Garvie & Craven, 1994), (Kaczmarek & Wolska, 1993). Furthermore, it

has been suggested that the absence of split $2p_{3/2}$ Mn^{3+} peaks in the measured Mn_3O_4 spectra is due to the Mn^{3+} being only approximately octahedrally coordinated **(Garvie & Craven, 1994)**.

Mn_2O_3

The Mn 2p spectra of Mn_2O_3 measured by STXM and TEY measurements consists of a broad peak at 641.4 eV with two shoulder peaks at 639.8 eV and 642.8 eV. Unlike the other manganese oxides, there is no clearly resolved multiplet splitting at the $2p_{3/2}$ edge. Mn_2O_3 has a d^4 configuration with a high-spin ground state (t_{2g}^3 e_g^1) **(Garvie & Craven, 1994; Gilbert et al., 2003)**. The manganese(III) ions are octahedrally complexed but are subject to strong Jahn-Teller distortion which results from the odd number of electrons in the triply degenerate t_{2g} orbital **(Garvie & Craven, 1994)**. The Jahn-Teller distortion causes elongation of the two trans Mn-O bonds, which results in a reduction of the symmetry from octahedral to tetragonal **(Garvie & Craven, 1994; Gilbert et al., 2003; Qiao et al., 2013)**.

α-MnO_2 and β-MnO_2

The Mn 2p spectra of α-MnO_2 (Hollandite) and β-MnO_2 (Pyrolusite) are compared in **Fig. 6.3A**. The spectrum of α-MnO_2 exhibits a sharp peak at 640.5 eV and broad peaks at 642.9 eV and 653.2 eV. In addition, there is a minor $2p_{3/2}$ shoulder peak at 639.5 eV, which was also observed in earlier studies **(Bourdelle et al., 2021; de Groot et al., 2010)**. While the Mn 2p spectrum of β-MnO_2 is similar to that of α-MnO_2, the broad $2p_{3/2}$ peak occurs at 643.5 eV, shifted +0.6 eV shift compared to α-MnO_2 **(Fig. 6.3B)**. Octahedrally coordinated MnO_2 has a t_{2g}^3 e_g^0 ground state configuration **(Gilbert et al., 2003; Risch et al., 2017)** where the lower energy t_{2g} orbital and higher energy e_g orbital are generated from the crystal field splitting of the Mn 3d orbital **(Bourdelle et al., 2021)**. The peaks at 640.5 eV and 642.9 eV (α-MnO_2) / 643.5 eV (β-MnO_2) correspond to the characteristic t_{2g} and e_g peaks, respectively. The positions of the main peaks in β-MnO_2 agree with those for β-MnO_2 reported by Gilbert et al. **(Gilbert et al., 2003)** within experimental uncertainty. However, they are 1.2 eV higher in energy than those reported for δ-MnO_2 (Birnessite) by Toner et al. **(Toner et al., 2005)** (see **Fig S6.7** and **Table 6.1**).
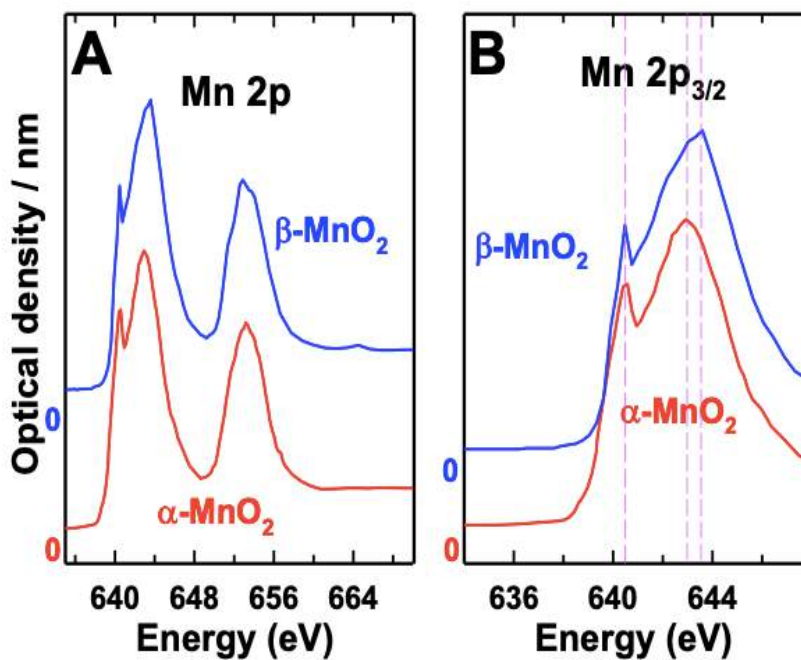
Figure 6.3 Comparison of Mn 2p spectra of α-MnO₂ (Hollandite) and β-MnO₂ (Pyrolusite) (A) full range Mn 2p spectra of α-MnO₂ and β-MnO₂. **(B)** Expansion of Mn 2p$_{3/2}$ spectra of α-MnO₂ and β-MnO₂ showing the shift in the position of the Mn 2p$_{3/2}$ → e$_g$ peak.

KMnO₄

In the MnO^{4-} permanganate ion, the Mn is tetrahedrally co-ordinated in the +7 oxidation state with a ground state electronic configuration of [Ar]3d^{0}4s^0 (Greaves et al., 1984). The large empty 3d density should lead to very intense Mn 2p → 3d transitions. The Mn 2p spectrum of KMnO₄ shows peaks at 640.5 eV and 642.9 eV which are assignable to 2p excitations into the empty t₂ and e orbitals, respectively. There is also a broad 2p$_{3/2}$ → 3d peak at 653.7 eV. The measured Mn 2p spectra of KMnO₄ (TEY) and KMnO₄ reported by Gilbert et al. (Gilbert et al., 2003) have the same features, although the TEY spectrum shows a more pronounced shoulder at 644.9 eV. The Mn 2p spectrum of KMnO₄ is very close to that of α-MnO₂ in both spectral shape and peak positions. However, the intensity of the 2p$_{3/2}$ broad peak corresponding to the Mn 2p e$_g$ orbital is relatively higher in KMnO₄ compared to that in MnO₂. The shapes and energy positions of the main Mn 2p peaks of MnO₂ and KMnO₄ are in

agreement with those reported in the literature (Gilbert et al., 2003). The calibrated $KMnO_4$ $2p_{3/2}$ peaks agree with those reported by Gilbert et al. (Gilbert et al., 2003) but the L_3 peak positions are 0.1 eV lower, while the L_2 peaks differ by 0.5 eV.

6.3.2 O 1s spectra of manganese oxides

Figure 6.4 presents the O 1s spectra of MnO, $MnSO_4$, Mn_3O_4, Mn_2O_3, α-MnO_2 and $KMnO_4$ measured by both STXM (thick solid line) and TEY-XAS (thin solid line). The energies of major features are compared to those reported in the literature, and tentative assignments are listed in **Table 6.2**. The O 1s spectra of the manganese oxides consist of two regions, (i) "pre-edge" peaks below 534 eV which arise from O 1s excitations to O 2p - Mn 3d hybridized orbitals which are characteristic of the oxidation state; and, (ii) broad peaks at higher energy (above 534 eV) which are O 1s excitations to the O 2p conduction band, with some interaction with Mn 4s and Mn 4p states (Cao et al., 2021; Qiao et al., 2013).

MnO and MnSO₄

The STXM O 1s spectrum of MnO shows 4 peaks at 532.9 eV, 534.4 eV, 536.5, 539.1, 544.4 corresponding to O 1s → 3d excitation to t_{2g} (up), e_g (up), e_g (down) and 3d - 4sp features, respectively (Frati et al., 2020; Gilbert et al., 2003). Aside from a systematic deviation of ~0.4 eV, the position and relative intensities of the spectral features of MnO are close to those reported by Gilbert et al. (Gilbert et al., 2003). (see **Table 6.2**). The O 1s spectrum of $MnSO_4$ is significantly different from that of MnO in both spectral shape and peak positions. The STXM and TEY-XAS O 1s spectra of $MnSO_4$ are quite similar in both shape and peak positions, showing one major, broad peak at 537.6 eV, and a minor, sharper peak at 541.5 eV.
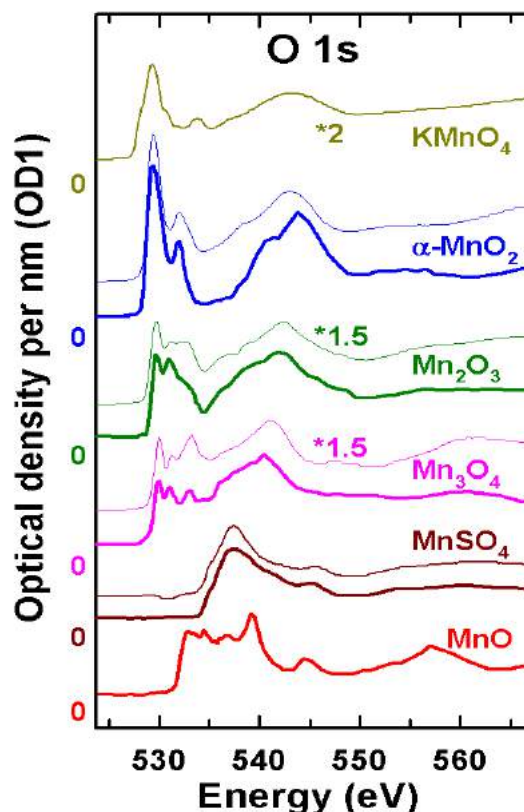
Figure 6.4   O 1s spectra of MnO, MnSO₄, Mn₃O₄, Mn₂O₃, α-MnO₂ and KMnO₄ measured by STXM (thick solid line) compared to those measured by TEY (thin solid line). The STXM-derived spectra are presented on quantitative OD1 intensity scales, with offsets for clarity. The intensities of the TEY spectra have been scaled for best match to the STXM spectra.

Although the O 1s spectrum of MnO has been published elsewhere (Frati et al., 2020; Gilbert et al., 2003; Qiao et al., 2013; Risch et al., 2017), the O 1s spectrum of MnSO₄ has not been reported in the literature, to the best of our knowledge. The Mn cation in MnO and MnSO₄ has a high spin $3d^5$ ground state with half-filled t_{2g} and e_g states. However, the different ligands and different Mn-ligand bond lengths (Frati et al., 2020; Gilbert et al., 2003) may lead to differences. **Figure S6.8** compares the O 1s spectra of MnO and MnSO₄ with those of H_2SO_4 and the SO_3^- group in perfluorosulfonic acid. This comparison clearly indicates the effect of the SO_4^- or SO_3^- ligand on the O 1s spectral shape. MnO is a rock-salt octahedral coordination system (Frati et al., 2020; Risch et al., 2017), The Mn^{2+} ion n MnSO₄ is in a slightly distorted

octahedral environment **(Held & Bohatý, 2002)** and the ligand field character of a sulfonate is significantly different from that of an oxide. The MnO O1s spectrum has a sharp O 1s → Mn 3d peak at 539 eV (Gilbert et al., 2003; Risch et al., 2017), and overlapping O 1s → –O 2p, Mn 4s, 4p features (Frati et al., 2020). The measured $MnSO_4$ O 1s spectra is also consistent with this observation. However, it has a stronger combination of the 3d and 4s, 4p parts of the spectrum which overlap as one peak.

Mn_3O_4 and Mn_2O_3

The O 1s STXM and TEY spectra of Mn_2O_3 and Mn_3O_4 exhibit similar O 1s → 3d features, with three peaks assigned to e_g-up, t_{2g}-down, and e_g-down (Frati et al., 2020) at 529.7 eV, 530.9 eV and 533.2 eV for Mn_2O_3 and 530.0 eV, 531.1 eV and 533.0 eV for Mn_3O_4 respectively. The spectra of each species match those reported by Gilbert et al. (2003), with energy scale deviations of 0.4 eV for Mn_2O_3 and 0.3 eV for Mn_3O_4. However, a 1.2 eV deviation was noticed in the position of the third peak of the O 1s spectrum of Mn_3O_4 (see **Table 6.2**).

α-MnO_2 and β-MnO_2

The O 1s spectrum of α-MnO_2 and β-MnO_2 measured by STXM (see **Fig. S6.9**) showed 2 sharp peaks in the O 1s → 3d "pre-edge" region at 529.4 eV and 531.9 eV and a broad peak at 543.8 eV. The first sharp peak at 529.4 eV is a combination of both spin-up e_g and the spin-down t_{2g} states, while the second sharp peak at 531.8 eV is related to the spin-down e_g state (Frati et al., 2020). The spectral shape and positions of peaks in the O 1s spectra of α-MnO_2 and β-MnO_2 are very similar. The TEY -XAS spectrum showed the same O 1s → 3d "pre-edge" peak positions and relative intensities as in the STXM spectrum. However, the broad peak corresponding to excitation to O 2p - Mn 4s, 4p hybridized states at 542.9 eV in TEY-XAS was 1.0 eV below the position of the corresponding feature in STXM. The spectra are in agreement with that for MnO_2 reported Gilbert et al. (Gilbert et al., 2003) but with an energy scale difference of 0.5 eV as shown in **Fig. S6.7** (see also **Table 6.2**).

KMnO$_4$

The O 1s spectrum of KMnO$_4$ has two O 1s → 3d pre-edge peaks at 529.3 eV and 533.6 eV, and a shoulder at 530.7 eV. These features have been assigned to O 1s promotions to 3de$_g$-up, 3de$_g$-down and 3dt$_{2g}$-down respectively (Frati et al., 2020),, There is also a broad peak at 543.2 eV corresponding to O 1s → O 2p - Mn 4s, 4p hybridized levels. The first sharp "pre-edge" peak at 529.3 eV was used to align the energy scale of our spectra with those reported in the literature (Gilbert et al., 2003; Müller et al., 2019).

6.3.3 Overall comparison of our spectra with literature spectra

In comparison to XAS data reported earlier, the Mn 2p and O 1s spectra of the MnOx reference compounds are in agreement with those reported in the literature: Mn 2p (Bourdelle et al., 2021; de Groot et al., 2010; Förster et al., 2021; Galezowski et al., 2020; Garvie & Craven, 1994; Gilbert et al., 2003; Müller et al., 2019; Pecher et al., 2003; Qiao et al., 2013; Risch et al., 2022; Risch et al., 2017; Shi et al., 2022; Toner et al., 2005) and O 1s (Frati et al., 2020; Gilbert et al., 2003; Müller et al., 2019; Qiao et al., 2013; Risch et al., 2017). The energy scales of the Mn 2p spectra reported here are very close to those reported by Gilbert et al. (Gilbert et al., 2003), with a maximum deviation of 0.2 eV. However, when compared to the spectra of δ-MnO$_2$ and Mn$_2$O$_3$ spectra reported by Toner et al. (Toner et al., 2005), there is a large deviation (1.3 eV, see **Table 6.1**). The degree of agreement with the literature O 1s spectra of MnO, Mn$_3$O$_4$, Mn$_2$O$_3$, α-MnO$_2$, β-MnO$_2$ and KMnO$_4$ was somewhat worse than for the Mn 2p spectra, with shifts of 0.3 - 0.5 eV in many features (see **Table 6.2**).

Table 6.1   Oxidation states and position(s) of major peaks in the Mn $2p_{3/2}$ spectra of manganese oxides

Sample	Mn Oxidation state	Major $2p_{3/2}$ peak position (eV)								
		This work	(Gilbert et al.)	$\Delta E(eV)^{(a)}$	(Toner et al.)	$\Delta E(eV)^{(a)}$	(Risch et al.)	$\Delta E (eV)^{(a)}$	(Garvie et al.)	$\Delta E (eV)^{(a)}$
MnO	+2	638.6	639.1	0.5	637.5	1.1	--	--	639.3	0.7
		639.7	640.3	0.6	638.5	1.2	--	--	640.3	0.6
		640.9	641.4	0.5	639.9	1.0	--	--	641.7	0.8
MnSO₄	+2	638.7	--	--	--	--	640.0	1.3	--	--
		639.8	--	--	--	--	641.1	1.3	--	--
		641.1	--	--	--	--	642.4	1.3	--	--
Mn₃O₄	+2/+3	639.6	639.5	0.1	--	--	--	--	640.2	0.6
		641.0	640.9	0.1	--	--	--	--	641.8	0.8
		641.7	641.6	0.1	--	--	--	--	642.3	0.6
Mn₂O₃	+3	641.4	641.5	0.1	640.1	1.3	642.4	1.0	641.8	0.4
α-MnO₂	+4	640.5	640.5	<0.1	639.3	1.2	--	--	--	--
		642.9	643.0	0.1	641.7	1.2	--	--	--	--
β-MnO₂	+4	640.5	640.5	<0.1	639.3	1.2	--	--	641.0	0.5
		643.5	643.0	0.5	641.7	1.8	--	--	643.8	0.3
KMnO₄	+7	640.5	640.4	0.1	--	--	--	--	--	--
		642.9	642.8	0.1	--	--	--	--	--	--

(a) ΔE is the peak energy measured in this work minus that given in the cited reference.

Table 6.2   Major O 1s → 3d "pre-edge" peak position(s) of manganese oxides

Sample	Mn Oxidation state	Major O 1s → 3d pre-edge peaks position (eV)		
		This work	(Gilbert et al., 2003)	ΔE (eV)[a]
MnO	+2	532.9	532.6	0.3
		534.4	533.9	0.5
		536.5	535.7	0.8
		539.1	539.0	0.1
		544.4	545.0	0.6
MnSO₄	+2	537.6	--	--
		545.2	--	--
Mn₃O₄	+2/+3	530.0	529.7	0.3
		531.1	531.5	0.4
		533.0	534.2	1.2
Mn₂O₃	+3	529.7	529.3	0.4
		530.9	530.7	0.2
		533.2	532.6	0.4
α-MnO₂	+4	529.4	528.9	0.5
		531.9	531.5	0.4
β-MnO₂	+4	529.4	528.9	0.5
		531.9	531.5	0.4
KMnO₄	+7	529.3	529.0	0.3
		530.7	531.2	0.5
		533.6	533.1	0.5

(a) ΔE is the peak energy measured in this work minus that given in the cited reference.

6.3.4   Example of quantitative oxidation state mapping of an energy material

Detailed information about complex MnOx systems can be obtained by deriving quantitative component maps from Mn 2p and/or O 1s STXM image sequences (Warwick et al., 2002) using reference spectra on OD1 intensity scales (Hitchcock, 2023a). The spatial distribution and quantitative thickness maps of each Mn component (Yang et al., 2022) can be

obtained through least squares fitting using the efficient singular value decomposition (SVD) method (Koprinarov et al., 2002). Although stacks using the full Mn 2p spectrum gives the best results, measuring only the Mn $2p_{3/2}$ (L_3) signal is usually enough to differentiate among Mn oxidation states. Simultaneous analysis of the O 1s and Mn 2p spectra provides even more reliable information.

Figure 6.5 presents quantitative chemical maps of the MnO, Mn_2O_3 and α-MnO_2 species in an α-MnO_2 cathode used in an experimental zinc-ion coin cell battery. These maps were obtained by fitting a Mn $2p_{3/2}$ STXM stack (70 energies, from $628 - 650$ eV) to the quantitative OD1 reference spectra of MnO, Mn_2O_3 and α-MnO_2 compounds presented in this chapter. The intensity scales indicate the thickness of the indicated species on the nm scale. Prior to this analysis the coin cell battery was subjected to 94 electrochemical charge (1.8 V) - discharge (1.2 V) cycles and left in the discharged state. After testing, the coin cell was taken apart and the cathode material was stripped off the separator, embedded in epoxy and microtomed to a thickness of 200 nm. **Figure 6.5D** is a color-coded composite of the quantitative component maps of the three MnOx species displayed in **Fig. 6.5A, B, C**.

After 94 charge-d cycles of the α-MnO_2 electrode, it was expected that α-MnO_2 will dominate all the sample as a result of oxidation processes. However, the results indicate that part of the α-MnO_2 was irreversibly reduced to MnO and Mn_2O_3 (**Fig. 6.6A**). In contrast, the Zn signals from the electrolyte ($ZnSO_4$) were observed in all MnOx regions, although with varying amounts (**Fig. 6.6B**). The quantitative chemical mapping showed that, despite a common understanding that this type of zinc-ion battery operates by shuttling Zn ions from the metallic Zn anode to the α-MnO_2 in the cathode (Liu et al., 2021), these results indicate negligible co-location of Zn^{2+} and α-MnO_2 (**Fig. 6.6D**). If there was partial co-location, the α-MnO_2 region would be partly reduced to lower oxidation states. Instead, the lower oxidation state domains are completely separated from the α-MnO_2, indicating the existence of unreactive reduced Mn species (in particular MnO, see **Fig. 6.6C**). This is consistent with the low capacity of this battery after the 94-cycle testing.
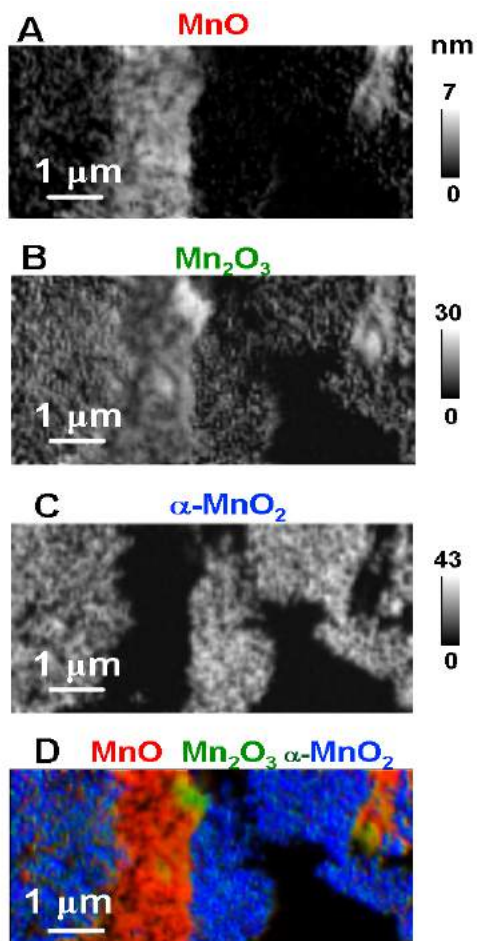
Figure 6.5   Example of identification and quantitative mapping of MnOx species in a discharged, Zn/α-MnO₂ battery cathode after 94 charge/discharge cycles (left discharged). (A) MnO component map. The grey scale indicates thickness in nm. **(B)** Mn_2O_3 component map. **(C)** α-MnO₂ component map. **(D)** Rescaled color composite of MnO (red), Mn_2O_3 (green) and α-MnO₂ (blue) component maps.
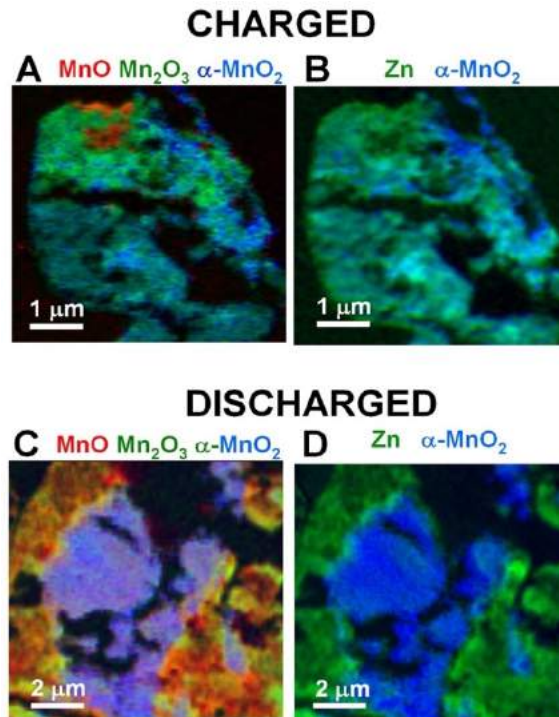
Figure 6.6   Comparing Mn and Zn maps of 94-cycled, charged and discharged Zn/α-MnO$_2$ battery derived from Mn 2p$_{3/2}$ and Zn 2p stacks. (A) Charged. Color coded composite of MnO (red), Mn$_2$O$_3$ (green), α-MnO$_2$ (blue) maps (rescaled) from a Mn 2p$_{3/2}$ stack. **(B)** Charged. Color coded composite of Zn map (green, from Zn 2p stack) and α-MnO$_2$ map (blue, from Mn 2p$_{3/2}$ stack) of the same region as (A) (rescaled). **(C)** Discharged. Color coded composite of MnO (red), Mn$_2$O$_3$ (green), α-MnO$_2$ (blue) maps (rescaled) from a Mn 2p$_{3/2}$ stack. **(D)** Discharged Color coded composite of Zn map (green, from Zn 2p stack) and α-MnO$_2$ map (blue, from Mn 2p$_{3/2}$ stack) of the same region as (C) (rescaled).

6.4   Discussion

STXM is a very powerful technique that provides spectroscopic characterization on a fine (sub 100 nm) spatial scale, which has significant advantages for quantitative mapping of chemical species in complex systems, such as polymer electrolyte membrane fuel cells (PEM-FC) (Hitchcock, 2023b). Manganese-based oxides are efficient electrode materials for different energy storage systems, in particular for supercapacitors and batteries (Parveen et al., 2022). Identification of changing Mn oxidation states and their spatial distributions during different electrochemical processes can provide insights into charge transfer mechanisms (Wang et al., 2018). Manganese oxides have various oxidation states (Mn^{2+} to Mn^{7+}) which, as shown in this

study as well in the literature (Garvie & Craven, 1994; Gilbert et al., 2003; Risch et al., 2022; Toner et al., 2005), have unique Mn 2p and O 1s spectral shapes and peaks positions which can be used to distinguish between different Mn oxidation states. Thus, the high-quality, accurately calibrated Mn 2p and O 1s pre-edge spectra provided in this research can be used to identify and map Mn oxidation states and intermediate components.

The Mn 2p and O 1s STXM and TEY-XAS spectra of the manganese oxides presented in **Fig. 6.1** and **Fig. 6.4** show there is a unique spectral shape for each Mn oxidation state. Nevertheless, there are some differences in the intensity of the finer features in spectra measured in TEY mode compared to that of STXM, which may relate to different energy resolution and/or surface oxidation/contamination. Mapping oxidation states can be performed using only the Mn $2p_{3/2} \rightarrow 3d$ features in the 630–650 eV region, which reduces acquisition time and radiation dose as compared to measuring full Mn 2p stacks. This can be particularly advantageous when performing *in-situ* STXM measurements (Hitchcock, 2023a; Zhang et al., 2023b; Zhang et al., 2023a), where speed of acquisition is critical.

The 2p absorption spectra of 3d transition metals (manganese in this case) are dominated by dipole allowed $2p \rightarrow 3d$ transitions which probe the empty valence levels of the absorbing atom which, in turn, depend on the geometric and electronic structure of the compound (Biesinger et al., 2011; Kosugi et al., 1997). As the Mn oxidation state increases, the binding energy of the Mn 2p core level increases leading to systematic shifts to higher energy. At the O 1s edge it is the presence of empty electronic states with both O 2p and Mn 3d character that leads to characteristic low energy O 1s $\rightarrow$ Mn 3d features, thus enabling differentiation Mn oxidation states at the O 1s edge (Qiao et al., 2013).

The sharp features in the manganese 2p spectra arise from transitions from the ($2p^6..3d^n$) ground state to ($2p^5..d^{n+1}$) excited states in which the dominant electronic configuration features a Mn 2p core hole and an excited electron in a specific unoccupied orbital / band. There are four major interactions which determine the fine details of the Mn 2p NEXAFS spectra. The strongest interaction is **spin-orbit splitting**, which gives rise to two distinct bands separated by ~11 eV. The spin-orbit splitting arises from the strong interaction of the net l=1 orbital angular momentum of the $2p^5$ core level with the unpaired spin (Bourdelle et al., 2021; R. Burns, 1993; Gilbert et al., 2003).

The next strongest interaction is the **crystal field splitting**, resulting from electrostatic interaction of the positively charged Mn ion and the field generated by the array of surrounding negatively charged O ions. The energy difference between the t_{2g} and e_g orbitals defines the crystal field strength (Δo or 10 Dq) (R. G. Burns, 1993). The magnitude of the crystal-field splitting depends on the Mn oxidation state and the nature of the coordinating anions, since the energies of the 3d-orbitals are influenced by ligand symmetries as well as strength of the Mn – O interaction (Garvie & Craven, 1994). The Mn 3d and O 2p atomic orbitals interact to form both σ-bonding and π-bonding orbitals (Garvie & Craven, 1994; Sherman, 1984). The σ-bonds can described in terms of lobes of the Mn $d(x^2 - y^2)$ and $d(3z^2 – r^2)$ orbitals being aligned with the lobes of the O 2p-orbitals.The π –bonds result from overlap of the Mn d(xy), d(yz) and d(xz) orbitals with O 2p-orbitals oriented perpendicular to the metal - ligand vector (Sherman, 1984).

Next, depending on the strength of the crystal field splitting relative to the **pairing energy** (stabilization of an electronic system by forming electron pairs), the electrons can be arranged in either high-spin or low-spin arrangements, which affects the occupancy of the unoccupied Mn 3d levels. The $3d^4$ configuration of Mn(II) and $3d^5$ configuration of Mn(III) can exist in either high-spin or low-spin arrangements. Low-spin Mn(II) compounds are rarely found in nature due to the large crystal field splitting. On the other hand, Mn(III) normally exists in the low-spin state, but can be stabilised in a high-spin state due to Jahn-Teller distortion of its coordination environment. The octahedrally coordinated Mn(IV) with a $3d^3$ electron configuration exists only in the high-spin configuration.

Finally, the spin-orbit interaction among partially filled Mn 3d levels gives rise to **atomic multiplet splittings** (de Groot et al., 1990). Manganese oxides can exhibit multiplet splittings, depending on the oxidation state. Since low-spin Mn(VII) configurations do not have unpaired electrons, multiplet splitting does not occur in $KMnO_4$. The Mn 2p spectra of MnO, Mn_2O_3 and MnO_2 can have multiplet splitting features since there are unpaired 3d electrons in all of these systems. The O 1s pre-edge reflects the O 2p component of the (Mn 3d, O 2p) hybridized empty states in which the overlap of the empty Mn 3d and O 2p states depends on the orbital symmetry and the Mn-O bond length.

The difference in the $Mn2p_{3/2}$ spectra of α-MnO_2 and β-MnO_2 indicates sensitivity to crystal structure changes. The differences in the spectra of these polymorphs can be ascribed to a larger crystal field in β-MnO_2 resulting from greater delocalization of the excited 3d electron. The phase dependence of the Mn 2p spectrum of MnO_2 is similar to that observed in the Ti 2p XAS spectra of the anatase and rutile polymorphs of TiO_2 (Sherman, 1984), where the main difference is the presence of a larger splitting and different peak intensities in the split Ti 2p $\rightarrow$ e_g band in anatase, relative to that rutile (Ruus et al., 1997).

Detailed quantum chemistry calculations and comparison of the results to experimental Mn 2p and O 1s spectra of the MnOx compounds have been reported in the literature (Gilbert et al., 2003). de Groot et al. (de Groot et al., 1990) reported spectral calculations of 3d transition-metal compounds including Mn^{4+}, Mn^{3+}, and Mn^{2+} using atomic multiplet theory. However, that study focused on the effect of a cubic crystal field on the shape of the $3d^N \rightarrow 2p^5 3d^{N+1}$ excitation spectra. A theoretical analysis of the O 1s spectra of $KMnO_4$ and MnO_2 was presented by Gilbert et al. (Gilbert et al., 2003) using spin dependent multiple scattering calculations. The peak separations in the calculated analysis are less than those in the experimental spectra.

As an example of the utility of Mn 2p spectroscopy in energy materials research, we have used the data presented here to perform quantitative analysis of Mn 2p and O 1s STXM results to track oxidation state changes after different electrode activation procedures of Mn_3O_4 supercapacitor electrodes (Yang et al., 2022). In a second example, Wang et al. (Wang et al., 2018) used Mn 2p TEY-XAS to study Mn oxidation states in different as-prepared Mn-based supercapacitor electrodes and correlated these changes to achieved capacitance performance.

6.5   Summary

High quality calibrated, quantitative Mn 2p and O 1s NEXAFS spectra of six different manganese oxide compounds have been measured by STXM and TEY-XAS. An example of their use in the analysis of an electrochemically degraded zinc-ion battery cathode was given. STXM and X-ray absorption spectroscopy measurements of different energy storage systems can be analyzed with the spectra reported in this work to study changes in Mn valence during different electrochemical processes.

Chapter 7

Scanning Transmission X-ray Microscopy Studies of Electrochemical Activation and Capacitive Behavior of Mn$_3$O$_4$ Supercapacitor Electrodes

This chapter presents experimental results of ex-situ STXM studies of Mn$_3$O$_4$-based supercapacitor electrode material subjected to different electrochemical activation procedures. The study provides detailed, quantitative results about gradual oxidation of the as-prepared Mn$_3$O$_4$ electrode to MnO$_2$, corresponding to a capacity increase.

Reprinted with permission from: Yang, W., Eraky, H., Zhang, C., Hitchcock, A.P. and Zhitomirsky, I., 2022. Scanning transmission X-ray microscopy studies of electrochemical activation and capacitive behavior of Mn$_3$O$_4$ supercapacitor electrodes. Journal of Materials Chemistry A, 10(35), 18267-18277.

The author of this thesis and Wenjuan Yang contributed equally. The author performed all of the STXM measurements and analyzed all STXM data in collaboration with Prof. A. P. Hitchcock. The electrode preparation and the electrochemical characterization were performed by Wenjuan Yang. (Zhitomirsky group). The author and Wenjuan Yang wrote the publication, with assistance in later stages by Prof. A. P. Hitchcock and Prof. Igor Zhitomirsky.

*The supplement information of this publication is in **Appendix D**.*
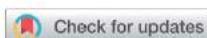
PAPER

Check for updates

Scanning transmission X-ray microscopy studies of electrochemical activation and capacitive behavior of Mn₃O₄ supercapacitor electrodes†

Wenjuan Yang,‡[a] Haytham Eraky, [ID] ‡[b] Chunyang Zhang,[bc] Adam P. Hitchcock [ID] [b] and Igor Zhitomirsky [ID] *[c]

This investigation, which is motivated by promising pseudocapacitive properties of Mn₃O₄ for energy storage in cathodes of supercapacitors, addresses the need to understand both the activation and the charge storage mechanisms of Mn₃O₄ electrodes. Specific activation protocols are shown to result in significant capacitance increase during cycling. For the first time scanning transmission X-ray microscopy (STXM) is used for analysis of Mn₃O₄ activation. STXM analyses at the Mn 2p and O 1s edges provide chemical mapping of different oxidation states with high spatial resolution. Mn₃O₄-carbon nanotube composite electrodes with commercially important high active mass loading of 40 mg cm⁻² are prepared using quercetin dispersant. The catecholate type polyaromatic quercetin facilitates co-dispersion of Mn₃O₄ with carbon nanotubes and allows enhanced electrode performance at high active mass loadings. Cyclic voltammetry, electrochemical impedance spectroscopy and galvanostatic charge–discharge are used for the capacitance monitoring during electrode activation. Two strategies are used for electrode activation in Na₂SO₄ electrolyte: electrochemical cycling at different scan rates and continuous cycling at a fixed scan rate. The capacitance variations are linked to STXM observations, which show gradual oxidation of Mn₃O₄ to form MnO₂ on the particle surface and in the bulk. The pseudocapacitive charge storage mechanism involves *in situ* oxidation of Mn₃O₄ and redox reactions of Mn⁴⁺/Mn³⁺ species on the particle surface and in the bulk.

1. Introduction

Mn₃O₄ is a promising charge storage material for applications in cathodes of asymmetric supercapacitor devices operating in a neutral Na₂SO₄ electrolyte.[1,2] Such devices offer advantages of enlarged voltage windows and enhanced power-energy characteristics. Investigations are focused on the development of advanced techniques for the deposition of nanostructured Mn₃O₄ films[1] and synthesis of Mn₃O₄ nanoparticles[1,3,4] for the fabrication of bulk electrodes with high active mass. Understanding the capacitive behavior and charging mechanism is crucial for the development of efficient electrodes and devices for practical applications.[5-7] Particular attention is focused on the charge storage behavior of nanostructured Mn₃O₄ and

composites.[8] Mn₃O₄ is usually combined with conductive additives for the fabrication of composites with enhanced conductivity and capacitance.[9-11] The charge storage mechanism of Mn₃O₄ electrodes in Na₂SO₄ electrolyte was analyzed in several investigations.[2,12] The first step involves solvation:[12]

$$Na_2SO_4(aq) + H_2O + Mn_3O_4 \rightarrow$$
$$(2 - \delta)Na^+(aq) + [Na_\delta Mn_3O_4 \cdot H_2O]^{\delta+} + SO_4{}^{2-}(aq) \, (1)$$
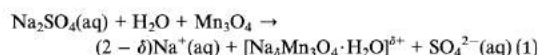
The subsequent charge–discharge steps are based on the reaction:[12]

$$Na_\delta MnO_x \cdot H_2O \leftrightarrow MnO_x \cdot H_2O + \delta Na^+ + \delta e^- \quad (2)$$
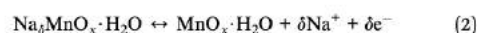
Previously, Mn K-edge X-ray absorption spectroscopy (XAS)[12] showed that Na₆MnOₓ is formed in the first charge–discharge cycle of Mn₃O₄ cathodes, which resulted in the reduction of the average oxidation state of Mn. Another investigation, using *in situ* XAS at the Mn K-edge, showed reduction of Mn³⁺ to Mn²⁺ at low potentials and oxidation of Mn³⁺ to Mn⁴⁺ or Mn⁶⁺ at higher potentials.[13] Significant changes in lattice constants (a and c) of the tetragonal Mn₃O₄ unit cell were observed during cycling in the positive potential range in the Na₂SO₄ electrolyte.[13]

[a]Dept. of Materials Science and Engineering, McMaster University, Hamilton, ON, L8S4M1, Canada

[b]Dept of Chemistry & Chemical Biology, McMaster University, Hamilton, ON, L8S4M1, Canada

[c]Dept. of Chemical Engineering, McMaster University, Hamilton, ON, L8S4M1, Canada. E-mail: zhitom@mcmaster.ca

‡ The authors contributed equally.

Journal of Materials Chemistry A

Paper

Despite the recent progress in the investigation of the deposition mechanism, the charge–discharge behavior of Mn_3O_4 electrodes is not well understood. The understanding of the charging mechanism is complicated due to the electrode activation phenomena. Several investigations analyzed activation of Mn_3O_4 electrodes, which resulted in capacitance increase during initial cycling.[2,14,15] A significant increase in capacitance was observed for electrodes with high active mass loading.[16-20] The activation process was linked to *in situ* modification of the electrode microstructure.[17,19,21,22] Previous investigations showed that capacitance variations during activation process can be diminished using mixed rhamnolipids as a capping agent for the synthesis of Mn_3O_4 particles and modification of particle morphology.[20] However, the origin of the capacitance variation during the activation process and charging mechanism are not well understood. Further analysis of activation behavior is critically important for better understanding of charging mechanism and applications of Mn_3O_4 electrodes in asymmetric supercapacitors.

Scanning transmission X-ray microscopy (STXM) is a promising technique for the investigation of activation behavior of Mn_3O_4 and analysis of the charging mechanism(s). STXM[23-25] is a synchrotron-based technique which provides chemically sensitive imaging with high spatial resolution (~30 nm). Chemical contrast is provided by near-edge X-ray absorption fine structure (NEXAFS) spectral signal.[26] STXM analytical studies provide spectroscopic identification and quantitative mapping of chemical components with 30 nm spatial resolution in both 2D and 3D projections.[23-25,27] Most of the electrochemical applications, particularly energy conversion and storage-related applications are associated with chemical reactions at the electrolyte and electrode interface.[27,28] STXM determination of the products of electrochemical reactions, along with quantitative spatial mapping, can provide a mechanistic understanding of electrochemical processes such as supercapacitor charging and discharging.

The objective of this investigation is the application of STXM for the analysis of activation behavior and charging mechanism of Mn_3O_4 based electrodes which contain multiwalled carbon nanotubes (MWCNT) as conductive additives. Investigations were performed using electrodes with high active mass loadings of 40 mg cm^{-2}, which is necessary for practical applications. High capacitance was achieved by the use of quercetin as a new catecholate-type dispersant, which facilitated co-dispersion of Mn_3O_4 and MWCNT. Testing results presented below revealed significant increase in capacitance during cycling. We describe the results of Mn 2p and O 1s STXM measurements of Mn_3O_4 – MWCNT samples subjected to different activation procedures. Our findings demonstrate that, as the number of charge–discharge cycles is increased, Mn_3O_4 is partially converted to MnO_2. This was correlated to the steady increase in the obtained capacitance. Testing results provide insight into the mechanism of activation and charge–discharge of Mn_3O_4 electrodes. In this case, the capacitance increase was linked to *in situ* oxidation of Mn_3O_4 during cycling.

2. Experimental procedures

2.1 Materials, synthesis of Mn_3O_4 particles and electrode fabrication

Quercetin (QC), $Mn(NO_3)_2 \cdot 4H_2O$, isopropanol, NaOH, Na_2SO_4, poly(vinyl butyral) binder (PVB, MilliporeSigma, Canada), multiwalled carbon nanotubes (MWCNT, ID 4 nm, OD 13 nm, length 1–2 μm, Bayer, Germany) and industrial Ni foam current collectors (95% porosity, 1.6 mm thickness, Vale, Canada) were used. A chemical precipitation method[16,20] was used for the synthesis of Mn_3O_4 nanoparticles from 0.07 M $Mn(NO_3)_2$ solution in DI water. The pH of the solution was adjusted to pH = 10 by aqueous 0.01 M NaOH for the synthesis of Mn_3O_4 nanoparticles. The obtained precipitate was washed with water and ethanol. Quercetin was used as a co-dispersant for the fabrication of stable suspensions of Mn_3O_4 and MWCNT in isopropanol (see ESI, Fig. S1†). The mass ratio of Mn_3O_4 : MWCNT : PVB binder in the suspensions was 80 : 20 : 3. The Ni foam current collectors were impregnated with the suspensions. The mass loading of the impregnated material after drying was 40 mg cm^{-2}. The impregnated foams were pressed to 30% of original thickness in order to improve electrical contact of the active material and current collector. Manganese dioxide (MnO_2), and trimanganese tetraoxide (Mn_3O_4) were purchased from Sigma-Aldrich and used as reference materials for STXM analysis. All reagents were used without further purification.

2.2 Microstructure and electrochemical characterization

Scanning electron microscopy (SEM) investigations were performed using a JEOL microscope, (JSM-7000F, Japan). X-ray diffraction (XRD) analysis was performed using a diffractometer (Bruker D8, Cu-Kα radiation, UK) at the scan rate of 1 degree per min. Electrochemical testing of capacitive behavior of the electrodes by cyclic voltammetry (CV) and electrochemical impedance spectroscopy (EIS) was performed using a PARSTAT 2273 (Ametek) potentiostat. Galvanostatic charge–discharge (GCD) studies were performed using a BioLogic VMP 300 potentiostat. Testing was carried out using aqueous 0.5 M Na_2SO_4 electrolyte in a 3-electrode electrochemical cell containing impregnated Ni foam as a working electrode, Pt mesh as a counter-electrode, and a saturated calomel electrode (SCE) as a reference.

Electrode capacitance was obtained from the CV, EIS and GCD data by methodology described in the literature[29,30] and presented as areal (C_S, F cm^{-2}) and gravimetric (C_m, Fg^{-1}) capacitance. Integral capacitances were derived from the CV and GCD data in a potential window of 0–0.9 V. CV was performed at scan rates of 2–100 mV s^{-1}. GCD testing was performed at current densities of 3–10 mA cm^{-2}. Differential capacitances were derived from the EIS data obtained at a voltage amplitude of 5 mV in the frequency range of 10 mHz–100 Hz at an open circuit potential. Analysis of the impedance data was performed using the commercial ZSimpWin software (Ametek) and an equivalent circuit developed for supercapacitor electrodes with high active mass loadings.[31]

C_S and C_m were derived from the CV data using the following equation:

$$C = \frac{\Delta Q}{\Delta U} = \frac{\left| \int_0^{t(U_{max})} I dt \right| + \left| \int_{t(U_{max})}^0 I dt \right|}{2(U_{max})} \qquad (3)$$

where ΔQ is charge, I – current and ΔU – the potential range. Capacitance was calculated from the chronopotentiometry data using the equation:

$$C = I\Delta t/\Delta U \qquad (4)$$

The complex capacitance $C^*(\omega) = C'(\omega) - iC''(\omega)$ was derived at different frequencies (ω) from the complex impedance $Z^*(\omega) = Z'(\omega) + iZ''(\omega)$:

$$C'(\omega) = \frac{-Z''(\omega)}{\omega |Z(\omega)|^2} \qquad (5)$$

$$C''(\omega) = \frac{-Z'(\omega)}{\omega |Z(\omega)|^2} \qquad (6)$$

The electrode activation was performed using CV at various scan rates (VSR) or at fixed scan rates (FSR). A VSR procedure (VSRP) involved CV at scan rates of 2, 5, 10, 20, 50 and 100 mV s^{-1}. EIS studies were performed after each VSRP. GCD testing was performed after five VSRPs. FSR testing involved 1000 CV cycles at a scan rate of 50 mV s^{-1}.

2.3. Methods: scanning transmission X-ray microscopy

Imaging, spectroscopy and spectromicroscopy measurements were performed using the ambient STXM at the spectromicroscopy (SM) beamline 10ID1 at the Canadian Light Source (CLS, Saskatoon, Canada),[32] a brief description of which is presented in ESI, Section S2.† The as-prepared active electrode materials (AEM) and AEM after VSRPs 1-5, or after 100 and 1000 FSR cycles were scratched to separate them from the Ni foam substrate. The AEM particles were drop-cast on formvar coated TEM grids (TED Pella Inc.). The grids were taped to standard trapezoidal STXM sample plates.[33] Spectra, images and image sequences were measured at the Mn 2p and O 1s edges. STXM measurements were performed with the chamber evacuated to <10^{-2} mbar and then backfilled with Helium (He) to a pressure of ~100 mbar. During the measurements, the X-ray beam is monochromated to a specific photon energy, then focused by a Fresnel zone plate (ZP) to a 40 nm spot, where the sample is placed (Fig. S2†). Images were measured by (x,y) raster scanning the sample while recording the intensity of the transmitted X-rays detected by a phosphor/photomultiplier tube (PMT) detector located behind the sample.[34,35] Spectromicroscopic data in the form of multi-energy image sequences (stacks[36]) were obtained at X-ray energies from ~10 eV below to ~40 eV above the onset of O 1s and Mn 2p absorption. STXM data was analyzed using aXis2000 software.[37] The transmitted X-ray flux through the sample (I) was converted to optical density (OD) using the Beer–Lambert Law: OD = $\ln(I_0/I) = \mu(E) \cdot \rho \cdot t$, where I_0 is the

incident X-ray flux, measured through an area devoid of the sample but with all other components (windows, zone plate, OSA, formvar); $\mu(E)$ is the energy dependent mass absorption coefficient; E is X-ray energy; ρ is sample density and t is the sample thickness.[23]

After Fourier cross-correlation alignment, the stacks were converted to OD using as I_0 the spectrum from areas of the stack devoid of sample. The OD stacks were then fit to suitable reference spectra, in this case, Mn_3O_4 and MnO_2, which were measured using both STXM and the CLS spherical grating monochromator (SGM) spectroscopy beamline, 11ID1. The results of the reference spectral study are described in ESI (Fig. S2, S3 and Table S1†). The Mn 2p spectrum of the commercial Mn_3O_4 sample, measured by both STXM and SGM, was significantly different from that reported in the literature.[38-40] The spectrum of the as-prepared electrode layer was in good agreement with the Mn 2p and O 1s spectra of Mn_3O_4 reported in the literature.[38,39] Thus we used the Mn 2p and O1s spectra of the as-prepared material as the reference for Mn_3O_4. The measured O 1s and Mn 2p spectra of Mn_3O_4 and MnO_2 were energy calibrated (see ESI, Section S3†) and placed on quantitative intensity scales, corresponding to the OD for 1 nm thickness of each material at its standard density using a method outlined in detail elsewhere.[23] These spectra were used in a singular value decomposition (SVD) analysis of the Mn 2p and O 1s stacks from each sample (SVD is a single pass matrix manipulation approximating linear least squares fitting[41]). Since quantitative reference spectra are used, the intensity scales of the resulting component maps give the local component thickness in nm.[23]

3. Results and discussion

3.1 Electrochemical and microstructure characterization

Fig. 1 shows X-ray diffraction pattern of obtained Mn_3O_4 particles. The observed diffraction peaks correspond to data in the JCPDS file 001-1127. It is suggested that the addition of alkali to the $Mn(NO_3)_2$ solutions resulted in the formation of unstable[42,43] $Mn(OH)_2$, which was oxidized in air to form Mn_3O_4.
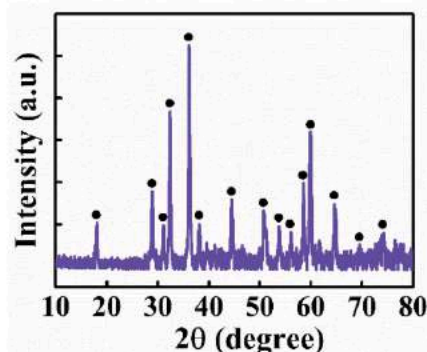
Fig. 1 X-ray diffraction pattern of as-prepared Mn_3O_4 (●-peaks corresponding to JCPDS file 001-1127).

This journal is © The Royal Society of Chemistry 2022

J. Mater. Chem. A, 2022, **10**, 18267–18277 | **18269**

151

Journal of Materials Chemistry A

The fabrication of Mn_3O_4 electrodes with high active mass requires the use of conductive additives because Mn_3O_4 exhibits low electronic conductivity. Therefore, MWCNT were used as conductive additives. As-received MWCNT formed large agglomerates with a typical diameter of 0.5 mm. The SEM images of such agglomerates were presented in a previous investigation.[44] Nanoparticles of Mn_3O_4 are also prone to agglomeration. Therefore, QC was used as a co-dispersant for Mn_3O_4 and MWCNT. QC was chosen due to its polyaromatic catecholate structure and redox properties. Fig. 2A shows the chemical structure of QC, which includes hydroxylated benzene rings. QC is a polyaromatic molecule, containing a catechol group. It has been widely reported that catechol and related molecules exhibit strong adsorption on surfaces of inorganic particles.[45–47] The interest in catechol anchoring groups resulted from the investigation of mussel adsorption on different surfaces, which involved dopamine-type catecholate monomers of proteins.[47–51] Fig. 2B shows adsorption of QC on the Mn_3O_4 surface, involving catecholate-type chelating bonding.[45] The polyaromatic structure of QC is beneficial[52] for its adsorption on MWCNT. This mechanism is based on π–π interactions.[52] Owing to its polyphenolic nature, QC exhibits redox-active properties.[53–55] It has previously been shown that catecholate-type redox-active molecules can act as charge transfer mediators, which facilitate charge–discharge reactions of supercapacitor materials.[56] Moreover, adsorbed catecholate molecules facilitate charge transfer in other processes, such as electropolymerization and photovoltaic current generation.[45]

Sedimentation tests showed enhanced suspension stability of Mn_3O_4 and MWCNT in the presence of QC as a dispersant (see Fig. S1†). Therefore, QC can be used as a co-dispersant for Mn_3O_4 and MWCNT. Fig. 3 shows microstructures of the electrodes prepared with and without QC. The electrodes prepared without QC showed poor mixing of Mn_3O_4 and MWCNT. The SEM image (Fig. 3A) shows large areas containing only MWCNT or Mn_3O_4. In contrast, the electrodes prepared using QC as a co-dispersant (Fig. 3B) showed reduced agglomeration and improved mixing of Mn_3O_4 and MWCNT. The improved mixing is beneficial for the fabrication of electrodes with enhanced capacitance. The electrodes prepared using QC were used for electrochemical characterization. Fig. 4A shows CVs at different
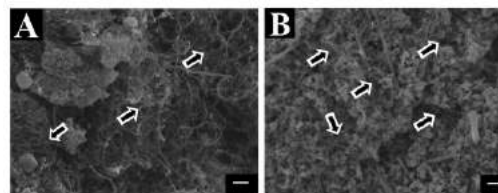
Fig. 3 SEM images for as-prepared Mn_3O_4-MWCNT electrodes (A) without QC and (B) with QC. The scale bars in the figures represent 250 nm, and arrows show MWCNT.

scan rates for VSRP 1 and indicate capacitive behavior in a potential window of 0–0.9 V. Fig. 4B compares CVs at a scan rate of 10 mV s^{-1} for VSRPs 1-5. It is seen that CV area increased from VSRP1 to VSRP5, indicating capacitance increase due to *in situ* activation of the electrodes. Moreover, the CV for VSRP 5 is nearly of rectangular shape, which indicates good pseudocapacitive response.

Fig. 4C and D shows capacitances and impedances for VSRPs 1-5. First cycle at 2 mV s^{-1} for VSR1 showed a capacitance of 1.5 F cm^{-2}. The capacitance decreased with increasing scan rate. The activation procedure resulted in capacitance increase from VSRP1 to VSRP5 (Fig. 4C). The capacitance at 2 mV s^{-1} for VSRP5 was found to be 3.3 F cm^{-2}. The decrease of real part of complex impedance with increasing TP number indicated beneficial decrease of resistance during the activation process (Fig. 4D). The decrease of the imaginary part indicated the increase of capacitance. The analysis of the impedance data using an equivalent circuit for high active mass electrodes[31] (see ESI, Section S4, Fig. S4†) for VSRPs 1-5 showed that changes in the real and imaginary parts of complex impedance resulted from the increase in capacitance and reduction of the charge transfer resistance. The components of complex capacitance were calculated from the impedance data and presented in Fig. 4E and F.

The AC capacitance derived from the impedance data increased with increasing VSRP number. The GCD data acquired after VSRP5 showed (Fig. 5) nearly ideal triangular charge–discharge curves. The capacitance decreased from 4.4 to 4.1 F cm^{-2} with increasing current density from 3 to 10 mA cm^{-2}. The obtained capacitances after VSRP5 were comparable with those reported in previous investigations.[17,19,22] Higher capacitances can be achieved using special techniques, such as electrostatic heterocoagulation,[21] liquid–liquid extraction[16] and synthesis in the presence of a capping agent.[20] However, to avoid the influence of different factors on Mn_3O_4 particles and with the goal of developing the STXM methodology, a traditional approach was used for the synthesis of Mn_3O_4 and electrode fabrication. This was important for monitoring the chemical modifications of Mn_3O_4 during activation and obtaining better understanding of the charging mechanism.

Another activation strategy was based on continuous cycling at a fast scan rate of 50 mV s^{-1}. Fig. 6 shows a continuous increase in normalized capacitance with increasing cycle number during 1000 FSR cycles. The capacitance for cycle 1 was only
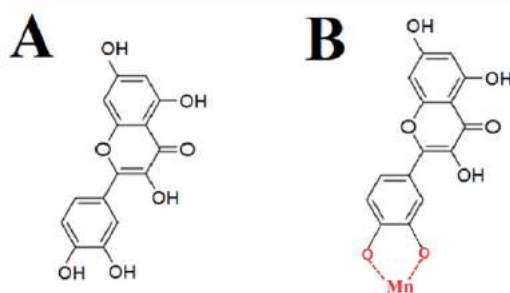
Fig. 2 . (A) Chemical structure of QC, (B) adsorption QC on Mn_3O_4 by chelation of surface Mn atoms.

152

Paper
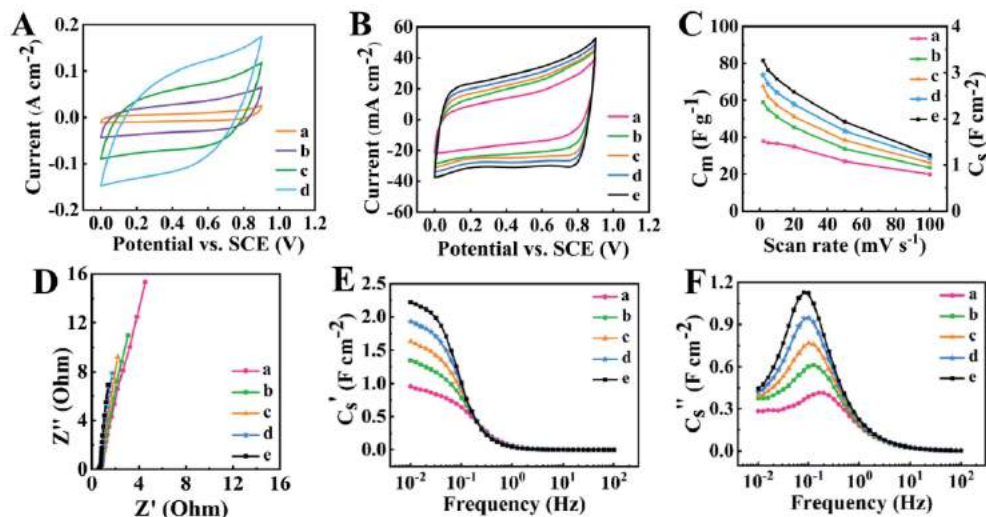
Fig. 4 (A) CVs for Mn_5O_4-MWCNT electrode at scan rates of (a) 5, (b) 20, (c) 50 and (d)100 mV s^{-1} for VSRP 1, (B) CVs at 10 mV s^{-1} for (a–e) VSRPs 1-5, (C) capacitance derived from CV data for (a–e) VSRPs 1-5, (D) Nyquist plot of complex impedance for (a–e) VSRPs 1-5, (E) real and (F) imaginary components of complex capacitances derived from the complex impedance data *versus* frequency for (a–e) VSRPs 1-5.

32.7% of the capacitance for FSR cycle 1000. The capacitance for FSR cycle 100 was 55.7%. Significant increase in capacitance was observed during the first 500 FSR cycles.

3.2 X-ray spectromicroscopy

3.2.1 Mn_3O_4 and MnO_2 reference spectroscopy. Fig. 7A and B present Mn 2p and O 1s spectra of the as-prepared Mn_3O_4 and MnO_2 reference spectra on OD1 intensity scales. The positions and relative intensities of the features in the measured Mn $L_{2,3}$ STXM reference spectra are in agreement in shape with the literature absorption spectra of Mn_3O_4 (hausmannite),[38] MnO_2 (pyrolusite)[38] and δ-MnO_2.[39] However there are discrepancies in the energy scales, with deviations from literature reports greater than 1 eV in some cases. These issues are documented and discussed in ESI, Section S5.† The first sharp peaks in the L_3 spectra of MnO_2 and Mn_3O_4 occur at 641.3 eV and 640.1 eV

respectively, and thus can be used to track sample oxidation. The O 1s → Mn3d electronic transitions in the O 1s spectra of MnO_2 and the as-prepared catalyst (Fig. 7B) occur at 529.7 eV and 530.6 eV respectively, again providing a useful tool to track oxidation. The shapes and energy positions of main features in the measured O 1s spectra are similar to those in the O 1s absorption spectra of MnO_2 and Mn_3O_4 reported previously.[38]

3.2.2 Mn 2p and O 1s results for the MnOx samples. Fig. 8A and B present Mn $L_{2,3}$ and O 1s spectra of as-prepared Mn_3O_4 and MnO_2 in comparison with spectra extracted from STXM stack measurements of the VSRP1, VSRP3 and VSRP5 processed samples. Mn $L_{2,3}$ and O 1s results for samples after FSR100 and FSR1000 cycles are presented in Fig. 8C and D. The Mn $L_{2,3}$ spectra were calibrated as discussed in ESI (Fig. S3 and Table S1†).

The Mn $L_{2,3}$ spectra (Fig. 8A) show that the Mn oxide in the as-prepared material is predominantly Mn_3O_4 showing three
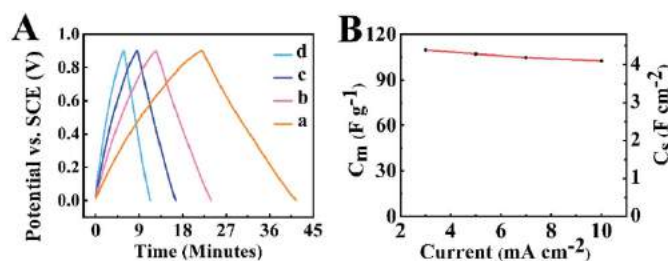
Fig. 5 (A) GCD data for current densities of (a) 3, (b) 5, (c) 7 and (d) 10 mA cm^{-2} and (B) capacitance *versus* current density obtained from the GCD data.

153

Journal of Materials Chemistry A
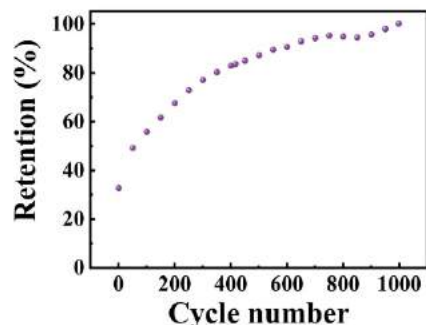
Fig. 6 Capacitance normalized by capacitance value for FSR cycle 1000 *versus* cycle number for continuous CV cycling at a scan rate of 50 mV s^{-1}.

sharp Mn L$_3$ peaks at 639.91 eV, 641.23 eV and 641.89 eV which is consistent with the XAS spectrum of an ensemble of the as-prepared material measured in TEY mode (ESI Section S6, Fig. S7†), and also with previous reports (Fig. S6B†).[38,39] At the early stages of the charge/discharge testing procedures (VSR1-VSR5), the Mn 2p spectra showed a noticeable change in the Mn L$_{2,3}$ peak positions, indicating partial conversion of Mn(II/III) to Mn(IV). On the contrary, the extracted spectra of the electrode material after FSR1000 cycles exhibited the Mn L$_{2,3}$ features characteristic of MnO$_2$, with sharp Mn 2p → 3d peaks at 641.1 (L$_3$) and 653.7 eV (L$_2$) and broad peak at (643.5 eV), respectively, indicating a remarkable change in both shape and peak positions compared to the spectra of as-prepared Mn$_3$O$_4$ which has a sharp L$_3$ peak at 640.1 and two broad peaks at (641.4 eV and 642.1 eV), respectively. In addition, the O 1s spectra after VSRP1,

VSRP3 and VSRP5 (Fig. 8B) were consistent with the Mn 2p measurements, indicating a significant change in the O 1s → 3d features in the 528–534 eV region consistent with partial conversion of the original Mn(II/III) (Mn$_3$O$_4$) material to Mn(IV) (MnO$_2$). The O 1s → Mn3d transition in the as-prepared material occurs at 530.6 eV, while after 1000 FSR cycles the O 1s → Mn3d transition occurs at 529.9 eV (Fig. 8D). Fig. 9 is an expansion of the low energy O 1s → Mn 3d region of the O 1s spectra and the Mn 2p$_{3/2}$ region, showing more clearly the systematic shift in the spectral peak positions with VSRPs 1,3,5 and FSR100, 1000 cycle samples.

The SGM-TEY measurements of Mn 2p spectra presented in Fig. S7† showed a remarkable change in the Mn L$_{2,3}$ peak positions of VSRs1, 3, 5 and FSR1000 cycles samples compared to the as-prepared Mn$_3$O$_4$, which are consistent with the STXM measurements of the same samples. However, the measured spectra of the VSR and FSR samples are similar, indicating that each consists of a mixture of Mn$_3$O$_4$ and MnO$_2$ species. On the other hand, the O 1s spectra of VSR1, VSR3, VSR5 and FSR1000 cycle samples showed the same O 1s → 3d features at 528–534 eV and are similar to the O 1s spectra of MnO$_2$, while the 536–548 eV region is different with no obvious trend. In contrast, the O 1s spectrum to the as-prepared Mn$_3$O$_4$ is very different from the measured spectra of the VSR and FSR samples (3 peaks instead of 2 in the 529–534 eV region).

3.2.3 Mapping of Mn species from the Mn 2p spectromicroscopy of the MnOx samples. The quantitative chemical mapping of the Mn(II/III) and Mn(IV) species on the VSRs1, 3, 5 and FSR100 and 1000 cycle samples that derived from fitting of Mn 2p stacks in a photon energy range of 630–670 eV to absolute intensity scale of MnO$_2$ and Mn$_3$O$_4$ reference spectrum showed a steady conversion of Mn(II/III) to Mn(IV) by increasing number of cycles.
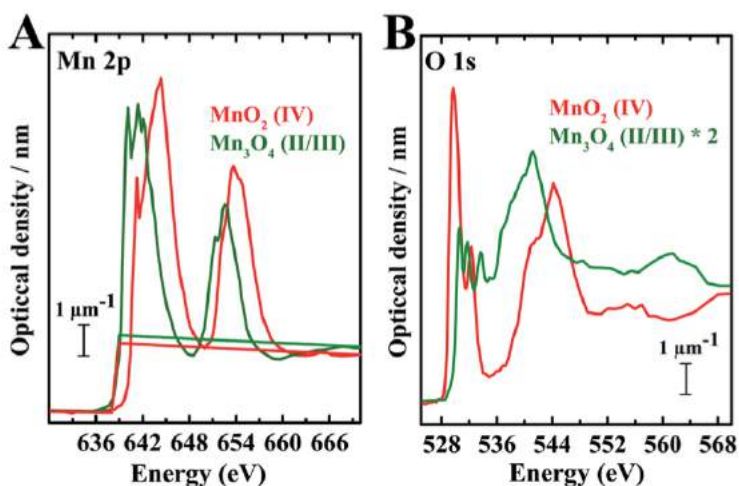
Fig. 7 (A) Quantitative Mn 2p spectra of Mn(II/III) (dark green) and Mn(IV) (red) on OD1 intensity scales. (B) Quantitative O 1s spectra of Mn(II/III) (dark green) and Mn(IV) (red) on OD1 intensity scales.

18272 | *J. Mater. Chem. A*, 2022, **10**, 18267–18277

This journal is © The Royal Society of Chemistry 2022
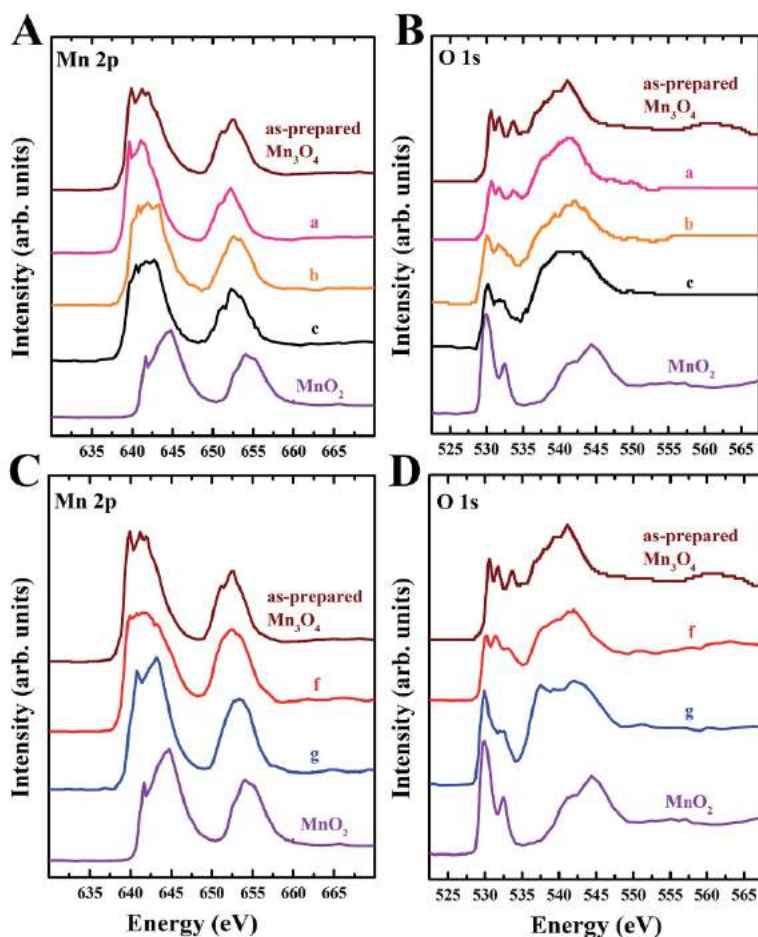
Fig. 8 (A) Mn 2p, (B) O 1s absorption spectra extracted from stacks measured for (a) VSRP1, (b) VSRP3 and (c) VSRP5, (C) Mn 2p, (D) O 1s absorption spectra extracted from stacks measured for (f) FSR cycle 100 and (g) FSR cycle 1000 samples.

Fig. 10A presents quantitative chemical mapping of the Mn(II/III) and Mn(IV) species in each of VSRs1, 3 and 5, while chemical maps for FSR100 and FSR1000 cycle samples presented in Fig. 10B. Each image is a color-coded composite of quantitative component maps derived by fitting the measured stacks with quantitative OD1 reference spectra of MnO_2 and Mn_3O_4 which are presented in Fig. 7A.

Fig. 11A and B plot the average volume of Mn(II/III) and Mn(IV) present for VSRPs1, 3, 5 samples and FSR100 and FSR1000 cycle samples. The chemical mapping and spatial distribution of Mn_3O_4 and MnO_2 shows only a small volume fraction of MnO_2 after VSRP1. Conversely, a considerable increase in MnO_2 contribution was observed after VSRPs 3 and 5. After FSR1000 cycles a 0.6 volume fraction of MnO_2 was obtained.

3.2.4 STXM spectromicroscopy. When compared to published Mn K-edge XAS results,[12,13] Mn L-edge spectromicroscopy

has the advantages of (i) higher energy resolution, thus achieving better chemical sensitivity – there are remarkable changes in both the Mn 2p and O 1s spectra when the oxidation state changes (Fig. 7); and (ii) nanoscale chemical imaging (Fig. 10). In particular, for the regions studied, it appears that the conversion of Mn(II/III) to Mn(IV) occurs to a greater extent in the core of the particles rather than at the edges. This is especially evident for the FSR 1000 cycles sample. The high spectral sensitivity has enabled observation of subtle changes in the Mn_3O_4 supercapacitor electrode material during the activation process. In particular, the improved capacitance can be seen to be the consequence of the increasing fraction of MnO_2. In contrast to the mechanism suggested in previous investigations[12,13] we did not observe capacitance decrease during initial cycling (Fig. 6). Very small Mn^{4+} content (Fig. 11A) in the particles after VSRP1 indicated that oxidation of Mn^{3+} ions on

155
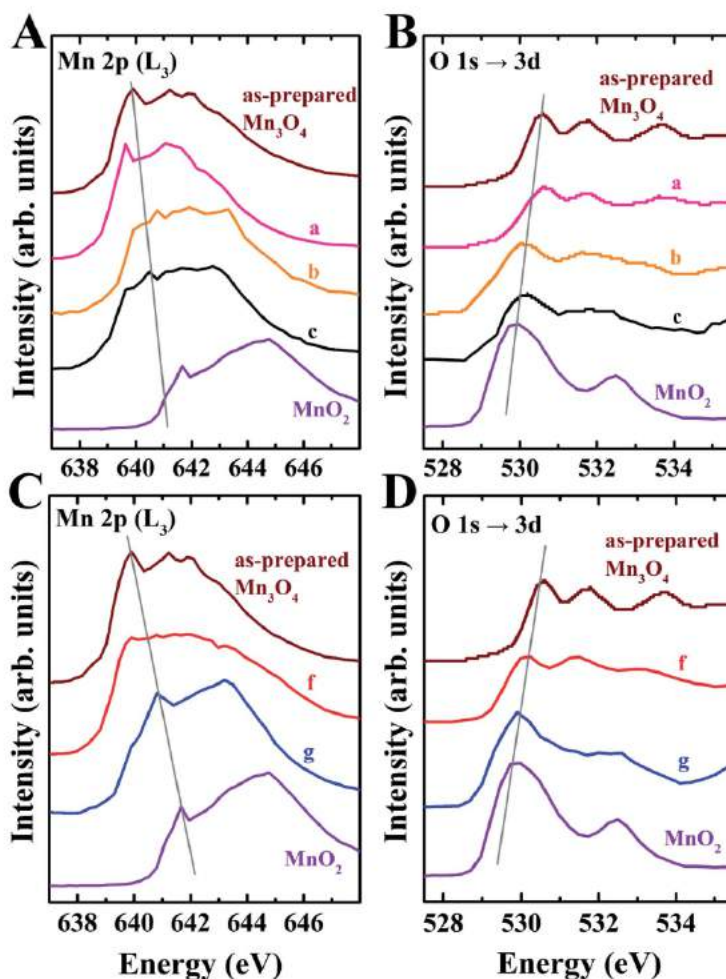
Fig. 9 Mn L$_3$ and O 1s → 3d features showing conversion of Mn(ɪɪ/ɪɪɪ) to Mn(ɪᴠ). (A) and (B) present (a) VSRP1, (b) VSRP2 and (c) VSRP3, (C) and (D) present (f) FSR100 and (g) FSR1000 cycle samples in comparison with as-prepared Mn$_3$O$_4$ catalyst and MnO$_2$ reference spectra.

the particle surfaces contributed to pseudocapacitive behavior. Continuous cycling resulted in oxidation of Mn^{2+} species in the bulk and enhanced contributions of bulk material to the total capacitance according to the reaction (2). It should be noted that previous investigations did not show a correlation between capacitance and BET surface area of MnO_2.[57,58] It was suggested that some pores accessible by nitrogen gas are not accessible by the solvated ions in the electrolyte. The STXM studies of this work showed that the bulk of the particles contributes significantly to the total capacitance.

Since this work is one of the first applications of STXM to supercapacitor materials, it is appropriate to compare its capabilities to complementary analytical imaging methods being applied to such problems. In terms of spectroscopies, X-

ray photoelectron spectroscopy (XPS) is often used to determine oxidation states of metal oxides. In the case of Mn oxides the range of oxidation state shifts from Mn(ɪɪ) to Mn(ɪᴠ) is less than 1 eV and the peak positions reported by various authors vary by up to 1 eV (see Table 2 in ref. 59). XPS is a very surface sensitive technique which is an advantage for studying surface dependent phenomena such as the mechanisms of charge transfer in supercapacitors. It is possible to perform XPS imaging, but the typical spatial resolution is 1–2 orders of magnitude lower than that provided by STXM. In terms of imaging, it is clear that electron microscopies such as SEM and TEM provide 1–2 orders of magnitude higher spatial resolution than STXM. However the analytical information provided is generally less sensitive that X-ray absorption. X-ray fluorescence (TEM-EDX) only provides

18274 | J. Mater. Chem. A, 2022, 10, 18267–18277

This journal is © The Royal Society of Chemistry 2022

156
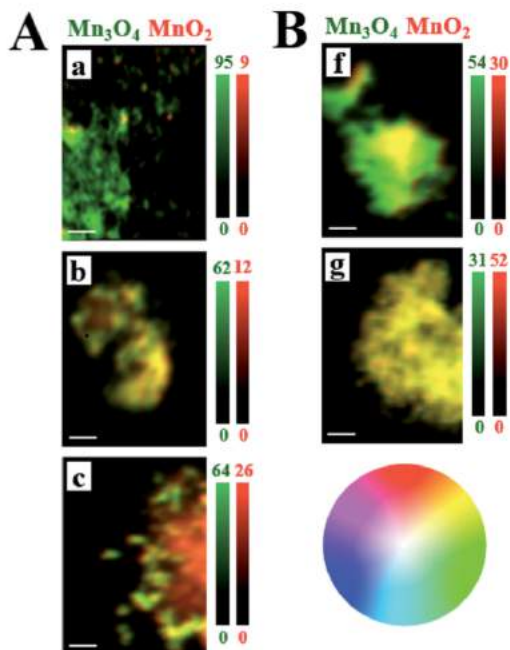
Fig. 10 Color coded composites of Mn(ɪɪ/ɪɪɪ) and Mn(ɪv) component maps derived by SVD fitting Mn 2p stacks measured on (A) VSRPs1, 3, 5 (a–c respectively), (B) FSR100 and FSR1000 cycle samples (f and g respectively), scale bar: 0.5 μm. Color scales are nm thickness. Color wheel indicates color expected for specific combinations of the red and green signals.
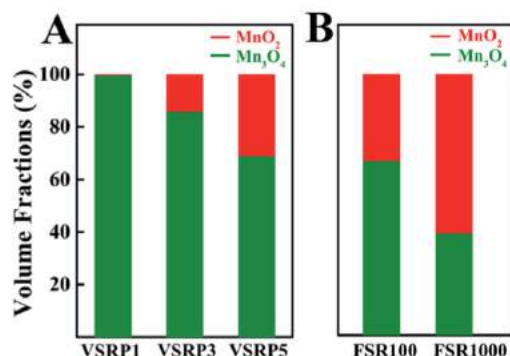
Fig. 11 Evolution of Mn(ɪɪ/ɪɪɪ) and Mn(ɪv) signals of (A) VSRP1, VSRP3 and VSRP5, (B) FSR100 and FSR1000 cycle sample represented in volume fractions.

elemental, not oxidation state, sensitivity. Core level electron energy loss (TEM-EELS) is the direct analog to STXM spectromicroscopy and thus has the same potential for oxidation state determination, but with the advantage of much higher spatial resolution. The most modern implementations of TEM-EELS provide a spectral resolution as STXM, but such measurements can be challenging due to the much greater extent of radiation damage in TEM than STXM.[60] In addition, since STXM is a photon-in, photon-out method, it is possible to adapt the system to *in situ* and *operando* studies of aqueous electrochemical phenomena such as charge/discharge mechanisms at supercapacitor electrodes. Such studies are currently underway.

4. Conclusions

For the first time scanning transmission X-ray microscopy (STXM) was used for the analysis of Mn_3O_4 activation. The use of QC as a dispersant facilitated fabrication of composite electrodes with high active mass and high areal capacitance. The beneficial effect of catecholate-type polyaromatic QC is related to co-dispersion and efficient mixing of different materials: pseudocapacitive Mn_3O_4 and conductive MWCNT additives. Monitoring the capacitance change by CV, EIS and GCD using VSRP and FSR activation methods and analysis of active material by STXM linked capacitance increase during activation and corresponding Mn_3O_4 oxidation on the surface and in the bulk of the particles. The capacitance increase during activation resulted from the gradual oxidation of Mn_3O_4 and increased contribution of the particle bulk to the total capacitance. The charge storage mechanism involved redox Mn^{3+}/Mn^{4+} reactions on the particle surface and in the bulk. It is expected that the approach developed in this investigation can be used for the analysis of activation behavior and charge storage mechanisms of other pseudocapacitive materials, such as V_2O_3.[44] In addition, we are actively developing *in situ* flow electrochemical devices for STXM,[61,62] which will enable *in situ* and operando types of studies of supercapacitor electrode materials.

Conflicts of interest

There are no conflicts to declare.

Acknowledgements

References

1 T. S. Patil, S. A. Gangawane and M. V. Takale, *Int. J. Sci. Res. Sci. Technol.*, 2021, **8**, 520.
2 S. G. Sayyed, A. V. Shaikh, D. P. Dubal and H. M. Pathan, *ES Energy Environ.*, 2021, **14**, 3.

This journal is © The Royal Society of Chemistry 2022

J. Mater. Chem. A, 2022, **10**, 18267–18277 | 18275

157

3 C. Liu, H. Song, C. Zhang, Y. Liu, C. Zhang, X. Nan and G. Cao, *Nano Res.*, 2015, **8**, 3372.

4 Z. Wang, J. Fang, Y. Hao, C. Chen and D. Zhang, *Mater. Sci. Semicond. Process.*, 2021, **130**, 105823.

5 H.-M. Lee, G. H. Jeong, D. W. Kang, S.-W. Kim and C.-K. Kim, *J. Power Sources*, 2015, **281**, 44.

6 G. Kerangueven, J. Faye, S. Royer and S. N. Pronkin, *Electrochim. Acta*, 2016, **222**, 755.

7 R. Aswathy, M. Ulaganathan and P. Ragupathy, *J. Alloys Compd.*, 2018, **767**, 141.

8 J. Vatamanu, O. Borodin, M. Olguin, G. Yushin and D. Bedrov, *J. Mater. Chem. A*, 2017, **5**, 21049.

9 Y. Wu, S. Liu, H. Wang, X. Wang, X. Zhang and G. Jin, *Electrochim. Acta*, 2013, **90**, 210.

10 Z. Nabti, T. Bordjiba, S. Poorahong, A. Boudjemaa, A. Benayahoum, M. Siaj and K. Bachari, *J. Mater. Sci.: Mater. Electron.*, 2018, **29**, 14813.

11 Y. Long, J. Xie, H. Li, Z. Liu and Y. Xie, *J. Solid State Chem.*, 2017, **256**, 256.

12 P. Suktha, N. Phattharasupakun, P. Dittanet and M. Sawangphruk, *RSC Adv.*, 2017, **7**, 9958.

13 M. P. Yeager, W. Du, Q. Wang, N. A. Deskins, M. Sullivan, B. Bishop, D. Su, W. Xu, S. D. Senanayake and R. Si, *ChemSusChem*, 2013, **6**, 1983.

14 C. Liu, Y. Chen, X. Sun, B. Chen, Y. Situ and H. Huang, *Electrochim. Acta*, 2019, **324**, 134894.

15 T.-H. Wu, D. Hesp, V. Dhanak, C. Collins, F. Braga, L. J. Hardwick and C.-C. Hu, *J. Mater. Chem. A*, 2015, **3**, 12786.

16 K. Rorabeck and I. Zhitomirsky, *Colloids Surf., A*, 2021, **618**, 126451.

17 R. Poon and I. Zhitomirsky, *Mater. Lett.*, 2018, **215**, 4.

18 N. Nagarajan, M. Cheong and I. Zhitomirsky, *Mater. Chem. Phys.*, 2007, **103**, 47.

19 J. Milne and I. Zhitomirsky, *J. Colloid Interface Sci.*, 2018, **515**, 50.

20 W. Yang and I. Zhitomirsky, *Nanomaterials*, 2022, **12**, 803.

21 R. Poon, W. Liang and I. Zhitomirsky, *Metall. Mater. Trans. A*, 2020, **51**, 855.

22 M. S. Ata, J. Milne and I. Zhitomirsky, *J. Colloid Interface Sci.*, 2018, **512**, 758.

23 A. P. Hitchcock, Soft X-ray imaging and spectromicroscopy, in *Handbook on Nanoscopy*, ed. G. Van Tendeloo, D. Van Dyck and S. J. Pennycook, Wiley, 2012, ch. 22, vol. 3, pp. 745–791.

24 A. P. Hitchcock, *J. Electron Spectrosc. Relat. Phenom.*, 2015, **200**, 49.

25 H. Ade and A. P. Hitchcock, *Polymer*, 2008, **49**, 643.

26 J. Stöhr, NEXAFS spectroscopy, in *Springer Series in Surface Sciences*, Springer, Germany, 1992, vol. 25.

27 A. P. Hitchcock and M. F. Toney, *J. Synchrotron Radiat.*, 2014, **21**, 1019.

28 K. T. Arul, H.-W. Chang, H.-W. Shiu, C.-L. Dong and W.-F. Pong, *J. Phys. D: Appl. Phys.*, 2021, **54**, 343001.

29 R. Chen, M. Yu, R. P. Sahu, I. K. Puri and I. Zhitomirsky, *Adv. Energy Mater.*, 2020, **10**, 1903848.

30 M. Nawwar, R. Poon, R. Chen, R. P. Sahu, I. K. Puri and I. Zhitomirsky, *Carbon Energy*, 2019, **1**, 124.

31 Y. Wang, Y. Liu and I. Zhitomirsky, *J. Mater. Chem. A*, 2013, **1**, 12519.

32 K. V. Kaznatcheev, C. Karunakaran, U. D. Lanke, S. G. Urquhart, M. Obst and A. P. Hitchcock, *Nucl. Instrum. Methods Phys. Res., Sect. A*, 2007, **582**, 96.

33 A. Kilcoyne, T. Tyliszczak, W. Steele, S. Fakra, P. Hitchcock, K. Franck, E. Anderson, B. Harteneck, E. Rightor and G. Mitchell, *J. Synchrotron Radiat.*, 2003, **10**, 125.

34 Y. Takeichi, N. Inami, H. Suga, C. Miyamoto, T. Ueno, K. Mase, Y. Takahashi and K. Ono, *Rev. Sci. Instrum.*, 2016, **87**, 013704.

35 T. Warwick, K. Franck, J. Kortright, G. Meigs, M. Moronne, S. Myneni, E. Rotenberg, S. Seal, W. Steele and H. Ade, *Rev. Sci. Instrum.*, 1998, **69**, 2964.

36 C. Jacobsen, S. Wirick, G. Flynn and C. Zimba, *J. Microsc.*, 2000, **197**, 173.

37 A.-P. Hitchcock, is written in Interactive Data Language (IDL). It is available free for non-commercial use from https://unicorn.mcmaster.ca/aXis2000.html.

38 B. Gilbert, B. Frazer, A. Belz, P. Conrad, K. Nealson, D. Haskel, J. Lang, G. Srajer and G. De Stasio, *J. Phys. Chem. A*, 2003, **107**, 2839.

39 B. Toner, S. Fakra, M. Villalobos, T. Warwick and G. Sposito, *Appl. Environ. Microbiol.*, 2005, **71**, 1300.

40 J. Kim, Y. H. Min, N. Lee, E. Cho, K. Y. Kim, G. Jeong, S. K. Moon, M. Joo, D. B. Kim and J. Kim, *ACS Omega*, 2017, **2**, 7424.

41 I. Koprinarov, A. Hitchcock, C. McCrory and R. Childs, *J. Phys. Chem. B*, 2002, **106**, 5358.

42 L. Wang, Y. Li, Z. Han, L. Chen, B. Qian, X. Jiang, J. Pinto and G. Yang, *J. Mater. Chem. A*, 2013, **1**, 8385.

43 A. Sukhdev, M. Challa, L. Narayani, A. S. Manjunatha, P. Deepthi, J. V. Angadi, P. M. Kumar and M. Pasha, *Heliyon*, 2020, **6**, e03245.

44 C. Wallar, R. Poon and I. Zhitomirsky, *J. Electrochem. Soc.*, 2017, **164**, A3620.

45 M. Ata, Y. Liu and I. Zhitomirsky, *RSC Adv.*, 2014, **4**, 22716.

46 K. Wu, Y. Wang and I. Zhitomirsky, *J. Colloid Interface Sci.*, 2010, **352**, 371.

47 J. L. Dalsin, B.-H. Hu, B. P. Lee and P. B. Messersmith, *J. Am. Chem. Soc.*, 2003, **125**, 4253.

48 B. P. Lee, P. B. Messersmith, J. N. Israelachvili and J. H. Waite, *Annu. Rev. Mater. Res.*, 2011, **41**, 99.

49 H. Lee, B. P. Lee and P. B. Messersmith, *Nature*, 2007, **448**, 338.

50 L. Petrone, *Adv. Colloid Interface Sci.*, 2013, **195**, 1.

51 M. Yu and T. J. Deming, *Macromolecules*, 1998, **31**, 4739.

52 M. S. Ata, R. Poon, A. M. Syed, J. Milne and I. Zhitomirsky, *Carbon*, 2018, **130**, 584.

53 A. Mattarei, N. Sassi, C. Durante, L. Biasutto, G. Sandonà, E. Marotta, S. Garbisa, A. Gennaro, C. Paradisi and M. Zoratti, Redox Properties and Cytotoxicity of Synthetic Isomeric Mitochondriotropic Derivatives of the Natural Polyphenol Quercetin, *Eur. J. Org. Chem.*, 2011, **2011**, **28**, 5577–5586.

18276 | *J. Mater. Chem. A*, 2022, **10**, 18267–18277

This journal is © The Royal Society of Chemistry 2022

158

Paper

54 E. Heřmánková, M. Zatloukalová, M. Biler, R. Sokolová, M. Bancířová, A. G. Tzakos, V. Křen, M. Kuzma, P. Trouillas and J. Vacek, *Free Radicals Biol. Med.*, 2019, **143**, 240.

55 A. M. O. Brett and M. E. Ghica, *Electroanalysis*, 2003, **15**, 1745.

56 M. Nawwar, R. Poon, R. P. Sahu, I. K. Puri and I. Zhitomirsky, *Ceram. Int.*, 2020, **46**, 18851.

57 R. N. Reddy and R. G. Reddy, *J. Power Sources*, 2003, **124**, 330.

58 Y. Jeong and A. Manthiram, *J. Electrochem. Soc.*, 2002, **149**, A1419.

59 H. Nesbitt and D. Banerjee, *Am. Mineral.*, 1998, **83**, 305.

60 J. Wang, G. A. Botton, M. M. West and A. P. Hitchcock, *J. Phys. Chem. B*, 2009, **113**, 1869.

61 V. Prabu, M. Obst, H. Hosseinkhannazer, M. Reynolds, S. Rosendahl, J. Wang and A. P. Hitchcock, *Rev. Sci. Instrum.*, 2018, **89**, 063702.

62 A. P. Hitchcock, C. Zhang, H. Eraky, L. Shahcheraghi, F. Ismail and D. Higgins, *Microsc. Microanal.*, 2021, **27**, 59.

This journal is © The Royal Society of Chemistry 2022

J. Mater. Chem. A, 2022, **10**, 18267–18277 | **18277**

159

Chapter 8

Scanning Transmission X-ray Microscopy of MnO$_2$ and Mn$_3$O$_4$ for Supercapacitor Cathodes: Influence of Fabrication Method and Electrochemical Activation on Charge Storage

This chapter presents experimental results of ex-situ STXM studies of MnO$_2$- and Mn$_3$O$_4$-based supercapacitor electrodes, fabricated by two different methods (high energy ball milling (HEBM) and using capping agent (quercetin) in the electrode material synthesis. The study provides detailed, quantitative results about the influence of the fabrication procedure on the capacitance increase during activation. The results show that the higher electrochemical performance of Mn$_3$O$_4$ prepared using quercetin in the synthesis was related to greater oxidation of the as-prepared Mn$_3$O$_4$ during the activation.

Reprinted with permission from: Yang, W., Eraky, H., Zhang, C., Hitchcock, A.P. and Zhitomirsky, I., 2024. Electrochemical and scanning transmission X-ray microscopy studies of MnO$_2$ and Mn$_3$O$_4$ for supercapacitor cathodes: Influence of fabrication method and electrochemical activation on charge storage. Chemical Engineering Journal, p.149391.

The author of this thesis and Wenjuan Yang contributed equally. The author performed all the STXM measurements and analyzed all STXM data (in collaboration with Prof. A. P. Hitchcock). The electrode preparations and the electrochemical characterizations were performed by Wenjuan Yang (Zhitomirsky group). The author and Wenjuan Yang wrote the publication, with assistance in later stages by Prof. A. P. Hitchcock and Prof. Igor Zhitomirsky.

*The supplement information of the publication is in **Appendix E**.*

Scanning Transmission X-ray Microscopy of MnO₂ and Mn₃O₄ for Supercapacitor Cathodes: Influence of Fabrication Method and Electrochemical Activation on Charge Storage

Wenjuan Yang,[1][§] Haytham Eraky,[2][§] Chunyang Zhang,[1,3] Adam P. Hitchcock[1] and Igor Zhitomirsky[2][*]
[1]Dept of Materials Science and Engineering, McMaster University, Hamilton, ON Canada L8S4M1
[2]Dept. of Chemistry & Chemical Biology, McMaster University, Hamilton, ON Canada L8S4M1
[3]Dept. of Chemical Engineering, McMaster University, Hamilton, ON Canada L8S4M1

Abstract

This investigation is motivated by increasing interest in Mn_3O_4 as a promising alternative to MnO_2 for supercapacitors with high active mass and the need for better understanding of charging and electrode activation mechanisms. High energy ball milling (HEBM) of chemically precipitated MnO_2 and Mn_3O_4 in the presence of quercetin resulted in significant capacitance increase. The use of Mn^{2+} salts for Mn_3O_4 synthesis facilitated the application of quercetin as a new chelating capping agent for synthesis of Mn_3O_4, which showed higher capacitance, compared to HEBM Mn_3O_4. The capacitance of Mn_3O_4 prepared using quercetin was 6.0 F cm^{-2} (149.50 F g^{-1}) for cyclic voltammetry at 2 mVs^{-1} and 8.03 F cm^{-2} (200.93 F g^{-1}) for chronopotentiometry at 3 mA cm^{-2}, which is on-par with the capacitance of MnO_2. The time-consuming activation procedure, which limits Mn_3O_4 applications, was significantly accelerated for HEBM Mn_3O_4 and practically eliminated for Mn_3O_4 prepared using quercetin as a capping agent. Soft X-ray scanning transmission X-ray microscopy (STXM), an advanced synchrotron based analytical microscopy, was used at the O 1s and Mn 2p edges to identify and quantitatively map the Mn oxidation states present in Mn_3O_4 materials. Variable and fixed sweep rate electrochemical cycling procedures were used for the analysis of oxidation state of Mn and charging mechanism using STXM analysis coupled with electrochemical testing. The combination of STXM and electrochemistry provided valuable insights into the activation kinetics and charging mechanism. The STXM results showed that the tested materials contained mixtures of Mn^{2+}, Mn^{3+} and Mn^{4+} oxides. A small amount of MnO phase in the tested samples indicated partial reduction. The higher content of MnO_2 phase in the tested Mn_3O_4 prepared using quercetin as a capping agent, compared to HEBM Mn_3O_4, corelated with higher capacitance and the ability to eliminate the activation procedure.

[§]These authors contributed equally

* Corresponding author, email: zhitom@mcmaster.ca

8.1   Introduction

Manganese oxides, such as MnO_2 and Mn_3O_4, are promising materials for the cathodes of energy storage supercapacitors (SC) [1-3]. MnO_2 has a high theoretical capacitance (1370 F g^{-1}) [4, 5] and a relatively large operational voltage window in neutral electrolytes, such as Na_2SO_4 and K_2SO_4. The theoretical capacitance of MnO_2 was estimated based on the Mn^{4+}/Mn^{3+} redox reactions and electrolyte cation adsorption and intercalation [6]. It is widely accepted that the charge storage mechanism of MnO_2 in neutral electrolytes involves the following reaction [4, 6]:

$$C_\delta MnO_2 \leftrightarrow MnO_2 + \delta C^+ + \delta e\text{-} \qquad (1)$$

where $C^+ = K^+, Na^+, Li^+, H^+$. The variation of the valence of Mn ions during charge-discharge has been confirmed by X-ray photoelectron spectroscopy [7]. However, investigations also showed that the charge storage mechanism is more complicated. It was found that electrolyte anions can contribute to charge compensation of Mn ions [7]. A hole redistribution model was proposed to explain higher-than-theoretical capacitance observed in experimental studies of MnO_2. It was hypothesized that not only change in the valence of the Mn ions, but also hole redistribution toward the oxygen sites, contribute to the charge-discharge mechanism [7]. These studies highlighted the benefits of non-stoichiometric MnOx phases for energy storage and generated interest in investigating charge storage by both Mn and O sites [7]. The formation of oxygen vacancies in MnO_2 was found to be a promising avenue for enhancing conductivity and capacitance [8, 9].

Equation (1) predicts that MnO_2 particle size reduction can potentially improve electrolyte access to the electrode material surface and enhance capacitance. Many investigations demonstrated capacitance increase [10, 11] in nanostructured MnO_2. However, experimental studies did not find correlation between BET surface area and pseudocapacitance [12, 13]. The materials with lower surface area showed higher capacitance, compared to the electrodes with higher surface area [12]. It was demonstrated that the charging mechanism is influenced by various factors, such as the nature of electrolyte, and MnO_2 transformation to a stable Mn_3O_4 spinel phase [4]. Operando Raman spectroscopy studies [14] revealed the electrolyte cation size effect on charge storage of MnO_2 electrodes. Other investigations showed the effect of physisorbed water [15], pH and other factors [16] on pseudocapacitance. *in-situ* quartz crystal microbalance studies [17] demonstrated the effect of ion desolvation kinetics at the electrode surface on capacitance. The variety of MnO_2 crystal structures provides multiple avenues for electrochemical performance optimization [7]. Despite the tremendous progress achieved in the synthesis of MnO_2, further advances are necessary to reach the full potential

of this material in high active mass electrodes (HAME) [10]. There is a high demand to improve the materials performance in HAME due to specific capacitance reduction with increasing active mass (AM), especially at fast charging speeds [10].

A major drawback of MnO_2 synthesis procedures is the need for permanganate precursors such as $KMnO_4$ or $NaMnO_4$, which react with organic capping agents. Therefore, it is challenging to reduce particle size and eliminate agglomeration during synthesis. The synthesis of MnO_2 from $KMnO_4$ solutions usually results in the formation of K_xMnO_{2+y} phases, which showed deviation from ideal capacitive behavior as was indicated by the appearance of redox peaks in the cyclic voltammograms [6]. Such redox peaks were not observed for pure MnO_2. However, the K-cation pre-inserted K_xMnO_{2+y} phases [6] showed higher capacitance, compared to MnO_2.

Mn_3O_4 represents a promising alternative to MnO_2 for charge storage in supercapacitor cathodes. The synthesis of Mn_3O_4 nanoparticles of controlled size is facilitated by the beneficial use of Mn^{2+} salts, which are chemically compatible with various organic capping agent molecules. Another attractive property of Mn_3O_4 is its ability to form solid solutions with other spinel compounds. Therefore, the properties of Mn_3O_4 can be modified by doping with different elements. The bottleneck limiting Mn_3O_4 applications in HAME is the need for electrode activation [18]. Cycling of Mn_3O_4 in Na_2SO_4 electrolyte resulted in a gradual capacitance increase [18]. This activation procedure is time-consuming and the activation process is influenced by sweep rate. It was hypothesized that activation leads to oxidation of Mn and adsorption of Na to form $Na_\delta MnO_x$ species:

$$3Na_2SO_4(aq) + Mn_3O_4 + (3x-4)/2O_2 \rightarrow$$

$$3(2-\delta)Na^+(aq) + 3Na_\delta MnO_x + 3SO_4^{2-}(aq) + (6x-3\delta-8)e^- \qquad (2)$$
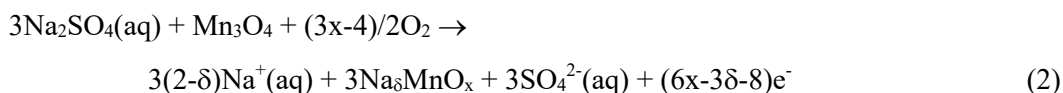
The charging mechanism for the activated Mn_3O_4 was suggested to be similar to that of MnO_2 and involved $Na_\delta MnO_x$ species in reaction (1). However, as it was described above, the charging mechanism of MnO_2 is not well understood. It is influenced by oxygen stoichiometry, hole redistribution, contribution of O sites, and other factors. Therefore, further investigations are necessary to better understand the charging mechanism and thereby develop advanced HAME.

Scanning transmission X-ray microscopy (STXM) [19-21] is a synchrotron-based technique that provides X-ray absorption based spectroscopic identification and spatially resolved quantitative mapping of chemical components with a spatial resolution of ~30 nm [19-22]. Chemical speciation is provided by near-edge X-ray absorption fine structure (NEXAFS) spectroscopy [23]. Most electrochemical applications, in particular, those related to energy conversion and storage, involve

chemical reactions that take place at an electrode - electrolyte interface [22], [24]. STXM analysis can provide insight into electrochemical charging and discharging processes in different systems, particularly, supercapacitors. Thus, STXM is a useful tool to investigate the activation of Mn_3O_4 based-electrodes as well as the charging/discharging mechanism [18].

In this investigation MnO_2 and Mn_3O_4 high active mass supercapacitor electrodes were fabricated using chemical precipitation followed by high energy ball milling (HEBM) or by synthesis of Mn_3O_4 using quercetin as a capping agent. Two different activation procedures were applied. Electrochemical testing methods were then used to investigate capacitive behavior while X-ray diffraction (XRD) and STXM were used to identify the oxidation state(s) of the Mn oxides in the electrodes at different conditions and with different electrode activation procedures.

8.2 Experimental procedures

8.2.1 Materials

$KMnO_4$, $Mn(NO_3)_2 \cdot 4H_2O$, ethanol, quercetin (QC), Na_2SO_4, poly(vinyl butyral) (PVB), NaOH, (MilliporeSigma), multiwalled carbon nanotubes (MWCNT, ID 4 nm, OD 13 nm, length 1–2 μm, Bayer,) and commercial Ni foam (Vale) current collectors were used for material synthesis, electrode fabrication and electrochemical testing. Commercial trimanganese tetraoxide (Mn_3O_4), manganese dioxide (MnO_2) (MilliporeSigma) and manganosite (MnO) (Alfa Aesar) were used to obtain reference spectra for STXM analysis.

8.2.2 Fabrication of MnO_2 and Mn_3O_4 for electrodes

MnO_2 was prepared by dissolving 1.6 g of $KMnO_4$ in 50 mL water, followed by a gradual addition of 25 mL ethanol and stirring continuously for 2 h. The reaction of $KMnO_4$ and ethanol formed MnO_2. After washing, filtration, and drying steps, **MnO_2-a** powder was obtained.

Mn_3O_4 was synthesized according to the previously described procedure [18] by dissolving 1.8 g $Mn(NO_3)_2 \cdot 4H_2O$ in 100 mL of water and slowly adding 0.01M NaOH solution to obtain pH=10. The resulting suspension was then subjected to centrifugation, washing, and drying, resulting in **Mn_3O_4-a** powder.

MnO_2-b and **Mn_3O_4-b** powders were prepared by high energy ball milling (HEBM) of corresponding MnO_2-a and Mn_3O_4-a powders. HEBM in aqueous medium was performed with a Mixer Mill MM 500 Nano (Retsch GmbH, Haan, Germany) at a frequency of 15 Hz during 2 h. QC was used as a dispersant. The mass ratio of manganese oxide: QC was 10:1. After HEBM the obtained **MnO_2-b** and **Mn_3O_4-b** powders were washed with water and dried.

The procedure for preparation of **Mn₃O₄-c** was similar to that for preparation of **Mn₃O₄-a**. However, in this case QC was added as a capping agent for synthesis. The mass ratio of $Mn(NO_3)_2 \cdot 4H_2O$:QC was 13:1. The obtained suspension was then subjected to centrifugation, washing, and drying, resulting in the **Mn₃O₄-c** powder. HEBM was not used for **Mn₃O₄-c**.

8.2.3   Fabrication of electrodes for supercapacitors

Suspensions for impregnation of Ni foam contained manganese oxide, MWCNT and PVB in ethanol in a mass ratio of 80:20:3. PVB was dissolved in ethanol prior to suspension fabrication. The suspensions were ultrasonicated for 30 min. The total mass of the impregnated material after drying was 0.04 g cm^{-2}. The impregnated Ni foams were pressed to 25% of their original thickness (1.6 mm). The area of electrodes used for electrochemical testing was 1 cm^{-2}.

8.2.4   X-ray diffraction and electrochemical studies.

A Bruker SMART CCD 600 Diffractometer with a Cu Kα radiation source was used for X-ray diffraction (XRD) characterization of the synthesized materials. The diffraction patterns were obtained at a scan speed of 0.5 deg min^{-1}. Cyclic voltammetry (CV), chronopotentiometry (CP) and electrochemical impedance spectroscopy (EIS) studies were performed in aqueous 0.5 M Na_2SO_4 electrolyte using a SP300 Biologic potentiostat. The three-electrode cell contained a working electrode, saturated calomel electrode (SCE) reference and Pt mesh counter electrode. Cyclic Voltammetry (CV), Chronopotentiometry (CP) and Electrochemical Impedance Spectroscopy (EIS) studies were performed in the ranges of sweep rates 2-100 mV s^{-1}, current densities 3-10 mA cm^{-2} and frequencies 10 mHz-100Hz, respectively. The capacitances C_m (F g^{-1}) and C_S (F cm^{-2}) were calculated as described in previous investigations [10, 25].

8.2.5   Scanning Transmission X-ray Microscopy

STXM imaging and spectromicroscopy measurements were performed using the STXM at the Softi-MAX beamline at Max IV (Lund, Sweden). Details of the SoftiMAX beamline [26] and the principles of STXM [27] have been presented elsewhere. Investigations were performed on both as-prepared and electrochemically tested samples. After electrochemical testing, particulate matter was scratched from the Ni foam substrate. The powders were drop-cast on a silicon nitride (SiNₓ) window (Norcada Inc.). After removing weakly adhering particles, the SiNx window was attached to a standard trapezoidal STXM sample plate using double sided tape [28]. Spectra, images, and image sequences (stacks [29]) were measured at the Mn 2p (L₃) and O 1s (K) edges. After mounting the sample in the STXM, the

chamber was evacuated to $<10^{-2}$ mbar and kept pumped during measurements. Spectromicroscopic data was obtained by recording multi-energy stacks at X-ray energies from ~10 eV below to ~40 eV above the Mn 2p and O 1s absorption onset. All STXM data was analyzed using aXis2000 software [30]. After alignment, the transmission signal was converted to optical density *(OD)* using as I_0 the spectrum from areas of the SiN_x window devoid of sample. After OD conversion and energy calibration, the stacks were fit to quantitative (OD1) reference spectra of MnO, Mn_3O_4 and MnO_2. The method to set the absolute intensity scales is outlined in detail elsewhere [23]. The Mn 2p reference spectra were used in a stack fit analysis of Mn $2p_{3/2}$ (L_3) stacks recorded from each sample. The stack fit produces component maps for each Mn species, a map of a constant signal (no spectral variation), and the residual of the fit. Since quantitative reference spectra are used, the intensity scales of the resulting component maps are the component thickness in nm [19].

8.3   Results and discussion

8.3.1   Electrochemical and microstructure characterization

Figure 8.1 shows XRD patterns of the **MnO_2-a, Mn_3O_4-a** and **Mn_3O_4-c** materials. The XRD studies of **MnO_2-a** revealed the formation of weakly crystallized material, which showed peaks corresponding to the birnessite phase (JCPDS file 00-018-0802). The general chemical formula of birnessite [31, 32] is C_xMnO_{2+y}, where C is K^+ or Na^+. It is known [31] that the oxidation state of Mn in this phase is typically 3.6-3.8, which is due to the dominant content of Mn^{4+} and minor Mn^{3+} and Mn^{2+} content. The XRD patterns of **Mn_3O_4-a** and **Mn_3O_4-c** materials showed the peaks of the hausmannite Mn_3O_4 phase (JCPDS file 04-007-1841).
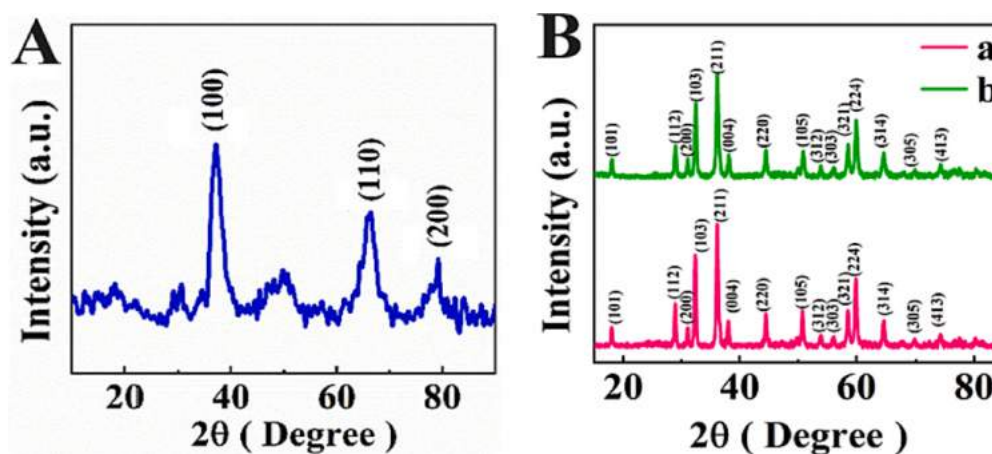
Figure 8.1 XRD patterns of (A) MnO_2-a and (B) (a) Mn_3O_4-a and (b) Mn_3O_4-c.

The crushing and grinding of the **MnO₂-a**, **Mn₃O₄-a** particles and their agglomerates during HEBM resulted in the formation of high energy surfaces, which can promote particle agglomeration. Therefore, HEBM was performed in the presence of the QC additive. It was hypothesized that QC adsorption on such surfaces during HEBM can prevent agglomeration. Moreover, QC was used as a capping agent to prevent particle growth and agglomeration in the synthesis of **Mn₃O₄-c**. The selection of QC for modification of manganese oxide particles was based on the unique chelating and adsorption properties of this molecule [33]. QC belongs to the group of natural flavonolid chelating agents produced in plants. The chelating properties of QC are important for various plant physiological processes [34]. Figure 8.2A shows the chemical structure of QC, which has aromatic rings and three chelating sites. Investigations showed the formation of QC complexes with Mn [35]. All three complexation sites (Figure 8.2B) can be involved in bonding Mn ions [35]. Of particular importance is the catechol ligand (Figure 8.2A). Previous investigations showed [36] strong adsorption of different catecholates on metal oxide particles by complexation of surface atoms on the particle surface. The adsorption mechanism is similar to that of mussel protein adsorption to inorganic materials, which involves catecholate monomers.
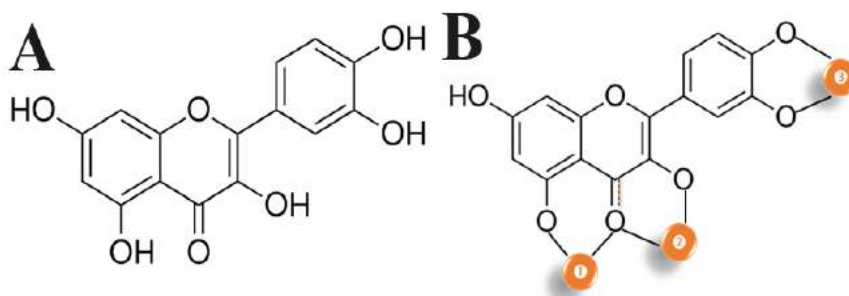
Figure 8.2 (A) Chemical structure of QC. (B) Bonding sites of QC for metal ions.

CV data for the **MnO₂-b** electrodes showed higher capacitance at low scan rates, compared to the capacitance of **MnO₂-a** (Figure 8.3 A-C). Capacitances of 4.75 F cm^{-2} (118.78 F g^{-1}) and 6.42 F cm^{-2} (160.53 F g^{-1}) were obtained for **MnO₂-a** and **MnO₂-b**, respectively, at 2 mV s^{-1}. However, HEBM resulted in enhanced capacitance only for sweep rates below 20 mV s^{-1}. EIS studies (Figure 8.3 D) showed slightly higher resistance (R=Z´) of **MnO₂-b** compared to **MnO₂-a**, which could be the result of QC adsorption. HEBM had only a slight effect on frequency dependencies of the complex capacitance components (Figure 8.3 E, F). CP studies (Figure 8.3G, H, I) showed an effect of HEBM on duration of charge-discharge at different current densities. The capacitances at 3 mA cm^{-2} were 7.00 F cm^{-2} (175.06 F g^{-1}) and 8.51 F cm^{-2} (212.68 F g^{-1}) for **MnO₂-a** and **MnO₂-b**, respectively. However,

the difference in capacitances of **MnO₂-a** and **MnO₂-b** decreased with increasing current density. In contrast to MnO₂ electrodes, the HEBM had a strong effect on capacitive performance of Mn₃O₄. The capacitive performance of **Mn₃O₄-a** was reported in a previous investigation [18]. Testing of **Mn₃O₄-a** showed a need for an electrode activation procedure. The electrode activation was dependent on sweep rate. Therefore, the electrode activation was investigated using different strategies. Electrochemical testing showed the influence of HEBM performed in the presence of QC (**Mn₃O₄-b**) and Mn₃O₄ synthesis using QC as a capping agent (**Mn₃O₄-c**) on the capacitive properties of the electrodes. Two different CV testing modes were used [18], which are labelled variable sweep rate and fixed sweep rate procedures (VSRP# and FSRP). VSRP# involved CV testing at sweep rates of # = 2, 5, 10, 20, 50 and 100 mV s⁻¹, whereas in FSRP the electrochemical cycling was performed at a fixed sweep rate of 50 mV s⁻¹ for 1000 cycles [18].
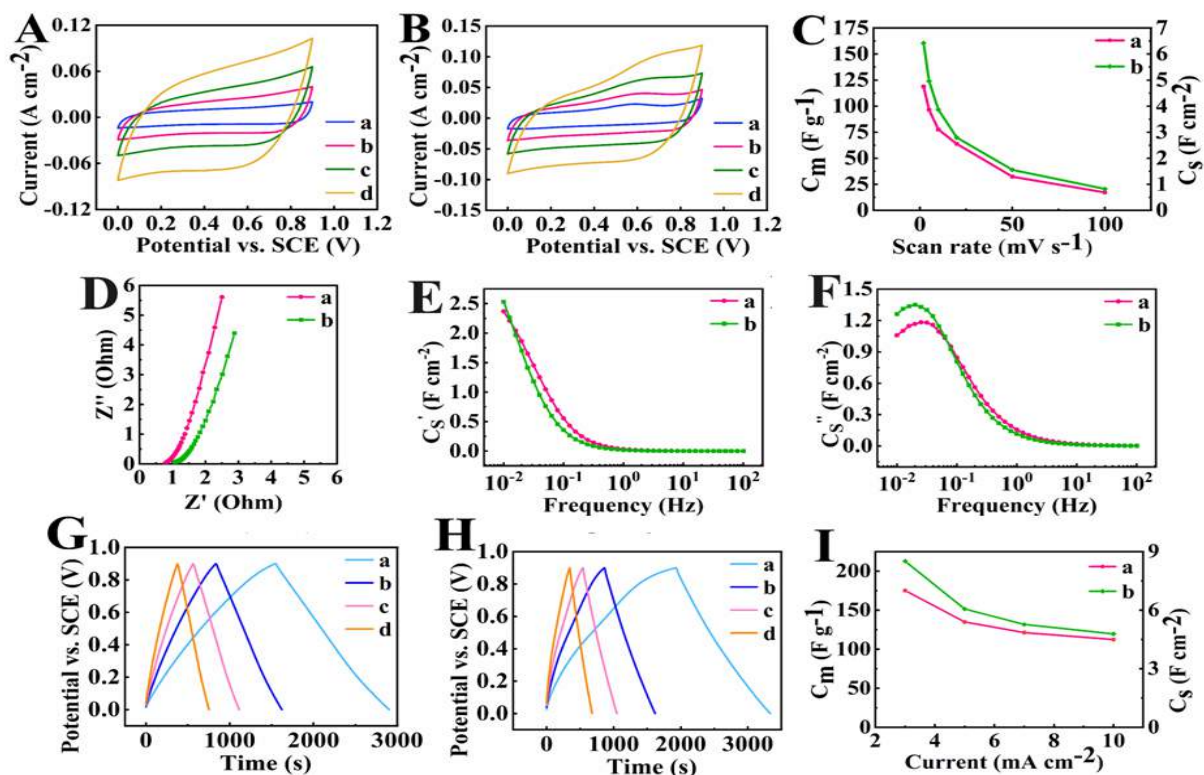
Figure 8.3 (A,B) CV data for (A) **MnO₂-a** and (B) **MnO₂-b** at (a) 2, (b) 5, (c) 10 and (d) 20 mV s⁻¹, (C) C$_S$ and C$_m$ versus scan rate, calculated from the CVs for (a) **MnO₂-a** and (b) **MnO₂-b**, (D,E,F) EIS data for complex impedance and capacitance: (D) Nyquist plot, (E) Cs' versus frequency, (F) Cs" versus frequency for (a) **MnO₂-a** (b) **MnO₂-b** , (G,H) CP data at (a) 3, (b) 5, (c) 7 and (d) 10 mA cm⁻² for (G) **MnO₂-a**, and (H) **MnO₂-b**, (I) C$_S$ and C$_m$ as functions of current density for (a) **MnO₂-a** and (b) **MnO₂-b**, calculated from CP data.

In this investigation, similar testing strategies were used for comparison. VSRP1 showed a capacitance of 1.5 F cm^{-2} for **Mn$_3$O$_4$-a** [18]. The capacitance gradually increased [18] with increasing VSRP numbers, and it was found to be to 3.3 F cm^{-2} for VSRP5 at 2 mV s^{-1}. Figure 4 (A-C) shows testing results for **Mn$_3$O$_4$-b** and **Mn$_3$O$_4$-c** for VSRP1. HEBM resulted in a capacitance of 5.06 F cm^{-2} (126.50 F g^{-1}) for VSRP1 for **Mn$_3$O$_4$-b** at 2 mV s^{-1}. The **Mn$_3$O$_4$-c** electrodes prepared using QC as a capping agent showed a capacitance of 6.0 F cm^{-2} (149.50 F g^{-1}) at 2 mVs^{-1}. Therefore, HEBM had two major effects on the capacitance of Mn$_3$O$_4$ electrodes: a significant increase in capacitance, and elimination of the need for electrode activation. The obtained capacitances for the **Mn$_3$O$_4$-b** and **Mn$_3$O$_4$-c** electrodes were comparable with those for the **MnO$_2$-a** and **MnO$_2$-b** electrodes.
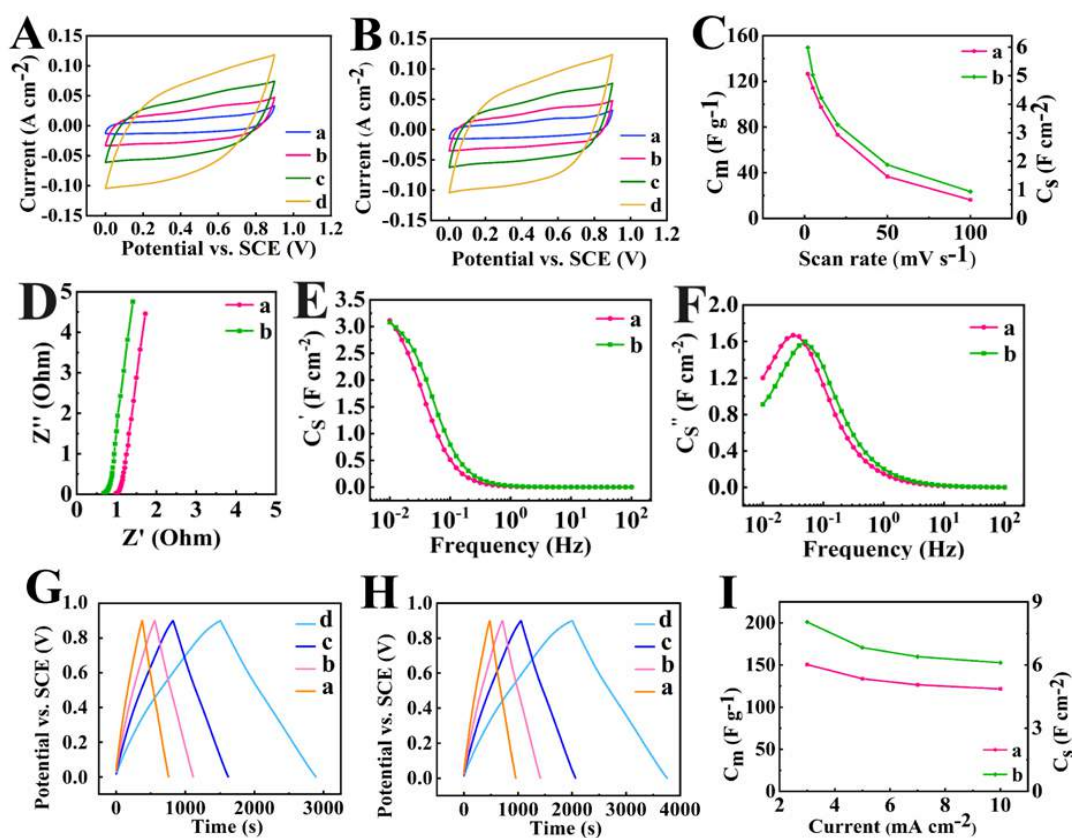
Figure 8.4 (A,B) CV data for (A) **Mn$_3$O$_4$-b** and (B) **Mn$_3$O$_4$-c** at (a) 2, (b) 5, (c) 10 and (d) 20 mV s^{-1}, (C) C$_S$ and C$_m$ versus scan rate, calculated from the CVs for (a) **Mn$_3$O$_4$-b** and (b) **Mn$_3$O$_4$-c**, (D,E,F) EIS data for complex impedance and capacitance: (D) Nyquist plot, (E) Cs' versus frequency, (F) Cs" versus frequency for (a) **Mn$_3$O$_4$-b** (b) **Mn$_3$O$_4$-c**, (G,H) CP data at (a) 3, (b) 5, (c) 7 and (d) 10 mA cm^{-2} for (G) **Mn$_3$O$_4$-b**, and (H) **Mn$_3$O$_4$-c**, (I) C$_S$ and C$_m$ as functions of current density for (a) **Mn$_3$O$_4$-b** and (b) **Mn$_3$O$_4$-c**, calculated from CP data.

Mn_3O_4-b and Mn_3O_4-c electrodes showed lower resistances compared to MnO_2-a and MnO_2-b electrodes, with the lowest resistances obtained for Mn_3O_4-c. Moreover, the EIS data for Mn_3O_4-c showed higher relaxation frequency [37], which corresponds to the maximum in the frequency dependence of C′′, and reduction of C′ in the corresponding frequency range. CP data obtained after VSRP1 (Figure 8.4 G-I) showed almost linear charging/discharging and capacitances of 6.02 Fcm^{-2} (150.54 F g^{-1}) and 8.03 F cm^{-2} (200.93 F g^{-1}) for Mn_3O_4-b and Mn_3O_4-c, respectively at a current density of 3 mA cm^{-2}. The capacitances decreased with increasing current density and Mn_3O_4-c showed higher capacitances, compared to Mn_3O_4-b. Previous studies of Mn_3O_4-a electrode activation at 50 mV s^{-1} (FSRP) showed a continuous increase in capacitance during 1000 cycles and the capacitance for the first cycle was only 32.7% of the capacitance for cycle 1000. The FSRP testing of Mn_3O_4-b showed significant capacitance increase during the first 400 cycles and the capacitance remained nearly constant after 600 cycles. The capacitance for cycle 1 was 32.3% of the capacitance for cycle 1000. Therefore, FSRP at the high sweep rate showed significant acceleration of the electrode activation procedure (Figure 8.5 A). The FSRP for Mn_3O_4-c showed improved electrode performance. Notable capacitance increase was observed for the first 200 cycles, and relatively small variation was observed between cycle 200 and 400. The capacitance remained practically constant after 400 cycles. The capacitance for cycle 1 was 61.8% of the capacitance for cycle 1000. Therefore, the Mn_3O_4-c electrodes showed faster activation, compared to Mn_3O_4-b for FSRP at high sweep rate (Figure 8.5 B).
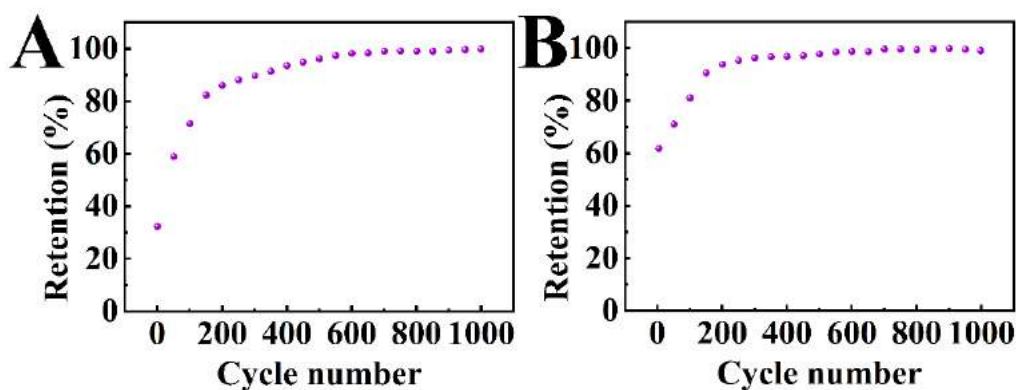
Figure 8.5 Capacitance retention of (A) **Mn_3O_4-b** and (B) **Mn_3O_4-c** electrodes at a scan rate of 50 mV s^{-1}.

8.3.2   X-ray spectromicroscopy

8.3.2.1 MnO, Mn₃O₄ and MnO₂ reference spectroscopy

Figure 8.6 presents the O 1s and Mn 2p X-ray absorption spectra of MnO, Mn_3O_4 and MnO_2 on OD1 intensity scales, measured by STXM for this study. The characteristic features and positions of peaks in these spectra are in excellent agreement with those for absorption spectra of Mn_3O_4 (hausmannite), MnO (manganosite) and α-MnO_2 reported in the literature [38-40]. These spectra were used as reference signals to identify, quantify and map the oxidation states of Mn in the supercapacitor electrode samples.
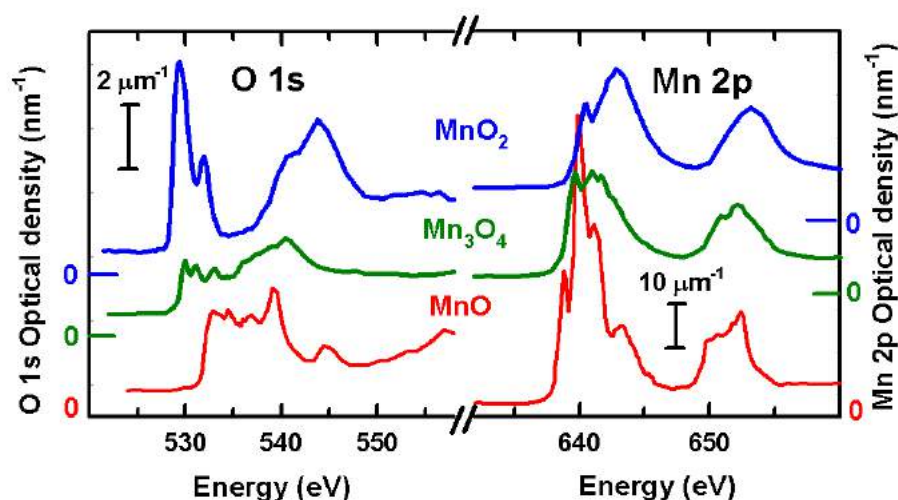
Figure 8.6 O 1s and Mn 2p X-ray absorption spectra of MnO (red), Mn_3O_4 (green) and MnO_2 (blue) plotted on an absolute intensity scale (OD1, optical density per nm thickness at standard densities).

8.3.2.2 Mn 2p and O 1s spectroscopic results for the Mn₃O₄ samples

Figure 8.7 A presents absorption spectra of **Mn₃O₄-b** and **Mn₃O₄-c** after VSRP and FSRP. Figure 8.7 B presents O 1s absorption spectra for **Mn₃O₄-c** after VSRP and FSRP. Based on the Mn 2p and O 1s spectral features, the **Mn₃O₄-c** sample contains 3 different MnO_x species after VSRP while that after FSRP contains only 2 different species. Figure 8.7 C presents O 1s absorption spectra for **Mn₃O₄-b** after VSRP and FSRP. The O 1s spectra indicate that there are two different MnO_x species present after both VSRP and FSRP tests. Figure 8.8 A is an expansion of the Mn $2p_{3/2}$ spectra of **Mn₃O₄-c** after VSRP and after FSRP. This presentation shows more clearly the presence of both Mn_3O_4 and MnO_2 in these samples. Figure 8.8 B is an expansion of the Mn $2p_{3/2}$ spectra of **Mn₃O₄-b** after VSRP and after

FSRP. Comparison with the reference spectra of pure MnO, Mn_3O_4 and MnO_2 indicates the presence of multiple oxidation states, with discernable features of all three species.
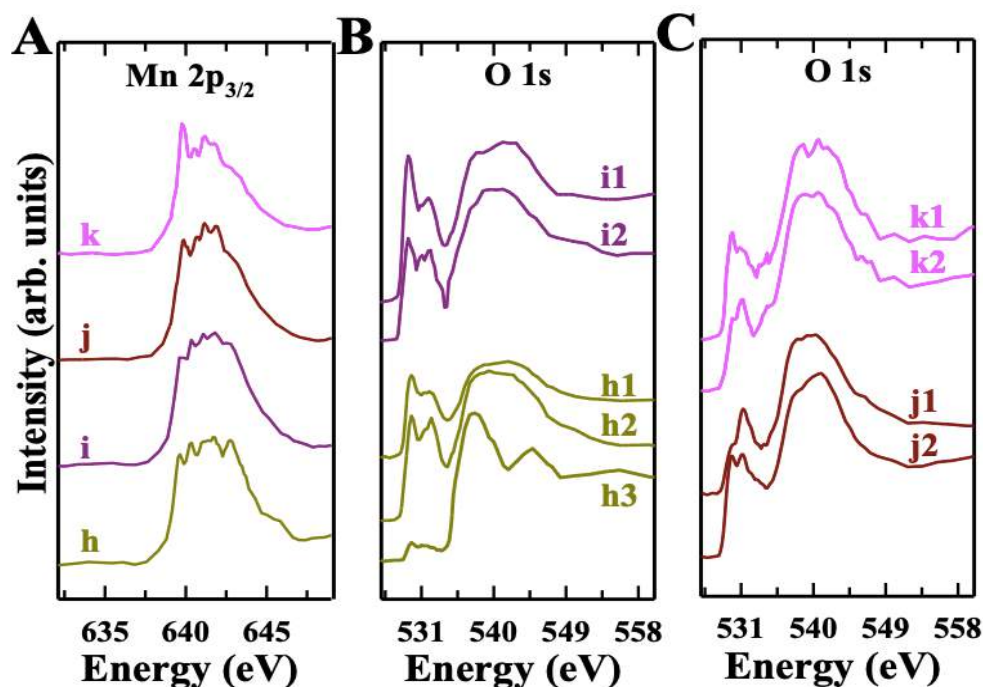
Figure 8.7 (A) Mn $2p_{3/2}$ absorption spectra of (h) **Mn₃O₄-c** after VSRP, (i) **Mn₃O₄-c** after FSRP, (j) **Mn₃O₄-b** after VSRP (k) **Mn₃O₄-b** after FSRP. (B) O 1s spectra for **Mn₃O₄-c** after VSRP (h1-h3) and after FSRP (i1-i2). (C) O 1s spectra for **Mn₃O₄-b** after VSRP (j1-j2) and after FSRP (k1-k2). The sub-coding (1,2 and 3) indicates different regions of the same sample.

The Mn $2p_{3/2}$ spectra of **Mn₃O₄-c** after VSRP and FSRP show that they are a mixture of Mn_3O_4 and MnO_2 species (Figure 8.8 A). The sharp peak at 639.6 eV and the two small peaks at 641.1 eV and 641.7 eV are from Mn_3O_4 while peaks at 640.4 eV and 642.8 eV are characteristic of MnO_2. The MnO_2 signal is more intense in the VSRP than in the FSRP activated sample. On the other hand, the Mn $2p_{3/2}$ spectra of **Mn₃O₄-b** after VSRP and FSRP showed much weaker MnO_2 signal than the correspondingly activated **Mn₃O₄-c** sample (Figure 8.8 B**).** However, **Mn₃O₄-b** after FSRP shows significant increase in MnO signal**.**
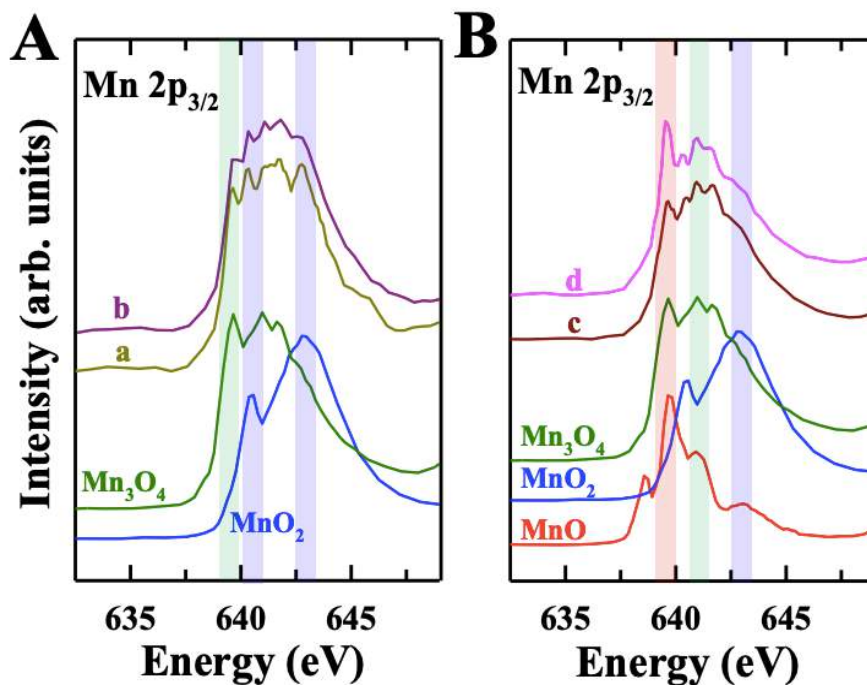
Figure 8.8 A. Mn $2p_{3/2}$ spectra of **Mn₃O₄-c** after (a) VSRP and (b) FSRP. B. Mn $2p_{3/2}$ spectra of **Mn₃O₄-b** after (c) VSRP and (d) FSRP. In each panel a direct comparison is made to the reference spectra.

Figure 8.9 A is the average of STXM images measured at 64 energies in an O 1s stack measured on **Mn₃O₄-b** after VSRP. Figure 8.9 B presents a color-coded composite of the maps of MnO, Mn₃O₄, and MnO₂ derived from a fit to the O 1s stack. Figure 8.9 (B1-B3) are the maps of each component. These results show clearly that Mn in various oxidation tend to be spatially localized. Figure 8.9 C plots the O 1s absorption spectra of the B-1, B-2 and B-3 regions, verifying the identity of these species.
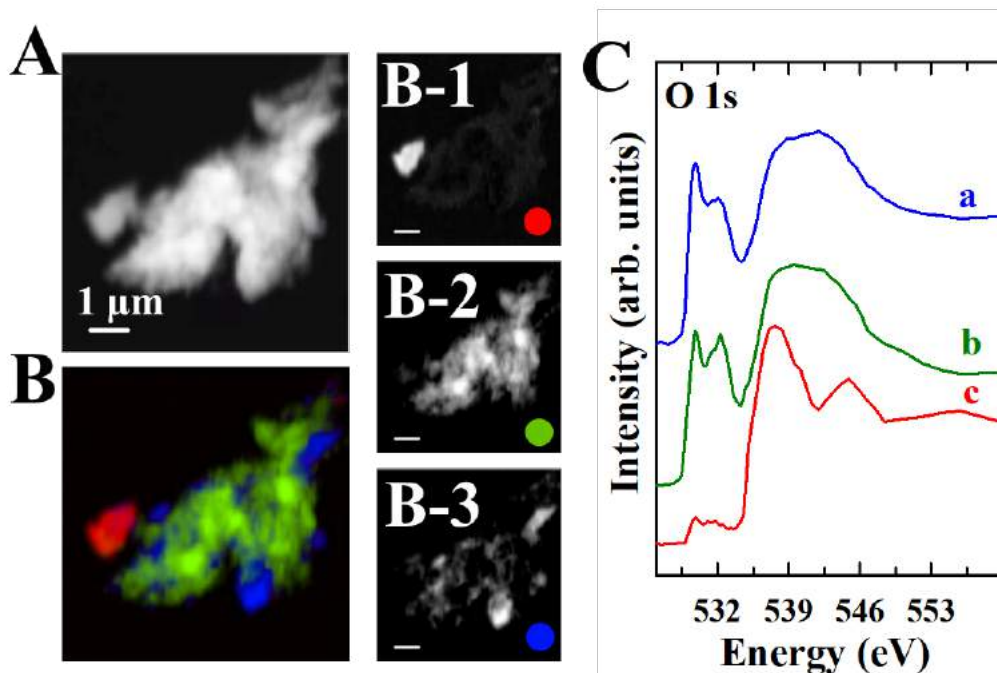
Figure 8.9 O 1s chemical mapping. (A) average of 64 images of O 1s stack of the **Mn₃O₄-c** after VSRP. (B) color coded composite of the MnO (red), Mn₃O₄ (green) and MnO₂ (blue) chemical maps derived from a stack fit to the O 1s stack. B-1, B-2 and B-3 are the component maps derived by fitting the O 1s stack to the O 1s spectra of MnO, Mn₃O₄, and MnO₂. (C) O 1s spectra extracted from the B-1, B-2 and B-3 regions. The color of each spectrum corresponds to the color-coding of the spatial regions from which the spectra were extracted.

The O 1s spectra of **Mn₃O₄-c** after VSRP and FSRP are different **(**Figure 8.7 B**)**. The O 1s spectra extracted from three different regions of **Mn₃O₄-c** after VSRP **(**Figure 8.9 C**)** show that it is a partially spatially segregated mixture of three different Mn oxidation states. The O 1s spectrum of the red area (Figure 8.9 B-1) showed low intensity peaks at 529.9 eV, 531.5 eV and 532.7 eV, which are a combination of the characteristic O 1s → Mn 3d features of Mn₃O₄ and MnO₂, and large broad peaks at 537.5 eV and 544.9 eV which correspond to MnO signals. The O 1s spectrum of the green area (Figure 8.9 B-2) exhibits O1s → Mn 3d transitions at 529.8 eV, 532.3 eV and a small shoulder peak at 531.5 eV, all of which correspond to Mn₃O₄. The O 1s spectrum of the blue area (Figure 8.9 B-3) has a high intensity O1s → Mn 3d peak at 529.8 eV and a weak peak at 532.1 eV corresponding to MnO₂. Similarly, the different spectra extracted from different regions of **Mn₃O₄-c** after FSRP are presented in supplemental information, Figure S8.1 C. The O 1s spectrum of the red area (Figure S8.1 B-1) showed high intensity peak at 529.4 eV and low intensity peak at 531.9 eV, which are close to the

characteristic O 1s → Mn 3d features of MnO_2. The O 1s spectrum of the green area (Figure S8.1 B-2) showed sharp O1s → Mn 3d transition at 529.3 eV and week peaks at 531.1 eV and 532.1 eV with a shoulder peak at 533.4 eV. These peaks represent a combination of the characteristic O 1s → 3d features of Mn_3O_4 and MnO_2.

Likewise, the O 1s spectra of **Mn_3O_4-b** after VSRP and FSRP show different O 1s → Mn3d features in different regions (see Figures S8.2 and S8.3). The O1s → Mn 3d transition in spectra extracted from different regions of the **Mn_3O_4-b** after VSRP sample has two characteristic peaks at 529.9 and 531.1 eV with a small shoulder peak at 533 eV, corresponding to Mn_3O_4. However, the intensity of the first peak at 529.9 eV is significantly different in both spectra which suggests there are multiple Mn oxidation states. Similarly, the O 1s spectra extracted from two different regions of **Mn_3O_4-b** after FSRP showed different intensities of the first (529.9 eV) and second (531.1 eV) peaks. The speciation derived from the O 1s and Mn 2p spectra of the same spatial region are consistent for each of the four samples measured by STXM. Together the Mn 2p and O 1s spectra indicate there is significant oxidation of the as-prepared Mn_3O_4 to MnO_2, even after only VSRP. The oxidation is more extensive in the **Mn_3O_4-c** than in the **Mn_3O_4-b** samples.

Figure S8.4 C presents the Mn $2p_{3/2}$ absorption spectra of the as-prepared **MnO_2-a** sample in comparison with that of the as-prepared **MnO_2-b**. The Mn 2p spectrum of **MnO_2-a** sample indicates there is a mixture of oxidation states. The Mn $2p_{3/2}$ characteristic features of MnO_2 at 640.5 eV and 642.8 eV are observed, while the low intensity peak at 639.8 eV arises from MnO and the weak signals at 641.2 eV and 642 eV are associated with Mn_3O_4. The component maps presented in Figure S8.4 A indicate almost equal amounts of MnO and MnO_2 in the measured sample. Both samples showed considerable contribution of Mn_3O_4 signals. In the contrast, the MnO signal (639.8 eV) in the Mn $2p_{3/2}$ spectrum of **MnO_2-b** is much lower than that in **MnO_2-a**, indicating a dominant content of MnO_2, as also indicated in the component maps presented in Figure S8.4 B. The O 1s spectra of as-prepared **MnO_2-a** and **MnO_2-b** are similar (Figure S8.5 B and D). They indicate there are mixed oxidation states in these samples, which are mapped in Figure S8.5 A and C.

8.3.2.3 Chemical Mapping of Mn species in the tested samples

Figure 8.10 presents quantitative chemical maps of the MnO, Mn_3O_4 and MnO_2 species for **Mn_3O_4-b** and **Mn_3O_4-c** after VSRP and FSRP, derived by fitting Mn $2p_{3/2}$ stacks (70 energies from 630 – 650 eV) to the quantitative OD1 reference spectra of MnO, Mn_3O_4 and MnO_2 (Figure 8.6). Each image is a

color-coded composite of the component maps for MnO (red), Mn_3O_4 (green) and MnO_2 (blue). The R-G-B color intensity scale bars indicate the thickness in nm of each species. The chemical mapping of the **Mn_3O_4-c** sample after VSRP (Figure 8.10 A) and after FSRP (Figure 8.10 B) clearly indicate extensive conversion of the as-synthesized Mn_3O_4 to MnO_2. In contrast, the chemical mapping of the **Mn_3O_4-b** sample after VSRP (Figure 8.10 C) and after FSRP (Figure 8.10 D) indicate a lower degree of conversion of the as-synthesized Mn_3O_4 to MnO_2. The curve fit analysis of the average Mn 2p spectrum of the **Mn_3O_4-c** sample after FRSP (Figure 8.11) indicates a similar amount of MnO_2 and Mn_3O_4 with a very small amount of MnO, consistent with the color-coded composite in (Figure 8.10 B).
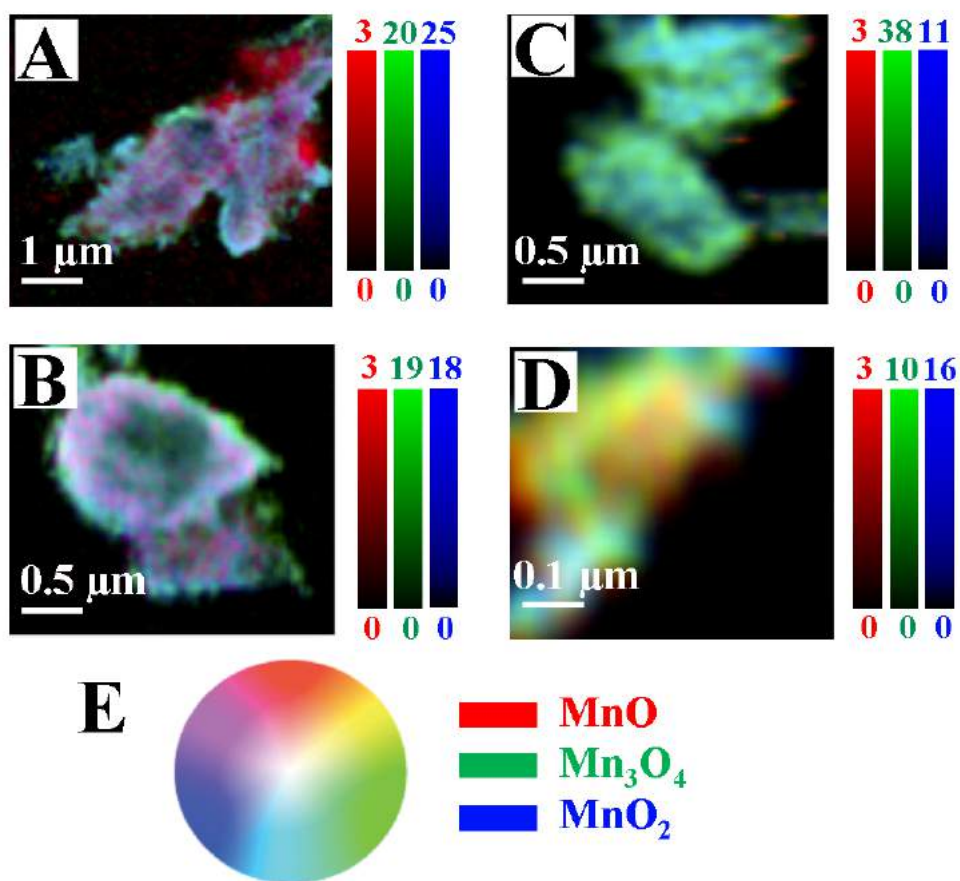
Figure 8.10 Color coded composites of MnO (red), Mn_3O_4 (green) and MnO_2 (blue) chemical maps derived by fitting Mn L_3 stacks. (A) **Mn_3O_4-c** after VSRP. (B) **Mn_3O_4-c** after FSRP. (C) **Mn_3O_4-b** after VSRP. (D) **Mn_3O_4-b** after FSRP. The intensity scale of each species is indicated. (E) Is a color wheel indicating how the color at any pixel indicates a specific combination of the three species.
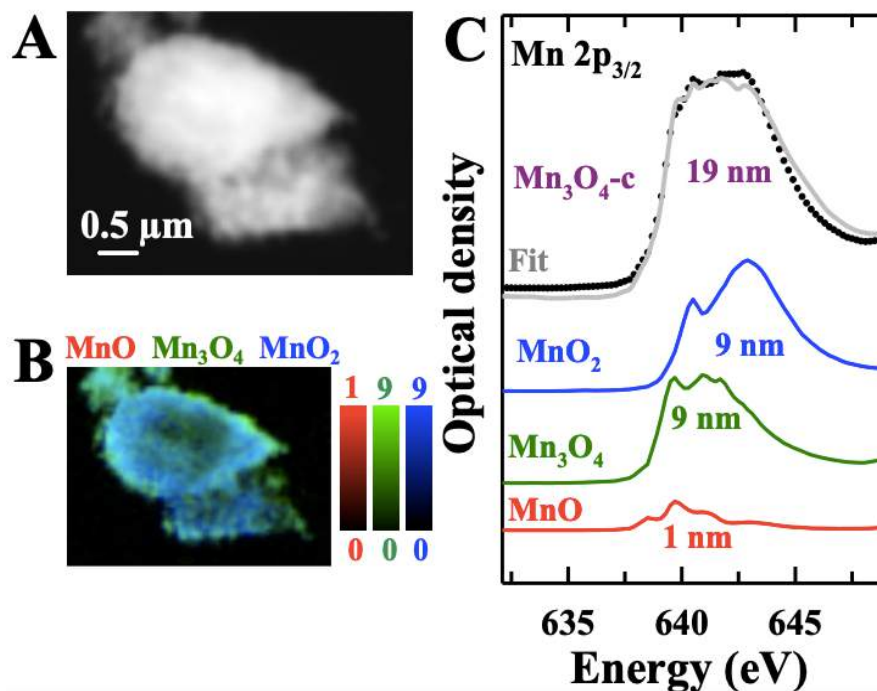
Figure 8.11 Volume fraction determination of the composition of **Mn₃O₄-c** after FSRP. (A) average STXM image of the measured sample. (B) color-coded map in absolute scale. (C) average spectrum (dots) compared to the calculated curve fit (grey) using the area of each component and the average thickness of each component.

Figure 8.12 A and 8.12 B plot the average volume fractions of MnO, Mn_3O_4 and MnO_2 in **Mn₃O₄-b** and **Mn₃O₄-c** after VSRP and FSRP. The relative volume fractions were obtained from the product of the area of each manganese oxide determined by threshold masking the component map (see Figure 8.10 and 8.11) and the average thickness of each species in the masked region. The volume fractions of each Mn component were calculated by ratio-ing the relative fraction of each species to the sum of that for all three species, expressed as a percentage. In this case the analysis shows that in **Mn₃O₄-b** subjected to FSRP, there is almost equal amounts of Mn_3O_4 (green, 46 ± 4 vol %) and MnO_2 (blue, 49 ± 4 vol %) with a small but measurable contribution of MnO (red, 5 ± 1 vol %). The same analysis showed **Mn₃O₄-c** consisted of 57 ± 2 vol % MnO_2 after VSRP and 49 ± 4 vol % after FSRP. In contrast, **Mn₃O₄-b** consisted of only 16 ± 1 vol % MnO_2 after VSRP and 34 ± 2 vol % after FSRP. There was a small amount of MnO in the **Mn₃O₄-c** sample after VSRP (5 ± 1 vol %) and after FSRP (5 ± 1 vol %). In contrast, for **Mn₃O₄-b** the amount of MnO was 2 ± 1 vol % after VSRP and increased to 10 ± 1 vol % after FSRP.
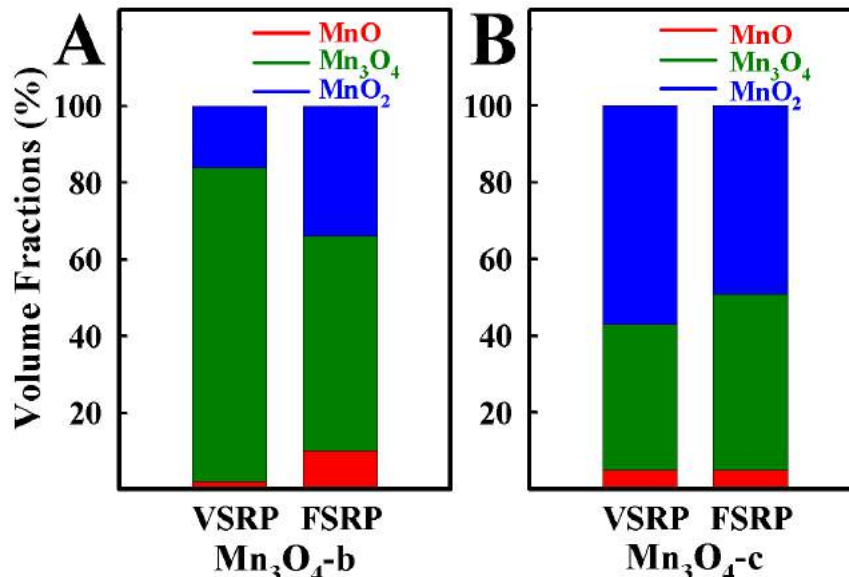
Figure 8.12 Volume fractions of MnO (red), Mn_3O_4 (green) and MnO_2 (blue) evaluated from the area and thickness of each component map (see the Supplemental Information for a description of the method). (A) VSRP and FSRP for **Mn_3O_4-b**. (B) VSRP and FSRP for **Mn_3O_4-c**.

Recently Suktha et al. [41] have estimated the average oxidation state of Mn from Mn K-edge (1s) X-ray absorption spectroscopy of Mn_3O_4 supercapacitors. The morphology of the nano-fibres they studied is quite different from the particulates studied in this work. Despite that, it is interesting to compare the average oxidation state values reported by Suktha et al. [41] to the results of this work. Suktha et al report the average oxidation state after first charge was 2.61 which decreased to 2.51 after the first discharge cycle. Moreover, after stability testing, the average Mn oxidation state decreased to 2.38. This decrease in average oxidation state is explained by reduction of Mn^{3+} to Mn^{2+} followed by extraction of Mn^{2+} from the crystal structure. These results are in reasonable agreement with the results of this study, where reduced (MnO) was found in all samples measured, especially in **Mn_3O_4-b** after FSRP. The as-prepared Mn_3O_4 after VSRP and FSR was significantly oxidized in both the **Mn_3O_4-b** and **Mn_3O_4-c** samples. The average oxidation state for **Mn_3O_4-b** after VSRP was 2.8 ± 0.1 and 3.1 ± 0.1 after FSRP. The average oxidation state of **Mn_3O_4-c** was 3.4 ± 0.1 after VSRP and 3.3 ± 0.1 after FSRP, clearly indicating more oxidation of the Mn_3O_4 in the **Mn_3O_4-c** samples.

The STXM analysis provided additional evidence of the beneficial effect of QC, which adsorbed on MnO_2 and Mn_3O_4 particles during HEBM and prevented their agglomeration. Moreover, QC adsorbed on Mn_3O_4 particles during synthesis and acted as a caping agent, which prevented particle

agglomeration and reduced particle growth. As a result, **MnO₂-b** and **Mn₃O₄-b** showed higher capacitances, compared to **MnO₂-a** and **Mn₃O₄-a**. Moreover **Mn₃O₄-c** electrodes showed significantly higher capacitance compared to that of the **Mn₃O₄-a** and **Mn₃O₄- b** electrodes. The adsorption of QC on MnO_2 and Mn_3O_4 was confirmed by FTIR studies (Fig. S8.6).

8.4 Summary

HEBM resulted in higher capacitances of **MnO₂-b** and **Mn₃O₄-b**, compared to as-prepared **MnO₂-a** and **Mn₃O₄-a**. QC is a promising chelating dispersant for HEBM and capping agent for Mn_3O_4 synthesis. The **Mn₃O₄-c** electrodes showed significantly higher capacitance compared to that of the **Mn₃O₄-a** and **Mn₃O₄-b** samples. The capacitance of **Mn₃O₄-c** was 6.0 F cm^{-2} (149.50 F g^{-1}) for cyclic voltammetry at 2 mVs^{-1} and 8.03 F cm^{-2} (200.93 F g^{-1}) for chronopotentiometry at 3 mA cm^{-2}, which in on par with capacitance of MnO_2. The time-consuming activation procedure, which limits Mn_3O_4 applications, was significantly accelerated for **Mn₃O₄-b** and practically eliminated for **Mn₃O₄-c**. Therefore, **Mn₃O₄-c** is a promising alternative to MnO_2 for the fabrication of HAME with high capacitance and low impedance. Further progress in the development of Mn_3O_4 HAME can potentially result in further improved performance compared to MnO_2, due to the ability to use capping agents for synthesis and to form solid solutions with improved properties. A combination of STXM and electrochemical testing for VSRP and FSRP provided a platform for improved understanding of HEBM and capping agent effects on capacitance increase, charging and activation mechanisms. The STXM results showed that tested materials contained mixtures of Mn^{2+}, Mn^{3+} and Mn^{4+} oxides. The small amount of MnO phase in the tested samples indicated partial reduction. The higher content of MnO_2 phase in the tested Mn_3O_4 prepared using QC as a capping agent (**Mn₃O₄-c**), compared to HEBM Mn_3O_4, correlated with higher capacitance and ability to eliminate the activation procedure. The combination of STXM analysis and electrochemical testing opens an avenue for further progress in the development of Mn_3O_4 and solid solution based HAME by the analysis of phase content of the tested electrodes and the ability to track variations in the oxidation states of ions during testing.

8.5 References

[1] C. Tang, X. Wang, M. Ma, Z. Wang, Y. Li, H. Li, B. Li, Y. Zhang, X. Zhu, Optimizing the electrons/ions diffusion kinetics in δ-MnO_2 for realizing an ultra-high rate-capability supercapacitor, Chemical Engineering Journal 471 (2023) 144784.

[2] H. Zhu, L. Li, M. Shi, P. Xiao, Y. Liu, X. Yan, Coupling of graphene quantum dots with MnO_2 nanosheets for boosting capacitive storage in ionic liquid electrolyte, Chemical Engineering Journal 437 (2022) 135301. https://doi.org/https://doi.org/10.1016/j.cej.2022.135301.

[3] M. Cheong, I. Zhitomirsky, Electrophoretic deposition of manganese oxide films, Surface Engineering 25(5) (2009) 346-352. https://doi.org/10.1179/174329408X281786.

[4] F. Jing, Z. Ma, J. Wang, Y. Fan, X. Qin, G. Shao, Oxygen vacancy inducing phase transition during charge storage in MnOx@ rGO supercapacitor electrode, Chemical Engineering Journal 435 (2022) 135103.

[5] N. Zarshad, A.U. Rahman, J. Wu, A. Ali, F. Raziq, L. Han, P. Wang, G. Li, H. Ni, Enhanced energy density and wide potential window for K incorporated MnO_2@carbon cloth supercapacitor, Chemical Engineering Journal 415 (2021) 128967. https://doi.org/https://doi.org/10.1016/j.cej.2021.128967.

[6] N. Jabeen, Q. Xia, S.V. Savilov, S.M. Aldoshin, Y. Yu, H. Xia, Enhanced pseudocapacitive performance of α-MnO_2 by cation preinsertion, ACS applied materials & interfaces 8(49) (2016) 33732-33740.

[7] J.-G. Wang, F. Kang, B. Wei, Engineering of MnO_2-based nanocomposites for high-performance supercapacitors, Progress in Materials Science 74 (2015) 51-124.

[8] A. Zhang, R. Gao, L. Hu, X. Zang, R. Yang, S. Wang, S. Yao, Z. Yang, H. Hao, Y.-M. Yan, Rich bulk oxygen Vacancies-Engineered MnO_2 with enhanced charge transfer kinetics for supercapacitor, Chemical Engineering Journal 417 (2021) 129186.

[9] P. Cui, Y. Zhang, Z. Cao, Y. Liu, Z. Sun, S. Cheng, Y. Wu, J. Fu, E. Xie, Plasma-assisted lattice oxygen vacancies engineering recipe for high-performing supercapacitors in a model of birnessite-MnO_2, Chemical Engineering Journal 412 (2021) 128676. https://doi.org/https://doi.org/10.1016/j.cej.2021.128676.

[10] R. Chen, M. Yu, R.P. Sahu, I.K. Puri, I. Zhitomirsky, The Development of Pseudocapacitor Electrodes and Devices with High Active Mass Loading, Advanced Energy Materials 10(20) (2020) 1903848. https://doi.org/https://doi.org/10.1002/aenm.201903848.

[11] J. Li, I. Zhitomirsky, Cathodic electrophoretic deposition of manganese dioxide films, Colloids and Surfaces A: Physicochemical and Engineering Aspects 348(1) (2009) 248-253. https://doi.org/https://doi.org/10.1016/j.colsurfa.2009.07.035.

[12] Y. Jeong, A. Manthiram, Nanocrystalline manganese oxides for electrochemical capacitors with neutral electrolytes, Journal of the Electrochemical Society 149(11) (2002) A1419.

[13] R.N. Reddy, R.G. Reddy, Sol–gel MnO_2 as an electrode material for electrochemical capacitors, Journal of Power Sources 124(1) (2003) 330-337.

[14] D. Chen, D. Ding, X. Li, G.H. Waller, X. Xiong, M.A. El-Sayed, M. Liu, Probing the charge storage mechanism of a pseudocapacitive MnO_2 electrode using in operando Raman spectroscopy, Chemistry of Materials 27(19) (2015) 6608-6619.

[15] M. Ghaemi, F. Ataherian, A. Zolfaghari, S.M. Jafari, Charge storage mechanism of sonochemically prepared MnO_2 as supercapacitor electrode: Effects of physisorbed water and proton conduction, Electrochimica Acta 53(14) (2008) 4607-4614. https://doi.org/https://doi.org/10.1016/j.electacta.2007.12.040.

[16] C. Tanggarnjanavalukul, N. Phattharasupakun, J. Wutthiprom, P. Kidkhunthod, M. Sawangphruk, Charge storage mechanisms of birnessite-type MnO_2 nanosheets in Na_2SO_4 electrolytes with different pH values: In situ electrochemical X-ray absorption spectroscopy investigation, Electrochimica Acta 273 (2018) 17-25.

[17] C.R. Arias, C. Debiemme-Chouvy, C. Gabrielli, C. Laberty-Robert, A. Pailleret, H. Perrot, O. Sel, New insights into pseudocapacitive charge-storage mechanisms in Li-birnessite type MnO_2 monitored by fast quartz crystal microbalance methods, The Journal of Physical Chemistry C 118(46) (2014) 26551-26559.

[18] W. Yang, H. Eraky, C. Zhang, A.P. Hitchcock, I. Zhitomirsky, Scanning transmission X-ray microscopy studies of electrochemical activation and capacitive behavior of Mn_3O_4 supercapacitor electrodes, Journal of Materials Chemistry A 10(35) (2022) 18267-18277. https://doi.org/10.1039/D2TA04702K.

[19] A.P. Hitchcock, Soft X-ray imaging and spectromicroscopy, Chapter 22 in Volume II of the Handbook on Nanoscopy, eds. Gustaaf Van Tendeloo, Dirk Van Dyck and Stephen J. Pennycook (Wiley), p 745-791, 2012.

[20] A.P. Hitchcock, Soft X-ray spectromicroscopy and ptychography, Journal of Electron Spectroscopy and Related Phenomena 200 (2015) 49-63.

[21] H. Ade, A.P. Hitchcock, NEXAFS microscopy and resonant scattering: Composition and orientation probed in real and reciprocal space, Polymer 49(3) (2008) 643-675.

[22] A.P. Hitchcock, M.F. Toney, Spectromicroscopy and coherent diffraction imaging: focus on energy materials applications, Journal of Synchrotron Radiation 21(5) (2014) 1019-1030.

[23] J. Stöhr, NEXAFS spectroscopy, Springer Series in Surface Sciences Vol. 25, (Springer, Germany, 1992).

[24] K.T. Arul, H.-W. Chang, H.-W. Shiu, C.-L. Dong, W.-F. Pong, A review of energy materials studied by in situ/operando synchrotron x-ray spectro-microscopy, Journal of Physics D: Applied Physics 54(34) (2021) 343001.

[25] K. Shi, I. Zhitomirsky, Asymmetric Supercapacitors Based on Activated-Carbon-Coated Carbon Nanotubes, ChemElectroChem 2(3) (2015) 396-403. https://doi.org/10.1002/celc.201402343.

[26] J. Schwenke, K. Thanell, I. Beinik, L. Roslund, T. Tyliszczak, Soft/MAX-A new Soft X-ray Microscopy and Coherent Imaging Beamline at the MAX IV Facility, Microscopy and Microanalysis 24(S2) (2018) 232-233.

[27] A.P. Hitchcock, Soft X-ray imaging and spectromicroscopy, Handbook of nanoscopy (2012) 745-791.

[28] A. Kilcoyne, T. Tyliszczak, W. Steele, S. Fakra, P. Hitchcock, K. Franck, E. Anderson, B. Harteneck, E. Rightor, G. Mitchell, Interferometer-controlled scanning transmission X-ray microscopes at the Advanced Light Source, Journal of synchrotron radiation 10(2) (2003) 125-136.

[29] C. Jacobsen, S. Wirick, G. Flynn, C. Zimba, Soft X-ray spectroscopy from image sequences with sub-100 nm spatial resolution, Journal of Microscopy 197(2) (2000) 173-184.

[30] A.P. Hitchcock, Analysis of X-ray images and spectra (aXis2000): A toolkit for the analysis of X-ray spectromicroscopy data, Journal of Electron Spectroscopy and Related Phenomena 266 (2023) 147360.

[31] S. Ching, D.J. Petrovay, M.L. Jorgensen, S.L. Suib, Sol− gel synthesis of layered birnessite-type manganese oxides, Inorganic Chemistry 36(5) (1997) 883-890.

[32] J. Wei, I. Zhitomirsky, Electrosynthesis of manganese oxide films, Surface Engineering 24(1) (2008) 40-46. https://doi.org/10.1179/174329408X271363.

[33] M.M. Kasprzak, A. Erxleben, J. Ochocki, Properties and applications of flavonoid metal complexes, Rsc Advances 5(57) (2015) 45853-45877.

[34] P. Singh, Y. Arif, A. Bajguz, S. Hayat, The role of quercetin in plants, Plant Physiology and Biochemistry 166 (2021) 10-19.

[35] L. Malacaria, J. Bijlsma, R. Hilgers, W.J. de Bruijn, J.-P. Vincken, E. Furia, Insights into the complexation and oxidation of quercetin and luteolin in aqueous solutions in presence of selected metal cations, Journal of Molecular Liquids 369 (2023) 120840.

[36] M. Ata, Y. Liu, I. Zhitomirsky, A review of new methods of surface chemical modification, dispersion and electrophoretic deposition of metal oxide particles, Rsc Advances 4(43) (2014) 22716-22732.

[37] K. Shi, I. Zhitomirsky, Asymmetric Supercapacitors Based on Activated-Carbon-Coated Carbon Nanotubes, ChemElectroChem 2(3) (2015) 396-403.

[38] B. Gilbert, B. Frazer, A. Belz, P. Conrad, K. Nealson, D. Haskel, J. Lang, G. Srajer, G. De Stasio, Multiple scattering calculations of bonding and X-ray absorption spectroscopy of manganese oxides, The Journal of Physical Chemistry A 107(16) (2003) 2839-2847.

[39] B. Toner, S. Fakra, M. Villalobos, T. Warwick, G. Sposito, Spatially resolved characterization of biogenic manganese oxide production within a bacterial biofilm, Applied and environmental microbiology 71(3) (2005) 1300-1310.

[40] M. Risch, D.M. Morales, J. Villalobos, D. Antipin, What X-ray absorption spectroscopy can tell us about the active state of earth-abundant electrocatalysts for the oxygen evolution reaction, Angewandte Chemie International Edition 61(50) (2022) e202211949.

[41] P. Suktha, N. Phattharasupakun, P. Dittanet, M. Sawangphruk, Charge storage mechanisms of electrospun Mn_3O_4 nanofibres for high-performance supercapacitors, RSC advances 7(16) (2017) 9958-9963

Chapter 9

In-situ STXM Studies of MnOx Electrodes Related to Energy Storage Applications

This chapter presents results of several in-situ STXM studies of electrodeposited MnO₂-based electrode materials for energy storage applications (supercapacitors and batteries). It reports the morphology and chemical structure (oxidation state) of the initial electrodeposit and how these change as a function of applied potential and pH. Redox reactions, their reversibility, and the dissolution of Mn^{2+} into the electrolyte are studied. Additionally, the spontaneous reduction of MnO₂ at open circuit potential was investigated at different electrolyte pH.

9.1   Introduction

Manganese oxides have attracted significant attention as a promising electrode material for different energy storage applications. This is due to their high electrochemical performance, low price, low toxicity, and abundant availability (Hu et al., 2018). Furthermore, the impressive electrocatalytic properties of MnO₂ make it a potential alternative electrode to noble metal-based materials such as platinum (Pt), iridium (Ir), and ruthenium, and expensive cobalt (Co) based electrodes (Kwon et al., 2021). Numerous studies have investigated extensively different MnO₂ materials as highly efficient electrodes for lithium-ion batteries (LIBs) (W. Wang et al., 2013) and other secondary batteries such as sodium-ion batteries (SIBs) and zinc-ion batteries (ZIBs). Moreover, MnO₂ is considered one of the most promising electrode materials for supercapacitors. In addition to the advantages of using MnO₂-based electrodes in energy storage applications, MnO₂ is widely used as an electrocatalyst for the oxygen evolution reaction (OER) (Elmaci et al., 2019) and the oxygen reduction reaction (ORR) (Majidi et al., 2019; Zheng et al., 2017).

Despite the excellent theoretical capacitance of MnO₂ (1370 F/g), the highest specific capacitance of actual devices is significantly lower than this value (Parveen et al., 2022; Yu et al., 2011). This performance limitation is due to low electronic conductivity and slow ionic diffusion, in addition to poor structural stability and cycling performance resulting from

reductive dissolution of MnO_2 into water soluble MnO species (Z. Wang et al., 2021; Wei et al., 2011). Nevertheless, the reversibility of the reductive dissolution is still in debate (Jing et al., 2022; Li et al., 2012; Sopčić et al., 2013). More details about the physical properties, electrochemical performance, and challenges of MnO_2 electrode materials are presented in **Chapter 2**. Redox reactions in MnO_2 systems are known to occur between Mn^{4+} and Mn^{3+} species. For instance, in supercapacitors, the redox reaction mainly occurs through the adsorption/desorption or intercalation/deintercalation of protons $[H^+]$ or electrolyte cations $[C^+]$ at the surface or into the bulk of the $MnO_2(IV)$ electrode material to form reduced $MnOOH^+$ and/or $MnOOC^+(III)$species (Tang et al., 2021). In α-MnO_2/Zn-ion batteries, the redox reaction occurs through intercalation/deintercalation of Zn^{2+} into the α-MnO_2 crystal structure to form $ZnMn_2O_4(III)$ redox species (Rubel et al., 2022). As described above and in **Chapter 2**, the dissolution of MnO_2 into an electrolyte, poor cycling performance, and morphological changes may hinder the electrochemical performance of MnO_2 electrode material. For these reasons, different *in-situ* STXM studies were performed to investigate the morphological changes and track oxidation state changes during charging and discharging processes using the developed *in-situ* flow electrochemical device described in **Chapter 4**.

9.2 Experimental Methods

9.2.1 Materials

Analytical grade manganese sulfate ($MnSO_4$), sodium sulfate (Na_2SO_4), sodium hydroxide (NaOH), and sulfuric acid (H_2SO_4) were purchased from Sigma-Aldrich. All reagents were used without further purification. All aqueous solutions were prepared using deionized water with >18 MΩ·cm resistivity.

9.2.2 STXM measurements

Imaging, spectroscopy, and spectromicroscopy measurements were performed using the ambient STXM at the spectromicroscopy (SM) beamline 10ID1 at the Canadian Light Source (CLS, Saskatoon, Canada) (Kaznatcheev et al., 2007). All *in-situ* STXM experiments reported in this chapter were performed using the developed *in-situ* flow electrochemical device described in **Chapter 4**. Spectromicroscopic data in the form of multi-energy image

sequences (stacks (C. Jacobsen et al., 2000)) were measured at X-ray energies from ~10 eV below to ~40 eV above the onset of O 1s and Mn 2p absorption.

9.2.3   *In-situ* electrochemical operation

After mounting the *in-situ* device and connecting the potentiostat, OCP was measured for 60 seconds in all experiments prior to closing the STXM chamber to confirm the stable connection. In all experiments, the OCP is < +100 mV (typically, ~+70 mV), and the fluctuation is ±5 mV. All MnO_2 electrodepositions were performed galvanostatically by operating the potentiostat in chronopotentiometry mode at a fixed current. All redox studies at different applied potentials were conducted using chronoamperometry mode at a fixed potential (**Table 9.1**). All electrodeposition and electrochemical characterizations were performed with a portable EmStat4 potentiostat (PalmSens, Houten, Netherlands). PSTrace 5.8 software was used to run the experiments and automatically record the experimental data.

9.2.4   *In-situ* electrochemical STXM measurements

Five different *in-situ* STXM measurements were performed. **Table 9.1** summarizes the experimental parameters of each run. **Exp-1, Exp-2,** and **Exp-3** were performed to track the morphology and oxidation state changes as a function of applied potentials. **Exp-4** was conducted at different electrolyte pH ($MnSO_4$ pH=4 and Na_2SO_4 pH=8) to understand the reason for spontaneous reduction of MnO_2 at open circuit potential. **Exp-5** was performed to investigate the reversibility of dissoluble Mn^{2+} species. In each of the five experiments, the protocol followed is similar to that indicated in **Section 4.2.8**. First, the *in-situ* electrochemical device was filled manually with 1 M $MnSO_4$ under the optical microscope. After confirming continuous flow and the absence of air bubbles or leakage, the cell was mounted in the STXM and connected via electrical and fluid feedthroughs to the potentiostat and syringe pump, which were external to the STXM tank. After a specific deposition protocol (see **Table 9.1**), a Mn L_3 stack was measured to verify that the electro-deposited material was MnO_2. Then, the electrolyte was changed from $MnSO_4$ to Na_2SO_4 over a period of 15 minutes. During this period, the cell was disconnected from the potentiostat. The electrolyte spectrum was measured to track the decrease in the amount of Mn^{2+} in the (aq) solution. The second inlet channel was opened 2 or 3 times for 30 seconds to reduce the electrolyte thickness.

Table 9.1   Parameters of *in-situ* STXM measurements

In-situ Exp.	Date	Experimental Parameters							
		Electrolyte				Galvanostatic Electrodeposition		Flow µL/hr	Measured Areas	Measured edges
		MnSO$_4$		Na$_2$SO$_4$						
		[ ]$^{(1)}$	pH	[ ]	pH	i (µA)	t/s			
EXP-1	Sep. 2021	0.5	5.2	0.5	6.1	0.1	30	25	WE	Mn L$_{2,3}$[2]
EXP-2	Mar. 2022	0.1	5.2	0.1	6.1	0.1	30	30	WE/CE	Mn L$_3$[3]
EXP-3	Jul. 2022	0.1	5.2	0.1	6.1	0.1	9	5	WE/CE	Mn L$_3$, O K[4]
EXP-4	Jun. 2023	0.1	4.0	0.1	8.0	0.1	30	5	WE/CE	Mn L$_3$, O K
EXP-5	Jun. 2023	0.1	5.2	0.1	6.1	0.1	10	5	WE/CE	Mn L$_3$

(1) [ ]: is the concentration in M (mol/L)
(2) Mn L$_{2,3}$: is stack measured in photon energy range of 625 - 670 eV (75 images).
(3) Mn L$_3$: is stack measured in photon energy range of 625 - 650 eV (54 images).
(4) O K: is stack measured in photon energy range of 525 - 542 eV (45 images).

9.2.4.1 *In-situ* experiment-1 (EXP-1)

In **EXP-1**, MnO$_2$ was deposited on the working electrode (WE) using chronopotentiometry at 0.10 µA for 30 s, using 0.5 M MnSO$_4$ solution as precursor and a flow rate of 25 µL/hr (see **Table 9.1** for summery of conditions for each experiment). After focusing and imaging the cell, a Mn 2p stack was measured on the working electrode (WE) to confirm MnO$_2$ deposition. Then, a two-step protocol was used to replace the MnSO$_4$ solution with a 0.5 M sodium sulphate (Na$_2$SO$_4$) solution. First, the bulk of the electrolyte in the second inlet channel was replaced manually using a 1 mL plastic syringe. Then the second channel was closed, and the plastic syringe was filled with the Na$_2$SO$_4$ electrolyte and placed into the syringe pump operated at a fast flow rate (50 µl/h) to push the fluid into the cell. After changing the electrolyte, Mn L$_{2,3}$ stacks were measured at open circuit potential (OCP) and while applying successive fixed potentials in chronoamperometric scans at 0.0, +0.1, +0.2, +0.3, +0.4 and +0.5V$_{Au}$.

9.2.4.2 *In-situ* experiment-2 (EXP-2)

In **EXP-2**, MnO_2 was deposited on the WE using chronopotentiometry at 0.10 µA for 30 seconds using 0.1 M $MnSO_4$ as precursor and a flow rate of 30 µL/hr. After confirming the deposit was MnO_2, the electrolyte was replaced with 0.1 M Na_2SO_4 and the syringe pump was operated at 30 µL/h. Mn L_3 stacks were performed on both working electrode (WE) and counter electrode (CE) regions over the photon energy range of 625 to 650 eV at OCP and at sequential fixed potentials in chronoamperometric scans at -0.3, -0.2, -0.1, 0.0, +0.1, +0.3 and +0.5 V_{Au}.

9.2.4.3 *In-situ* experiment-3 (EXP-3)

In **EXP-3**, galvanostatic deposition of MnO_2 on the WE was performed from 0.1 M $MnSO_4$ solution. In order to avoid a thick deposition and thus Mn 2p spectral saturation, the deposition was performed in two steps, first at 0.1 µA for 2 s and then at 0.1 µA for 7 s. The corresponding potential during both depositions was +1.1V_{Au}. After focusing and imaging the cell, Mn L_3 and O K stacks were measured on regions of the WE and CE. After confirming the deposition of MnO_2, the 0.1 M $MnSO_4$ solution was replaced with 0.1 M Na_2SO_4 purged with N_2 gas using a 1 mL plastic syringe. A flow rate of 5 µL/h was used. Stacks were measured at different applied potentials. First, a Mn L_3 stack was measured without connecting the potentiostat and then at open circuit potential (OCP) after connecting the potentiostat but without applying a potential. The measured OCP was 65 ± 10 mV_{Au}. Then, Mn L_3 and O K stacks were measured chronoamperometrically while applying successive fixed potentials of +0.1, +0.3, +0.5, +0.7 and +0.9 V_{Au}. After returning the electrochemical state to OCP, Mn L_3 and O K stacks were performed, followed by measurements at -0.1, -0.3, and -0.5 V_{Au} and finally, again at OCP. Since the most reliable results were obtained from **EXP-3** (due to minimal absorption saturation), a schematic diagram for the sequence of steps in **EXP-3** is presented in **Figure 9.1.**

9.2.4.4 *In-situ* experiment-4 (EXP-4)

In **EXP-4**, MnO_2 was deposited galvanostatically from 0.1 M $MnSO_4$ at 0.1 µA for 30 s (see **Table 9.1** for details). After confirming the deposition is MnO_2, the 0.1 M $MnSO_4$ electrolyte (pH=5.2) was changed to 0.1 M $MnSO_4$ (pH=4) after adjusting the pH using 0.01M

H_2SO_4. A Mn L_3 stack was measured on a region of the WE at OCP. After that, the electrolyte was changed again from 0.1 M $MnSO_4$ electrolyte (pH=4) to 0.1 M Na_2SO_4 (pH=8) (pH was adjusted using 0.01M NaOH). After changing the electrolyte, a Mn L_3 stack was measured at OCP (+75 mV_{Au}). The applied potential was increased to +0.7 V_{Au} in order to oxidize the reduced Mn^{2+}/Mn^{3+} species back to MnO_2. Then, a Mn L_3 stack was measured at OCP again. To verify the electrolyte exchange in this experiment, the pH of the exit fluid from the second inlet channel was measured each time the electrolyte was changed. The measured pH was pH=4 when the electrolyte was changed to 0.1M $MnSO_4$ (pH4), and pH=8 when the electrolyte was changed to 0.1M Na_2SO_4 (pH8). The pump was operated at a flow rate of 50 µL/h for 30 min to ensure the electrolyte replacement inside the microchips.

9.2.4.5 *In-situ* experiment-5 (EXP-5)

In **EXP-5**, MnO_2 was deposited galvanostatically on the WE from 0.1 M $MnSO_4$ at 0.1 µA for 10 s (see **Table 9.1** for details). After confirming the deposition is MnO_2, the electrolyte was changed from 0.1 M $MnSO_4$ to 0.1 M Na_2SO_4. After that, Mn L_3 stacks were measured on WE and CE regions at OCP and at different applied oxidative and reductive potentials: -0.2, -0.3, +0.4, -0.2 and +0.4 V_{Au}. This experiment was conducted to investigate the extent of reversibility of reductive dissolution of MnO_2 to form Mn^{2+}(aq) species in the electrolyte, and subsequently leading to deposition of MnO_2 on the CE.
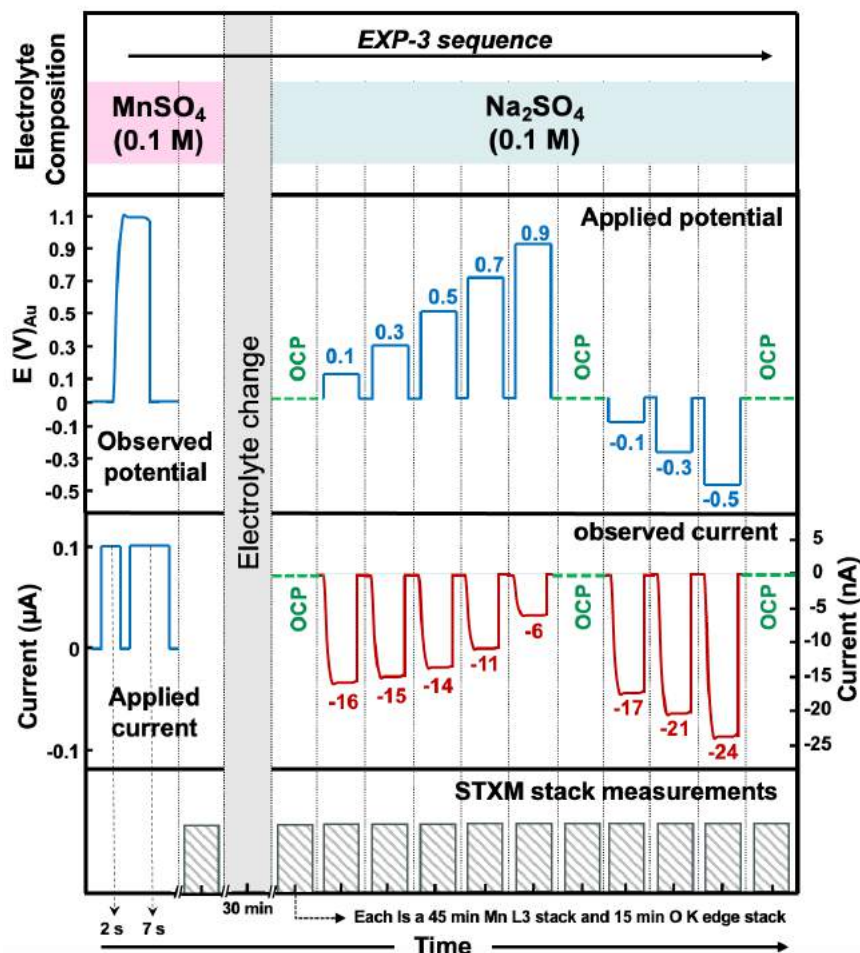
Figure 9.1 Schematic of the typical sequence of steps in the *in-situ* STXM **EXP-3** measurements.

9.3   Results

9.3.1   *In-situ* MnO₂ deposition: morphology and spectroscopy

Figure 9.2 presents images and chronopotentiometry traces from the electrodeposition of MnO₂ in **EXP-3**. **Figure 9.2A** shows a STXM transmission image of the full silicon nitride (SiN$_x$) window of the *in-situ* device prior to the electrodeposition. The gold working (WE) and counter electrodes (CE) are clean. **Figure 9.2B** presents the chronopotentiometric plots of the 2-stage electrochemical deposition (0.1 µA for 2s, then 7s). The MnO₂ film was electrochemically deposited onto the WE according to the following reaction (Devaraj & Munichandraiah, 2009; Hem, 1963):

189

$$Mn^{2+}(aq) + 2H_2O(aq) \rightarrow MnO_2(s) + 4H^+ + 2e^- \qquad \textbf{Eq. 9.1}$$
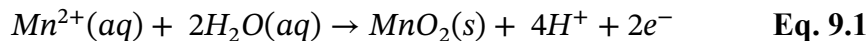
At the same time, reduction occurred at the counter electrode (CE) as follows:

$$2H^+ + 2e^- \rightarrow H_2 \qquad\qquad \textbf{Eq. 9.2}$$

Figure 9.2C presents a STXM image of the WE after the galvanostatic deposition. **Figure 9.2D** presents a rescaled color-coded composite of the MnO, Mn$_2$O$_3$, and MnO$_2$ component maps derived from the Mn L$_3$ stack measured at OCP (+80 mV$_{Au}$). The deposited film did not cover some areas of the WE, which may be due to patches of impurities on the Au electrode surface. In the areas where the deposit occurred, the film is relatively uniform, with an average thickness of 15 ± 2 nm. The CE was imaged after the electrodeposition in **EXP-2** and **EXP-3** measurements, but no deposition was observed.
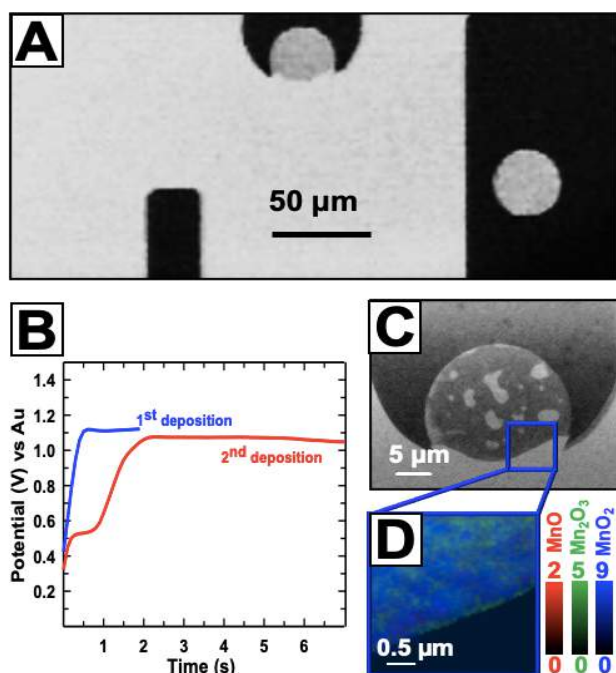
Figure 9.2 *In-situ* **MnO₂ electrodeposition (EXP-3). (A)** STXM image of the flow electrochemistry cell at 640 eV before the galvanostatic deposition. **(B)** Chronopotentiometric plot of the electrochemical deposition (galvanostatic at 0.1 μA for 2s then 7 s from 0.1 M MnSO₄(aq). **(C)** STXM image of WE at 640 eV after the galvanostatic deposition. **(D)** color coded composite of quantitative MnO, Mn₂O₃ and MnO₂ component maps after the electrodeposition of MnO₂ derived by fitting the Mn L₃ stack.

Figure 9.3 presents the average Mn L_3 (**Fig. 9.3A**) and O K (**Fig. 9.3B**) spectra of the electrodeposit and that of the electrolyte (**Fig. 9.3C**). The average Mn L_3 spectrum of the as-deposited film is dominated by the MnO_2 contribution, although it also contains features from lower oxidation state species, in particular Mn_2O_3. Although the O K-edge region is dominated by the spectrum of the aqueous electrolyte (which is heavily absorption saturated), water is X-ray transparent between 524 and 532 eV, the region of the O $1s \rightarrow 3d$ transitions of the Mn oxides. In this region (**Fig. 9.3B**), the O1s spectra of the electrodeposited MnOx exhibit a sharp peak at 529.6 eV, which is characteristic of MnO_2.
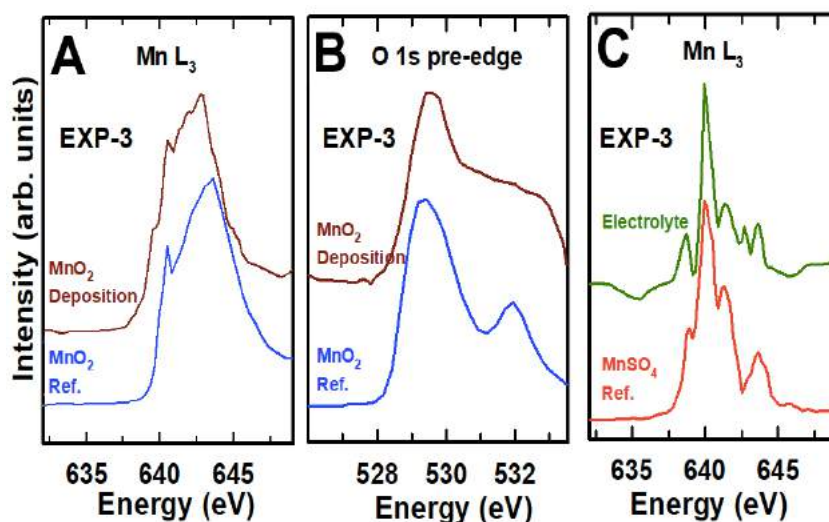
Figure 9.3   Analysis of the EXP-3 electro-deposition. (A) Average Mn L_3 spectrum of the galvanostatic deposit, compared to the reference spectrum of MnO_2 (Chapter 6). **(B)** O K-edge spectrum of the galvanostatic deposit, compared to that of pure MnO_2 (Chapter 6), The signal above 532 eV is heavily distorted by absorption saturation from the electrolyte. **(C)** Mn L_3 spectrum of the electrolyte compared to that of $MnSO_4$ (see **Chapter 6** for reference spectroscopy).

The Mn 2p spectromicroscopy measured after the electrodeposition performed in **EXP-1** and **EXP-2** confirmed the formation of MnO_2 on the WE, as presented in **Fig. 9.4A (a-d)** and **Fig. 9.4B (a-d)**. However, in both of those experiments, the Mn L_3 signal was significantly absorption saturated because the electrolyte layer in each case was too thick (~4 $\pm$ 0.2 μm in **EXP-1** (**Fig. 9.5A**) and ~3.6 μm in **EXP-2** (**Fig. 9.5B**). The electrolyte thickness in **EXP-3,** averaged over 5 measurements, was ~2.6 $\pm$ 0.2 μm, as shown in **Fig. 9.5C.**
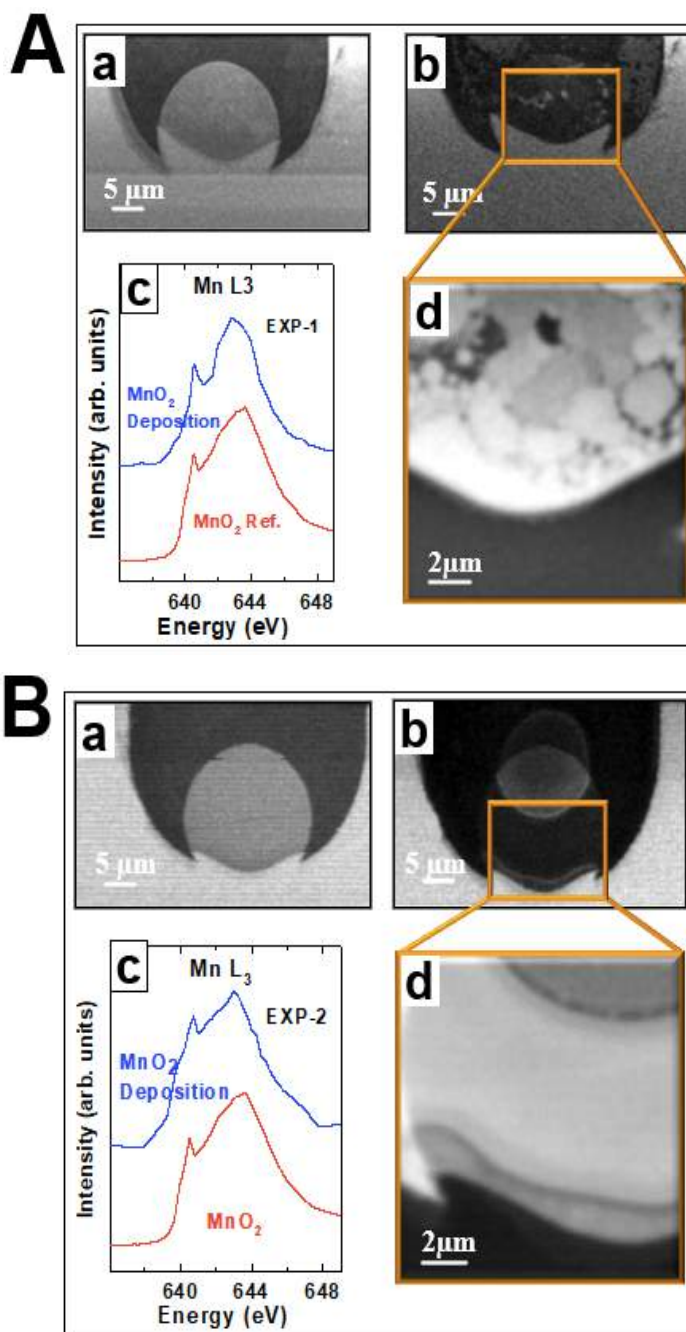
Figure 9.4   MnO₂ deposition performed in (A) EXP-1, **(B)** EXP-2. a), b) and d) STXM image of the *in-situ* cell window at 640 eV before and after the galvanostatic deposition, respectively, c) Mn L_{23} or Mn L_3 absorption spectra extracted from stack measured at WE after galvanostatic deposition, d) magnification of the measured region of WE area.
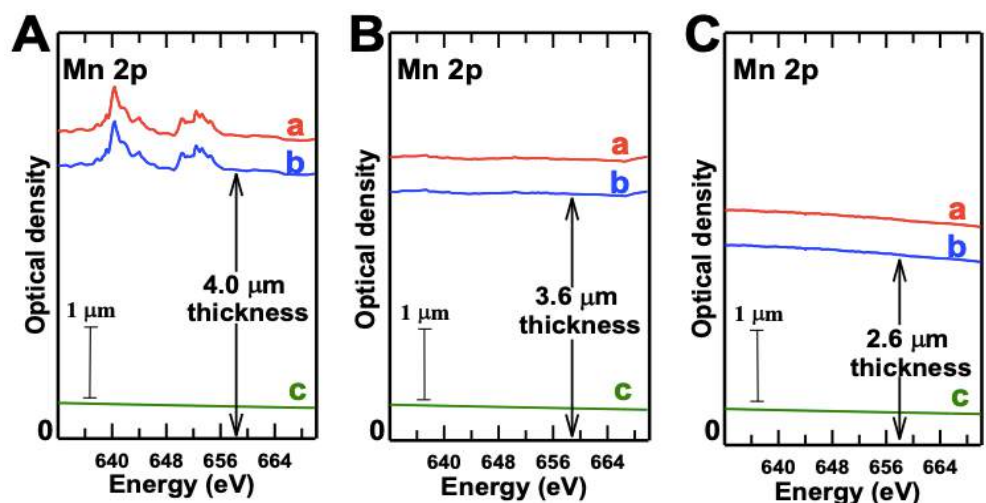
Figure 9.5   Electrolyte thickness measurement in (A) EXP-1 (measured in MnSO$_4$). **(B)** EXP-2 (measured in Na$_2$SO$_4$) and **(C)** EXP-3 (measured in Na$_2$SO$_4$). a) refer to electrolyte spectra OD (red), b) refer to electrolyte spectra OD after subtracting the Si3N4 window OD (blue), and c) SiNx window OD (150 nm thick) (green).

9.3.2   *In-situ* MnO$_2$ at different applied potentials: morphology and spectroscopy

After changing the electrolyte in **EXP-1** from 0.5 M MnSO$_4$ to 0.5 M Na$_2$SO$_4$, Mn L$_{2,3}$ stacks of the WE were measured at OCP (+ 90 mV$_{Au}$) and at applied potentials of 0.0, +0.1, +0.2V, +0.3, +0.4 and +0.5 V$_{Au}$. The Mn L$_{2,3}$ spectra of the WE at OCP and at all applied potentials (**Fig. 9.6A**) exhibit the typical Mn 2p features of MnO$_2$, with a sharp peak at 640.7 eV and broad peak at 642.9 eV, with no significant evolution in spectral shape over the sequence of potentials. Owing to the thickness of the MnO$_2$ deposit (approximately 40 nm), its low electronic conductivity (Wang et al., 2015), and poor cation diffusivity in bulk MnO$_2$ (Cao et al., 2015)ʼ (Ma et al., 2021), it is possible that the Mn 2p spectra of the deposited layer is dominated by the bulk MnO$_2$ signal even if reduced Mn species (Mn^{3+} or Mn^{2+}) were formed at the surface of the deposited film. In addition, the morphology of the measured WE area significantly changed during the oxidation measurements. A continued growth of Mn oxide species on the WE was observed during the stack performed at +0.5 V$_{Au}$. Moreover, the electrolyte layer in **EXP-1** was relatively thick (4.0 ± 0.2 µm), which also increased the absorption saturation and reduced the sensitivity to other Mn oxide species.
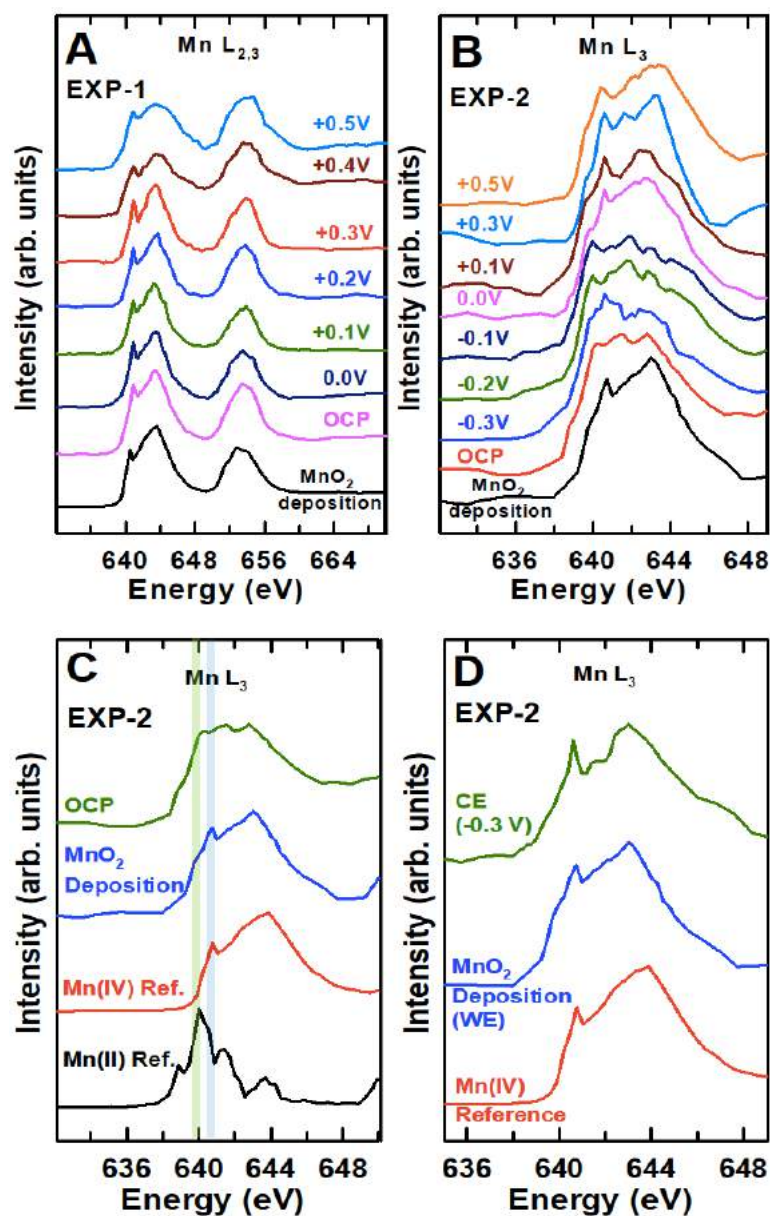
Figure 9.6 *In-situ* **spectroscopy of Mn oxides modified electrochemically in EXP-1 and EXP-2 at different applied potentials. (A)** Mn L_{23} absorption spectra of WE measured in EXP-1. **(B)** Mn L_3 absorption spectra of WE measured in EXP-2. **(C)** Mn L_3 absorption spectrum of WE after MnO_2 deposition in EXP-3 compared to the spectra of MnO_2 and MnO reference compounds (Chapter 6). **(D)** Mn L_3 absorption spectrum of the CE measured at -0.3 V_{Au} in EXP-3 in comparison to the spectrum of the MnO_2 deposit on the WE and MnO_2 reference spectrum.

In order to improve the sensitivity to electrochemical changes, **EXP-2** was performed using 0.1M $MnSO_4$ and 0.1M Na_2SO_4 instead of the 0.5 M concentrations used in **EXP-1**. Also, negative potentials were applied first (-0.1, -0.2, and -0.3 V_{Au}) before applying positive potentials (0.0, +0.1, +0.3, and +0.5 V_{Au}). Mn L_3 stacks were measured on both WE and CE at each potential. **Figure 9.6B** presents Mn L_3 spectra extracted from stack measurements performed on the WE at these applied potentials. Relative to the spectrum of the as-deposited material, with $MnSO_4$ electrolyte present, the Mn L_3 spectrum measured at OCP showed considerable change in the spectral shape – in particular, a -0.5 eV shift of the first sharp L_3 peak to a position that is consistent with Mn^{2+}, as shown in **Fig. 9.6C**. The Mn L_3 spectra at -0.3, -0.2, and -0.1V_{Au} systematically showed an increase in the intensity of first Mn^{2+} L_3 peak, compared to its intensity in the Mn L_3 spectrum of the as-deposited MnO_2. These observations are consistent with a partial reduction of Mn^{4+} to Mn^{2+}/Mn^{3+}. By reversing the applied potentials to positive values (0.0 V_{Au} → +0.5V_{Au}), the Mn L_3 spectra showed a gradual conversion in both spectral shape and peak positions back to that of MnO_2, corresponding to oxidation of Mn^{2+}/ Mn^{3+} to Mn^{4+}. Although we decreased the concentrations of $MnSO_4$ and Na_2SO_4 to 0.1 M, all the measured spectra exhibited significant absorption saturation, which is associated with the thick electrolyte layer (3.6 ± 0.2 μm). **Figure 9.6D** shows Mn L_3 spectra extracted from stacks performed on CE at -0.3 V_{Au}. The measured spectrum is characteristic of MnO_2, as indicated by comparison to the as-deposited spectrum and the reference spectrum of MnO_2. The spectra measured at different potentials on the CE also showed absorption saturation (not presented).

The results of **EXP-1** and **EXP-2** show that the Mn L_3 spectra are distorted by absorption saturation if the electrolyte layer is thicker than 3 μm. Moreover, due to the need for higher sensitivity to surface changes, depositing thinner MnO_2 film is crucial. The microfluidic cell used in **EXP-3** was prepared using a 500 nm rather than a 1000 nm spacer (F-Chip) (see **Section 4.2.3**), which resulted in a thinner electrolyte layer, which was determined from the total absorption spectrum to be 2.6 ± 0.2 μm (**Fig. 9.5C**). Additionally, the galvanostatic deposition was conducted for only 9 seconds (**Fig. 9.2**) instead of 30 seconds, as used in **EXP-1** and **EXP-2**. These experimental conditions resulted in lower absorption

saturation and, thus, more trustworthy spectroscopic and microscopic measurements. Therefore, from this point on, only results from **EXP-3** are discussed.

After changing the electrolyte from 0.1M $MnSO_4$ to 0.1 Na_2SO_4 in **EXP-3**, Mn L_3 and O K stacks were measured on the WE and CE at OCP and at five positive applied potentials ($+0.1$ to $+0.9$ V_{Au} in $+0.2$ V steps), followed by measurements at OCP, then three applied potentials from -0.1 to -0.5 V_{Au} (in -0.2 V steps), and finally at OCP. **Figure 9.7A** plots the current as a function of time for all applied potentials during stack measurements. **Figure 9.7B** presents the observed current as a function of the applied potential (the current response showed fluctuations of ± 5 nA). **Figure 9.7C** presents the average of the 75 stack images after MnO_2 deposition. The dotted blue line shows the thin region where spectra in **Fig. 9.8** are extracted.
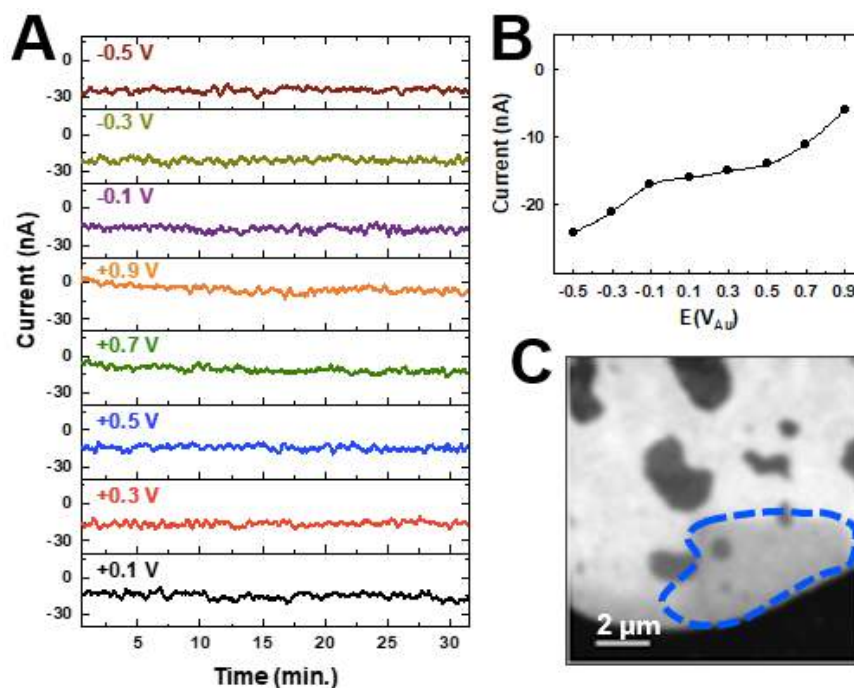
Figure 9.7   Chronoamperometric plot during stack measurements at different applied potentials. (A) current versus time. **(B)** current versus applied potential. **(C)** average stack image after MnO_2 deposition, the dashed area indicates a thin region used to track spectral features changes as a function of applied potential.
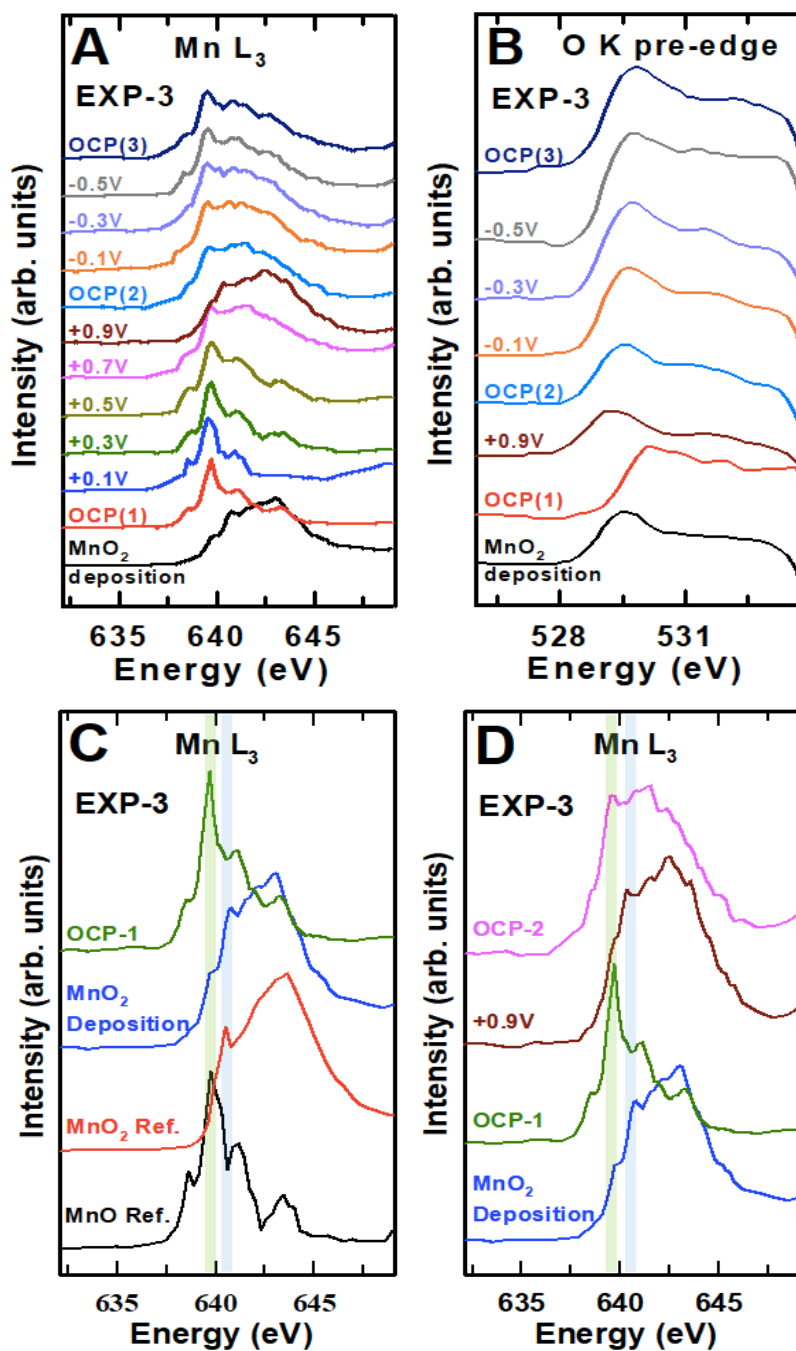
Figure 9.8   *In-situ* **spectroscopy of Mn oxides modified electrochemically in EXP-3. (A)** Mn L_3 and **(B)** O K absorption spectra of the WE region at different applied potentials. **(C)** Mn L_3 absorption spectra of WE region measured after MnO_2 deposition (in $MnSO_4$) and at first OCP measurement (after changing the electrolyte from $MnSO_4$ to Na_2SO_4) compared to MnO_2 and MnO reference spectra. **(D)** Mn 2p (L_3) absorption spectra of the WE after MnO_2 deposition, at +0.9 V_{Au}, and at first and second OCP measurements.

The Mn L_3 and O K pre-edge spectra extracted from all stack measurements performed on the WE are presented in **Fig.9.8A** and **9.8B**, respectively. *At the very first measurement at OCP, the Mn L_3 spectrum was very different from that of the deposited MnO_2 film*. The measurement at OCP was performed while the potentiostat was disconnected and after connecting the potentiostat under OCP measurement conditions (+65 mV$_{Au}$). Both measurements indicate the same spectral shape and peak positions. **Figure 9.8C** presents the Mn L_3 spectra measured directly after the electrochemical deposition from $MnSO_4$ compared to that after changing the electrolyte from $MnSO_4$ to Na_2SO_4 (with the potentiostat disconnected). The dramatic change in the Mn L_3 spectrum (**Fig. 9.8C**) indicates that <u>most</u> of the MnO_2 deposited film was reduced to a mixture of Mn^{2+}/Mn^{3+} over a period of 20 m, as the overlying electrolyte was changed from 0.1 M $MnSO_4$ (pH = 5.2) to 0.1 M Na_2SO_4 electrolyte (pH = 6.1), <u>without applying any potential</u>. This spectroscopic change was also observed in **EXP-2, EXP-4,** and **EXP-5**. However, the reaction (Moon et al., 2021):

$$MnO_2(s) + 2H^+(aq) + 2e^- \rightarrow Mn^{2+}(aq) + 2OH^-(aq) \qquad \textbf{Eq. 9.3}$$
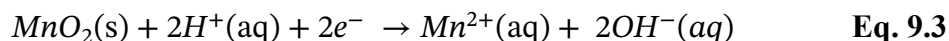
is <u>thermodynamically unfavorable in neutral media.</u> Further details of this observation, and possible interpretations, are deferred to the **Section 9.4.1**.

When an increasingly positive potential was applied (+0.1 to +0.9 V$_{Au}$), the Mn^{2+} on the WE gradually converted to Mn^{4+} (**Fig. 9.8A**). The spectrum measured at +0.9 V$_{Au}$ exhibited the typical Mn L_3 features of MnO_2, with the characteristic sharp peak at 640.4 eV. This indicates re-oxidation of Mn^{2+} to Mn^{4+} as described in **Eq. 9.1**. **Figure 9.8D** presents the Mn L_3 spectra at the first and second OCP measurements, compared to the spectrum of the as-deposited MnO_2 and the spectrum at +0.9V$_{Au}$. The spectrum at the second OCP indicates a mixture of Mn^{2+}/Mn^{3+} oxidation states. These results confirm that oxidation occurred at +0.9 V$_{Au}$ and reduction occurred at the first and second OCP stages. Overall, the spectroscopy is consistent with reduction of the Mn^{4+} to Mn^{2+}/Mn^{3+} at the first OCP condition, followed by forced oxidation back to Mn^{4+} at +0.9 V$_{Au}$, and then reduction of the Mn^{4+} back to a mixture of Mn^{2+}/Mn^{3+} at the second OCP condition.
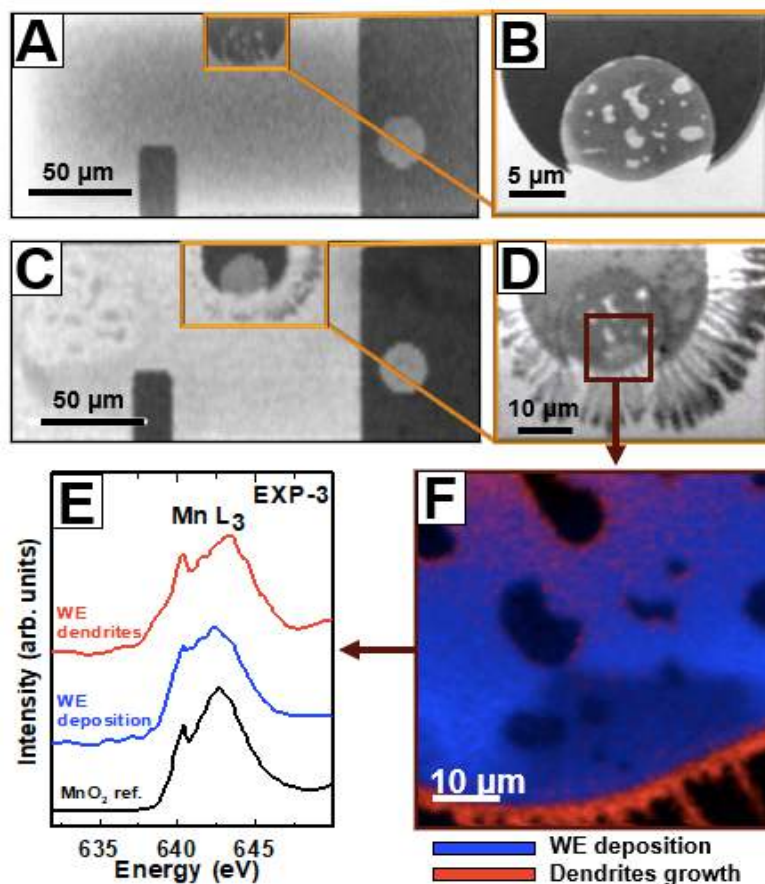
Figure 9.9   Dendritic growth of MnO₂ at +0.9 V_{Au} (EXP-3). 640 eV STXM image of the full flow cell window at **(A)** first OCP and **(C)** +0.9 V_{Au} measurements. STXM images of WE region at 640 eV at **(B)** first OCP and at **(D)** +0.9 V_{Au} measurements. **(E)** Mn L₃ absorption spectra of the deposit on the surface and the dendritic growth at +0.9 V_{Au} compared to the spectrum of MnO₂. **(F)** color-coded map of the initial MnO₂ deposition and the dendrite growths derived by fitting internal spectra extracted from the blue region (initial MnO₂ deposition) and the red region (dendrite growths).

Interestingly, at +0.9 V_{Au}, there was a very large change in the morphology of the MnO₂ film at the WE. This phenomenon is consistent with the MnO₂ morphology changes observed in all experiments (**EXP 1- 5**). At +0.9 V_{Au}, the deposit in **EXP-3** has a patchy coverage of the WE (**Fig. 9.9A** and **Fig. 9.9B**) and a distinct dendritic structure (**Fig. 9.9C** and **Fig. 9.9D).** The Mn L₃ absorption spectra extracted from the stack measured at +0.9 V_{Au} indicate that the

dendrites are MnO_2, as presented in **Fig. 9.9E**. **Figure 9.9F** presents a color-coded composite of the component maps of initial MnO_2 deposition (blue) and the dendrites (red) derived by fitting the measured Mn L_3 stack at +0.9 V_{Au} to internal spectra extracted from dendrite growth and working electrode region. This confirms that, during the measurements, Mn^{2+} in the electrolyte was electro-oxidized onto the WE as MnO_2. The dendrite growth occurred only after applying the potential of +0.9 $V_{Au.}$

Figure 9.10A presents the O K-edge spectra in the region of O 1s → 3d transitions of the deposited MnO_2 after changing the electrolyte to Na_2SO_4 at the first OCP measurement compared to the O K spectrum of MnO_2 and MnO (**Chapter 6**) and the spectrum of the deposit on the WE in $MnSO_4$ (before changing the electrolyte). The O K-edge spectrum at OCP is very different from that of the initially deposited material, measured while the electrolyte was still $MnSO_4$. The initial deposit is MnO_2, whereas the spectrum measured under the first OCP conditions is consistent with the deposit being in a reduced form of Mn^{2+}/Mn^{3+} species. The changes in the O K-edge spectra are consistent with the Mn L_3 measurements reported in **Fig. 9.8**. The O 1s → Mn 3d transition of the deposited MnO_2 and at OCP occurs at 529.5 eV and 530.1 eV, respectively, indicating a shift of 0.6 eV. Furthermore, the O K spectra at +0.9V_{Au} showed a -0.3 eV shift compared to the first OCP spectra, while the extracted spectrum at the second OCP showed an opposite shift of + 0.5 V compared to spectra at +0.9 V_{Au} as presented in **Fig. 9.10A**. The chemical changes indicated from the O K spectral measurements **(Fig. 9.10B)** agree with those deduced from the Mn L_3 measurements, indicating oxidation at +0.9V and reduction at OCP, respectively.
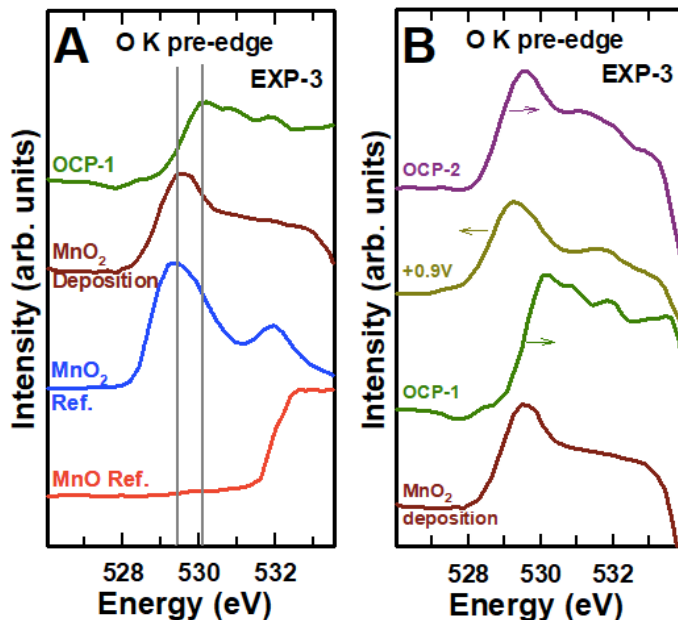
Figure 9.10 O K-edge spectra of WE in Exp-3. (A) O K-edge spectrum of the WE after electrodeposition and at first OCP measurement, compared to the O K-edge reference spectrum of MnO and MnO_2 (Chapter 6). **(B)** O K-edge spectrum of the WE at +0.9 V_{Au}, and first and second OCP measurements, compared to that of MnO_2.

The Mn L_3 spectra extracted from the thin region illustrated in **Fig. 9.7C** at different applied potentials showed gradual shifts to higher energy when the applied potential was increased from +0.1 to +0.9 V_{Au}, indicating oxidation from Mn^{2+} to Mn^{4+}. On the other hand, after applying negative potentials (-0.1 → -0.5 V_{Au}), the intensity of the sharp peak at 639.8 eV indicative of Mn^{2+} gradually increased. **Figure 9.11A** and **9.11B** present average Mn L_3 STXM image and quantitative component maps of MnO, Mn_2O_3, and MnO_2 derived from a stack measured at -0.5 V_{Au} on the WE area. **Fig. 9.11(C-E)** presents the component map of each Mn species. The intensity grey scales indicate the thickness in nm of each component. **Figure 9.11F** presents the internal Mn L_3 absorption spectrum extracted from the thin region (**Fig. 9.7C**) of the same stack measurement in comparison to the spectra of pure MnO, Mn_2O_3, and MnO_2 (**Chapter 6**). The measured spectrum showed Mn L_3 peaks at 639.8 eV (MnO) and 643.5 eV (Mn_2O_3). Both the quantitative chemical maps and the measured absorption spectra indicate partial reduction of MnO_2 to Mn^{2+} and Mn^{3+} at negative applied potentials.
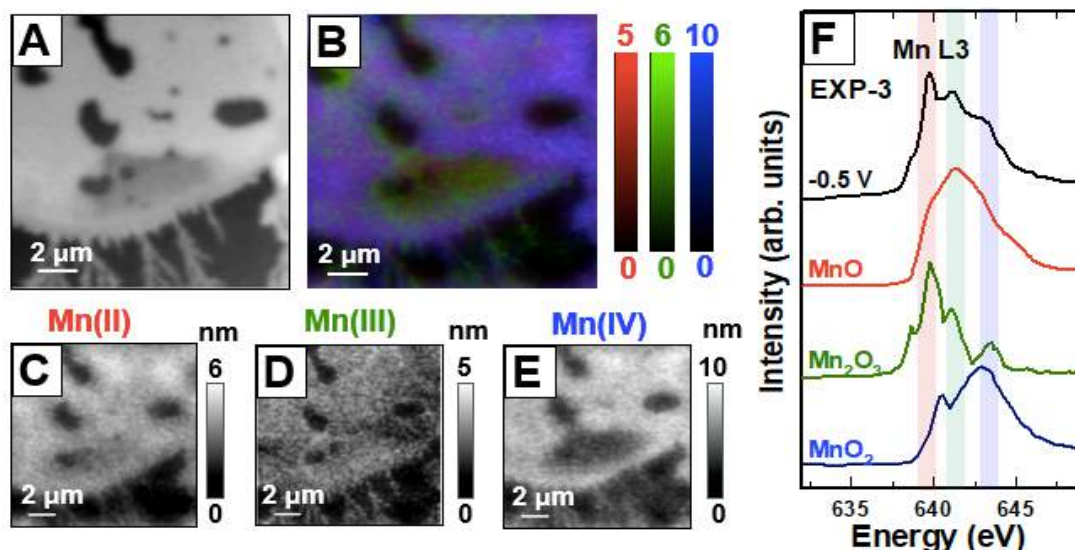
Figure 9.11 Component maps and spectra at -0.5 V_{Au} of the electrochemically modified deposit in EXP-3. (A) average STXM image of Mn L_3 stack at -0.5 V_{Au}. **(B)** color coded composite of the quantitative component maps of MnO, Mn_2O_3 and MnO_2 derived from the stack. **(C-E)** component map of each Mn species. **(F)** Comparison of the Mn L_3 spectrum of the WE to the spectra of MnO, Mn_2O_3 and MnO_2.

Although MnO_2 (s) is insoluble, when it is reduced, the reduced oxide species (MnO) can dissolve. (Chen et al., 2017) Imaging and Mn L_3 stacks were measured at the CE at different applied potentials to investigate the possible oxidation of dissolved Mn^{2+} to form MnO_2 on the CE, which may occur if there is a reduction dissolution of MnO_2 at the WE. STXM images of the thin region of the CE (averaged over all energies of Mn L_3 stacks) measured at all applied potentials are shown in **Fig. 9.12(A-K)**. Mn oxide species started to deposit on the CE at -0.5 V_{Au}. **Figure 9.13A** presents the Mn L_3 absorption spectra of those deposits (**Fig. 9.12J** and **K**) compared to MnO, Mn_2O_3, and MnO_2 reference spectra. The Mn L_3 spectra of the Mn species deposited on CE at -0.5V_{Au} exhibited a sharp peak at 640.4 eV, indicating an Mn(IV) species, likely MnO_2.
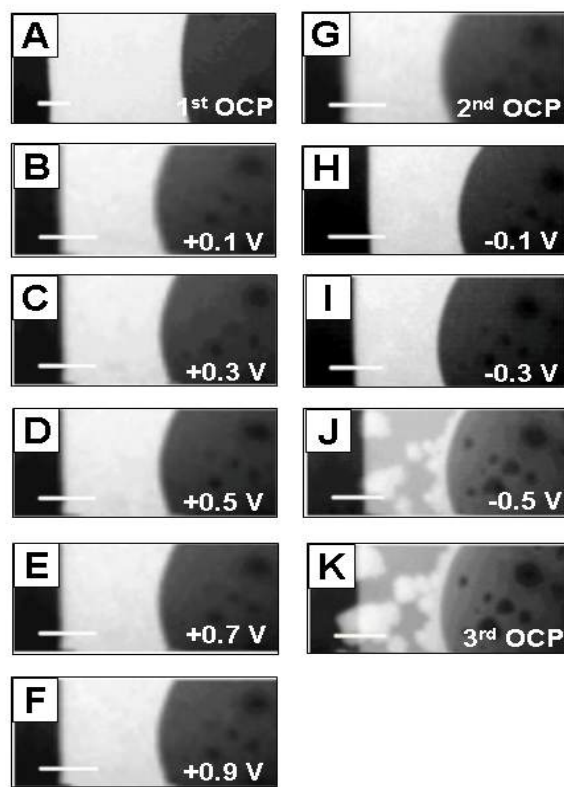
Figure 9.12 STXM transmission images of the CE at 640 eV in Exp-3 at various potentials. **(A- K)** Average STXM images of the CE at different applied potentials. Scale bar is 5 μm.

The deposits at the CE are the product of electrochemical oxidation of Mn^{2+}(aq) to form electrodeposited MnO_2. This oxidation occurs in conjunction with reductive dissolution of MnO_2 (s) to Mn^{2+}(aq) at the WE. The Mn L_3 spectrum of the deposit on the CE at the third OCP (after applying -0.5 V_{Au}) showed partial conversion of MnO_2 to a mixture of MnO and Mn_2O_3 compared to the measurement at -0.5 V_{Au}, which is consistent with the reduction of MnO_2 to MnO/Mn_2O_3 in neutral Na_2SO_4 electrolyte at OCP. The O 1s → Mn 3d features in the O K-edge spectrum of the CE at the third OCP (**Fig. 9.13B**) shifted to higher energy (+0.25 eV) compared to the position of the O K pre-edge peak measured at -0.5 V_{Au}. Moreover, the STXM image of the CE at the third OCP (**Fig. 9.12K**) indicates more deposition compared to that at -0.5 V_{Au}, which may be attributed to increases in the amount of Mn^{2+}(aq) in the electrolyte from reductive dissolution of higher oxidation state species.
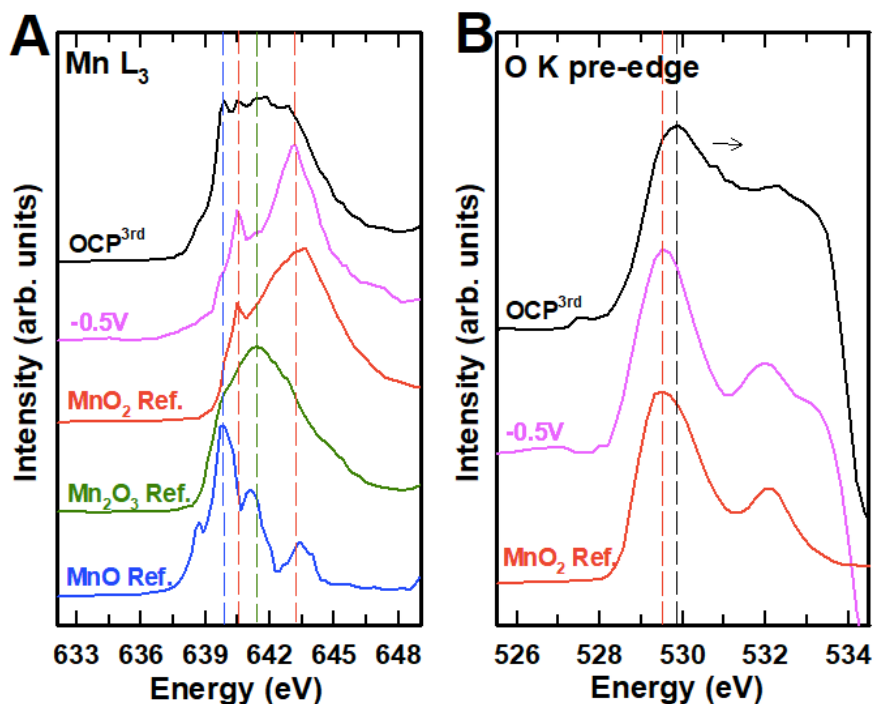
Figure 9.13 Mn L$_3$ and O K spectra of CE in EXP-3 at different potentials. (A) Mn L$_3$ spectra of the CE at -0.5V$_{Au}$ and at third OCP, compared to the spectra of MnO$_2$, Mn$_2$O$_3$ and MnSO$_4$. **(B)** O K-edge spectra of WE at -0.5 V$_{Au}$ and at third OCP, in comparison to the spectrum of MnO$_2$.

Figure 9.14 presents quantitative component maps of MnO, Mn$_2$O$_3$, and MnO$_2$ derived from stacks of the CE deposits measured at -0.5 V$_{Au}$ (**Fig. 9.14A**) and at the third OCP (**Fig. 9.14B**). The chemical mapping indicates that MnO$_2$ is the dominant species deposited at -0.5 V$_{Au}$. The contributions of MnO and Mn$_2$O$_3$ increased significantly at the third OCP. The quantitative volume analysis (**Fig. 9.14C**) showed the deposit on the CE was more than 95 ± 2 % MnO$_2$ at -0.5 V$_{Au}$, while on the contrary, the volume of MnO and Mn$_2$O$_3$ species increased to 29 ± 2 % and 24 ± 2 % at the third OCP.
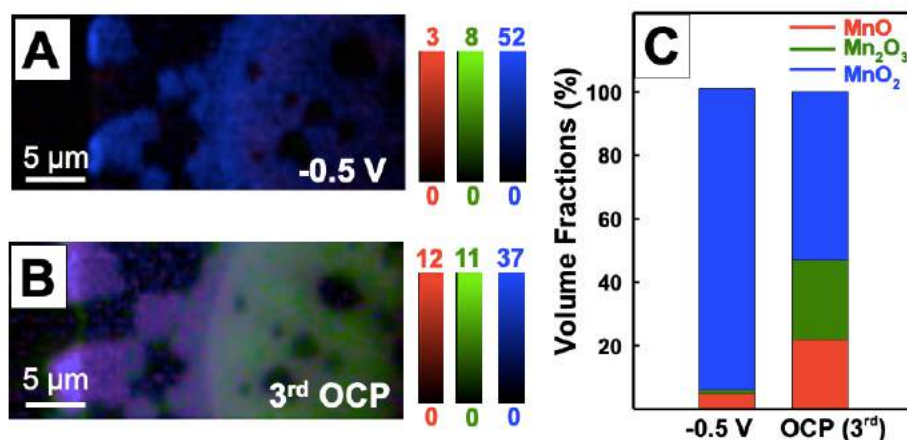
Figure 9.14 Oxidation state mapping and evolution of MnO, Mn₂O₃ and MnO₂ volume fractions of the CE in EXP-3 derived by fitting Mn L₃ stacks. (A) at -0.5 V_{Au}. **(B)** at third OCP. **(C)** volume fractions percentage of MnO (red), Mn₂O₃ (green) and MnO₂ (blue). These values are estimated from the quantitative component maps using the data processing described in **Section 5.1.17**.

9.3.3 Chemical mapping of Mn species at different applied potentials

Figure 9.15(A-K) presents average stack images extracted from all stack measurements (**EXP-3**) conducted on WE at different applied potentials. To demonstrate the capability of *in-situ* STXM to map out different oxidation states of manganese in a given region, **Figure 9.16(A-K)** presents quantitative chemical mapping of MnO, Mn₂O₃, and MnO₂ from SVD fitting analysis of Mn L₃ stacks (70 energies, 630 – 650 eV) measured during **EXP-3** at different applied potentials. The intensity scales in each measurement present the nm thickness of the indicated Mn species. The chemical mapping showed a steady conversion of MnO to MnO₂ as the applied potential was increased from +0.1 → +0.5V_{Au}. The largest thickness of MnO₂ was observed at +0.9V_{Au} which is consistent with the oxidation process. However, by reversing the applied potentials (-0.1 → -0.5 V_{Au}), the amount of MnO and Mn₂O₃ started to increase again, confirming a reduction process. The volume fraction presented in **Fig. 9.17**, showed gradual increase in MnO₂ species to ∼94% at +0.9 V_{Au}, while MnO and Mn₂O₃ decreased to 1% and 5% respectively. On the contrary, by applying potentials of -0.1 to -0.5V_{Au}, MnO₂ decreases to 49%, while MnO and Mn₂O₃ increased again to 28% and 23%

respectively. For all calculated volume fraction %, an uncertainty of ± 10 % is estimated from a combination of statistical and systematic uncertainties. Overall, in all measured stacks, the quantitative chemical mapping and the volume fraction % have the same trend of increasing and decreasing the amount of MnO, Mn_2O_3, and MnO_2 during the oxidation and reduction processes.
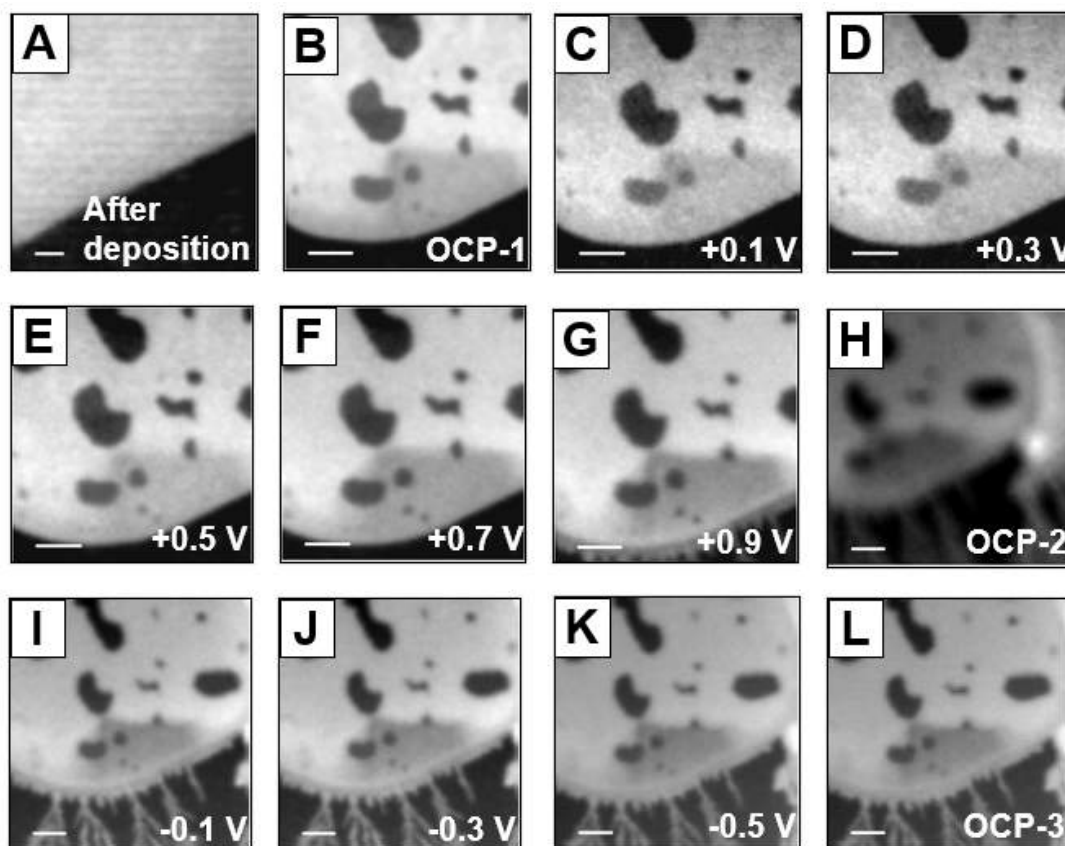
Figure 9.15 (A-L) Average STXM images of WE extracted from stack measurements at different applied potentials performed in EXP-3. scale bar: 2 μm.
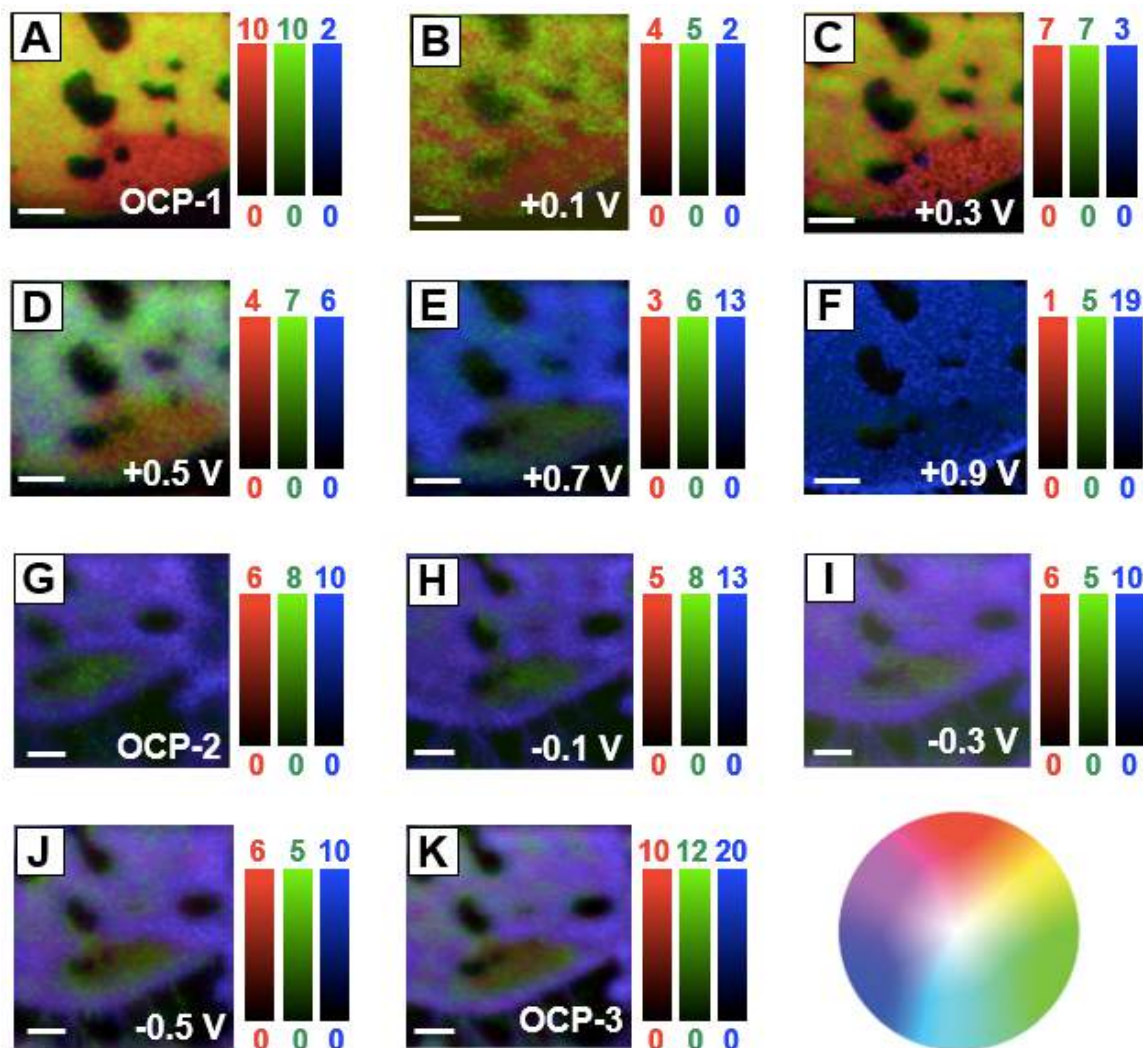
Figure 9.16 **Oxidation state quantitative mapping of the WE as a function of applied potential in EXP-3.** **(A-K)** Color coded composites of MnO, Mn_2O_3 and MnO_2 component maps of the WE derived by fitting Mn L_3 stacks (70 energies over the photon energy range of 625 to 650 eV), at the potentials indicated in each map. The color wheel indicates the color expected for different combinations of the red, green, and blue signals. Scale bar is 2 μm.
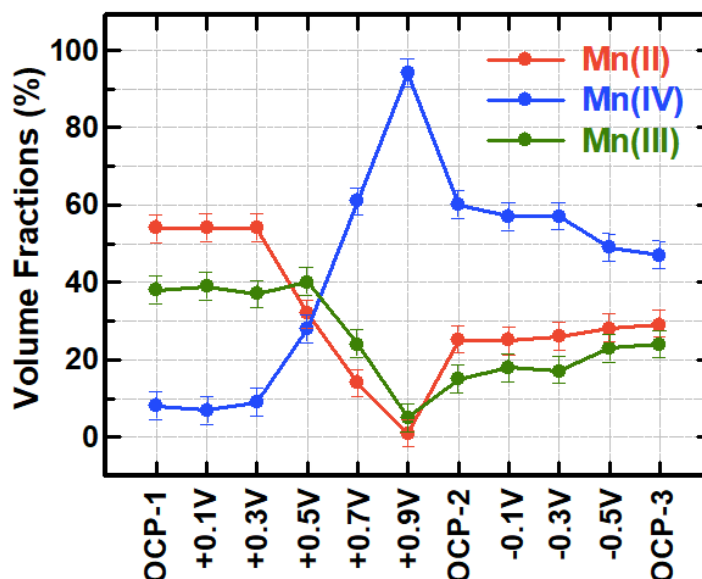
Figure 9.17 Evolution of MnO, Mn_2O_3 and MnO_2 volume fractions with applied potential in EXP-3. The volume fraction of MnO (in red), Mn_2O_3 (in green) and MnO_2 (in blue) are plotted as a function of the applied potential.

As described in **Section 5.5.4**, the volume (and volume fractions %) can be calculated from the average thickness and area of each Mn component. **Figure 9.18** presents SF curve fitting to determine the average thickness of the MnOx species from the stack measured at -0.5 $V_{Au.}$ This analysis indicates maximum thickness of 7 nm MnO_2 (red), 6 nm Mn_2O_3 (green) and 12 nm MnO (blue). The average spectra extracted from stack measurement (dotted purple) is in a good agreement with the calculated curve fit (grey).
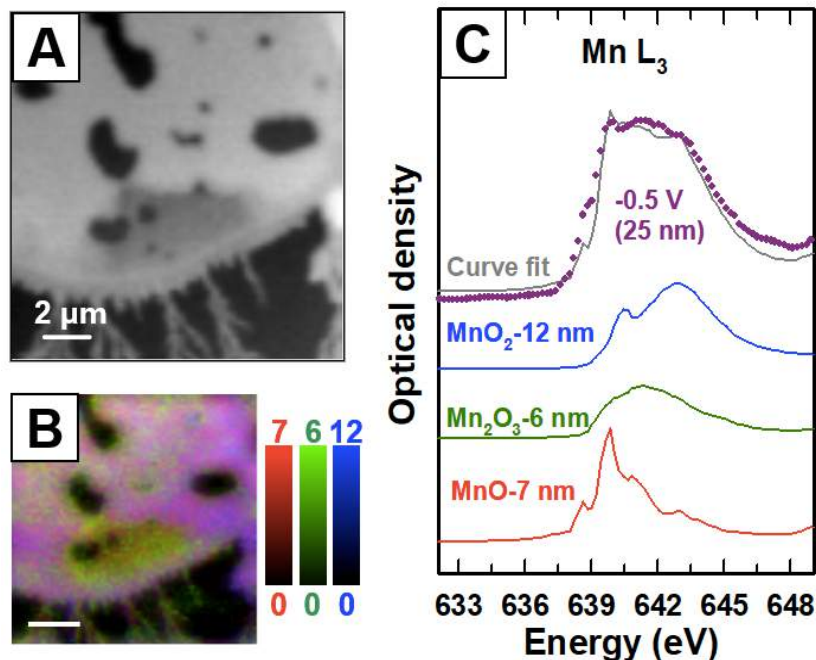
Figure 9.18 Details of volume fraction calculation of deposited MnOx at applied potential of -0.5V$_{Au}$. (A) average STXM image of the measured area. (B) relative component map. (C) average spectra (dark purple) from MnO$_2$ region (red), Mn$_2$O$_3$ region (green) and MnO region (blue), using SF curve-fitting.

9.3.4   *In-situ* MnO$_2$ in different electrolyte pH

The apparently spontaneous reduction of the electrodeposited MnO$_2$ to a mixture of Mn^{2+}/Mn^{3+} at OCP was observed in almost all *in-situ* STXM experiments at the point where the electrolyte was changed from MnSO$_4$(aq) to Na$_2$SO$_4$ (aq). I hypothesized that a local pH change was the reason for this reduction.

To follow up this hypothesis, *in-situ* STXM measurements of **EXP-4** were performed on the electrodeposited MnO$_2$ at different electrolyte pH, both with MnSO$_4$ present and in Na$_2$SO$_4$. First, in **EXP-4**, after confirming the electrodeposition of MnO$_2$ (from MnSO$_4$ – pH=5.2), the electrolyte was changed to MnSO$_4$ (pH 4) and then an Mn L$_3$ stack was measured at OCP (while the potentiostat was disconnected). **Figure 9.19A** presents the average Mn L$_3$ absorption spectrum extracted from all areas of the electrodeposited MnO$_2$ (in MnSO$_4$ – pH 5.2) compared to the absorption spectrum at OCP (MnSO$_4$ (pH=4), measured while the potentiostat was disconnected). Despite the spectral saturation, the Mn L$_3$ spectra at OCP

(pH=4) showed different spectral shape and peak positions confirming the partial reduction of Mn^{+4} to Mn^{+3}/Mn^{+2}. After this measurement, the electrolyte was changed to Na_2SO_4 (pH=8) and a Mn L_3 stack was measured while applying a fixed potential of +0.7 V_{Au} to oxidize the reduced Mn species again to MnO_2. Then, another stack measurement was performed in Na_2SO_4 (pH=8) at OCP (while the potentiostat was disconnected). **Figure 9.19D** presents the Mn L_3 absorption spectrum extracted from all areas of WE at +0.7 V_{Au} (in Na_2SO_4 – pH 8) in comparison to the Mn L3 absorption spectrum measured at OCP (in Na_2SO_4 – pH 8). The Mn L_3 spectrum at OCP was very close to that of MnO_2 with no spectral evidence for reduction. Even so, the quantitative volume fractions and the color-coded composites of the component maps derived from fitting the measured stack to MnO, Mn_2O_3 and MnO_2 reference spectra at pH=4 indicate the presence of reduced Mn^{2+}/Mn^{3+} species **(Fig. 9.19B, C and G)**. In contrast, the color-coded composites and the quantitative volume fractions **(Fig. 9.19E, F and H)** of the component maps derived from Mn L_3 stacks measured after reducing the pH from 4 to 8, confirm that the oxidation state did not change in the alkaline medium (Na_2SO_4 adjusted to pH=8) at OCP.

On the other hand, as always observed, when Mn^{2+}(aq) is oxidized to MnO_2 at positive applied potential, MnO_2 dendritic growth occurs at the edge of the WE. Interestingly, in **EXP-4** at pH 8 we observed less morphology change compared to **EXP-3.** The growth of MnO_2 (at +0.7 V_{Au}) occurred on the electrode itself <u>without dendrite formation</u>. **Figure 9.20** compares the morphology change in **EXP-3** (**Fig. 9.20B**) when the electrolyte was 0.1M Na_2SO_4 (pH=6.1) to that in **EXP-4** (**Fig. 9.20A**) when the pH of the 0.1M Na_2SO_4 electrolyte was pH=8. Clearly shifting the pH of the electrolyte to alkaline conditions is very effective at suppressing the dendrite formation, a phenomenon which is a major challenge in many energy storage devices due to the possibility of a catastrophic short.
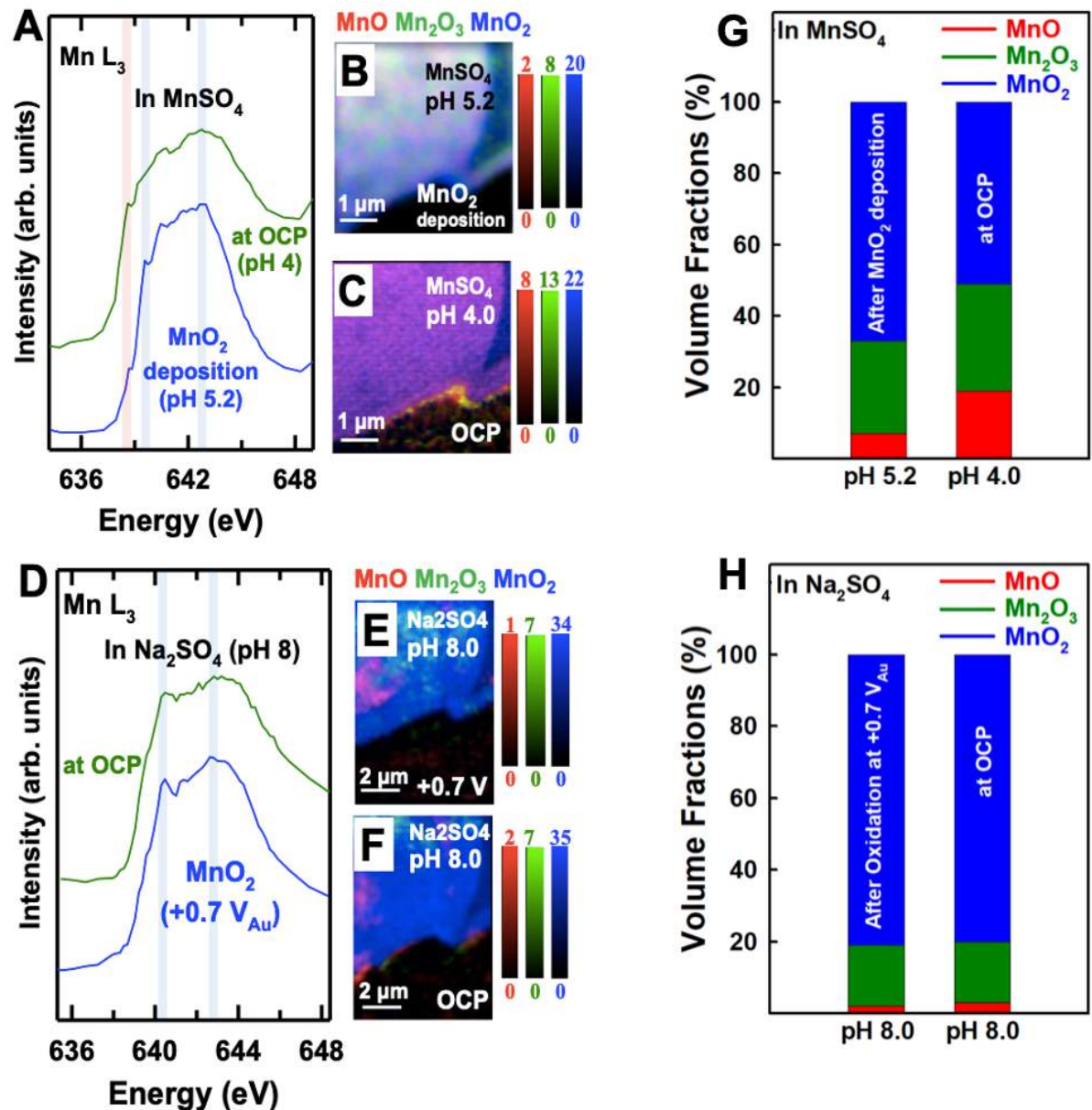
Figure 9.19 Results from EXP-4. Mn L₃ absorption spectra and composite map of deposited MnO₂ in different pH. (A) Mn L₃ spectra after the electrodeposition in MnSO₄ (pH=5.2) compared to measurement at OCP after changing the electrolyte to MnSO₄ (pH=4). **(B and C)** MnO, Mn₂O₃ and MnO₄ component map of measured stacks at pH=5.2 and pH=4. **(D)** Mn L₃ spectra of oxidized MnO₂ at +0.7V$_{Au}$ in Na₂SO₄ (pH=8) compared to OCP measurement. **(E and F)** MnO, Mn₂O₃ and MnO₄ component map of measured stacks at pH=8. **(G and H)** volume fractions percentage of MnO (red), Mn₂O₃ (green) and MnO₂ (blue) in MnSO₄ (pH=4) and Na₂SO₄ (pH=8), respectively.
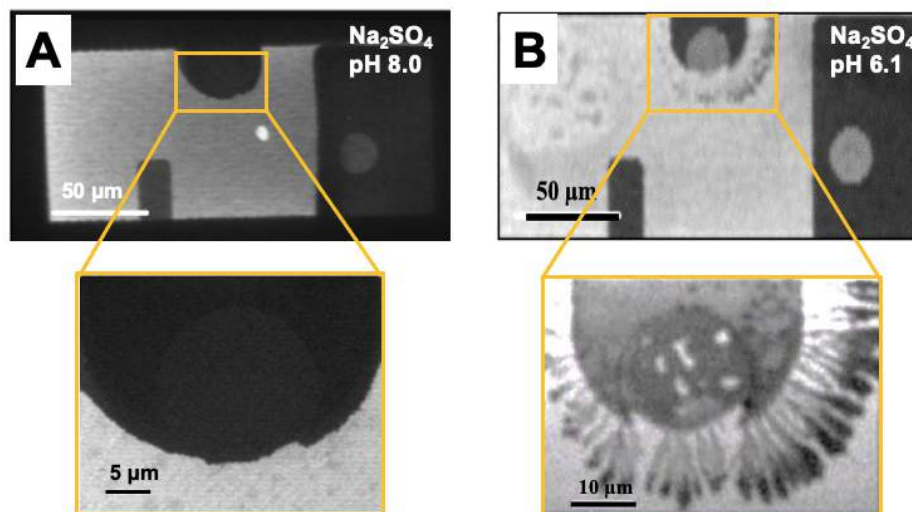
Figure 9.20 STXM images at 640 eV showing morphology change at different electrolyte pH. (A) EXP-4 (0.1M Na_2SO_4 - pH=8). **(B)** EXP-3 (0.1M Na_2SO_4 - pH=6.1).

9.3.5 *In-situ* MnO_2 system reversibility

In order to investigate the reversibility of dissoluble Mn^{2+} species, **EXP-5** was conducted at repeatable oxidative and reductive applied potentials (-0.2 and +0.4 V_{Au}). The main Mn L_3 peak of MnO (639.8 eV) and the sharp Mn L_3 peak of MnO_2 (640.5 eV) were used to track reversibility of the reductive dissolution of Mn^{2+} into the electrolyte. **Figure 9.21A** presents Mn L_3 absorption spectra extracted from stacks measured at WE region at OCP and at -0.2, -0.3, +0.4, -0.2 and + 0.4V_{Au}, in comparison to the MnO_2 reference spectrum. **Figure 9.21B** presents Mn L_3 absorption spectra extracted from stacks measured on the CE at same applied potentials as the WE.
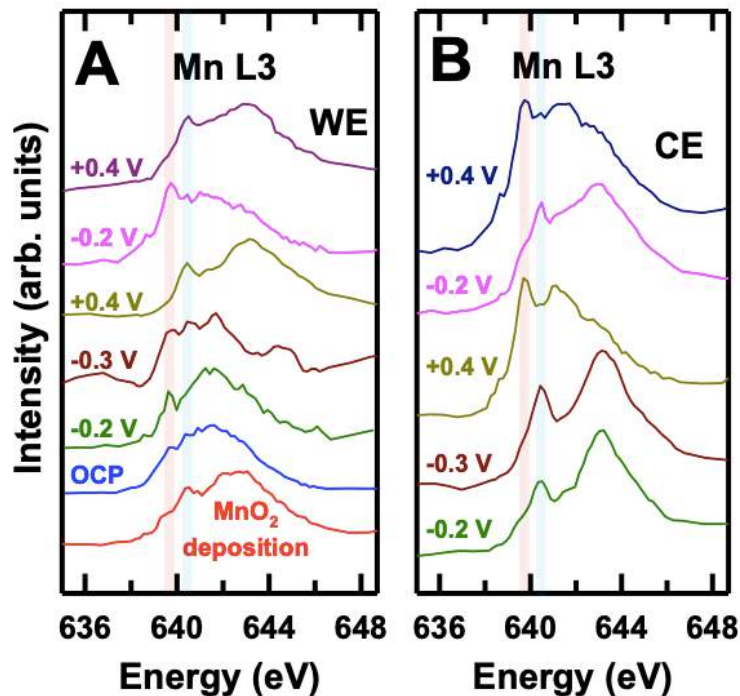
Figure 9.21 Mn L_3 absorption spectra at repeatable oxidative and reductive potentials at: **(A)** working electrode region. **(B)** counter electrode region.

As illustrated in **Fig. 9.21A**, the measurements at the WE indicate that the intensity of the main peak position of Mn^{2+} at 639.8 eV is increased at $-0.2V_{Au}$, while significantly decreased at $+0.4V_{Au}$. On the contrary, the characteristic sharp peak of MnO_2 at 640.5 eV increased at $+0.4V_{Au}$ and decreased at $-0.2V_{Au}$. At $-0.2 V_{Au}$, the dissolved Mn^{2+} migrates to the CE, so that MnO_2 oxidation at the CE occurs in conjunction with reductive dissolution at the WE. The spectrum of the CE deposit showed an increase in Mn^{2+} signals at $+0.4 V_{Au}$, while Mn^{4+} signals increased at $-0.2 V_{Au}$ **(Fig. 9.21B)**. **Figure 9.22(A-G)** and **Figure 9.23(A-G)** present quantitative chemical mapping of MnO, Mn_2O_3 and MnO_2 on the WE and CE, respectively, during **EXP-5** at different applied potentials derived by fitting Mn L_3 stacks (70 energies, 630 – 650 eV). The intensity scales in each measurement indicate the nm thickness of the indicated Mn species.
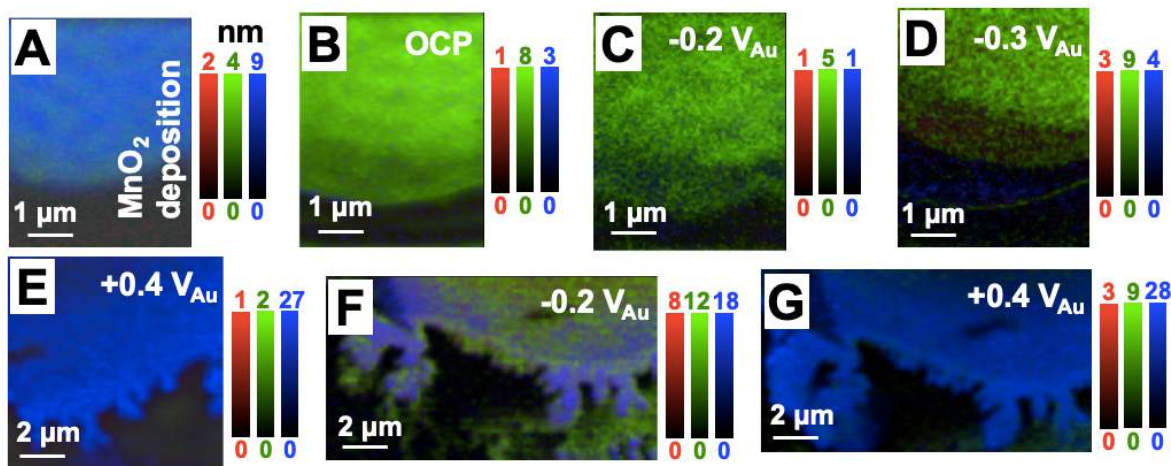
Figure 9.22 Quantitative mapping of the WE as a function of applied potential in EXP-5.
A-G) Color coded composites of MnO (red), Mn_2O_3 (green), and MnO_2 (blue) component maps of the WE derived by fitting Mn L_3 stacks at the potentials indicated in each map.
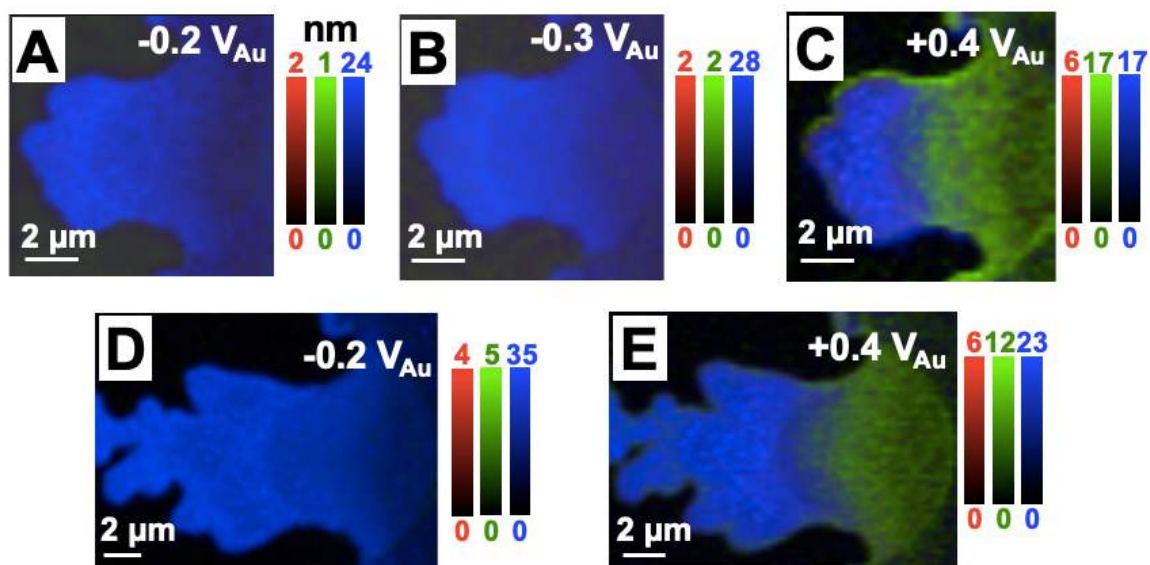
Figure 9.23 Quantitative mapping of the CE as a function of applied potential in EXP-5.
(A-E) Color coded composites of MnO (red), Mn_2O_3 (green), and MnO_2 (blue) component maps of the CE derived by fitting Mn L_3 stacks at the potentials indicated in each map.

9.4 Discussion

9.4.1 Spontaneous reduction with change of electrolyte

The *in-situ* STXM results (**EXP-1, EXP-2, and EXP-3**) demonstrate that the initially deposited MnO_2 is "spontaneously" partially reduced to Mn^{2+} and Mn^{3+} when the electrolyte is changed from 0.1 M $MnSO_4$ (pH 5.2) to 0.1 M Na_2SO_4 (pH 6.1). The conversion of Mn^{4+} to a mixture of Mn^{2+} and Mn^{3+} at the first OCP may be attributed to change in the local pH at WE to lower values. To support this hypothesis, after the MnO_2 electro-deposition was performed in **EXP-4**, the electrolyte was changed from $MnSO_4$(aq) at pH=5.2 to $MnSO_4$(aq) with pH=4. The subsequent Mn L_3 stack indicated reduction of Mn^{4+} to a mixture of Mn^{2+} and Mn^{3+} (see **Fig. 9.19A**). When the electrolyte was changed to Na_2SO_4 (pH=8), and a potential of $+0.7V_{Au}$ was applied, the reduced Mn species was oxidized to MnO_2 as indicated by the Mn L_3 results (**Fig. 9.19B**). Further, the Mn L_3 results obtained from the Mn L_3 stack measured at OCP (while the potentiostat was disconnected) showed that the MnO_2 spectral shape and peak positions didn't change or reduce to Mn^{2+}/Mn^{3+} species (when compared to the MnO_2 spectra at +0.7 V_{Au}). This is in contrast to the reduction that occurred at OCP in pH=4 (see **Fig. 9.19A**). These results indicates that, if the local pH changes to a more acidic value, the MnO_2 will be reduced to a lower oxidation state.

Chan et al. (Tanggarnjanavalukul et al., 2018) presented an extensive study of MnO_2 nanosheets in Na_2SO_4 electrolytes at different pH, which illustrated that the oxidation state of Mn on the electrode is decreased because of a concentration gradient between the bulk electrolyte and electrode/electrolyte, resulting in more diffusion of Na^+ or H^+ into the electrode tunnels. The reported results indicate that the average oxidation state of the as-prepared MnO_2 (IV) changed to 3.02 at pH 5.9 (at OCP). In the performed *in-situ* experiments (presented in the thesis), the 0.1M Na_2SO_4 has pH=6.1, which is very close to the experimental conditions used by Chen et al. (Tanggarnjanavalukul et al., 2018). If the local pH at the electrode changed from 6.1 to a value <6.1, that change may lead to reduction of Mn(IV) to Mn(III).

The initially deposited MnO_2 is always accompanied with small fractions of Mn^{2+} species (**Fig 9.2D** and **Fig 9.22A**). The **acid-base reaction** occurring in the slightly acidic medium can be described by **Eq. 9.4** (Lee et al., 1977; Nijjer et al., 2000; Ruetschi & Giovanoli,

1982). The direct reduction of MnO_2 to MnO is also possible in acidic medium and can be described by **Eq. 9.5** (Ruetschi et al., 1982):

$$MnO_2\ (s)\ +\ Mn^{2+}\ (aq)\ +\ 2H_2O \rightarrow 2MnOOH\ (s)\ +\ 2H^+ \qquad \textbf{Eq. 9.4}$$

$$MnO_2(s)\ +\ 2H^+(aq) \rightarrow Mn^{2+}(aq) + H_2O\ +\ \tfrac{1}{2}O_2 \qquad \textbf{Eq. 9.5}$$
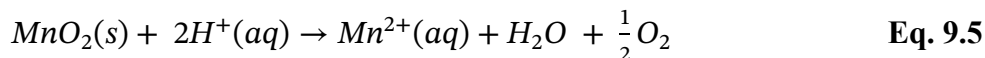
Therefore, the reduced Mn species at OCP in **EXP-2** and **EXP-3** is consistent with the results of **EXP-4**, and the results obtained by Chan et al. (Tanggarnjanavalukul et al., 2018). The pH of 0.1M Na_2SO_4 used in **EXP-2** and **EXP-3** is 6.1. The spontaneous insertion of H^+ and the predicted change in the local pH can result in changing the pH at the WE electrode to < 5.9 and consequently reducing the as-prepared $MnO_2(IV)$ to Mn^{3+}.

At a reductive potential, the formation of Mn^{2+} as a discharge product resulted from the reduction of Mn^{4+} has been reported previously (Jiang et al., 2020; Rodrigues et al., 1998). Therefore, I suggest that the reduction of Mn^{4+} occurs in two steps. First, MnO_2 is reduced to MnOOH/MnOONa. This is then followed by formation of Mn^{2+} through the disproportionation reaction of Mn^{3+}, as represented in **Eq. 9.6** (Devaraj & Munichandraiah, 2009; Rodrigues et al., 1998):

$$MnOOH\ (s)\ +\ 3H^+(aq) +\ e^- \rightarrow Mn^{2+}(aq) + 2H_2O \qquad \textbf{Eq. 9.6}$$

Another alternative could be a direct, one step conversion of Mn^{4+} into Mn^{2+} through a $2e^-$ reaction, as presented in **Eq. 9.7** (Moon et al., 2021)

$$MnO_2(s)\ +\ 2H^+(aq) +\ 2e^- \rightarrow Mn^{2+}(aq) + 2OH^-(aq) \qquad \textbf{Eq. 9.7}$$
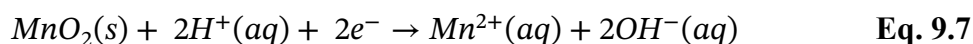
The Pourbaix diagram **(**Yi & Majid, 2018**) (Fig. 9.24A)**, plots the aqueous phase stability of various oxidation states (Mn^{2+}, Mn^{3+}, and Mn^{4+}) as a function of pH and redox potential (vs SHE). It is widely accepted that the electrochemical charging and discharging processes of MnO_2 electrodes involves a $Mn^{3+} \leftrightarrow Mn^{4+}$ redox reaction. From a thermodynamic viewpoint and as illustrated in the Mn–H_2O system Pourbaix diagram, some of the deposited MnO_2 will dissolve into the 0.1 M Na_2SO_4 electrolyte (pH ≈ 6) as MnO species at potentials of -0.1 → -0.5V_{Au} (which is equivalent to +0.3 → -0.1V_{SHE} (see **Section 5.1.4)**), This is confirmed by the migration of reductively dissolved Mn^{2+} species and their oxidative redeposition on the

CE at $-0.5V_{Au}$. This reductive dissolution is consistent with the Mn L_3 and O K pre-edge spectra extracted from stacks measured on the WE region at those potentials **(Exp-3, Fig. 9.13)**. Moreover, as illustrated in the Pourbaix diagram (**Fig. 9.24A**), by increasing the acidic conditions (decreasing the electrolyte pH), the MnO_2 can be converted to Mn^{2+} (aq) as described by **Eq. 9.7**.

In contrast, and based on the Pourbaix diagram, by increasing the applied potential from $+0.1$ to $+0.9$ V_{Au} (equivalent to $+0.5V \rightarrow +1.3V_{SHE}$ (see **Section 5.1.4**)) some of the dissolved Mn^{2+} species will be oxidized to MnO_2 and redeposited on the electrode surface. This change is also confirmed by the significant dendrite growth on the WE surface at $+0.9$ V_{Au} as presented in **Fig. 9.9**. **Figure 9.24B** presents Mn L_3 spectra of the Na_2SO_4 electrolyte (**in EXP-3**) at $-0.5V_{Au}$ and $+0.9V_{Au}$ compared to reference MnO spectra. The Mn^{2+} signals at $-0.5V_{Au}$ indicate the dissolution of MnO_2 to MnO at reductive potential, while at $+0.9V$ (oxidative potential), the Mn^{2+} signals disappeared, which is consistent with the redeposition of MnO $\rightarrow$ MnO_2 on the WE and the formation of the dendrite growth.
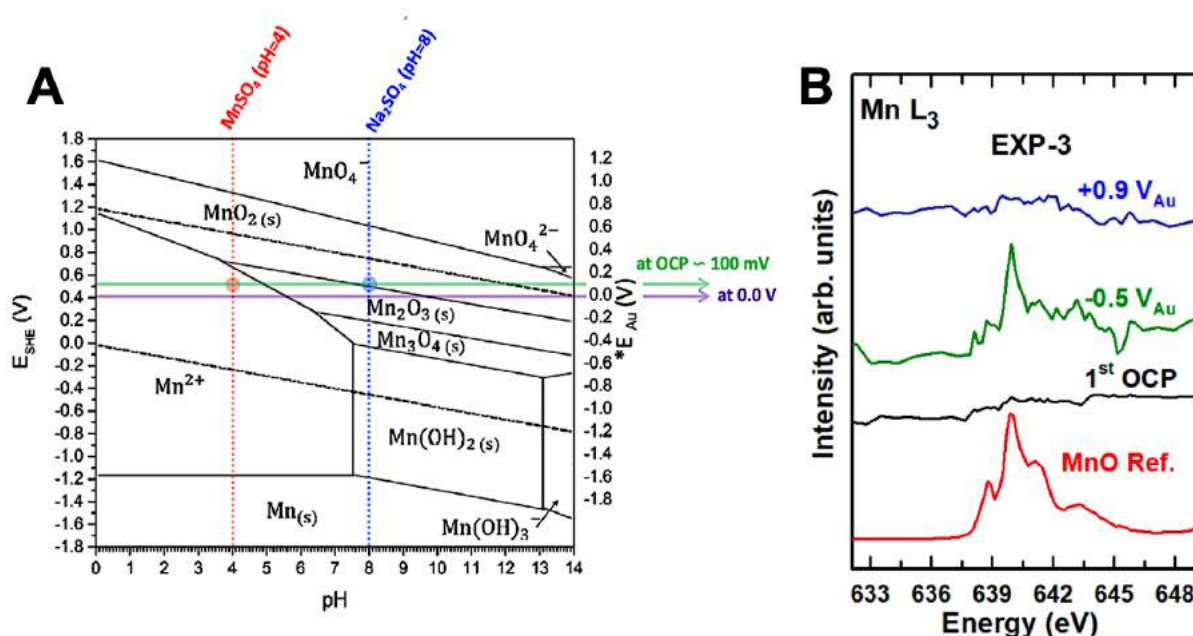
Figure 9.24 (A) Pourbaix diagram of the Mn/H_2O system at 25 °C. Reprinted and adapted from (Bordbar-Khiabani, 2022). With permission from Elsevier. **(B)** Mn L_3 absorption spectra of Na_2SO_4 electrolyte in **EXP-3**, at 1st OCP (black), $-0.5V_{Au}$ (green) and $+0.9V_{Au}$ (blue), compared to MnO reference spectra (red).

It is generally accepted that MnOOH is an inactive species in neutral aqueous solution (Hu et al., 2008; Xu et al., 2010). However, I claim that the reduction of Mn^{4+} to Mn^{2+}/Mn^{3+} occurred at OCP because the local pH changed, leading to insertion of $[H^+]$ into MnO_2 bulk (as discussed in presentation of the results on **EXP-5**). Thus, it is suggested that the $[H^+]$ and electrolyte cation $[Na^+]$ are **both** active agents for reducing MnO_2 in neutral media, while $[Na^+]$ intercalation is the active agent at the surface of the deposited MnO_2 film. Therefore, as suggested by others (Hu et al., 2008; Xu et al., 2010), the MnO_2 charge storage mechanism depends on the adsorption and tunnel storage of the alkaline metal cations $[Na^+]$. This is similar to the predicted mechanism of the intercalation of zinc cation $[Zn^+]$ into the α-MnO_2 lattice structure in α-MnO_2/ZIBs during the discharging process (see **Chapter 6**).

I tried to investigate the reduction of MnO_2 to $MnOONa$ through an adsorption/insertion of the electrolyte cation $[Na^+]$ at the surface of the electrodeposited MnO_2 by performing Na 1s point spectral measurements (see **Section 5.4.3.2**) while applying a potential of -0.2 V_{Au} and comparing the intensity of the Na signal at the edge of the working electrode and in the electrolyte. However, this experiment did not succeed). The Na 1s signals were too weak to track any change in the spectral intensity as illustrated in **Fig. 9.25**.
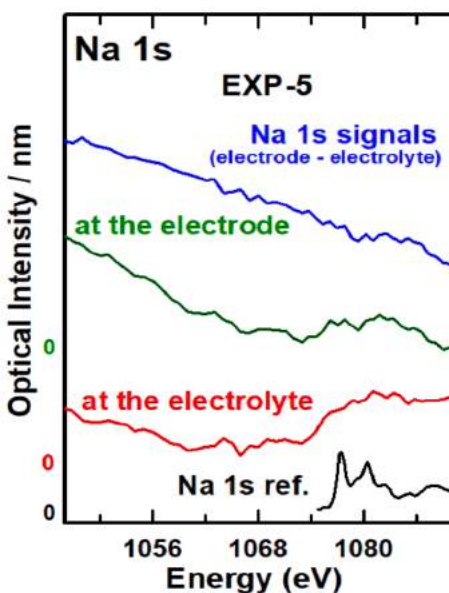
Figure 9.25 Na 1s absorption spectra at the edge of the WE (green) and at the electrolyte (red) compared to reference Na 1s spectra of NaCl. The blue spectra is the difference between Na 1s signals of the electrode and the electrolyte.

9.4.2 Redox cycling

The measured Mn L_3 and O K-edge stacks indicate the reduced Mn species observed at OCP (in Na_2SO_4) were gradually oxidized to MnO_2 when potentials from +0.1 to +0.9 V_{Au} were applied. In contrast, MnO_2 was partially reduced to Mn^{2+} and Mn^{3+} at applied potentials of -0.1V to -0.5 V_{Au} and at OCP relaxation (< +100 mV).

The dendrite growth only occurred at +0.9 V_{Au} (**EXP-3**). This is due to dissolution and redeposition of the initially deposited MnO_2 (Wu et al., 2021). Therefore, the formation of the dendrites mostly relies on the reduction of MnO_2 to Mn^{3+} at OCP (discharging process), followed by a disproportionation reduction to form Mn^{2+}. The dissolved Mn^{2+} is consequently deposited again on the surface and at the edge of the WE at high applied potential (+0.9 V_{Au}). The redeposition of MnO_2 and the spectroscopic and microscopic results obtained from **EXP-5** confirm the partial reversibility of Mn^{2+} species through the oxidation/reduction processes. The heterogeneous formation of MnO_2 dendrites can significantly impact the safety and durability of MnO_2-based supercapacitors or battery systems, leading to internal short circuits if the dendrite growth reaches the anode. The obtained result from **EXP-4** indicates that alkaline electrolyte pH can decrease the formation of dendrites in MnO_2-based energy storage devices.

In general, the spontaneous reduction of the initially deposited MnO_2 to lower Mn oxidation states (Mn^{2+} and Mn^{3+}) occurs due to a change in the local pH at the WE. While the significant change from a quasi-uniform MnO_2 film to a dendritic MnO_2 structure resulted from the redeposition of dissoluble Mn^{2+} species at positive applied potentials (+0.9V_{Au}). At the same time, the remarkable deposition of MnOx species at CE resulted from the migration of dissoluble Mn^{2+} species which subsequently oxidized to MnO_2 at the CE at negative applied potentials (-0.5V_{Au}). Additionally, the charging/discharging processes occur through the Mn^{4+} ↔ Mn^{2+}/Mn^{3+} redox reaction (i.e. it is not limited to Mn^{4+} ↔ Mn^{3+} only).

For better performance of the MnO_2 system, it is crucial to control the dissolution of MnO_2. This can be achieved by different approaches. For instance, in ZIBs, incorporating potassium ions [K^+] into the α-MnO_2 lattice can stabilize the tunnel structure and minimize the dissolution process (Fang et al., 2019). Another approach involves using electrolyte additives such as Bi_2O_3, which can suppress the reduction of MnO_2 during cycling (Duan et al., 2022).

Furthermore, MnO_2 coating (e.g., with other metal oxides) is a widely used method in supercapacitor applications to control the dissolution of MnO_2 (Zhang & Mo, 2014).

9.5   Summary

The *in-situ* STXM studies presented in this chapter provided spectro-microscopic insights into MnO_2-based electrode behavior during charging/discharging processes. Different *in-situ* STXM experiments were successfully conducted at different electrochemical conditions and different electrolyte pH. The results indicate a spontaneous reduction of initially deposited MnO_2 at OCP and a significant morphological change at oxidative applied potential. Additionally, the measurements indicate a partial revisability of dissoluble Mn^{2+} species.

The *in-situ* STXM technique reported here can be used to study different electrochemical materials/processes related to energy storage applications such as ZIBs, SIBs, and SCs. Thus, provide mechanistic insight into the spatially resolved chemical structures and morphological changes present in further electrochemically developed active materials.

Chapter 10
Summary and Future Work

This chapter summarizes the work performed in this thesis and highlights the contributions I have made to improved understanding of manganese oxide electrochemistry relevant to several different energy materials applications. Suggestions for future in-situ STXM studies of supercapacitor and battery electrode materials are provided.

10.1   Summary

Synchrotron-based soft X-ray scanning transmission X-ray microscopy (STXM) was used to characterize manganese-based electrodes relevant to several different energy materials applications. A major contribution I made, in collaboration with fellow PhD student, Chunyang Zhang, was to develop an *in-situ* flow electrochemical device optimized for soft X-ray STXM (**Chapter 4**). My research consisted of three main parts: (1) *ex-situ* STXM studies of various manganese oxide reference compounds and different Mn_3O_4 supercapacitor electrode materials; (2) development of a custom flow electrochemical device for *in-situ* STXM characterization of different electrochemical systems; (3) *in-situ* STXM studies of MnO_2-based electrode material for energy storage applications.

For *ex-situ* STXM studies, accurately calibrated and quantitative NEXAFS spectra of various manganese oxide compounds (MnO, $MnSO_4$, Mn_3O_4, Mn_2O_3, α-MnO_2, β-MnO_2, and $KMnO_4$) were measured at the Mn 2p and O 1s core edges using both STXM and TEY-XAS (**Chapter 6**). Although NEXAFS spectra of the common MnOx species were reported earlier, some discrepancies existed in the literature. Therefore, this study provided reliable and quantitative reference spectra essential for analyses of STXM data of complex MnOx systems.

In a collaboration with PhD student, Wenjuan Yang and Prof. Igor Zhitomirsky, Mn_3O_4 supercapacitor electrode materials, subjected to different activation procedures and electrochemical testing were characterized at the Mn 2p and O 1s edges to understand the activation behavior of Mn_3O_4 electrodes (**Chapter 7**) and the influence of fabrication method and electrochemical activation on charge storage (**Chapter 8**). In the first study, Mn_3O_4-

MWCNT supercapacitor electrode materials prepared using quercetin as a dispersant were characterized after variable scan rate and fixed scan rate electrochemical activation procedures. The STXM results indicate that by increasing the number of charging/discharging cycles, the prepared Mn_3O_4 electrode is partially converted to MnO_2. This result was correlated to a gradual increase in the capacitance performance as the number of cycles was increased. In the second study, *ex-situ* STXM was used to analyse Mn_3O_4 electrode materials fabricated using a chemical precipitation method followed by high energy ball milling (HEBM) or by synthesis of Mn_3O_4 using quercetin as a capping agent, without HEBM. The STXM results indicate that the higher electrochemical performance of Mn_3O_4 prepared using quercetin in the synthesis is due to the partial oxidation of the initially prepared Mn_3O_4 electrodes to MnO_2.

An *in-situ* flow electrochemical device optimized for STXM microscopes was adapted from a design by the Obst group (BayCEER, University of Bayreuth, Germany). **Chapter 4** of this thesis outlines the step-by-step fabrication procedure and operational guidelines for the *in-situ* flow electrochemical STXM device.

Using the newly developed device, *in-situ* STXM measurements were conducted on electrodeposited MnO_2 films (**Chapter 9**). Measurements at the Mn L_3 and O K edges were used to assess the change in the oxidation state of MnO_2 as a function of electrolyte pH and applied potentials. At the open circuit potential (OCP), I observed a partial reduction of Mn^{4+} to a mixture of Mn^{2+}/Mn^{3+}, which oxidized back to Mn^{4+} when positive potentials (+0.1 to +0.9 V_{Au}) were applied (in Na_2SO_4 electrolyte, pH=6.1). The morphology of the pre-deposited MnO_2 on the working electrode (WE) dramatically changed into a dendritic structure at +0.9 V_{Au}. The STXM results indicate that the dendrite growth resulted from oxidative deposition of the reductively dissolved $Mn^{2+}(aq)$ from the electrolyte to $Mn^{+4}(s)$ (likely MnO_2). To follow up the observation of the partial reduction of Mn^{4+} to a mixture of Mn^{2+}/Mn^3 at OCP, *in-situ* STXM studies were performed at different electrolyte pH (= 4 and 8). The STXM results showed that at pH=4, Mn^{4+} was reduced to lower oxidation states, while at pH=8, no reduction occurred. These results indicate that the reduction of Mn^{4+} at OCP may be attributed to the change in the local pH at the working electrode to a lower value. Additionally, at pH=8 The WE did not exhibit any dendritic growth when subjected to an oxidative potential, which indicates that the alkaline electrolyte pH can suppress the MnO_2 dendritic formation. Dendritic

growth is considered one of the most critical challenges for developing MnO_2-based energy storage devices (particularly ZIBs and LIBs). If these dendrites reach the anode, it can result in internal short circuits and can significantly affect the safety and durability of these devices. In general, these *in-situ* STXM studies provided detailed information and quantitative insight into the morphology and spatially resolved chemical structures of MnO_2-based electrodes under different electrochemical conditions. This research is the first use of *in-situ* STXM to characterize MnO_2-based electrodes for energy storage applications.

10.2   Original contributions to this thesis

My original contributions to this thesis are:

- I performed STXM and TEY-XAS measurements of accurate, quantitative, and high-statistical precision O 1s and Mn 2p NEXAFS spectra of various Mn compounds in the common oxidation states for subsequent analyses and precise quantitative information of STXM data of different complex MnOx systems (**Chapter 6**).

- With assistance from Dr. Chunyang Zhang, Pablo Ingino, and Prof. Martin Obst and advice from Prof. Adam Hitchcock, I developed and fabricated a flow electrochemical device for *in-situ* STXM characterization (**Chapter 4**).

- In collaboration with Wenjuan Yang (Zhitomirsky group), I used *ex-situ* STXM to characterize different Mn_3O_4-based supercapacitor electrodes with different fabrication methods and electrochemical activation procedures (**Chapters 7** and **8**).

- Together with Dr. Chunyang Zhang, I performed *in-situ* STXM studies of MnO_2-based electrodes for energy storage applications. I also assisted Chunyang's *in-situ* STXM studies of Cu CO_2 reduction (CO_2R) catalysts under electrochemical conditions similar to those where CO_2 reduction occurred (Zhang et al., 2023c; Zhang et al., 2023b; Zhang et al., 2023a). Together, these studies have provided spectro-microscopic insight into several important electrochemical systems and highlighted the advantage of using *in-situ* STXM over bulk-averaged *in-situ* techniques (**Chapter 9**).

10.3   Future work

10.3.1 Improvement of the *in-situ* device

I. Most of the *in-situ* experiments performed using the *in-situ* device under vacuum condition failed due to breaking of the SiNx window, followed by electrolyte leakage inside STXM (see **Section 4.2.10**). The main reason for that is the presence of pressure points at the edges of the microchips, which may be generated from the uneven edges of the inside margins of PCB, and the amount of Torr-Seal used to bond the microchips. In order to address this issue, it is essential to improve the fabrication process of PCBs by using a higher-precision CNC machine. Additionally, performing the gluing of the microchips under a long-distance stereo microscope is crucial to minimize the amount of Torr-Seal used for bonding. Furthermore, creating a mold with precise positioning of the microchips on the microfluidic cell is highly necessary. This mold will ensure that the microchips are precisely bonded to the cell in the correct position, which should prevent creating stress points. In addition, a portable vacuum test system should be developed to confirm the vacuum integrity of the *in-situ* device prior to mounting it into the STXM chamber.

II. The syringe pump system (used to flow the electrolyte inside the *in-situ* device) should be replaced by a multiple channel pressure-driven flow controller (**Fig. 10.1**). The flow controller can control the flow rate with a sub-second response time and achieve a highly stable pulse-less flow rate. The multiple-channel pressure system can allow simultaneous pushing of the electrolyte into the inlet channels and withdraw from the exit channels very precisely. Thus, better control of the electrolyte thickness can be achieved. Also, a multiple channel system can allow performing *in-situ* experiments that require creating a specific chemical reaction inside the *in-situ* device by controlling the flow rate of two different electrolytes being introduced into the two inlet channels of the *in-situ* device. Moreover, the multiple channel pressure-driven flow controller has some advantages over the syringe pump system. During the *in-situ* STXM experiments, it is sometimes necessary to remove the plug of the second inlet channel to reduce the internal pressure inside the cell or disconnect the plastic syringe from the pump to change the electrolyte.

Opening the first or second inlet channels can generate air bubbles into the system. Using the multiple channel pressure-driven flow controller allows exchange the electrolyte (from the first inlet channel) and reduces the internal pressure (by withdrawing the electrolyte from the other channels) without opening the system. Additionally, the multiple channel flow controller can be adapted to purge or saturate the electrolyte with an appropriate gas (based on the experimental conditions) during the *in-situ* experiment.

III. In order to perform successful *in-situ* experiments and avoid device leakage or spectral saturation, the *in-situ* device should be filled with the appropriate electrolyte at McMaster, and the electrolyte thickness should be examined using laser fluorescence microscopy (should be < 3 μm) using the CALM facilities prior to STXM beam time. To ensure that filled cells will not be affected during transportation (to Saskatoon or Europe), I have tested this approach by filling some *in-situ* cells with electrolytes and transporting them to MaxIV (Sep. 2023).
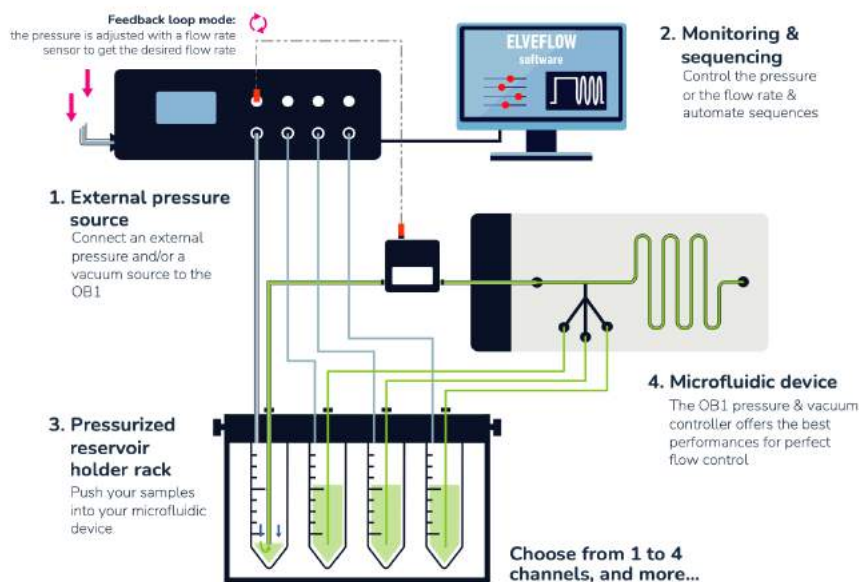
Figure 10.1 Diagram of pressure-driven flow controlled microfluidic system. (https://www.elveflow, 2024, Jan. 12)

10.3.2 *In-situ* STXM study of MnO₂-based electrodes in different electrolytes

Electrolytes play a crucial role in energy storage devices, since their physical and chemical properties significantly impact the electrochemical performance of these devices (Pal et al., 2019). Among different types of electrolytes (aqueous, organic, ionic liquids, and solid or quasi solid-state electrolytes), aqueous electrolytes such as Na_2SO_4, KCl, NaOH, and KOH attract great attention owing to their excellent conductivity and faster carrier rates. Additionally, they offer advantages such as being cost-effective, non-toxic (dilute concentrations), and easy to handle during experiments (Chakraborty & Mary, 2022; Jayachandran et al., 2021). On the other hand, the electrolyte pH significantly affects the electrochemical performance of MnO_2-based electrodes in different energy storage applications (Dai et al., 2022).

In the *in-situ* STXM experiments performed on electrodeposited MnO_2 (**Chapter 9**), I observed significant changes when the electrolyte was changed from $MnSO_4$ (pH = 5.4) to a slightly acidic $MnSO_4$ (pH = 4) or alkaline Na_2SO_4 (pH = 8). The experiments at forced acidic and alkaline pH (**Chapter 9**) were carried out to investigate the spontaneous reduction of the pre-deposited MnO_2 at OCP. However, more *in-situ* experiments are required to understand the effect of the electrolyte pH on the chemical and morphological changes during the charging and discharging processes.

It is expected that, in acidic electrolytes, the excess H^+ will induce the reduction of Mn^{3+} to Mn^{2+} based on **Eq. 10.1** and **10.2** (Dai et al., 2022; Guo et al., 2019), whereas at alkaline pH, the interaction between the OH^- ions and MnO_2 at the surface will generate an insulating layer of $Mn(OH)_2$ (s), which may prevent the dissolution of Mn^{2+} into the electrolyte (**Eq. 10.3-10.7**) (Dai et al., 2022; Guo et al., 2019).

- <u>In acidic electrolyte:</u>

$$MnO_2 + H^+ + e^- \rightarrow MnOOH \qquad\qquad \textbf{Eq. 10.1}$$

$$MnOOH + 3H^+ + e^- \rightarrow Mn^{2+}_{(aq)} + 2H_2O \qquad\qquad \textbf{Eq. 10.2}$$

- <u>In alkaline electrolyte:</u>

$$MnO_2 + H_2O + e^- \rightarrow MnOOH + OH^- \qquad\qquad \textbf{Eq. 10.3}$$

$$MnOOH + H_2O + e^- \rightarrow Mn(OH)_2 + OH^- \qquad\qquad \textbf{Eq. 10.4}$$

$$3Mn(OH)_2 \leftrightarrow Mn_3O_4.2H_2O + 2H^+ + 2e^- \qquad \textbf{Eq. 10.5}$$

$$Mn_3O_4.2H_2O + OH^- \leftrightarrow 2MnOOH + Mn(OH)_3 + e^- \qquad \textbf{Eq. 10.6}$$

$$MnOOH + 2Mn(OH)_3 + 6OH^- \leftrightarrow 6MnO_2.5H_2O + 3H_2O + 6e^- \qquad \textbf{Eq. 10.7}$$
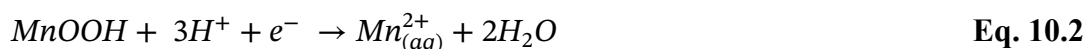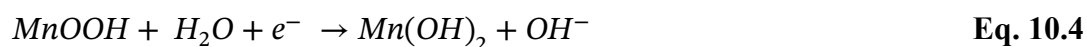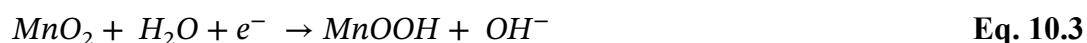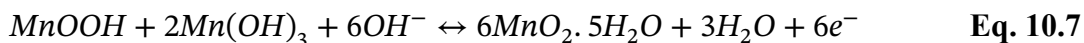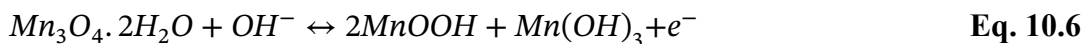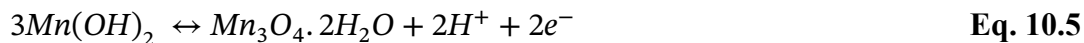
Additionally, using a redox additive with the alkaline electrolyte can enhance the electrochemical performance of the MnO_2-based electrodes by providing an electron buffer source to facilitate the $Mn^{4+} \leftrightarrow Mn^{3+}$ redox reaction (Kumar et al., 2018; Maiti et al., 2014). Ferri/ferro cyanide could be used as a redox additive to an alkaline electrolyte or using neutral buffer electrolyte to control the dissolution of MnO_2 and enhance formation of Mn^{3+} species during the reduction process.

Different hypotheses and suggestions for future *in-situ* STXM studies of MnO_2-based electrodes at different electrolytes and different pH are listed below:

Testable Hypothesis (TH-a)
Electrolyte with a redox additive will enhance the intercalation/deintercalation of the electrolyte cation, increase the formation of Mn^{3+} species and minimize the dissolution of MnO_2 (Kumar et al., 2018; Maiti et al., 2014).

Testable Hypothesis (TH-b)
Buffered electrolyte (in neutral pH) will control the dissolution of MnO_2 to Mn^{2+} species that results from local pH change.

These hypotheses can be investigated through the following experimental design:
1- In two separate *in-situ* experiments, after galvanostatic deposition of MnO_2 on the WE, the oxidation and reduction processes will be investigated in different electrolytes:
   - KOH with (pH=8) with $K_3[Fe(CN)_6]$/ $K_4[Fe(CN)_6]$ mixture as redox additive.
   - Na_2SO_4 with a phosphate buffer (pH=7).
2- In each experiment, three CV measurements will be performed in potential window of -0.4 to +0.8 V_{Au} (0.0 to +1.2 V_{SHE}). The potential will be held at +0.8V_{Au} after the 3rd CV (oxidative potential).

3- STXM measurement will be performed at Mn 2p (L_3) edge on both WE and CE.

4- Another three CV measurements will be performed in each experiment, in the same potential window. The potential will be held at $-0.4V_{Au.}$ after the 3rd CV (reductive potential).

5- STXM measurement will be conducted again at Mn 2p (L_3) edge on both WE and CE.

Predicted outcomes are:

A- Using $K_3[Fe(CN)_6]$/ $K_4[Fe(CN)_6]$ as redox additive

- If: $Mn^{3+} \gg Mn^{2+}$ at 0.0VAu, then THa is TRUE.
- If: $Mn^{3+} \geqq Mn^{2+}$ at 0.0VAu, then THa is FALSE.
- If: $Mn^{3+} < Mn^{2+}$ at 0.0VAu, then THa is FALSE.

B- Using buffered Na_2SO_4 electrolyte (pH=7)

- If: $Mn^{3+} \gg Mn^{2+}$ at 0.0VAu, then THb is TRUE.
- If: $Mn^{3+} \geqq Mn^{2+}$ at 0.0VAu, then THb is FALSE.
- If: $Mn^{3+} < Mn^{2+}$ at 0.0VAu, then THb is FALSE.

10.3.3 *In-situ* STXM study of V_2O_5-based electrodes for supercapacitors

Vanadium pentoxide (V_2O_5) is one of the most promising electrode materials for supercapacitors due to its high theoretical specific capacity (2120 Fg^{-1}), mixed valance states (V^{3+}, V^{4+} and V^{5+}), and large lattice-spacing that facilitate the easy intercalation/deintercalation of electrolyte cations with larger ionic radii, such as Na^+ and K^+ (Chen et al., 2019). Nevertheless, its capacitive performances are significantly hindered by poor structural stability (caused by high dissolution of V_2O_5 in aqueous electrolyte) and low electrical conductivity (Zheng et al., 2018). On the other hand, conducting polymers such as polypyrrole (PPY), polythiophene (PTH), polyaniline (PANI), and polyacetylene (PA) attracted great attention as a potential electrode material for supercapacitors (Zhang et al., 2022). A composite of a binder-free PPY and V_2O_5 (PPY@V_2O_5) can improve the electrical conductivity of V_2O_5-based electrodes and prevent the dissolution of V_2O_5 into the electrolyte (Qian et al., 2014; Zhang et al., 2022).

One step electrodeposition of PPY@V_2O_5 can be performed using chronoamperometric method at +0.8$V_{Ag/AgCl}$ (Asen & Shahrokhian, 2017) (equivalent to +0.6V_{Au}, see Section **5.1.4**) using a mixture precursors of PPY and vanadyl acetate. <u>PPY is not soluble in water</u> and the particles size is ∼50–100 nm in diameter (Kausaite-Minkstimiene et al., 2015). Thus, it is important to use a dispersing agent such as quercetin to prevent the agglomeration.

Therefore, I suggest performing *in-situ* STXM studies on electrodeposited V_2O_5 and PPY@V_2O_5 to investigate the ability of PPY to suppress the dissolution of V_2O_5 to V^{2+} and V^{3+}. <u>However, it is crucial to use small molar ratio of PPY to prevent *in-situ* cell tubing blockage or thick deposition on WE.</u> Different oxidation states of vanadium oxides have different spectral shape and peak positions at V 2p, and O k edges, as presented in **Fig. 10.2A** and **10.2B**, respectively (Santos et al., 2022). Therefore, STXM can efficiently track the oxidation state change of V_2O_5 during oxidation/reduction processes.

Testable Hypothesis

Dissolution of V_2O_5 to V^{2+} and V^{3+} will be suppressed in the PPY@V_2O_5 composite compared to pure V_2O_5 material.

Predicted outcomes are:

- If: $V^{2+}/V^{3+} \ll V^{4+}$ at reductive potential compared to pure V_2O_5, then TH is TRUE.
- If: $V^{2+}/V^{3+} > V^{4+}$ at reductive potential compared to pure V_2O_5, then TH is FALSE.
- If: $V^{2+}/V^{3+} = V^{4+}$ at reductive potential compared to pure V_2O_5, then TH is FALSE.
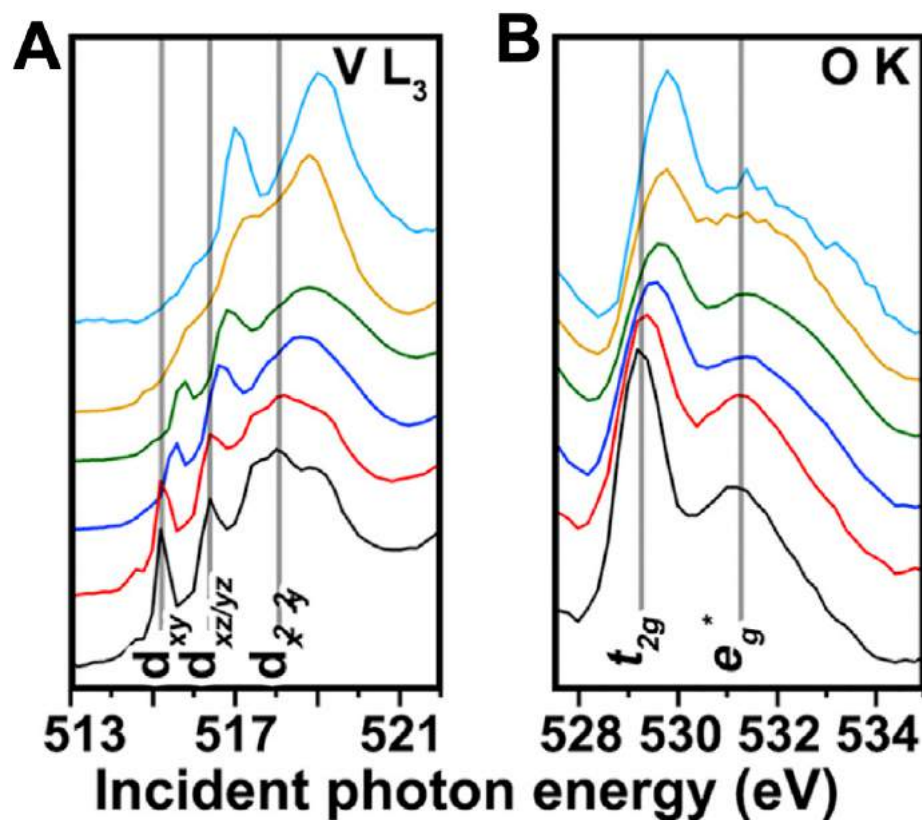
Figure 10.2 Absorption spectra of different oxidation states of vanadium oxides due to the intercalation of Li ion into the crystal structure of V_2O_5 cathode in LIB. (A) at V 2p edge. **(B)** at O K edge. Reprinted from (Santos et al., 2022). With permission from Elsevier.

10.3.4 *In-situ* STXM and *Operando* XAS studies of α-MnO₂ electrode in α-MnO₂/Zn-ion batteries

Zn-ion batteries (ZIBs) are attracting significant attention as a competitive alternative to Li-ion batteries (LIBs) owing to their relatively high operational voltage, low cost, and safe operation (Nguyen Thanh Tran et al., 2022). Among different cathode materials, manganese-based oxides, particularly α-MnO₂, are widely used as the positive electrode material in aqueous rechargeable ZIBs because of their natural abundance, low cost, low toxicity, and relatively high reduction potentials (Tran et al., 2021). However, due to the dissolution of the active cathode material into the electrolyte and the formation of irreversible phases, α-MnO₂-

ZIBs are typically limited by capacity fade (Alfaruqi et al., 2018; Rubel et al., 2022). Reversible Zn^{2+} intercalation/deintercalation combined with H^+ co-intercalation is considered the main redox mechanism in α-MnO_2-ZIBs. Nevertheless, the detailed mechanisms of the charging/discharging processes are not known and structure stability has not been fully addressed (Tran et al., 2021), (Zhao et al., 2019). Understanding how charge is efficiently stored in MnO_2 electrodes or across the electrode/electrolyte interface is the key to developing improved α-MnO_2-ZIBs electrodes.

During my PhD, I collaborated with Thomas Baker and Alejandra Espinoza (Higgins group), and Salient Energy (https://salientenergyinc.com) in a side project of α-MnO_2/ZIBs. STXM studies were performed on microtomed coin cell α-MnO_2/ZIB cathode samples that had been subjected to different electrochemical charging and discharging cycles. NEXAFS spectra of the microtome α-MnO_2 electrodes were measured with high spatial resolution at the Mn L_3, O 1s, Zn $L_{2,3}$, and C 1s edges. Spatially resolved (~40 nm) spectroscopy and quantitative chemical mapping at Mn L_3 and O 1s edges demonstrated that MnO_2 is reduced to both Mn^{3+} and Mn^{2+} oxidation states through a reversible $Mn^{4+} \leftrightarrow Mn^{3+}/Mn^{2+}$ redox reaction **(Fig. 10.3A and 10.3B)**. At the same time, some areas remain as MnO_2(IV), which may be attributed to the re-deposition of the dissoluble Mn species. However, this possibility cannot be confirmed through *ex-situ* measurements.

Investigating the intercalation of Zn cations in the discharged samples was challenging. Tracking the Zn signals at Zn $L_{2,3}$ edge showed Zn in electrode areas dominated by Mn^{2+}/Mn^{3+} species after 94 discharged samples (left in discharged state) **(Fig.10.3C)**. It was not clear if the Zn cation is a residual from the $ZnSO_4$(aq) electrolyte or if it was the result of formation of $ZnMn_2O_4$ (Mn^{3+}) through intercalation of Zn^{2+} ions into the α-MnO_2 crystal structure. Although measurements have already been performed on Zn/α-MnO_2 battery electrode samples to try to differentiate these possibilities, the results so far are inconclusive. Understanding the detailed redox mechanism and morphological changes remains challenging.
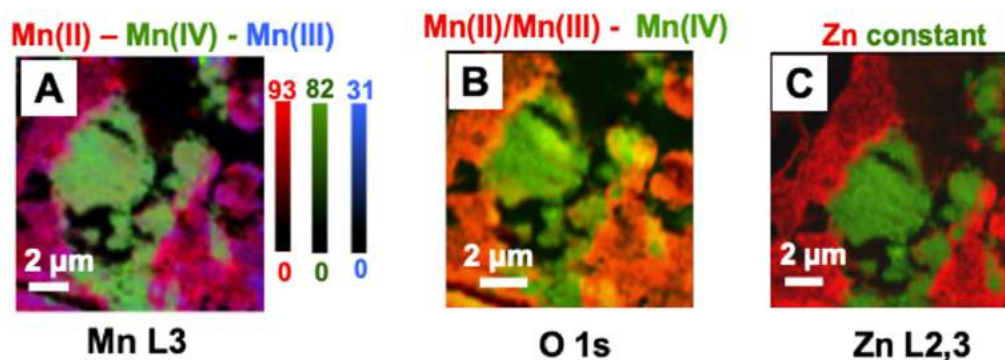
Figure 10.3 Quantitative chemical mapping microtome sample after 94 discharged cycles at (A) Mn L3 edge. **(B)** O 1s edge and **(C)** Zn L2,3 edge.

Therefore, I propose an interesting and useful *in-situ* STXM study would be to set up a Zn ion/α-MnO$_2$ system in the *in-situ* device, using ZnSO$_4$ as the electrolyte. The question to be answered is: *Is the Zn$^+$ or H$^+$ intercalation responsible for the electrochemical performance of α-MnO$_2$/Zn batteries?*

It is expected that, the H$^+$ can intercalate into of α-MnO$_2$ tunnel structure and the oxidation/reduction processes in α-MnO$_2$/Zn batteries take place through the Mn^{4+} $\leftrightarrow$ Mn^{3+} redox reaction based on the following equation (Pan et al., 2016):

$$MnO_2 + \tfrac{1}{2}Zn + \tfrac{x}{6}H_2O + \tfrac{1}{6}ZnSO_4 \leftrightarrow MnOOH + \tfrac{1}{6}ZnSO_4[Zn(OH_2)]_3 . xH_2O \quad \textbf{Eq. 10.8}$$

On the other hand, Zn$^+$ could also intercalate into the α-MnO$_2$ tunnel structure and form ZnMn$_2$O$_4$ based on the following equation (Meng et al., 2023; Rubel et al., 2022):

$$Zn + \ 2MnO_2 \leftrightarrow \ ZnMn_2O_4 \qquad\qquad \textbf{Eq. 10.9}$$

In order to perform this experiment, it is necessary to externally deposit the active material of α-MnO$_2$ on the WE and nanoparticles of Zn metal on the CE. While this is <u>very challenging</u>, some efforts in that direction have already been made using (i) a precise micromanipulator, (ii) a shadow mask chip (provided by Norcada), (ii) placing microtome sample sections on the WE. I already attempted to externally deposit active electrode powder on the WE, as presented in **Section 10.3.5**. The most applicable method to perform the deposition on the WE and CE is to use the shadow mask chip (**Fig. 10.7**). The shadow mask

has an aperture with a size of 50 μm x 70 μm over the WE. After the external deposition on WE, the mask's aperture can be repositioned on the CE, as illustrated in **Fig.10.4**.
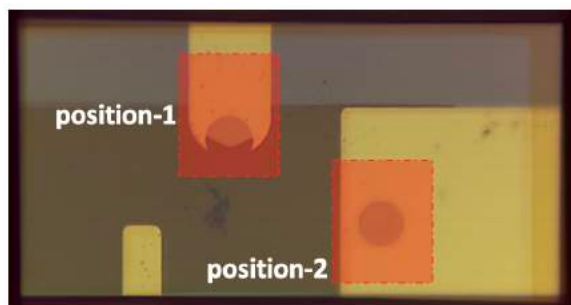
Figure 10.4   Optical microscope image of the SiNx window showing the position of the shadow mask aperture. position-1 on the WE, and position-2 on the CE

Testable Hypothesis

Zn^+ ions will intercalate into the α-MnO_2 tunnel structure and form $ZnMn_2O_4$.

Predicted outcomes are:

In-situ STXM measurements at Mn 2p and Zn 2p edges will be performed on samples in discharge state:

- If: Mn^{3+} detected while Zn signals increased, then TH is TRUE.
- If: Mn^{3+} detected while Zn signals didn't change, then TH is FALSE.

Furthermore, STXM measurements can be performed at different applied potentials (oxidative and reductive). Performing *in-situ* STXM measurements at the Zn 2p, Mn 2p and O 1s will provide insights into the redox reaction and degradation mechanism of α-MnO_2-ZIBs. Zn intercalation/deintercalation through charging/discharging processes can be confirmed If the spatial distribution of Zn can be differentiated at charging ($1.8V_{Zn}$) and discharging ($1.2V_{Zn}$) potentials. Since the potential difference between Zn and SHE is −0.762 V (Li et al., 2021), and $V_{Au} = V_{SHE} - 0.4$ (in pH 6) (see **Section 5.1.4**), the charging and discharging processes in the *in-situ* device will be performed in a potential window of +0.64 V to +0.04 V versus Au, which is within the *in-situ* device capability limits.

Despite the applicability of depositing α-MnO$_2$ on WE and Zn metal nanoparticles on CE in the proposed *in-situ* STXM experiment, X-ray penetration through the deposited materials at the Mn 2p edge may be challenging if the particle thickness is >100 nm or the electrolyte layer thickness is >3 μm, which significantly can attenuate the transmitted X-rays (see **Section 4.2.9**).

Therefore, and as an alternative method, I propose *in-situ/operando* XAS study at Mn K edge and Zn K edge to investigate the intercalation/deintercalation of Zn$^+$ ions during chagrining/discharging processes. The penetrating power of the hard X-rays (at Mn and Zn K edges) is much more than soft X-ray used in STXM, which allow using practical α-MnO$_2$ and Zn electrodes. **Fig. 10.5** presents *operando* X-ray absorption near edge structure (XANES) measurements of MnO$_2$/ZIB electrode at Mn K edge during different cycles (Wu et al., 2022). Tracking changes that may occur at Zn K edge during charging and discharging processes can support the hypothesis of intercalation/deintercalation of Zn$^+$ ions into α-MnO$_2$ crystal structure during charging/discharging processes.
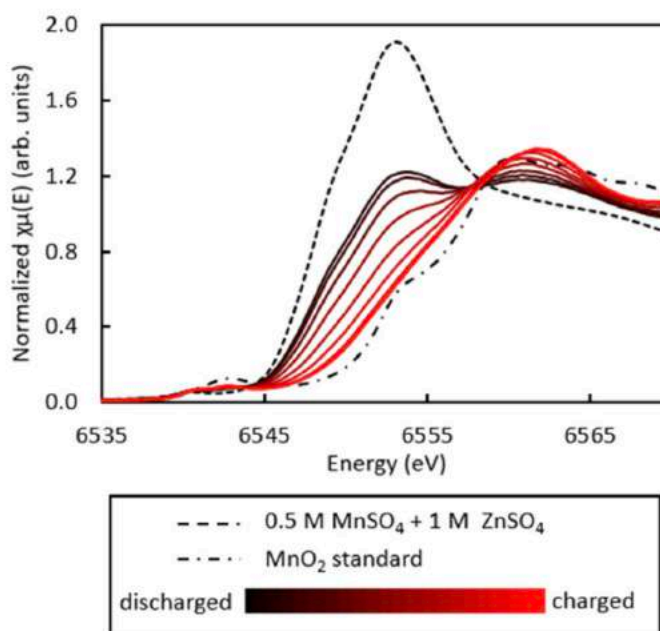
Figure 10.5 Operando XANES study of Aqueous MnO$_2$/ZIB in ZnSO$_4$ electrolyte. Reprinted from (Wu et al., 2022). With permission from American Chemical Society.

10.3.5 External deposition on microchips WE for *in-situ* STXM measurements

In order to enhance the flexibility of the *in-situ* device, it is desirable to develop capabilities to externally deposit powders on the working electrode. I have tried two different methods to externally deposit an electrocatalyst, Mn_3O_4 SC electrode material in this case (Yang et al., 2022), on the WE prior to bonding the two chips (E and F). These methods are:

I. Using a precise micromanipulator (provided by Obst group, Bayreuth University, Germany – Feb. 2023), an as-prepared Mn_3O_4 electrode material (1 mg) was suspended in 1 mL isopropanol/deionized water (1:1). 30 µl Nafion (Sigma-Aldrich, 5 wt % Nafion in ethanol) was added as a binder. The viscous solution was ultrasonicated for 15 min at room temperature. A pulled glass capillary tube attached to the micromanipulator was inserted in the top layer of the suspension to take up some of the solution. The tip of the capillary was then positioned on top of the WE under an optical microscope. Then, a very small volume at the tip of the capillary tube was pushed out using a micrometer drive (see **Fig. 10.6A** and **10.6B**).

II. Using shadow masks (provided by Norcada): The mask chip (15.0 mm x 7.0 mm) has an aperture with a size of 50 µm x 70 µm centered to the tip of the working electrode (chip E) (**Fig. 10.7A** and **10.7B**). The mask chip is attached to chip E with Kapton tape. Using a capillary tube, a small drop of the Mn_3O_4 suspended solution was placed over the WE through the mask chip aperture and left to dry at room temperature. After confirming the deposition on the WE under the optical microscope, the mask chip was carefully removed from chip E with the Kapton tape using a sharp tweezer **(Fig. 10.7C)**. Then chip E with a WE deposition was bonded to chip F (spacer).

These methods still have many challenges. One *in-situ* experiment has been performed on an externally deposited Mn_3O_4 SC electrode material. In that case a bubble was generated which removed the deposited particles from the WE. A solution more concentrated in the nafion binder should be explored to provide a more robust attachment to the WE. There are also significant concerns about the extent to which there is electrical contact between the particles in the deposit and the Au WE. Further improvement is required. The suspension recipe could be improved by preparing different suspension solutions of the electrocatalytic materials using different concentrations of Nafion (as a binder) and performing

electrochemical experiments similar to electrochemical and syringe pump flow rate setup of the *in-situ* STXM experiments under the optical microscope to get the right recipe of active material/binder that maintains the electrical conductivity and prevent the detaching of the deposited particles from the WE.
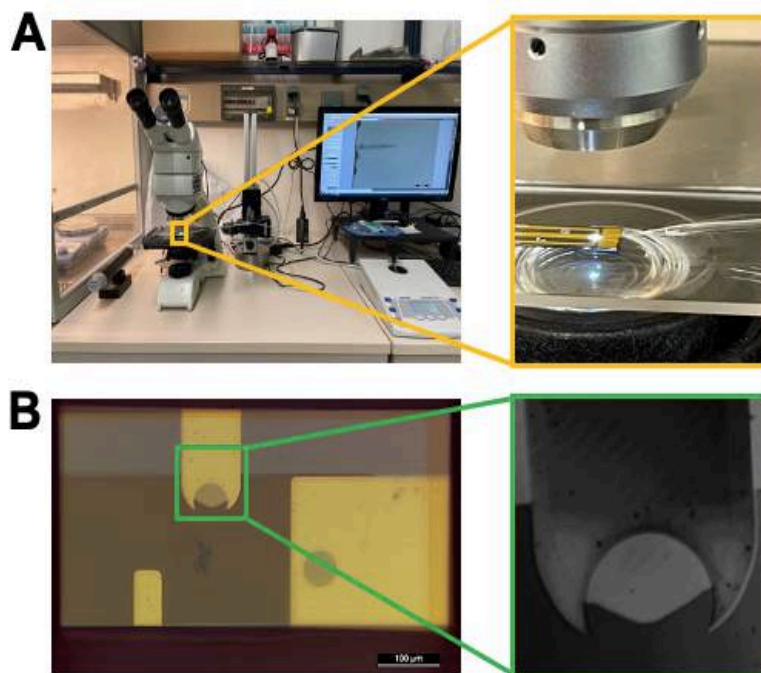
Figure 10.6 External deposition of Mn₃O₄ SC electrode material on WE using micromanipulator technique at the University of Bayreuth (Germany). (A) micromanipulator setup (The magnification showing chip E under the optical microscope while depositing the particles on the WE by the capillary tube). **(B)** optical microscope reflection image of the SiNx window after the deposition (The magnified image shows the WE after depositing material particles on the WE).
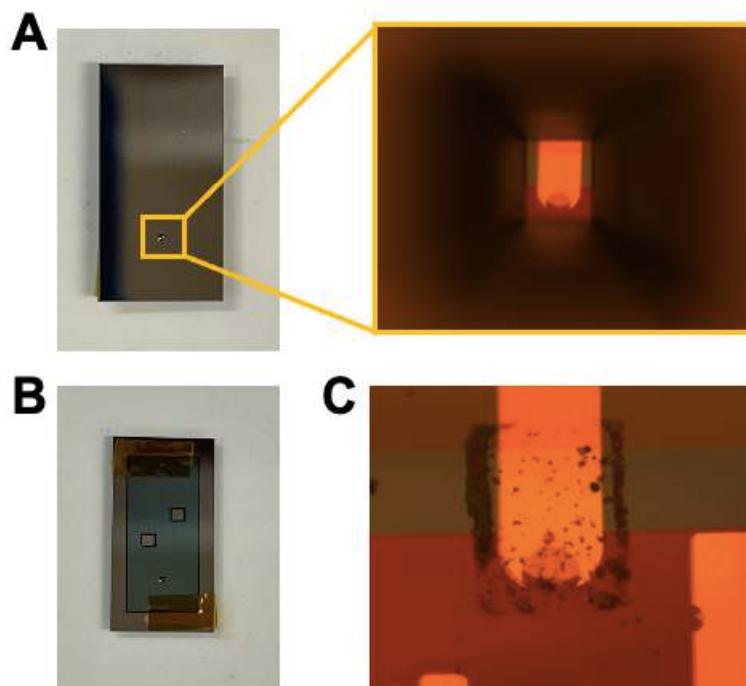
Figure 10.7 External deposition of Mn_3O_4 SC electrode material (Yang et al., 2022) on WE using Norcada shadow mask chip. (A) front side of the shadow mask chip showing the aperture over the WE (The magnification showing optical microscope image (20X) of WE through the mask chip). (B) back side of the shadow mask chip. (C) Mn_3O_4 deposited particles on WE under the optical microscope (20X) after removal of the shadow mask.

References

Aastrup, T., Persson, D., Wallinder, I. O., & Leygraf, C. (1998). In situ infrared reflection absorption spectroscopy studies of sulfuric acid formation on platinum and palladium surfaces. *Journal of the electrochemical Society*, *145*(2), 487.

Abbate, M., Goedkoop, J., De Groot, F., Grioni, M., Fuggle, J., Hofmann, S., Petersen, H., & Sacchi, M. (1992). Probing depth of soft x-ray absorption spectroscopy measured in total-electron-yield mode. *Surface and interface analysis*, *18*(1), 65-69.

Abderezzak, B. (2018). *Introduction to transfer phenomena in PEM fuel cells*. Elsevier.

Abruña, H. D., Kiya, Y., & Henderson, J. C. (2008). Batteries and electrochemical capacitors. *Physics Today*, *61*(12), 43-47.

Achkar, A., Regier, T., Monkman, E., Shen, K., & Hawthorn, D. (2011). Determination of total x-ray absorption coefficient using non-resonant x-ray emission. *Scientific reports*, *1*(1), 182.

Ade, H. (1998). Experimental Methods in the Physical Sciences (Vol. 32). *Academic Press, New York.*

Alfaruqi, M. H., Islam, S., Putro, D. Y., Mathew, V., Kim, S., Jo, J., Kim, S., Sun, Y.-K., Kim, K., & Kim, J. (2018). Structural transformation and electrochemical study of layered MnO2 in rechargeable aqueous zinc-ion battery. *Electrochimica Acta*, *276*, 1-11.

Arul, K. T., Chang, H.-W., Shiu, H.-W., Dong, C.-L., & Pong, W.-F. (2021). A review of energy materials studied by in situ/operando synchrotron x-ray spectro-microscopy. *Journal of Physics D: Applied Physics*, *54*(34), 343001.

Asen, P., & Shahrokhian, S. (2017). One step electrodeposition of V_2O_5/polypyrrole/graphene oxide ternary nanocomposite for preparation of a high performance supercapacitor. *International Journal of Hydrogen Energy*, *42*(33), 21073-21085.

Attwood, D. (2000). *Soft x-rays and extreme ultraviolet radiation: principles and applications*. Cambridge university press.

Augustyn, V., Simon, P., & Dunn, B. (2014). Pseudocapacitive oxide materials for high-rate electrochemical energy storage. *Energy & Environmental Science*, *7*(5), 1597-1614.

Awad, M., & Zhitomirsky, I. (2023). Boosting the activation rate and capacitance retention of MnOx electrodes prepared using capping agents. *Colloids and Surfaces A: Physicochemical and Engineering Aspects*, *676*, 132176.

Bard, A. J., Faulkner, L. R., & White, H. S. (2022). *Electrochemical methods: fundamentals and applications*. John Wiley & Sons.

Barkla, C. G. (1903). LXXV. Secondary radiation from gases subject to X-rays. *The London, Edinburgh, and Dublin Philosophical Magazine and Journal of Science*, *5*(30), 685-698.

Beckhoff, B., Klein, R., Krumrey, M., Scholze, F., Thornagel, R., & Ulm, G. (2000). X-ray detector calibration in the PTB radiometry laboratory at the electron storage ring BESSY II. *Nuclear Instruments and Methods in Physics Research Section A: Accelerators, Spectrometers, Detectors and Associated Equipment*, *444*(1-2), 480-483.

Beknalkar, S., Teli, A., Bhat, T., Pawar, K., Patil, S., Harale, N., Shin, J., & Patil, P. (2022). Mn3O4 based materials for electrochemical supercapacitors: Basic principles, charge storage mechanism, progress, and perspectives. *Journal of Materials Science & Technology*, *130*, 227-248.

Belmonte, N., Luetto, C., Staulo, S., Rizzi, P., & Baricco, M. (2017). Case studies of energy storage with fuel cells and batteries for stationary and mobile applications. *Challenges*, *8*(1), 9.

Bhatia, A., Cretu, S., Hallot, M., Folastre, N., Berthe, M., Troadec, D., Roussel, P., Pereira-Ramos, J. P., Baddour-Hadjean, R., & Lethien, C. (2022). In Situ Liquid Electrochemical TEM Investigation of $LiMn_{1.5}Ni_{0.5}O_4$ Thin Film Cathode for Micro-Battery Applications. *Small Methods*, *6*(2), 2100891.

Bi, R., Liu, G., Zeng, C., Wang, X., Zhang, L., & Qiao, S. Z. (2019). 3D Hollow α-MnO_2 framework as an efficient electrocatalyst for lithium–oxygen batteries. *Small*, *15*(10), 1804958.

Biesheuvel, P., Van Soestbergen, M., & Bazant, M. Z. (2009). Imposed currents in galvanic cells. *Electrochimica Acta*, *54*(21), 4857-4871.

Biesinger, M. C., Payne, B. P., Grosvenor, A. P., Lau, L. W., Gerson, A. R., & Smart, R. S. C. (2011). Resolving surface chemical states in XPS analysis of first row transition metals, oxides and hydroxides: Cr, Mn, Fe, Co and Ni. *Applied Surface Science*, *257*(7), 2717-2730.

Bilal, M., Rehman, Z. U., Hou, J., Ali, S., Ullah, S., & Ahmad, J. (2022). Metal oxide–carbon composite: synthesis and properties by using conventional enabling technologies. In *Metal Oxide-Carbon Hybrid Materials* (pp. 25-60). Elsevier.

Bohr, N. (1913). I. On the constitution of atoms and molecules. *The London, Edinburgh, and Dublin Philosophical Magazine and Journal of Science*, *26*(151), 1-25.

Borch, T., Kretzschmar, R., Kappler, A., Cappellen, P. V., Ginder-Vogel, M., Voegelin, A., & Campbell, K. (2010). Biogeochemical redox processes and their impact on contaminant dynamics. *Environmental science & technology*, *44*(1), 15-23.

Bourdelle, F., Lloret, E., Durand, C., & Airaghi, L. (2021). Evaluation of scanning transmission X-ray microscopy at the Mn L2,3-edges as a potential probe for manganese redox state in natural silicates. *Physics and Chemistry of Minerals*, *48*(4), 18.

Bozzini, B., D'Urzo, L., Gianoncelli, A., Kaulich, B., Kiskinova, M., Prasciolu, M., & Tadjeddine, A. (2009a). Synchrotron-based in situ soft X-ray microscopy of Ag corrosion in aqueous chloride solution. *Journal of Physics: Conference Series*, *186*(1), 2103.

Bozzini, B., D'Urzo, L., Gianoncelli, A., Kaulich, B., Kiskinova, M., Prasciolu, M., & Tadjeddine, A. (2008). In situ soft X-ray dynamic microscopy of electrochemical processes. *Electrochemistry communications*, *10*(11), 1680-1683.

Bozzini, B., D'Urzo, L., Gianoncelli, A., Kaulich, B., Prasciolu, M., Sgura, I., Tondo, E., & Kiskinova, M. (2009b). An in situ synchrotron-based soft X-ray microscopy investigation of Ni electrodeposition in a thin-layer cell. *The Journal of Physical Chemistry C*, *113*(22), 9783-9787.

Bozzini, B., Gianoncelli, A., Bocchetta, P., Dal Zilio, S., & Kourousias, G. (2014). Fabrication of a sealed electrochemical microcell for in situ soft X-ray microspectroscopy and testing with in situ co-polypyrrole composite electrodeposition for Pt-free oxygen electrocatalysis. *Analytical chemistry*, *86*(1), 664-670.

Bozzini, B., Gianoncelli, A., Kaulich, B., Kiskinova, M., Mele, C., & Prasciolu, M. (2011a). Corrosion of Ni in 1-butyl-1-methyl-pyrrolidinium bis (trifluoromethylsulfonyl) amide room-temperature ionic liquid: an in situ X-ray imaging and spectromicroscopy study. *Physical Chemistry Chemical Physics*, *13*(17), 7968-7974.

Bozzini, B., Gianoncelli, A., Kaulich, B., Mele, C., Prasciolu, M., & Kiskinova, M. (2012b). Electrodeposition of manganese oxide from eutectic urea/choline chloride ionic liquid: An in situ study based on soft X-ray spectromicroscopy and visible reflectivity. *Journal of Power Sources*, *211*, 71-76.

Bozzini, B., Kourousias, G., Gianoncelli, A., Jones, M. W., Van Riessen, G., & Kiskinova, M. (2017). Soft X-ray ptychography as a tool for in operando morphochemical studies of electrodeposition processes with nanometric lateral resolution. *Journal of Electron Spectroscopy and Related Phenomena*, *220*, 147-155.

Bozzini, B., Mele, C., Gianoncelli, A., Kaulich, B., Kiskinova, M., & Prasciolu, M. (2011b). In situ X-ray spectromicroscopy study of bipolar plate material stability for nano-fuel-cells with ionic-liquid electrolyte. *Microelectronic engineering*, *88*(8), 2456-2458.

Bragg, W. H., & Bragg, W. L. (1913). The reflection of X-rays by crystals. *Proceedings of the Royal Society of London. Series A, Containing Papers of a Mathematical and Physical Character*, *88*(605), 428-438.

Buckley, C., Rarback, H., Alforque, R., Shu, D., Ade, H., Hellman, S., Iskander, N., Kirz, J., Lindaas, S., & McNulty, I. (1989). Soft-x-ray imaging with the 35 period undulator at the NSLS. *Review of Scientific Instruments*, *60*(7), 2444-2447.

Burns, R. (1993). Outline of crystal field theory. *Cambridge Topics in Mineral Physics and Chemistry. Cambridge University Press*, 7.

Burns, R. G. (1993). *Mineralogical applications of crystal field theory*. Cambridge university press.

Butt, A. M., Batool, M., Abi Jaoude, M., & Qurashi, A. (2023). Recent Advancement in Manganese-based Electrocatalyst for Green Hydrogen Production. *Journal of Electroanalytical Chemistry*, 117393.

Cairns, E. J. (2004). Batteries, overview. *Encyclopedia of Energy*, *1*, 117-126.

Cao, C., Toney, M. F., Sham, T.-K., Harder, R., Shearing, P. R., Xiao, X., & Wang, J. (2020). Emerging X-ray imaging technologies for energy materials. *Materials Today*, *34*, 132-147.

Cao, J., Li, X., Wang, Y., Walsh, F. C., Ouyang, J.-H., Jia, D., & Zhou, Y. (2015). Materials and fabrication of electrode scaffolds for deposition of MnO2 and their true performance in supercapacitors. *Journal of Power Sources*, *293*, 657-674.

Cao, X., Li, H., Qiao, Y., Jia, M., Li, X., Cabana, J., & Zhou, H. (2021). Stabilizing anionic redox chemistry in a Mn-based layered oxide cathode constructed by Li-deficient pristine state. *Advanced Materials*, *33*(2), 2004280.

Chakraborty, S., & Mary, N. (2022). An overview on supercapacitors and its applications. *Journal of the electrochemical Society*, *169*(2), 020552.

Chang, J.-K., Lee, M.-T., & Tsai, W.-T. (2007). In situ Mn K-edge X-ray absorption spectroscopic studies of anodically deposited manganese oxide with relevance to supercapacitor applications. *Journal of Power Sources*, *166*(2), 590-594.

Chen, D., Ding, D., Li, X., Waller, G. H., Xiong, X., El-Sayed, M. A., & Liu, M. (2015). Probing the charge storage mechanism of a pseudocapacitive MnO_2 electrode using in operando Raman spectroscopy. *Chemistry of materials*, *27*(19), 6608-6619.

Chen, D., Li, J., & Wu, Q. (2019). Review of V_2O_5-based nanomaterials as electrode for supercapacitor. *Journal of Nanoparticle Research*, *21*, 1-15.

Chen, H., Zeng, S., Chen, M., Zhang, Y., & Li, Q. (2017). A new insight into the rechargeable mechanism of manganese dioxide based symmetric supercapacitors. *RSC advances*, *7*(14), 8561-8566.

Chen, S.-M., Ramachandran, R., Mani, V., & Saraswathi, R. (2014). Recent advancements in electrode materials for the highperformance electrochemical supercapacitors: a review. *International Journal of Electrochemical Science*, *9*(8), 4072-4085.

Chen, Y., Jing, C., Fu, X., Shen, M., Cao, T., Huo, W., Liu, X., Yao, H.-C., Zhang, Y., & Yao, K. X. (2020). In-situ fabricating MnO_2 and its derived FeOOH nanostructures on mesoporous carbon towards high-performance asymmetric supercapacitor. *Applied Surface Science*, *503*, 144123.

Chodankar, N. R., Pham, H. D., Nanjundan, A. K., Fernando, J. F., Jayaramulu, K., Golberg, D., Han, Y. K., & Dubal, D. P. (2020). True meaning of pseudocapacitors and their performance metrics: asymmetric versus hybrid supercapacitors. *Small*, *16*(37), 2002806.

Choudhary, Y. S., Jothi, L., & Nageswaran, G. (2017). Electrochemical characterization. In *Spectroscopic Methods for Nanomaterials Characterization* (pp. 19-54). Elsevier.

Chua, K. H., Bong, H. L., Lim, Y. S., Wong, J., & Wang, L. (2020). The state-of-the-arts of peak shaving technologies: A review. 2020 International Conference on Smart Grid and Clean Energy Technologies (ICSGCE),

Crapnell, R. D., & Banks, C. E. (2022). Electroanalytical overview: The determination of manganese. *Sensors and Actuators Reports*, *4*, 100110.

Cui, M., & Meng, X. (2020). Overview of transition metal-based composite materials for supercapacitor electrodes. *Nanoscale Advances*, *2*(12), 5516-5528.

Cutler, J., Chapman, D., Dallin, L., & Lamb, R. (2017). The Brightest Light in Canada: The Canadian Light Source. *Quantum Beam Science*, *1*(1), 4.

Cutler, J., Chapman, D., & Lamb, R. (2018). Brightest light in canada: The canadian light source. *Synchrotron Radiation News*, *31*(1), 26-31.

Cutler, J., Christensen, C., Kotzer, T., Ogunremi, T., Pushparajah, T., & Warner, J. (2007). The Canadian Light Source–A new tool for industrial research. *Nuclear Instruments and Methods in Physics Research Section B: Beam Interactions with Materials and Atoms*, *261*(1-2), 859-862.

Dai, H., Zhou, R., Zhang, Z., Zhou, J., & Sun, G. (2022). Design of manganese dioxide for supercapacitors and zinc-ion batteries: similarities and differences. *Energy Mater.*, *2*, 200040.

Dai, Z., Peng, C., Chae, J. H., Ng, K. C., & Chen, G. Z. (2015). Cell voltage versus electrode potential range in aqueous supercapacitors. *Scientific reports*, *5*(1), 9854.

De Groot, F., & Kotani, A. (2008). *Core level spectroscopy of solids*. CRC press.

de Groot, F. M., de Smit, E., van Schooneveld, M. M., Aramburo, L. R., & Weckhuysen, B. M. (2010). In-situ scanning transmission X-ray microscopy of catalytic solids and related nanomaterials. *ChemPhysChem*, *11*(5), 951-962.

de Groot, F. M., Fuggle, J., Thole, B., & Sawatzky, G. (1990). 2p x-ray absorption of 3d transition-metal compounds: An atomic multiplet description including the crystal field. *Physical Review B*, *42*(9), 5459.

Dell, R., & Rand, D. A. J. (2001). Understanding batteries. *Royal society of chemistry*, *doi.org/10.1039/9781847552228*.

Deslattes, R. D., Kessler Jr, E. G., Indelicato, P., De Billy, L., Lindroth, E., & Anton, J. (2003). X-ray transition energies: new approach to a comprehensive evaluation. *Reviews of Modern Physics*, *75*(1), 35.

Devaraj, S., & Munichandraiah, N. (2009). EQCM investigation of the electrodeposition of MnO_2 and its capacitance behavior. *Electrochemical and Solid-State Letters*, *12*(9), F21.

Dey, S., & Kumar, V. P. (2020). The performance of highly active manganese oxide catalysts for ambient conditions carbon monoxide oxidation. *Current Research in Green and Sustainable Chemistry*, *3*, 100012.

Divyashree, A., & Hegde, G. (2015). Activated carbon nanospheres derived from bio-waste materials for supercapacitor applications–a review. *RSC advances*, *5*(107), 88339-88352.

Dokko, K., Shi, Q., Stefan, I. C., & Scherson, D. A. (2003). In situ Raman spectroscopy of single microparticle Li$^+$− intercalation electrodes. *The Journal of Physical Chemistry B*, *107*(46), 12549-12554.

Dong, C. L., & Vayssieres, L. (2018). In Situ/Operando X-ray Spectroscopies for Advanced Investigation of Energy Materials. *Chemistry–A European Journal*, *24*(69), 18356-18373.

dos Santos, J. P. A., Rufino, F. C., Ota, J. I. Y., Fernandes, R. C., Vicentini, R., Pagan, C. J., Da Silva, L. M., & Zanin, H. (2023). Best practices for electrochemical characterization of supercapacitors. *Journal of Energy Chemistry*.

Duan, Q., Wang, Y., Dong, S., & Denis, Y. (2022). Facile electrode additive stabilizes structure of electrolytic MnO_2 for mild aqueous rechargeable zinc-ion battery. *Journal of Power Sources*, *528*, 231194.

Dynes, J. J., Arthur, Z., Read, S., Stobbs, J., Regier, T. Z., & Rosendahl, S. M. (2018). Correlative Spectromicroscopy Software Development on the SGM and Mid-IR Beamlines at the CLS. *Microscopy and Microanalysis*, *24*(S2), 494-495.

Edenhofer, O., Seyboth, K., & Shogren, J. (2013). Intergovernmental panel on climate change (IPCC). In *Encyclopedia of Energy, Natural Resource, and Environmental Economics (Volume 1: ENERGY)* (pp. 48-56). Elsevier.

Eftekhari, A., & Mohamedi, M. (2017). Tailoring pseudocapacitive materials from a mechanistic perspective. *Materials today energy*, *6*, 211-229.

Elliott, W., Salemmilani, R., Mubeen, S., Meinhart, C. D., Stucky, G. D., & Moskovits, M. (2019). Changes in the structure of electrodeposited manganese oxide water oxidation catalysts revealed by in-operando Raman spectroscopy. *Journal of catalysis*, *371*, 287-290.

Ellis, T., & Hallin, E. (2011). Status of the CLS-New Opportunities for Physics Research in Canada. *Physics in Canada*, *67*, 21-24.

Elmaci, G., Cerci, S., & Sunar-Cerci, D. (2019). The evaluation of the long-term stability of α-MnO$_2$ based OER electrocatalyst in neutral medium by using data processing approach. *Journal of Molecular Structure*, *1195*, 632-640.

Falcone, R., Jacobsen, C., Kirz, J., Marchesini, S., Shapiro, D., & Spence, J. (2011). New directions in X-ray microscopy. *Contemporary Physics*, *52*(4), 293-318.

Fan, Z., Yan, J., Wei, T., Zhi, L., Ning, G., Li, T., & Wei, F. (2011). Asymmetric supercapacitors based on graphene/MnO$_2$ and activated carbon nanofiber electrodes with high power and energy density. *Advanced Functional Materials*, *21*(12), 2366-2375.

Fan, Z., Zhang, L., Baumann, D., Mei, L., Yao, Y., Duan, X., Shi, Y., Huang, J., Huang, Y., & Duan, X. (2019). In situ transmission electron microscopy for energy materials and devices. *Advanced Materials*, *31*(33), 1900608.

Fang, G., Zhu, C., Chen, M., Zhou, J., Tang, B., Cao, X., Zheng, X., Pan, A., & Liang, S. (2019). Suppressing manganese dissolution in potassium manganate with rich oxygen defects engaged high-energy-density and durable aqueous zinc-ion battery. *Advanced Functional Materials*, *29*(15), 1808375.

Feggeler, T., Levitan, A., Marcus, M. A., Ohldag, H., & Shapiro, D. A. (2023). Scanning transmission X-ray microscopy at the Advanced Light Source. *Journal of Electron Spectroscopy and Related Phenomena*, *267*, 147381.

Ferrario, A., Scaramuzza, M., Pasqualotto, E., De Toni, A., & Paccagnella, A. (2012). Development of a disposable gold electrodes-based sensor for electrochemical measurements of cDNA hybridization. *Procedia Chemistry*, *6*, 36-45.

Fischel, M. H., Fischel, J. S., Lafferty, B. J., & Sparks, D. L. (2015). The influence of environmental conditions on kinetics of arsenite oxidation by manganese-oxides. *Geochemical transactions*, *16*, 1-10.

Foo, C. Y., Sumboja, A., Tan, D. J. H., Wang, J., & Lee, P. S. (2014). Flexible and highly scalable V$_2$O$_5$-rGO electrodes in an organic electrolyte for supercapacitor devices. *Advanced Energy Materials*, *4*(12), 1400236.

Förster, J.-D., Bykova, I., Macholdt, D. S., Jochum, K. P., Kappl, M., Kilcoyne, A. D., Müller, M., Sorowka, A., Weber, B., & Weigand, M. (2021). X-ray Microspectroscopy and Ptychography on Nanoscale Structures in Rock Varnish. *The Journal of Physical Chemistry C*, *125*(41), 22684-22697.

Frackowiak, E., & Béguin, F. (2013). Supercapacitors: Materials, Systems and Applications. *Poznan: Wiley-VCH Verlag GmbH & Co*.

Frati, F., Hunault, M. O., & De Groot, F. M. (2020). Oxygen K-edge X-ray absorption spectra. *Chemical reviews*, *120*(9), 4056-4110.

Frenzel, N., Hartley, J., & Frisch, G. (2017). Voltammetric and spectroscopic study of ferrocene and hexacyanoferrate and the suitability of their redox couples as internal standards in ionic liquids. *Physical Chemistry Chemical Physics*, *19*(42), 28841-28852.

Galezowski, L., Recham, N., Larcher, D., Miot, J., Skouri-Panet, F., & Guyot, F. (2020). Microbially induced mineralization of layered Mn oxides electroactive in Li batteries. *Frontiers in microbiology*, *11*, 2031.

Ganguly, D., Pahari, D., Das, N., Howli, P., Das, B., Banerjee, D., & Chattopadhyay, K. (2016). All-amorphous CNT-MnO_2 nanoflaky hybrid for improved supercapacitor applications. *Journal of Electroanalytical Chemistry*, *778*, 12-22.

Garvie, L., & Craven, A. (1994). High-resolution parallel electron energy-loss spectroscopy of Mn L2,3-edges in inorganic manganese compounds. *Physics and Chemistry of Minerals*, *21*(4), 191-206.

Geyer, U., Siegel, F., Kreutzer, A., Blaudeck, T., & Reinhard, R. B. (2009). Printing electrode materials for rechargeable lithium thin-film batteries. *LOPE-C Conference*, *(ISBN 978-3-00-028063-4)*.

Ghosh, S. K. (2020). Diversity in the family of manganese oxides at the nanoscale: from fundamentals to applications. *ACS omega*, *5*(40), 25493-25504.

Ghosh, S. K., & Ghosh, B. K. (2020). Fossil fuel consumption trend and global warming scenario: Energy overview. *Glob J Eng Sci*, *5*(2), 2641-2039.

Gilbert, B., Frazer, B., Belz, A., Conrad, P., Nealson, K., Haskel, D., Lang, J., Srajer, G., & De Stasio, G. (2003). Multiple scattering calculations of bonding and X-ray absorption spectroscopy of manganese oxides. *The Journal of Physical Chemistry A*, *107*(16), 2839-2847.

Gogotsi, Y., & Penner, R. M. (2018). Energy storage in nanomaterials–capacitive, pseudocapacitive, or battery-like? *ACS nano*, *12*(3), 2081-2083.

Goodenough, J. B., Abruna, H. D., & Buchanan, M. V. (2007). Basic research needs for electrical energy storage. . *report of the basic energy sciences workshop on electrical energy storage, april 2-4, 2007*, *DOI: 10.2172/935429*.

Gorlin, Y., Chung, C.-J., Benck, J. D., Nordlund, D., Seitz, L., Weng, T.-C., Sokaras, D., Clemens, B. M., & Jaramillo, T. F. (2014). Understanding interactions between manganese oxide and gold that lead to enhanced activity for electrocatalytic water oxidation. *Journal of the American Chemical Society*, *136*(13), 4920-4926.

Greaves, G., Simkiss, K., Taylor, M., & Binsted, N. (1984). The local environment of metal sites in intracellular granules investigated by using X-ray-absorption spectroscopy. *Biochemical Journal*, *221*(3), 855-868.

Grieshaber, D., MacKenzie, R., Vörös, J., & Reimhult, E. (2008). Electrochemical biosensors-sensor principles and architectures. *Sensors*, *8*(3), 1400-1458.

Guay, D., Stewart-Ornstein, J., Zhang, X., & Hitchcock, A. P. (2005). In situ spatial and time-resolved studies of electrochemical reactions by scanning transmission X-ray microscopy. *Analytical chemistry*, *77*(11), 3479-3487.

Gulzar, U., Goriparti, S., Miele, E., Li, T., Maidecchi, G., Toma, A., De Angelis, F., Capiglia, C., & Zaccaria, R. P. (2016). Next-generation textiles: from embedded supercapacitors to lithium ion batteries. *Journal of Materials Chemistry A*, *4*(43), 16771-16800.

Guo, D., Hu, Z., Li, Q., Bian, L., Song, Y., & Liu, X. (2022). Mixed-valence manganese oxide/reduced graphene oxide composites with enhanced pseudocapacitive performance. *Journal of Materials Science*, 1-13.

Guo, W., Yu, C., Li, S., Wang, Z., Yu, J., Huang, H., & Qiu, J. (2019). Strategies and insights towards the intrinsic capacitive properties of MnO_2 for supercapacitors: challenges and perspectives. *Nano Energy*, *57*, 459-472.

Guo, X., Zhou, J., Bai, C., Li, X., Fang, G., & Liang, S. (2020). Zn/MnO_2 battery chemistry with dissolution-deposition mechanism. *Materials today energy*, *16*, 100396.

Haas, O., & Cairns, E. J. (1999). Electrochemical energy storage. *Annual Reports Section" C"(Physical Chemistry)*, *95*, 163-198.

Han, S., Park, S., Yi, S.-H., Im, W. B., & Chun, S.-E. (2020). Effect of potential and current on electrodeposited MnO_2 as a pseudocapacitor electrode: Surface morphology/chemistry and stability. *Journal of Alloys and Compounds*, *831*, 154838.

Han, Z. J., Bo, Z., Seo, D. H., Pineda, S., Wang, Y., Yang, H. Y., & Ostrikov, K. (2016). High pseudocapacitive performance of MnO_2 nanowires on recyclable electrodes. *ChemSusChem*, *9*(9), 1020-1026.

Hardwick, L. J., Ruch, P. W., Hahn, M., Scheifele, W., Kötz, R., & Novák, P. (2008). In situ Raman spectroscopy of insertion electrodes for lithium-ion batteries and supercapacitors: First cycle effects. *Journal of Physics and Chemistry of Solids*, *69*(5-6), 1232-1237.

Hashem, A. M., Abuzeid, H. M., Narayanan, N., Ehrenberg, H., & Julien, C. (2011). Synthesis, structure, magnetic, electrical and electrochemical properties of Al, Cu and Mg doped MnO_2. *Materials Chemistry and Physics*, *130*(1-2), 33-38.

Held, P., & Bohatý, L. (2002). Manganese (II) sulfate tetrahydrate (ilesite). *Acta Crystallographica Section E: Structure Reports Online*, *58*(12), i121-i123.

Hem, J. D. (1963). Chemical equilibria and rates of manganese oxidation. *US Government printing office*, *https://doi.org/10.3133/wsp1667A*.

Hitchcock, A., Johansson, G., Mitchell, G., Keefe, M., & Tyliszcak, T. (2008). 3-d chemical imaging using angle-scan nanotomography in a soft X-ray scanning transmission X-ray microscope. *Applied Physics A*, *92*, 447-452.

Hitchcock, A., Qin, Z., Rosendahl, S. M., Lee, V., Reynolds, M., & Hosseinkhannazer, H. (2016). Electro-deposition of Cu studied with in situ electrochemical scanning transmission x-ray microscopy. AIP conference proceedings,

Hitchcock, A. P. (2012). Soft X-ray imaging and spectromicroscopy. *Handbook of nanoscopy*, 745-791.

Hitchcock, A. P. (2015). Soft X-ray spectromicroscopy and ptychography. *Journal of Electron Spectroscopy and Related Phenomena*, *200*, 49-63.

Hitchcock, A. P. (2022). 3 Polymer surface characterization by near-edge X-ray absorption fine structure spectroscopy. *Polymer Surface Characterization*, *De Gruyter, Berlin, Germany* 89.

Hitchcock, A. P. (2023a). Analysis of X-ray images and spectra (aXis2000): A toolkit for the analysis of X-ray spectromicroscopy data. *Journal of Electron Spectroscopy and Related Phenomena*, *266*, 147360.

Hitchcock, A. P. (2023b). PEMFC analysis using soft X-ray spectromicroscopy: methods and applications. *PEM Fuel Cells: Characterization and Modeling*, 137-196.

Hitchcock, A. P., Berejnov, V., Lee, V., West, M., Colbow, V., Dutta, M., & Wessel, S. (2014). Carbon corrosion of proton exchange membrane fuel cell catalyst layers studied by scanning transmission X-ray microscopy. *Journal of Power Sources*, *266*, 66-78.

Hitchcock, A. P., Dynes, J. J., Johansson, G., Wang, J., & Botton, G. (2008). Comparison of NEXAFS microscopy and TEM-EELS for studies of soft matter. *Micron*, *39*(6), 741-748.

Hitchcock, A. P., & Toney, M. F. (2014). Spectromicroscopy and coherent diffraction imaging: focus on energy materials applications. *Journal of Synchrotron Radiation*, *21*(5), 1019-1030.

Hitchcock, A. P., Zhang, C., Eraky, H., Shahcheraghi, L., Ismail, F., & Higgins, D. (2021). In-situ and Operando Studies with Soft X-Ray Transmission Spectromicroscopy. *Microscopy and Microanalysis*, *27*(S2), 59-60.

Hosseini, S. S., Badri, A., & Parvania, M. (2014). A survey on mobile energy storage systems (MESS): Applications, challenges and solutions. *Renewable and Sustainable Energy Reviews*, *40*, 161-170.

Howells, M., Jacobsen, C., Warwick, T., & Van den Bos, A. (2007). Principles and applications of zone plate X-ray microscopes. *Science of microscopy*, 835-926.

https://sgm.lightsource.ca. (2023 Nov. 19).

Hu, C.-C., Wu, Y.-T., & Chang, K.-H. (2008). Low-temperature hydrothermal synthesis of Mn_3O_4 and MnOOH single crystals: determinant influence of oxidants. *Chemistry of materials*, *20*(9), 2890-2894.

Hu, Q., Gu, Z., Zheng, X., & Zhang, X. (2016). Three-dimensional Co_3O_4@ NiO hierarchical nanowire arrays for solid-state symmetric supercapacitor with enhanced electrochemical performances. *Chemical Engineering Journal*, *304*, 223-231.

Hu, Y., & Wang, J. (2015). MnOx nanosheets for improved electrochemical performances through bilayer nano-architecting. *Journal of Power Sources*, *286*, 394-399.

Hu, Y., Wu, Y., & Wang, J. (2018). Manganese-oxide-based electrode materials for energy storage applications: how close are we to the theoretical capacitance? *Advanced Materials*, *30*(47), 1802569.

Hu, Y., Zhang, Y., Yuan, D., Li, X., Cai, Y., & Wang, J. (2017). Controllable structure transitions of Mn_3O_4 nanomaterials and their effects on electrochemical properties. *Nanoscale Horizons*, *2*(6), 326-332.

Huang, H., Wang, J., Yang, X., Hu, R., Liu, J., Zhang, L., & Zhu, M. (2020). Unveiling the advances of nanostructure design for alloy-type potassium-ion battery anodes via in situ TEM. *Angewandte Chemie*, *132*(34), 14612-14618.

Huang, J., Yuan, K., & Chen, Y. (2022). Wide voltage aqueous asymmetric supercapacitors: advances, strategies, and challenges. *Advanced Functional Materials*, *32*(4), 2108107.

Huang, M., Li, F., Dong, F., Zhang, Y. X., & Zhang, L. L. (2015). MnO_2-based nanostructures for high-performance supercapacitors. *Journal of Materials Chemistry A*, *3*(43), 21380-21423.

Huang, M., Zhang, Y., Li, F., Zhang, L., Wen, Z., & Liu, Q. (2014). Facile synthesis of hierarchical $Co_3O_4@ MnO_2$ core–shell arrays on Ni foam for asymmetric supercapacitors. *Journal of Power Sources*, *252*, 98-106.

Huang, W., Chen, J., Wang, G., Yao, Y., Zhuang, X., Pankow, R. M., Cheng, Y., Marks, T. J., & Facchetti, A. (2021). Dielectric materials for electrolyte gated transistor applications. *Journal of Materials Chemistry C*, *9*(30), 9348-9376.

Huang, Z.-H., Song, Y., & Liu, X.-X. (2019). Boosting operating voltage of vanadium oxide-based symmetric aqueous supercapacitor to 2 V. *Chemical Engineering Journal*, *358*, 1529-1538.

Hwang, S., Chen, X., Zhou, G., & Su, D. (2020). In situ transmission electron microscopy on energy-related catalysis. *Advanced Energy Materials*, *10*(11), 1902105.

Hynek, D. J., Pondick, J. V., & Cha, J. J. (2019). The development of 2D materials for electrochemical energy applications: A mechanistic approach. *APL materials*, *7*(3), 030902.

Iamprasertkun, P., Tanggarnjanavalukul, C., Krittayavathananon, A., Khuntilo, J., Chanlek, N., Kidkhunthod, P., & Sawangphruk, M. (2017). Insight into charge storage mechanisms of layered MnO_2 nanosheets for supercapacitor electrodes: in situ electrochemical X-ray absorption spectroscopy. *Electrochimica Acta*, *249*, 26-32.

Ingino, P., Eraky, H., Zhang, C., Hitchcock, A. P., & Obst., M. (2024). Soft X-ray spectromicroscopic proof of a reversible oxidation/reduction of individual microbial biofilm structures using a novel microfluidic in situ electrochemical device. *(in preparation)*.

Jacobsen, Wirick, Flynn, & Zimba. (2000). Soft X-ray spectroscopy from image sequences with sub-100 nm spatial resolution. *Journal of Microscopy*, *197*(2), 173-184.

Jacobsen, C. (2019). *X-ray Microscopy*. Cambridge University Press.

Jacobsen, C., Wirick, S., Flynn, G., & Zimba, C. (2000). Soft X-ray spectroscopy from image sequences with sub-100 nm spatial resolution. *Journal of Microscopy*, *197*(2), 173-184.

Jayachandran, M., Rose, A., Maiyalagan, T., Poongodi, N., & Vijayakumar, T. (2021). Effect of various aqueous electrolytes on the electrochemical performance of α-MnO2 nanorods as electrode materials for supercapacitor application. *Electrochimica Acta*, *366*, 137412.

Jiang, L., Roh, H.-S., Caliskan, S., Qin, F., & Lee, J.-K. (2020). Pseudocapacitance of chemically stable MnO_2-NiO mixture layer on highly conductive Sb doped SnO_2 nanowire arrays. *Materials Science and Engineering: B*, *260*, 114637.

Jing, F., Ma, Z., Wang, J., Fan, Y., Qin, X., & Shao, G. (2022). Oxygen vacancy inducing phase transition during charge storage in MnOx@ rGO supercapacitor electrode. *Chemical Engineering Journal*, *435*, 135103.

Jung, H., Taillefert, M., Sun, J., Wang, Q., Borkiewicz, O. J., Liu, P., Yang, L., Chen, S., Chen, H., & Tang, Y. (2020). Redox cycling driven transformation of layered manganese oxides to tunnel structures. *Journal of the American Chemical Society*, *142*(5), 2506-2513.

Kaczmarek, J., & Wolska, E. (1993). Cation and vacancy distribution in nonstoichiometric hausmanite. *Journal of Solid State Chemistry*, *103*(2), 387-393.

Kaliva, M., & Vamvakaki, M. (2020). Nanomaterials characterization. In *Polymer science and nanotechnology* (pp. 401-433). Elsevier.

Kang, J., Hirata, A., Kang, L., Zhang, X., Hou, Y., Chen, L., Li, C., Fujita, T., Akagi, K., & Chen, M. (2013). Enhanced supercapacitor performance of MnO_2 by atomic doping. *Angewandte Chemie International Edition*, *52*(6), 1664-1667.

Kausaite-Minkstimiene, A., Mazeiko, V., Ramanaviciene, A., & Ramanavicius, A. (2015). Evaluation of chemical synthesis of polypyrrole particles. *Colloids and Surfaces A: Physicochemical and Engineering Aspects*, *483*, 224-231.

Kawai, J., Mizutani, Y., Sugimura, T., Sai, M., Higuchi, T., Harada, Y., Ishiwata, Y., Fukushima, A., Fujisawa, M., & Watanabe, M. (2000). High resolution soft X-ray absorption

spectroscopy for the chemical state analysis of Mn. *Spectrochimica Acta Part B: Atomic Spectroscopy*, *55*(9), 1385-1395.

Kaznatcheev, K. V., Karunakaran, C., Lanke, U. D., Urquhart, S. G., Obst, M., & Hitchcock, A. P. (2007). Soft X-ray spectromicroscopy beamline at the CLS: commissioning results. *Nuclear Instruments and Methods in Physics Research Section A: Accelerators, Spectrometers, Detectors and Associated Equipment*, *582*(1), 96-99.

Ke, Z., Zhang, L., Liu, Q., Zhu, Q., Liu, C., & Hu, G. (2023). MnO_2 regulated potential window and storage capacity of $Co_xNi_{1-x}(OH)_2@$ MnO_2 freestanding electrode for promoted membrane-less and decoupled water splitting. *International Journal of Hydrogen Energy*.

Khan, F. N. U., Rasul, M. G., Sayem, A., & Mandal, N. K. (2023). Design and optimization of lithium-ion battery as an efficient energy storage device for electric vehicles: A comprehensive review. *Journal of energy storage*, *71*, 108033.

Kilcoyne, A., Tyliszczak, T., Steele, W., Fakra, S., Hitchcock, P., Franck, K., Anderson, E., Harteneck, B., Rightor, E., & Mitchell, G. (2003). Interferometer-controlled scanning transmission X-ray microscopes at the Advanced Light Source. *Journal of Synchrotron Radiation*, *10*(2), 125-136.

Kim, J.-S., Lee, D.-C., Lee, J.-J., & Kim, C.-W. (2020). Optimization for maximum specific energy density of a lithium-ion battery using progressive quadratic response surface method and design of experiments. *Scientific reports*, *10*(1), 15586.

Kim, M., Kim, N., Hosseinkhannazer, H., Kim, K.-J., & Shin, H.-J. (2022). In-Situ High-Temperature Heating Setup for Spectronanoscopy at Pohang Light Source. *Applied Science and Convergence Technology*, *31*(1), 9-11.

Kim, T., Choi, W., Shin, H.-C., Choi, J.-Y., Kim, J. M., Park, M.-S., & Yoon, W.-S. (2020). Applications of voltammetry in lithium ion battery research. *Journal of Electrochemical Science and Technology*, *11*(1), 14-25.

Kirz, J., & Rarback, H. (1985). Soft x-ray microscopes. *Review of Scientific Instruments*, *56*(1), 1-13.

Kitajima, Y., Nanba, Y., Tanaka, M., Koga, Y., Ueno, A., Nakagawa, K., Tokoro, H., Ohkoshi, S.-i., Iwazumi, T., & Okada, K. (2013). Observation of π backbonding features appearing in Fe 2p X-ray absorption spectra and Fe 1s-4p-1s resonant X-ray emission spectra of RbMn [Fe(CN)$_6$]. *Journal of Physics: Conference Series*, *430*(1), 012082.

Kitchaev, D. A., Dacek, S. T., Sun, W., & Ceder, G. (2017). Thermodynamics of phase selection in MnO_2 framework structures through alkali intercalation and hydration. *Journal of the American Chemical Society*, *139*(7), 2672-2681.

Koprinarov, I., Hitchcock, A., McCrory, C., & Childs, R. (2002). Quantitative mapping of structured polymeric systems using singular value decomposition analysis of soft X-ray images. *The Journal of Physical Chemistry B*, *106*(21), 5358-5364.

Kosugi, N., Cavell, R., & Hitchcock, A. P. (1997). versus (jj) coupling in P 2p inner-shell excited states of PF3. *Chemical physics letters*, *265*(3-5), 490-496.

Kouchachvili, L., Yaïci, W., & Entchev, E. (2018). Hybrid battery/supercapacitor energy storage system for the electric vehicles. *Journal of Power Sources*, *374*, 237-248.

Kour, S., Tanwar, S., & Sharma, A. (2022). A review on challenges to remedies of MnO_2 based transition-metal oxide, hydroxide, and layered double hydroxide composites for supercapacitor applications. *Materials Today Communications*, 104033.

Kowalski, G., Panaś, R., & Wawrzyniak, A. (2021). Insertion devices impact on SOLARIS storage ring optics. *12th Int. Particle Acc. Conf.*, *JACoW Publishing*.

Kumar, N., Prasad, K. G., Sen, A., & Maiyalagan, T. (2018). Enhanced pseudocapacitance from finely ordered pristine α-MnO_2 nanorods at favourably high current density using redox additive. *Applied Surface Science*, *449*, 492-499.

Kunnus, K., Zhang, W., Delcey, M. G., Pinjari, R. V., Miedema, P. S., Schreck, S., Quevedo, W., Schröder, H., Föhlisch, A., & Gaffney, K. J. (2016). Viewing the valence electronic structure of ferric and ferrous hexacyanide in solution from the Fe and cyanide perspectives. *The Journal of Physical Chemistry B*, *120*(29), 7182-7194.

Kwon, N. H., Lee, K.-G., Kim, H. K., & Hwang, S.-J. (2021). MnO_2-based nanostructured materials for various energy applications. *Materials Chemistry Frontiers*, *5*(9), 3549-3575.

Lambert, J. H. (1760). *Photometria sive de mensura et gradibus luminis, colorum et umbrae*. sumptibus vidvae E. Klett, typis CP Detleffsen.

Langmuir, D. (1997). Aqueous environmental. *Geochemistry Prentice Hall: Upper Saddle River, NJ*, *600*.

Lech, M., & Węgierek, P. (2022). Breakdown Initiation and Electrical Strength of a Vacuum Insulating System in the Environment of Selected Noble Gases at AC Voltage. *Energies*, *15*(3), 1154.

Lee, H. Y., & Goodenough, J. B. (1999). Supercapacitor behavior with KCl electrolyte. *Journal of Solid State Chemistry*, *144*(1), 220-223.

Lee, J., Maskell, W., & Tye, F. (1977). The electrochemical reduction of manganese dioxide in acidic solutions: Part I. Voltammetric peak 1. *Journal Of Electroanalytical Chemistry And Interfacial Electrochemistry*, *79*(1), 79-104.

Lee, S.-Y., Housel, L. M., Huang, J., Wu, L., Takeuchi, E. S., Marschilok, A. C., Takeuchi, K. J., Kim, M., & Zhu, Y. (2019). Inhomogeneous structural evolution of silver-containing Alpha-MnO_2 nanorods in sodium-ion batteries investigated by comparative transmission electron microscopy approach. *Journal of Power Sources*, *435*, 226779.

Leontowich, A. F., Berg, R., Regier, C. N., Taylor, D. M., Wang, J., Beauregard, D., Geilhufe, J., Swirsky, J., Wu, J., & Karunakaran, C. (2018). Cryo scanning transmission x-ray microscope optimized for spectrotomography. *Review of Scientific Instruments*, *89*(9), 093704.

Li, D., Cao, L., Deng, T., Liu, S., & Wang, C. (2021). Design of a solid electrolyte interphase for aqueous Zn batteries. *Angewandte Chemie International Edition*, *60*(23), 13035-13041.

Li, L., Hu, Z. A., An, N., Yang, Y. Y., Li, Z. M., & Wu, H. Y. (2014). Facile synthesis of MnO2/CNTs composite for supercapacitor electrodes with long cycle stability. *The Journal of Physical Chemistry C*, *118*(40), 22865-22872.

Li, L., Wu, Z., Yuan, S., & Zhang, X.-B. (2014). Advances and challenges for flexible energy storage and conversion devices and systems. *Energy & Environmental Science*, *7*(7), 2101-2122.

Li, Q., Anderson, J. M., Chen, Y., & Zhai, L. (2012). Structural evolution of multi-walled carbon nanotube/MnO_2 composites as supercapacitor electrodes. *Electrochimica Acta*, *59*, 548-557.

Liao, M., Liu, Y., Hu, Z., & Yu, Q. (2013). Novel morphologic Co_3O_4 of flower-like hierarchical microspheres as electrode material for electrochemical capacitors. *Journal of Alloys and Compounds*, *562*, 106-110.

Libich, J., Máca, J., Vondrák, J., Čech, O., & Sedlaříková, M. (2018). Supercapacitors: Properties and applications. *Journal of energy storage*, *17*, 224-227.

Lim, J., Li, Y., Alsem, D. H., So, H., Lee, S. C., Bai, P., Cogswell, D. A., Liu, X., Jin, N., & Yu, Y.-s. (2016). Origin and hysteresis of lithium compositional spatiodynamics within battery primary particles. *Science*, *353*(6299), 566-571.

Lin, F., Liu, Y., Yu, X., Cheng, L., Singer, A., Shpyrko, O. G., Xin, H. L., Tamura, N., Tian, C., & Weng, T.-C. (2017). Synchrotron X-ray analytical techniques for studying materials electrochemistry in rechargeable batteries. *Chemical reviews*, *117*(21), 13123-13186.

Ling, J. K., & Jose, R. (2021). Metal oxide composite cathode material for high energy density batteries. In *Chemically Deposited Nanocrystalline Metal Oxide Thin Films: Synthesis, Characterizations, and Applications* (pp. 509-530). Springer.

Liu, D., Wang, X., Wang, X., Tian, W., Liu, J., Zhi, C., He, D., Bando, Y., & Golberg, D. (2013). Ultrathin nanoporous Fe_3O_4–carbon nanosheets with enhanced supercapacitor performance. *Journal of Materials Chemistry A*, *1*(6), 1952-1955.

Liu, H., Wang, J.-G., You, Z., Wei, C., Kang, F., & Wei, B. (2021). Rechargeable aqueous zinc-ion batteries: Mechanism, design strategies and future perspectives. *Materials Today*, *42*, 73-98.

Liu, J., Wang, J., Xu, C., Jiang, H., Li, C., Zhang, L., Lin, J., & Shen, Z. X. (2018). Advanced energy storage devices: basic principles, analytical methods, and rational materials design. *Advanced science*, *5*(1), 1700322.

Liu, T. C., Pell, W., Conway, B., & Roberson, S. (1998). Behavior of molybdenum nitrides as materials for electrochemical capacitors: comparison with ruthenium oxide. *Journal of the electrochemical Society*, *145*(6), 1882.

Liu, X., & Weng, T.-C. (2016). Synchrotron-based x-ray absorption spectroscopy for energy materials. *MRS Bulletin*, *41*(6), 466-472.

Lou, S., Zhang, F., Wang, H., & Wang, J. (2021). A Category of Synchrotron X-ray Imaging Methods. *Advanced X-ray Imaging of Electrochemical Energy Materials and Devices*, *Springer, Singapore.* , 1-25. https://doi.org/10.1007/1978-1981-1016-5328-1005_1001.

Low, W. H., Khiew, P. S., Lim, S. S., Siong, C. W., & Ezeigwe, E. R. (2019). Recent development of mixed transition metal oxide and graphene/mixed transition metal oxide based hybrid nanostructures for advanced supercapacitors. *Journal of Alloys and Compounds*, *775*, 1324-1356.

Lu, W., Yuan, Z., Zhao, Y., Zhang, H., Zhang, H., & Li, X. (2017). Porous membranes in secondary battery technologies. *Chemical society reviews*, *46*(8), 2199-2236.

Ma, K., Li, Q., Hong, C., Yang, G., & Wang, C. (2021). Bi Doping-Enhanced Reversible-Phase Transition of α-MnO_2 Raising the Cycle Capability of Aqueous Zn–Mn Batteries. *ACS Applied Materials & Interfaces*, *13*(46), 55208-55217.

Maiti, S., Pramanik, A., & Mahanty, S. (2014). Interconnected network of MnO_2 nanowires with a "cocoonlike" morphology: redox couple-mediated performance enhancement in symmetric aqueous supercapacitor. *ACS Applied Materials & Interfaces*, *6*(13), 10754-10762.

Majidi, M. R., Farahani, F. S., Hosseini, M., & Ahadzadeh, I. (2019). Low-cost nanowired α-MnO_2/C as an ORR catalyst in air-cathode microbial fuel cell. *Bioelectrochemistry*, *125*, 38-45.

Mansour, A. N., Ko, J. K., Zhou, X., Wang, Y., Qiao, X., Yan, Z., Akin, M., Zhang, C., & Balasubramanian, M. (2022). In Situ XAS Investigation of $K_4Fe(CN)_6 \cdot xH_2O$ and $K_3Fe(CN)_6$ Redox Activity in Solid-State Supercapacitors. *Journal of the electrochemical Society*, *169*(4), 040544.

Marichi, R., Sahu, V., Sharma, R., & Singh, G. (2017). Efficient, sustainable, and clean energy storage in supercapacitors using biomass-derived carbon materials. *Handbook of ecomaterials*, 1-26.

Massé, R. C., Liu, C., Li, Y., Mai, L., & Cao, G. (2017). Energy storage through intercalation reactions: electrodes for rechargeable batteries. *National Science Review*, *4*(1), 26-53.

Meng, L., Zhu, Y., Lu, Y., Liang, T., Zhou, L., Fan, J., Kuo, Y. C., Guan, P., Wan, T., & Hu, L. (2023). Rechargeable Zn−MnO_2 Batteries: Progress, Challenges, Rational Design, and Perspectives. *ChemElectroChem*, e202300495.

Mhaisalkar, S. G., Zhang, X., Shi, W., Zhu, J., Zhao, W., Ma, J., Lim, T. M., Yang, Y., Zhang, H., & Hng, H. H. (2010). Synthesis of porous NiO nanocrystals with controllable surface area and their application as supercapacitor electrodes. *Nano Research*, *3*(9), 643–652. https://doi.org/610.1007/s12274-12010-10024-12276.

Minakshi, M., Mitchell, D. R., Jones, R. T., Pramanik, N. C., Jean-Fulcrand, A., & Garnweitner, G. (2020). A hybrid electrochemical energy storage device using sustainable electrode materials. *ChemistrySelect*, *5*(4), 1597-1606.

Monk, P. M. (2008). *Fundamentals of electroanalytical chemistry*. John Wiley & Sons.

Moon, H., Ha, K. H., Park, Y., Lee, J., Kwon, M. S., Lim, J., Lee, M. H., Kim, D. H., Choi, J. H., & Choi, J. H. (2021). Direct Proof of the Reversible Dissolution/Deposition of

Mn2+/Mn4+ for Mild-Acid Zn-MnO$_2$ Batteries with Porous Carbon Interlayers. *Advanced science*, *8*(6), 2003714.

Moseley, H. G. (1914). LXXX. The high-frequency spectra of the elements. Part II. *The London, Edinburgh, and Dublin Philosophical Magazine and Journal of Science*, *27*(160), 703-713.

Moseley, H. G. J. (1913). XCIII. The high-frequency spectra of the elements. *The London, Edinburgh, and Dublin Philosophical Magazine and Journal of Science*, *26*(156), 1024-1034.

Müller, M., Schellhorn, M., & Mann, K. (2019). Laboratory-scale near-edge X-ray absorption fine structure spectroscopy with a laser-induced plasma source. *Journal of Analytical Atomic Spectrometry*, *34*(9), 1779-1785.

Nagasaka, M., Hatsui, T., Horigome, T., Hamamura, Y., & Kosugi, N. (2010). Development of a liquid flow cell to measure soft X-ray absorption in transmission mode: A test for liquid water. *Journal of Electron Spectroscopy and Related Phenomena*, *177*(2-3), 130-134.

Nakanishi, K., & Ohta, T. (2012). Improvement of the detection system in the soft X-ray absorption spectroscopy. *Surface and interface analysis*, *44*(6), 784-788.

Newman, J., & Balsara, N. P. (2021). *Electrochemical systems*. John Wiley & Sons.

Nguyen, T., & Savinell, R. F. (2010). Flow batteries. *The Electrochemical Society Interface*, *19*(3), 54.

Nguyen Thanh Tran, T., Zhao, M., Geng, S., & Ivey, D. G. (2022). Ethylene Glycol as an Antifreeze Additive and Corrosion Inhibitor for Aqueous Zinc-Ion Batteries. *Batteries & Supercaps*, *5*(6), e202100420.

Nichols, J. B., Voltolini, M., Gilbert, B., MacDowell, A. A., & Czabaj, M. W. (2022). The hard x-ray nanotomography microscope at the advanced light source. *Review of Scientific Instruments*, *93*(2).

Nijjer, S., Thonstad, J., & Haarberg, G. (2000). Oxidation of manganese (II) and reduction of manganese dioxide in sulphuric acid. *Electrochimica Acta*, *46*(2-3), 395-399.

Niu, S., Li, S., Du, Y., Han, X., & Xu, P. (2020). How to reliably report the overpotential of an electrocatalyst. *ACS Energy Letters*, *5*(4), 1083-1087.

Nolle, D., Weigand, M., Audehm, P., Goering, E., Wiesemann, U., Wolter, C., Nolle, E., & Schütz, G. (2012). Note: Unique characterization possibilities in the ultra high vacuum scanning transmission x-ray microscope (UHV-STXM)"MAXYMUS" using a rotatable permanent magnetic field up to 0.22 T. *Review of Scientific Instruments*, *83*(4).

Obst, M., Ingino, P., Hitchcock, A., Prabu, V., & Picard, A. (2018). Redox-chemistry of environmental biofilms probed on the submicron scale by in-situ electrochemistry scanning transmission (soft) X-ray microscopy. *Microscopy and Microanalysis*, *24*(S2), 502-505.

Obst, M., & Schmid, G. (2014). 3D chemical mapping: application of scanning transmission (soft) X-ray microscopy (STXM) in combination with angle-scan tomography in bio-, geo-, and environmental sciences. *Electron Microscopy: Methods and Protocols*, 757-781.

Ohigashi, T., Yuzawa, H., & Kosugi, N. (2020). A low-pass filtering Fresnel zone plate for soft x-ray microscopic analysis down to the lithium K-edge region. *Review of Scientific Instruments*, *91*(10).

Pajkossy, T., Ceblin, M. U., & Meszaros, G. (2021). Dynamic electrochemical impedance spectroscopy for the charge transfer rate measurement of the ferro/ferricyanide redox couple on gold. *Journal of Electroanalytical Chemistry*, *899*, 115655.

Pal, B., Yang, S., Ramesh, S., Thangadurai, V., & Jose, R. (2019). Electrolyte selection for supercapacitive devices: a critical review. *Nanoscale Advances*, *1*(10), 3807-3835.

Pan, H., Shao, Y., Yan, P., Cheng, Y., Han, K. S., Nie, Z., Wang, C., Yang, J., Li, X., & Bhattacharya, P. (2016). Reversible aqueous zinc/manganese oxide energy storage from conversion reactions. *Nature Energy*, *1*(5), 1-7.

Parratt, L., Hempstead, C., & Jossem, E. (1957). " Thickness Effect" in Absorption Spectra near Absorption Edges. *Physical Review*, *105*(4), 1228.

Parveen, N., Ansari, S. A., Ansari, M. Z., & Ansari, M. O. (2022). Manganese oxide as an effective electrode material for energy storage: A review. *Environmental Chemistry Letters*, 1-27.

Patra, A., Namsheer, K., Jose, J. R., Sahoo, S., Chakraborty, B., & Rout, C. S. (2021). Understanding the charge storage mechanism of supercapacitors: in situ/operando spectroscopic approaches and theoretical investigations. *Journal of Materials Chemistry A*, *9*(46), 25852-25891.

Paulose, R., Mohan, R., & Parihar, V. (2017). Nanostructured nickel oxide and its electrochemical behaviour—A brief review. *Nano-Structures & Nano-Objects*, *11*, 102-111.

Pecher, K., McCubbery, D., Kneedler, E., Rothe, J., Bargar, J., Meigs, G., Cox, L., Nealson, K., & Tonner, B. (2003). Quantitative charge state analysis of manganese biominerals in aqueous suspension using scanning transmission X-ray microscopy (STXM). *Geochimica et cosmochimica acta*, *67*(6), 1089-1098.

Perez, N., & Perez, N. (2016). Electrochemical corrosion. *Electrochemistry and Corrosion Science*, 1-23.

Petrovic, S. (2021). *Electrochemistry Crash Course for Engineers*. Springer.

Piancastelli, M., Kivimäki, A., Kempgens, B., Neeb, M., Maier, K., & Bradshaw, A. (1997). High-resolution study of resonant decay following the O $1s \rightarrow \pi*$ excitation (s) in CO_2: evidence for an overlapping Rydberg transition. *Chemical physics letters*, *274*(1-3), 13-17.

Pires, V. F., Romero-Cadaval, E., Vinnikov, D., Roasto, I., & Martins, J. (2014). Power converter interfaces for electrochemical energy storage systems–A review. *Energy conversion and management*, *86*, 453-475.

Poonguzhali, R., Shanmugam, N., Gobi, R., Senthilkumar, A., Shanmugam, R., & Sathishkumar, K. (2015). Influence of Zn doping on the electrochemical capacitor behavior of MnO_2 nanocrystals. *RSC advances*, *5*(56), 45407-45415.

Prabu, V. (2017). Development of in-situ flow electrochemical Scanning Transmission X-ray Microscopy. *MSc Thesis, McMaster University.* .

Prabu, V., Obst, M., Hosseinkhannazer, H., Reynolds, M., Rosendahl, S., Wang, J., & Hitchcock, A. P. (2018). Instrumentation for in situ flow electrochemical scanning transmission X-ray microscopy (STXM). *Review of Scientific Instruments*, *89*(6), 063702.

Prince, K., Avaldi, L., Coreno, M., Camilloni, R., & De Simone, M. (1999). Vibrational structure of core to Rydberg state excitations of carbon dioxide and dinitrogen oxide. *Journal of Physics B: Atomic, Molecular and Optical Physics*, *32*(11), 2551.

Pyun, S.-I., Shin, H.-C., Lee, J.-W., Go, J.-Y., & Paccagnella, A. (2012). Electrochemical Methods: Electrochemistry of Insertion Materials for Hydrogen and Lithium. *Springer, Berlin*, 11-32.

Qian, T., Xu, N., Zhou, J., Yang, T., Liu, X., Shen, X., Liang, J., & Yan, C. (2014). Interconnected three-dimensional V_2O_5/polypyrrole network nanostructures for high performance solid-state supercapacitors.

Qiao, R., Chin, T., Harris, S. J., Yan, S., & Yang, W. (2013). Spectroscopic fingerprints of valence and spin states in manganese oxides and fluorides. *Current Applied Physics*, *13*(3), 544-548.

Rajagopalan, K., Ramasubramanian, B., Velusamy, S., Ramakrishna, S., Kannan, A. M., Kaliyannan, M., & Kulandaivel, S. (2022). Examining the economic and energy aspects of manganese oxide in Li-Ion batteries. *Materials Circular Economy*, *4*(1), 22.

Rajoria, S., Vashishtha, M., & Sangal, V. K. (2021). Review on the treatment of electroplating industry wastewater by electrochemical methods. *Materials Today: Proceedings*, *47*, 1472-1479.

Rarback, H., Shu, D., Feng, S., Ade, H., Kirz, J., McNulty, I., Kern, D., Chang, T., Vladimirsky, Y., & Iskander, N. (1988). Scanning x-ray microscope with 75-nm resolution. *Review of Scientific Instruments*, *59*(1), 52-59.

Regier, T., Krochak, J., Sham, T., Hu, Y., Thompson, J., & Blyth, R. (2007). Performance and capabilities of the Canadian Dragon: The SGM beamline at the Canadian Light Source. *Nuclear Instruments and Methods in Physics Research Section A: Accelerators, Spectrometers, Detectors and Associated Equipment*, *582*(1), 93-95.

Regier, T., Paulsen, J., Wright, G., Coulthard, I., Tan, K., Sham, T., & Blyth, R. (2007). Commissioning of the spherical grating monochromator soft x-ray spectroscopy beamline at the Canadian Light Source. *AIP conference proceedings*, *879*(1), 473-476. https://doi.org/410.1063/1061.2436101.

Risch, M., Morales, D. M., Villalobos, J., & Antipin, D. (2022). What X-ray absorption spectroscopy can tell us about the active state of earth-abundant electrocatalysts for the oxygen evolution reaction. *Angewandte Chemie International Edition*, *61*(50), e202211949.

Risch, M., Stoerzinger, K. A., Han, B., Regier, T. Z., Peak, D., Sayed, S. Y., Wei, C., Xu, Z., & Shao-Horn, Y. (2017). Redox processes of manganese oxide in catalyzing oxygen evolution and reduction: an in situ soft X-ray absorption spectroscopy study. *The Journal of Physical Chemistry C*, *121*(33), 17682-17692.

Risch, M., Stoerzinger, K. A., Regier, T. Z., Peak, D., Sayed, S. Y., & Shao-Horn, Y. (2015). Reversibility of ferri-/ferrocyanide redox during operando soft x-ray spectroscopy. *The Journal of Physical Chemistry C*, *119*(33), 18903-18910.

Rodrigues, S., Shukla, A., & Munichandraiah, N. (1998). A cyclic voltammetric study of the kinetics andmechanism of electrodeposition of manganese dioxide. *Journal of applied electrochemistry*, *28*(11), 1235-1241.

Rodriguez-Romero, J., Ruiz de Larramendi, I., & Goikolea, E. (2022). Nanostructured Manganese Dioxide for Hybrid Supercapacitor Electrodes. *Batteries*, *8*(12), 263.

Rong, X., & Kolpak, A. M. (2015). Ab initio approach for prediction of oxide surface structure, stoichiometry, and electrocatalytic activity in aqueous solution. *The journal of physical chemistry letters*, *6*(9), 1785-1789.

Röntgen, W. C. (1896). On a new kind of rays. *Science*, *3*(59), 227-231.

Rooney, M. B., Coomber, D. C., & Bond, A. M. (2000). Achievement of near-reversible behavior for the $[Fe(CN)_6]^{3-/4-}$ redox couple using cyclic voltammetry at glassy carbon, gold, and platinum macrodisk electrodes in the absence of added supporting electrolyte. *Analytical chemistry*, *72*(15), 3486-3491.

Rubel, O., Tran, T. N. T., Gourley, S., Anand, S., Van Bommel, A., Adams, B. D., Ivey, D. G., & Higgins, D. (2022). Electrochemical stability of $ZnMn_2O_4$: Understanding Zn-ion rechargeable battery capacity and degradation. *The Journal of Physical Chemistry C*, *126*(27), 10957-10967.

Ruetschi, P., & Giovanoli, R. (1982). The behaviour of MnO_2 in strongly acidic solutions. *Journal of applied electrochemistry*, *12*(1), 109-114.

Ruus, R., Kikas, A., Saar, A., Ausmees, A., Nommiste, E., Aarik, J., Aidla, A., Uustare, T., & Martinson, I. (1997). Ti 2p and O 1s X-ray absorption of TiO_2 polymorphs. *Solid State Communications*, *104*(4), 199-203.

Santos, D. A., Andrews, J. L., Lin, B., De Jesus, L. R., Luo, Y., Pas, S., Gross, M. A., Carillo, L., Stein, P., & Ding, Y. (2022). Multivariate hyperspectral data analytics across length scales to probe compositional, phase, and strain heterogeneities in electrode materials. *Patterns*, *3*(12).

Santos, M. S. F., Ameku, W. A., Gutz, I. G. R., & Paixão, T. R. L. C. (2018). Gold leaf: From gilding to the fabrication of disposable, wearable and low-cost electrodes. *Talanta*, *179*, 507-511.

Savéant, J.-M. (2006). *Elements of molecular and biomolecular electrochemistry: an electrochemical approach to electron transfer chemistry*. John Wiley & Sons.

Scholz, F. (2010). *Electroanalytical methods* (Vol. 1). Springer.

Schwenke, J., Thanell, K., Beinik, I., Roslund, L., & Tyliszczak, T. (2018). Soft/MAX-A new Soft X-ray Microscopy and Coherent Imaging Beamline at the MAX IV Facility. *Microscopy and Microanalysis*, *24*(S2), 232-233.

Sherman, D. M. (1984). The electronic structures of manganese oxide minerals. *American Mineralogist*, *69*(7-8), 788-799.

Shi, Y., Li, J., Zhang, X., Zhao, K., Wang, Z., Wang, Z., & Peng, X. (2022). Regulating the pyrolysis process of cation intercalated MnO_2 nanomaterials for electrocatalytic urea oxidation performance. *RSC advances*, *12*(47), 30605-30610.

Shin, J., Seo, J. K., Yaylian, R., Huang, A., & Meng, Y. S. (2020). A review on mechanistic understanding of MnO_2 in aqueous electrolyte for electrical energy storage systems. *International Materials Reviews*, *65*(6), 356-387.

Simon, P., Gogotsi, Y., & Dunn, B. (2014). Where do batteries end and supercapacitors begin? *Science*, *343*(6176), 1210-1211.

Sodhi, R. N., & Brion, C. (1984). Reference energies for inner shell electron energy-loss spectroscopy. *Journal of Electron Spectroscopy and Related Phenomena*, *34*(4), 363-372.

Sopčić, S., Peter, R., Petravić, M., & Mandić, Z. (2013). New insights into the mechanism of pseudocapacitance deterioration in electrodeposited MnO_2 under negative potentials. *Journal of Power Sources*, *240*, 252-257.

Stöhr, J. (1992). *NEXAFS spectroscopy* (Vol. 25). Springer, Berlin.

Suktha, P., Phattharasupakun, N., Dittanet, P., & Sawangphruk, M. (2017). Charge storage mechanisms of electrospun Mn_3O_4 nanofibres for high-performance supercapacitors. *RSC advances*, *7*(16), 9958-9963.

Sun, Q., Yao, K., & Zhang, Y. (2020). MnO_2-directed synthesis of NiFe-LDH@ FeOOH nanosheeet arrays for supercapacitor negative electrode. *Chinese Chemical Letters*, *31*(9), 2343-2346.

Sung, J., & Shin, C. (2020). Recent studies on supercapacitors with next-generation structures. *Micromachines*, *11*(12), 1125.

Takashima, T., Yamaguchi, A., Hashimoto, K., Irie, H., & Nakamura, R. (2014). In situ UV-vis absorption spectra of intermediate species for oxygen-evolution reaction on the Surface of MnO_2 in neutral and alkaline media. *Electrochemistry*, *82*(5), 325-327.

Tang, C.-L., Wei, X., Jiang, Y.-M., Wu, X.-Y., Han, L. N., Wang, K.-X., & Chen, J.-S. (2015). Cobalt-doped MnO_2 hierarchical yolk–shell spheres with improved supercapacitive performance. *The Journal of Physical Chemistry C*, *119*(16), 8465-8471.

Tang, X.-n., Zhu, S.-k., Ning, J., Yang, X.-f., Hu, M.-y., & Shao, J.-j. (2021). Charge storage mechanisms of manganese dioxide-based supercapacitors: A review. *New Carbon Materials*, *36*(4), 702-710.

Tanggarnjanavalukul, C., Phattharasupakun, N., Wutthiprom, J., Kidkhunthod, P., & Sawangphruk, M. (2018). Charge storage mechanisms of birnessite-type MnO_2 nanosheets in Na_2SO_4 electrolytes with different pH values: In situ electrochemical X-ray absorption spectroscopy investigation. *Electrochimica Acta*, *273*, 17-25.

Tavares, P. F., Al-Dmour, E., Andersson, Å., Cullinan, F., Jensen, B. N., Olsson, D., Olsson, D. K., Sjöström, M., Tarawneh, H., & Thorin, S. (2018). Commissioning and first-year operational results of the MAX IV 3 GeV ring. *Journal of Synchrotron Radiation*, *25*(5), 1291-1316.

Thompson, A., Attwood, D., Gullikson, E., Howells, M., Kim, K., Kirz, J., Kortright, J., Lindau, I., Pianetta, P., & Robinson, A. (2001). X-ray Data Booklet, edited by AC Thompson & D. *Vaughan. Berkeley: Lawrence Berkeley National Laboratory*.

Toner, B., Fakra, S., Villalobos, M., Warwick, T., & Sposito, G. (2005). Spatially resolved characterization of biogenic manganese oxide production within a bacterial biofilm. *Applied and environmental microbiology*, *71*(3), 1300-1310.

Tran, T. N. T., Jin, S., Cuisinier, M., Adams, B. D., & Ivey, D. G. (2021). Reaction mechanisms for electrolytic manganese dioxide in rechargeable aqueous zinc-ion batteries. *Scientific reports*, *11*(1), 20777.

van der Wal, L. I., Turner, S. J., & Zečević, J. (2021). Developments and advances in in situ transmission electron microscopy for catalysis research. *Catalysis Science & Technology*, *11*(11), 3634-3658.

Velasco-Velez, J.-J., Mom, R. V., Sandoval-Diaz, L.-E., Falling, L. J., Chuang, C.-H., Gao, D., Jones, T. E., Zhu, Q., Arrigo, R., & Roldan Cuenya, B. (2020). Revealing the active phase of copper during the electroreduction of CO_2 in aqueous electrolyte by correlating in situ X-ray spectroscopy and in situ electron microscopy. *ACS Energy Letters*, *5*(6), 2106-2111.

Verink, E. (2011). Simplified procedure for constructing Pourbaix diagrams. *Uhlig's corrosion handbook*, *7*, 111-124.

Verma, S., Mishra, S., Gaur, A., Chowdhury, S., Mohapatra, S., Dwivedi, G., & Verma, P. (2021). A comprehensive review on energy storage in hybrid electric vehicle. *Journal of Traffic and Transportation Engineering (English Edition)*, *8*(5), 621-637.

Vijayakumar, M., Santhosh, R., Adduru, J., Rao, T. N., & Karthik, M. (2018). Activated carbon fibres as high performance supercapacitor electrodes with commercial level mass loading. *Carbon*, *140*, 465-476.

von Laue, M. (1915). Concerning the detection of X-ray interferences. *Nobel lecture*, *13*.

Wadati, H., Achkar, A., Hawthorn, D., Regier, T., Singh, M., Truong, K., Fournier, P., Chen, G., Mizokawa, T., & Sawatzky, G. (2012). Utility of the inverse partial fluorescence for electronic structure studies of battery materials. *Applied Physics Letters*, *100*(19).

Wang, B., Ruan, T., Chen, Y., Jin, F., Peng, L., Zhou, Y., Wang, D., & Dou, S. (2020). Graphene-based composites for electrochemical energy storage. *Energy storage materials*, *24*, 22-51.

Wang, G., Liu, L., Zhang, L., & Zhang, J. (2013). Nickel, cobalt, and manganese oxide composite as an electrode material for electrochemical supercapacitors. *Ionics*, *19*, 689-695.

Wang, H., Forse, A. C., Griffin, J. M., Trease, N. M., Trognko, L., Taberna, P.-L., Simon, P., & Grey, C. P. (2013). In situ NMR spectroscopy of supercapacitors: insight into the charge storage mechanism. *Journal of the American Chemical Society*, *135*(50), 18968-18980.

Wang, H., Sayed, S. Y., Luber, E. J., Olsen, B. C., Shirurkar, S. M., Venkatakrishnan, S., Tefashe, U. M., Farquhar, A. K., Smotkin, E. S., & McCreery, R. L. (2020). Redox flow batteries: how to determine electrochemical kinetic parameters. *ACS nano*, *14*(3), 2575-2584.

Wang, J. (2011). Radiation chemistry by soft X-ray spectromicroscopy. *PhD Thesis, McMaster University*.

Wang, J.-G., Kang, F., & Wei, B. (2015). Engineering of MnO_2-based nanocomposites for high-performance supercapacitors. *Progress in Materials Science*, *74*, 51-124.

Wang, L., Lee, C.-Y., & Schmuki, P. (2013). Solar water splitting: preserving the beneficial small feature size in porous α-Fe_2O_3 photoelectrodes during annealing. *Journal of Materials Chemistry A*, *1*(2), 212-215.

Wang, S., Xu, H., Hao, T., Wang, P., Zhang, X., Zhang, H., Xue, J., Zhao, J., & Li, Y. (2021). In situ XRD and operando spectra-electrochemical investigation of tetragonal WO3-x nanowire networks for electrochromic supercapacitors. *NPG Asia Materials*, *13*(1), 51.

Wang, T., Chen, H. C., Yu, F., Zhao, X., & Wang, H. (2019). Boosting the cycling stability of transition metal compounds-based supercapacitors. *Energy storage materials*, *16*, 545-573.

Wang, T., Huang, L., Zhu, Y., Giorgio, S., Boccabella, P., Bouet, N., & Idir, M. (2023). Ion Beam Figuring System for Synchrotron X-Ray Mirrors Achieving Sub-0.2-µrad and Sub-0.5-nm Root Mean Square. *Nanomanufacturing and Metrology*, *6*(1), 20.

Wang, W., Choi, D., & Yang, Z. (2013). Li-ion battery with $LiFePO_4$ cathode and $Li_4Ti_5O_{12}$ anode for stationary energy storage. *Metallurgical and Materials Transactions A*, *44*, 21-25.

Wang, Z., Pan, S., Wang, B., Qi, J., Tang, L., & Liu, L. (2021). Asymmetric Supercapacitors Based on Co_3O_4@ MnO_2@ PPy Porous Pattern Core-Shell Structure Cathode Materials. *Journal of Electrochemical Science and Technology*, *12*(3), 346-357.

Wang, Z., Yang, D., & Sham, T.-K. (2018). Effect of oxidation state of manganese in manganese oxide thin films on their capacitance performances. *Surface Science*, *676*, 71-76.

wanson, H. E., McMurdie, H. F., Morris, M. C., Evans, E. H., & Paretzkin, B. (1972). Standard X-ray Diffraction Powder Patterns: . Data for 84 Substances.

Warwick, T., Ade, H., Kilcoyne, D., Kritscher, M., Tylisczcak, T., Fakra, S., Hitchcock, A., Hitchcock, P., & Padmore, H. (2002). A new bend-magnet beamline for scanning transmission X-ray microscopy at the Advanced Light Source. *Journal of Synchrotron Radiation*, *9*(4), 254-257.

Watts, B., Thomsen, L., & Dastoor, P. (2006). Methods in carbon K-edge NEXAFS: Experiment and analysis. *Journal of Electron Spectroscopy and Related Phenomena*, *151*(2), 105-120.

Wawrzyniak, A., Curcio, A., Guła, K., Knafel, M., Kowalski, G., Marendziak, A., Panaś, R., Waniczek, M., & Wiśniowski, M. (2021). Solaris Storage Ring Performance After 6 Years of Operation. *doi:10.18429/JACoW-IPAC2021-TUPAB065*.

Wei, W., Cui, X., Chen, W., & Ivey, D. G. (2011). Manganese oxide-based materials as electrochemical supercapacitor electrodes. *Chemical society reviews*, *40*(3), 1697-1721.

Wen, H., Cherukara, M. J., & Holt, M. V. (2019). Time-resolved X-ray microscopy for materials science. *Annual Review of Materials Research*, *49*, 389-415.

Winter, M., & Brodd, R. J. (2004). What are batteries, fuel cells, and supercapacitors? *Chemical reviews*, *104*(10), 4245-4270.

Wiza, J. L. (1979). Microchannel plate detectors. *Nucl. Instrum. Methods*, *162*(1-3), 587-601.

Wu, D., Housel, L. M., King, S. T., Mansley, Z. R., Sadique, N., Zhu, Y., Ma, L., Ehrlich, S. N., Zhong, H., & Takeuchi, E. S. (2022). Simultaneous Elucidation of Solid and Solution Manganese Environments via Multiphase Operando Extended X-ray Absorption Fine Structure Spectroscopy in Aqueous Zn/MnO_2 Batteries. *Journal of the American Chemical Society*, *144*(51), 23405-23420.

Wu, J., Huang, Y., Ye, W., & Li, Y. (2017). CO_2 reduction: from the electrochemical to photochemical approach. *Advanced science*, *4*(11), 1700194.

Wu, M.-S. (2005). Electrochemical capacitance from manganese oxide nanowire structure synthesized by cyclic voltammetric electrodeposition. *Applied Physics Letters*, *87*(15).

Wu, T.-H., Hesp, D., Dhanak, V., Collins, C., Braga, F., Hardwick, L. J., & Hu, C.-C. (2015). Charge storage mechanism of activated manganese oxide composites for pseudocapacitors. *Journal of Materials Chemistry A*, *3*(24), 12786-12795.

Wu, T.-H., Lin, Y.-Q., Althouse, Z. D., & Liu, N. (2021). Dissolution–Redeposition Mechanism of the MnO_2 Cathode in Aqueous Zinc-Ion Batteries. *ACS Applied Energy Materials*, *4*(11), 12267-12274.

Wu, Y., Fee, J., Tobin, Z., Shirazi-Amin, A., Kerns, P., Dissanayake, S., Mirich, A., & Suib, S. L. (2020). Amorphous manganese oxides: an approach for reversible aqueous zinc-ion batteries. *ACS Applied Energy Materials*, *3*(2), 1627-1633.

Xie, C., Liu, Y., Lu, W., Zhang, H., & Li, X. (2019). Highly stable zinc–iodine single flow batteries with super high energy density for stationary energy storage. *Energy & Environmental Science*, *12*(6), 1834-1839.

Xu, C., Kang, F., Li, B., & Du, H. (2010). Recent progress on manganese dioxide based supercapacitors. *Journal of materials research*, *25*(8), 1421-1432.

Xue, M., Xie, Z., Zhang, L., Ma, X., Wu, X., Guo, Y., Song, W., Li, Z., & Cao, T. (2011). Microfluidic etching for fabrication of flexible and all-solid-state micro supercapacitor based on MnO_2 nanoparticles. *Nanoscale*, *3*(7), 2703-2708.

Yan, J., Fan, Z., Wei, T., Qian, W., Zhang, M., & Wei, F. (2010). Fast and reversible surface redox reaction of graphene–MnO_2 composites as supercapacitor electrodes. *Carbon*, *48*(13), 3825-3833.

Yan, J., Li, S., Lan, B., Wu, Y., & Lee, P. S. (2020). Rational design of nanostructured electrode materials toward multifunctional supercapacitors. *Advanced Functional Materials*, *30*(2), 1902564.

Yan, Y., Tang, H., Qu, Z., Zhang, W., Schmidt, O. G., & Zhu, M. (2023). Dynamic Switching and Energy Storage Unified by Electrochemical Ion Intercalation. *Advanced Materials Technologies*, *8*(1), 2200466.

Yang, L. W., & Zhitomirsky, I. (2023). Influence of Capping Agents on the Synthesis of Mn_3O_4 Nanostructures for Supercapacitors. *ACS Applied Nano Materials*, *6*(6), 4428-4436.

Yang, W., Eraky, H., Zhang, C., Hitchcock, A. P., & Zhitomirsky, I. (2022). Scanning transmission X-ray microscopy studies of electrochemical activation and capacitive behavior of Mn_3O_4 supercapacitor electrodes. *Journal of Materials Chemistry A*, *10*(35), 18267-18277.

Yi, C. P., & Majid, S. R. (2018). The electrochemical performance of deposited manganese oxide-based film as electrode material for electrochemical capacitor application. *Semiconductors-Growth and Characterization*, 1193. doi.org/1110.5772/intechopen.71957.

Yoon, C. S., Park, K.-J., Kim, U.-H., Kang, K. H., Ryu, H.-H., & Sun, Y.-K. (2017). High-Energy Ni-Rich $Li[Ni_xCo_yMn_{1-x-y}]O_2$ Cathodes via Compositional Partitioning for Next-Generation Electric Vehicles. *Chemistry of materials*, *29*(24), 10436-10445.

Yu, G., Hu, L., Liu, N., Wang, H., Vosgueritchian, M., Yang, Y., Cui, Y., & Bao, Z. (2011). Enhancing the supercapacitor performance of graphene/MnO_2 nanostructured electrodes by conductive wrapping. *Nano letters*, *11*(10), 4438-4442.

Yu, N., Yin, H., Zhang, W., Liu, Y., Tang, Z., & Zhu, M. Q. (2016). High-performance fiber-shaped all-solid-state asymmetric supercapacitors based on ultrathin MnO_2 nanosheet/carbon fiber cathodes for wearable electronics. *Advanced Energy Materials*, *6*(2), 1501458.

Yu, P., Zhang, X., Wang, D., Wang, L., & Ma, Y. (2009). Shape-controlled synthesis of 3D hierarchical MnO_2 nanostructures for electrochemical supercapacitors. *Crystal Growth and Design*, *9*(1), 528-533.

Yuan, Y., Nie, A., Odegard, G. M., Xu, R., Zhou, D., Santhanagopalan, S., He, K., Asayesh-Ardakani, H., Meng, D. D., & Klie, R. F. (2015). Asynchronous crystal cell expansion during lithiation of K^+-stabilized α-MnO_2. *Nano letters*, *15*(5), 2998-3007.

Zan, G., Pianetta, P., & Liu, Y. (2021). Synchrotron-based battery imaging with multi-modal x-ray signals. In *Batteries: Materials principles and characterization methods* (pp. 3-1-3-27). IOP Publishing Bristol, UK.

Zeng, X., Li, M., Abd El-Hady, D., Alshitari, W., Al-Bogami, A. S., Lu, J., & Amine, K. (2019). Commercialization of lithium battery technologies for electric vehicles. *Advanced Energy Materials*, *9*(27), 1900161.

Zhang, C. (2023). In situ Soft X-Ray Spectro-Microscopic Characterization of Catalysts for Electrochemical CO_2 Reduction *PhD Thesis, McMaster University*.

Zhang, C., Eraky, H., Ingino, P., Obst, M., Wang, J., Higgins, D., & Hitchcock, A. P. (2023c). In-situ STXM characterization of Cu/Cu_2O electrocatalysts for CO_2 reduction. *15th Int. Conf. on X-ray Microscopy, Taiwan, 19-24Jun 2022. AIP Conference Proceedings.*, *2990*.

Zhang, C., Eraky, H., Tan, S., Hitchcock, A., & Higgins, D. (2023b). In-situ Studies of Copper-based CO_2 Reduction Electrocatalysts by Scanning Transmission Soft X-ray Microscopy. *ACS Nano 2023*, *17*(21), 21337–21348.

Zhang, C., Mille, N., Eraky, H., Stanescu, S., Swaraj, S., Belkhou, R., Higgins, D., & Hitchcock, A. (2023a). Copper CO_2 Reduction Electrocatalysts Studied by In-situ Soft X-ray Spectro-Ptychography. *Cell Reports Physical Science*, *12*, 101665.

Zhang, N., Cheng, F., Liu, J., Wang, L., Long, X., Liu, X., Li, F., & Chen, J. (2017). Rechargeable aqueous zinc-manganese dioxide batteries with high energy and power densities. *Nature communications*, *8*(1), 405.

Zhang, N., Dong, Y., Jia, M., Bian, X., Wang, Y., Qiu, M., Xu, J., Liu, Y., Jiao, L., & Cheng, F. (2018). Rechargeable aqueous $Zn–V_2O_5$ battery with high energy density and long cycle life. *ACS Energy Letters*, *3*(6), 1366-1372.

Zhang, Y., Huang, R., Wang, X., Wang, Z., Song, B., Du, Y., Lu, Q., Chen, X., & Sun, J. (2022). Facile large-scale preparation of vanadium pentoxide-polypyrrole composite for aqueous zinc-ion batteries. *Journal of Alloys and Compounds*, *907*, 164434.

Zhang, Y., & Mo, Y. (2014). Preparation of MnO_2 electrodes coated by Sb-doped SnO_2 and their effect on electrochemical performance for supercapacitor. *Electrochimica Acta*, *142*, 76-83.

Zhang, Z., Qian, J., Lu, W., Chan, C. H., Lau, S. P., & Dai, J.-Y. (2018). In situ TEM study of the sodiation/desodiation mechanism of MnO_2 nanowire with gel-electrolytes. *Energy storage materials*, *15*, 91-97.

Zhao, Q., Chen, X., Wang, Z., Yang, L., Qin, R., Yang, J., Song, Y., Ding, S., Weng, M., & Huang, W. (2019). Unravelling H^+/Zn^{2+} synergistic intercalation in a novel phase of manganese oxide for high-performance aqueous rechargeable battery. *Small*, *15*(47), 1904545.

Zheng, H., Modibedi, M., Mathe, M., & Ozoemena, K. (2017). The thermal effect on the catalytic activity of MnO_2 (α, β, and γ) for oxygen reduction reaction. *Materials Today: Proceedings*, *4*(11), 11624-11629.

Zheng, J., Zhang, Y., Hu, T., Lv, T., & Meng, C. (2018). New strategy for the morphology-controlled synthesis of V_2O_5 microcrystals with enhanced capacitance as battery-type supercapacitor electrodes. *Crystal Growth & Design*, *18*(9), 5365-5376.

Zheng, J. P., Huang, J., & Jow, T. (1997). The limitations of energy density for electrochemical capacitors. *Journal of the electrochemical Society*, *144*(6), 2026.

Zhou, J., & Wang, J. (2021). Applications of Soft X-ray Spectromicroscopy in Energy Research from Materials to Batteries. *Advanced X-ray Imaging of Electrochemical Energy Materials and Devices*, 141-178.

Zhu, X. (2016). Studies of Magnetotactic Bacteria by Soft X-Ray Microscopy. *PhD Thesis, McMaster University*.

Zoski, C. G. (2006). *Handbook of electrochemistry*. Elsevier.

Appendix A

Publications and Conference Presentations

This appendix lists the publications which are published, accepted, in press and in preparation.

A.1 Publications (Journal articles and conference proceedings)

Eraky. H, Dynes J.J., and Hitchcock, A.P., (2023). Mn L2,3 and O 1s X-ray absorption spectroscopy of different manganese oxide compounds. *J. Electron Spectrosc. Rel. Phenom.* (submitted).

Yang, W., **Eraky, H.,** Zhang, C., Hitchcock, A.P. and Zhitomirsky, I., (2022). Scanning transmission X-ray microscopy studies of electrochemical activation and capacitive behavior of Mn_3O_4 supercapacitor electrodes. *Journal of Materials Chemistry A*, *10*(35), pp.18267-18277.

Yang, W., **Eraky, H.,** Zhang, C., Hitchcock, A.P. and Zhitomirsky, I., (2023). Scanning transmission X-ray microscopy of MnO_2 and Mn_3O_4 for supercapacitor cathodes: influence of fabrication method and electrochemical activation on charge storage. *Chemical Engineering Journal*, 5:149391.

Eraky, H., Zhang, C., Higgins, D.H. and Hitchcock, A. P., (2023). *In-situ* Scanning Transmission X-Ray Microscopy Studies of MnO_2-Based Supercapacitor Electrodes. In *244th ECS Meeting (October 8-12, 2023)*. ECS.

Zhang, C., **Eraky, H.,** Tan, S., Hitchcock, A. P., & Higgins, D. (2023). *In-situ* Studies of Copper-based CO_2 Reduction Electrocatalysts by Scanning Transmission Soft X-ray Microscopy. *ACS Nano*, 17(21), 21337–21348.

Zhang, C., Mille, N., **Eraky, H.,** Stanescu, S., Swaraj, S., Belkhou, R., Higgins, D. and Hitchcock, A. P., (2023). Copper CO_2 Reduction Electrocatalysts Studied by *In-situ* Soft X-ray Spectro-Ptychography. *Cell Reports Physical Science*,101665.

Zhang, C., **<u>Eraky, H.,</u>** Ingino, P., Obst, M., Wang, J., Higgins, D. and Hitchcock, A.P., (2023, September). *In-situ* STXM characterization of Cu/Cu_2O electrocatalysts for CO_2 reduction. In *AIP Conference Proceedings* (Vol. 2990, No. 1). AIP Publishing.

Zhang, C., Shahcheraghi, L., Ismail, F., **Eraky, H.,** Yuan, H., Hitchcock, A.P. and Higgins, D., (2022). Chemical Structure and Distribution in Nickel–Nitrogen–Carbon Catalysts for CO_2 Electroreduction Identified by Scanning Transmission X-ray Microscopy. *ACS catalysis*, *12*(15), pp.8746-8760.

Hitchcock, A.P., Zhang, C., **Eraky, H**., Shahcheraghi, L., Ismail, F. and Higgins, D., (2021). *In-situ* and Operando Studies with Soft X-Ray Transmission Spectromicroscopy. *Microscopy and Microanalysis*, *27*(S2), pp.59-60.

Higgins, D.H., Abdellah, A., Zhang, C., Abousalem, K., Black, R., **Eraky, H.** and Hitchcock, A., (2023). *In-situ* Transmission Electron Microscopy and Soft X-Ray Spectro-Microscopy to Understand Electrochemical Processes. In *244th ECS Meeting (October 8-12, 2023)*. ECS.

Zhang, C., Ingino, P., Obst, M., Shahcheraghi, L., Yuan, H., **Eraky, H.,** Wang, J., Higgins, D. and Hitchcock, A.P., 2020, November. *In-situ* Soft X-Ray Spectromicroscopy Characterization of Electrochemical Processes. In *Electrochemical Society Meeting Abstracts prime2020* (No. 62, pp. 3176-3176). The Electrochemical Society, Inc.

Ingino, P., **Eraky, H.,** Zhang, C., Hitchcock, A. P., & Obst., M. (2023). Soft X-ray spectromicroscopic proof of a reversible oxidation/reduction of individual microbial biofilm structures using a novel microfluidic *in-situ* electrochemical device *(in preparation)*.

A.2   Conference presentations

Eraky, H., Zhang, C., Higgins, D.H. and Hitchcock, A., 2023, October. *In-situ* Scanning Transmission X-Ray Microscopy Studies of MnO_2-Based Supercapacitor Electrodes. In 244th ECS Meeting (October 8-12, 2023).

Eraky, H., Chunyang Zhang, Adam P. Hitchcock and Drew Higgins, *In-situ* STXM Studies of Redox Reactions of MnO_2-based Supercapacitor Electrodes, Surface Canada, Hamilton, Canada, (14-17 May 2023).

Eraky, H., Wenjuan Yang, Chunyang Zhang, Igor Zhitomirsky, and Adam P. Hitchcock STXM studies of electrochemical activation of Mn_3O_4 supercapacitor electrodes, 15th Intl Conf X-ray Microscopy (XRM2022), (Hsinchu, Taiwan, June 19-24, 2022).

Eraky, H., Chunyang Zhang, Adam P. Hitchcock and Drew Higgins, Scanning Transmission X-ray Microscopy (STXM) Studies of Active MnO_2-based ZIBs Electrodes, PRiME, Electrochemical Society meeting, (Honolulu, HI, Oct 2020).

Appendix B

Software Packages Used for This Thesis

This appendix lists all the software packages used for this thesis.

1. **aXis2000**

   aXis2000 is a freeware program developed by Adam Hitchcock and written in Interactive Data Language (IDL) (Hitchcock, 2023a). It is available from http://unicorn.mcmaster.ca/aXis2000.html. It was used for the spectromicroscopy data analysis: images, stack and spectral analyses.

2. **Sigma Plot 2000**

   Sigma Plot 2000 (by Jandel Scientific) was used to plot spectroscopy data.

3. **STXM Control**

   This software program controls all the STXM microscopes used in this thesis. It was initially written in 1998-2001 by Dr. Tolek Tyliszczak and Peter Hitchcock, and extensively further developed from 2002-2006 by Dr. Tyliszczak.

4. **PSTrace**

   PSTrace is the software used to control the Palmsens EmStat4S potentiostat. It is available from https://www.palmsens.com/software/ps-trace/.

5. **Autodesk Fusion 360**

   Autodesk Fusion 360 is computer-aided design (CAD) and computer-aided manufacturing (CAM) software applications developed by Autodesk (https://www.autodesk.com). Autodesk Fusion provides an extensive set of tools for creating parametric 3D models, assemblies, and detailed drawings. It was used to generate the toolpaths and G-codes for CNC (computer numerical control) machine to fabricate the PCB using in the developed *in-situ* device.

6.   **ImageJ (FIJI)**

ImageJ is a Java-based image processing program used for visualization, calculation and reconstructed the laser fluorescence microscopy 3D images presented in thesis. It is available from https://fiji.sc.

Appendix C

Supplemental Information for Chapter 6

Mn 2p and O 1s X-ray Absorption Spectroscopy of Manganese Oxides

Contents

S6.1 X-ray diffraction powder patterns

      Figure S6.1 shows the X-ray diffraction patterns of the MnO, $MnSO_4$, Mn_3O_4, Mn_2O_3, α-MnO_2 and $KMnO_4$ samples studied. Comparison of the observed diffraction patterns with those in the Joint Committee on Powder Diffraction Standards (JCPDS) data base indicate the presence of pure phases for all measured Mn oxides of manganosite MnO (JCPDS PDF 04-008-0277), Szmikite $MnSO_4.(H_2O)$ (JCPDS PDF 04-008-9679), Bixbyite Mn_2O_3 (PDF 00-041-1442), hausmannite Mn_3O_4 (JCPDS PDF 001-1127), α-MnO_2 (JCPDS PDF 00-044-0141), and $KMnO_4$ (JCPDS PDF 04-008-2764).
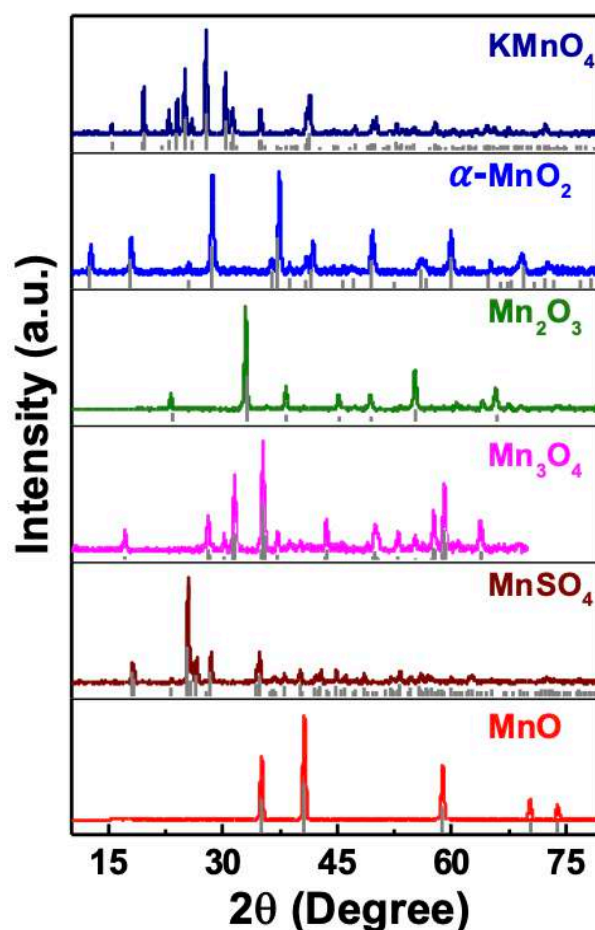
Fig. S6.1 X-ray diffraction patterns of MnO, $MnSO_4$, Mn_3O_4, Mn_2O_3, α-MnO_2 and $KMnO_4$. The grey lines are the JCPDS patterns for each compound.

S6.2 Incident flux normalization in STXM and TEY

Figure S6.2A presents the measured sample current and gold-mesh Io signals recorded for the O 1s TEY spectrum of α-MnO$_2$. While there is observable O 1s spectral features in the Io signal, it does not appreciable affect the normalized O 1s spectral shape (**Fig. S.62B**). **Figure S6.2C** presents the measured O 1s transmission signal from the MnO$_2$ sample in the region indicated in the insert image, and the Io signal from an adjacent region off the sample. Again, there is significant O 1s spectral features. It is necessary to use the Beers-Law normalization *OD = -ln (I/Io)*, to obtain the correct spectral shape (**Fig. S6.2D**).
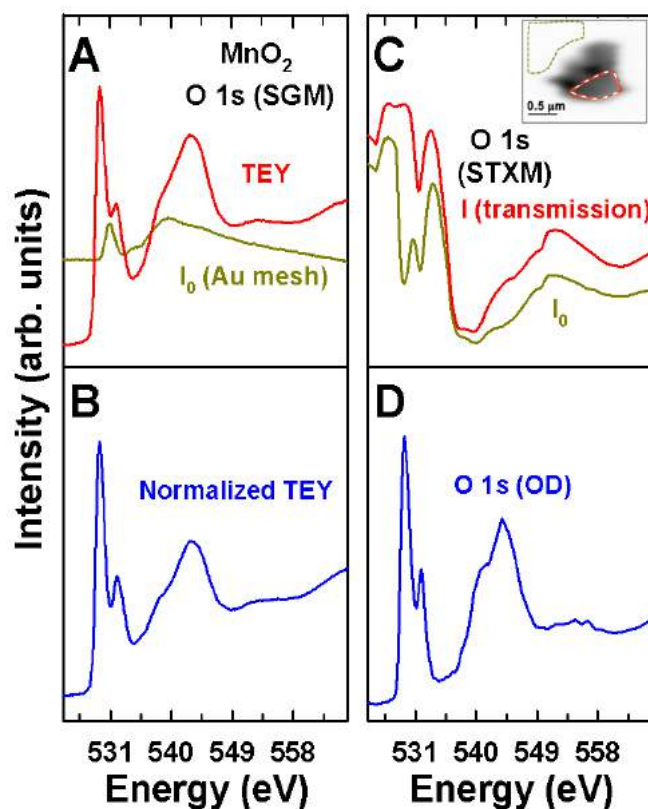
Fig. S6.2 Effect of structured Io signals on TEY and STXM O 1s spectra of α-MnO$_2$. (A) Plot of O 1s TEY (sample current) spectra of α-MnO$_2$ and the signal from the upstream Au mesh. (**B**) TEY spectrum divided by the Io mesh signal. (**C**) Plot of the O 1s transmission signal for α-MnO$_2$ and the I$_0$ transmission signal recorded from an adjacent off-sample location (see red (I) and green (I$_0$) outlined areas of the inserted image). (**D**) O 1s absorption spectrum of α-MnO$_2$ derived by Beer's Law conversion [OD = -ln(I/Io)] of the I and Io transmission signals in **C**.

S6.3 Comparison of MnO$_2$ spectra measured in TEY and PFY modes

Figure S6.3 compares the Mn 2p absorption spectra measured in SGM using TEY, TFY and Mn Lα PFY mode. The Mn 2p$_{3/2}$ band on the spectra measured in the TFY and PFY modes is dramatically distorted relative to the Mn 2p$_{3/2}$ band in the TEY spectrum.
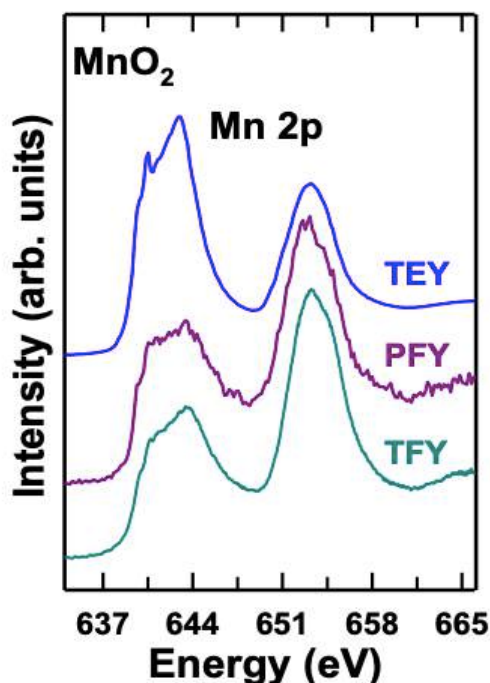
Figure S6.3 Mn 2p spectra of α-MnO2 measured in SGM (TEY, TFY and PFY modes).

S.4 Conversion of measured OD spectra to quantitative OD1 spectra

Figure S6.4A plots the STXM-derived, O 1s OD spectrum of α-MnO$_2$. The step curve is the OD1 elemental response function multiplied by 110. **Figure S6.4B** plots the STXM-derived, Mn 2p OD spectrum of α-MnO$_2$. The step curve is the OD1 elemental response function multiplied by 35. **Figure S6.4C** plots the Mn 2p OD1 spectrum of α-MnO$_2$ in comparison with the elemental OD1 step curve. **Figure S6.4D** plots the Mn 2p OD1 spectrum of α-MnO$_2$ in comparison with the elemental OD1 step curve. The OD1 elemental response is the spectrum predicted for 1 nm of α-MnO$_2$ from the elemental cross-sections of Mn and O [S1], and the density of α-MnO$_2$ (5.08 g/cm^{-3} [S2]).
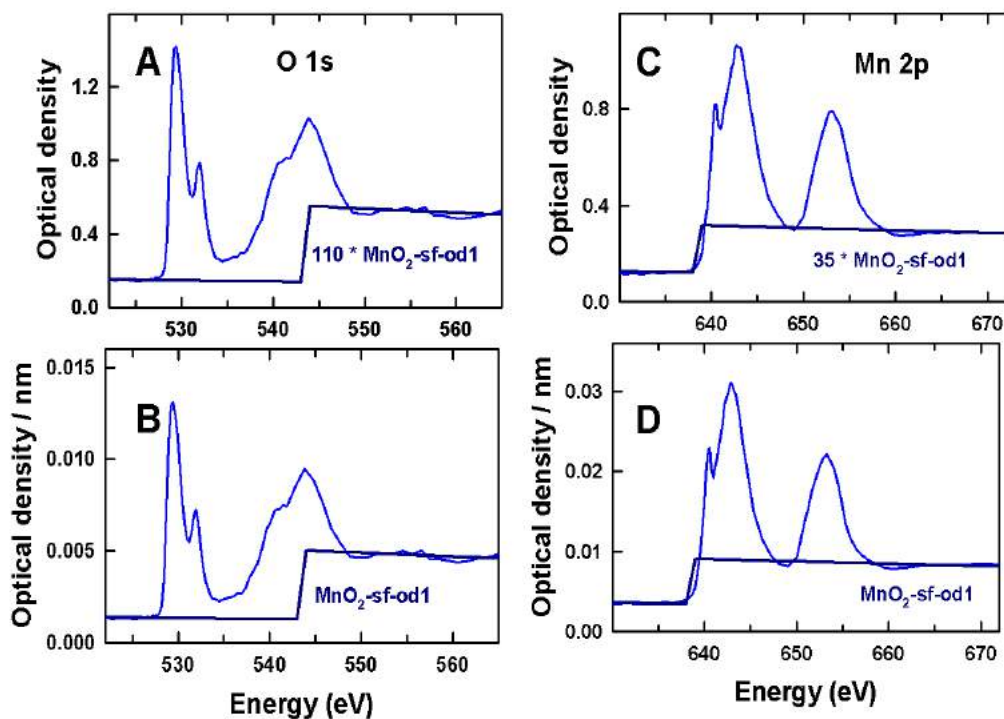
Fig. S6.4   Generation of absolute intensity reference spectra. (A) plot of the measured O 1s STXM spectrum of α-MnO$_2$ compared to that of 110 nm of the elemental response. **(B)** plot of the O 1s OD1 spectrum (OD / 110) compared to the elemental OD1 spectrum of α-MnO$_2$. **(C)** Plot of the measured Mn 2p STXM spectrum of α-MnO$_2$ compared to that of 35 nm of the elemental response. A thinner region was measured to avoid absorption saturation. **(D)** plot of the Mn 2p OD1 spectrum (OD / 35) compared to the elemental OD1 spectrum of α-MnO$_2$.

S.5 Spectral energy calibration using gas phase spectroscopy

Figure S6.5A presents STXM measurement of SF$_6$ gas in comparison with the literature F 1s spectrum of SF$_6$ [S3] **Figure S6.5B** and **S6.5C** present SGM (TEY mode) measurements of SF$_6$ gas and CO$_2$ gas measured in both fast scan and step scan modes before and after the MnOx sample measurements, respectively. The dotted lines indicate the position of the F 1s $\rightarrow$ a$_{1g}$ peak (688.27 eV [S3]) and O 1s $\rightarrow$ 3s peak (538.9 eV [S4]) used for calibration. The similarity of the positions of these peaks in both step and fast scans spectra confirm correct generation of the energy scale in the fast scan mode, as well as the excellent stability of the SGM energy scale.
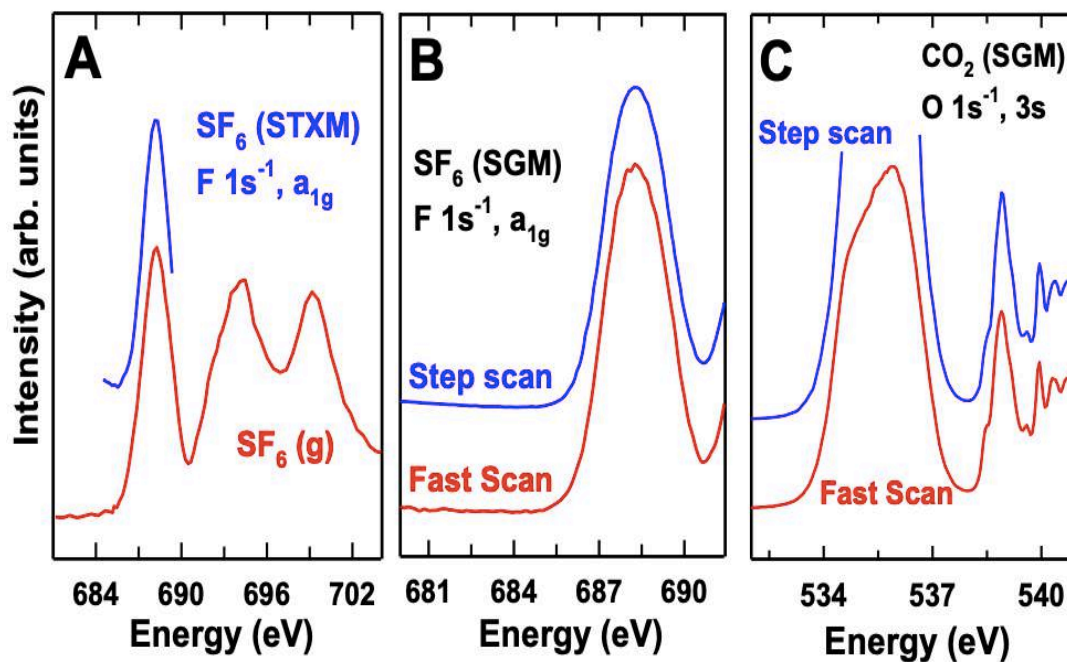
Fig. S6.5 **Energy calibration using gas phase spectroscopy (A)** F 1s spectra of SF_6 gas measured by STXM in comparison with literature F 1s spectrum of SF_6 [S3]. **(B)** F 1s spectra of SF_6 gas measured with the step scan and fast scan (continuous non-linear slewing of the monochromator). **(C)** O 1s spectra of CO_2 gas measured with the step scan and fast scan (continuous non-linear slewing of the monochromator). The difference of the observed position and the known positions (SF_6 688.27(5) eV [S3]; O 1s, 3s peak, 538.9(1) eV [S4]) was used to calibrate the energy scales of the Mn 2p and O 1s spectra, respectively.

S6.6 Sensitivity of the Mn 2p spectrum of MnO to absorption saturation

Figure S6.6 prevents evidence of the ready distortion by absorption saturation of the strong Mn 2p peak of MnO.
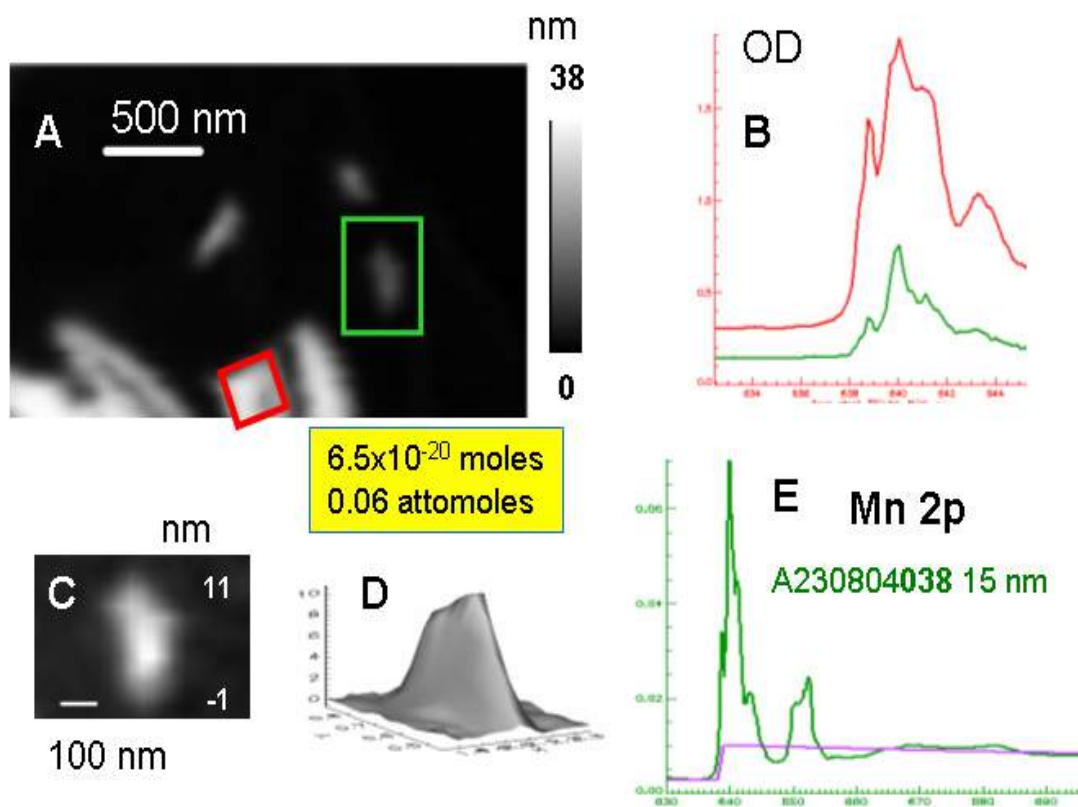
Figure S6.6   Demonstration of sensitivity to absorption saturation of the Mn 2p spectrum of MnO. **(A)** Quantitative map of (absorption unsaturated) MnO from a stack measured on an 80 nm thick microtomed sample. **(B)** Mn 2p spectra of the red and green areas highlighted in A. **(C)** quantitative thickness map of the small particle in the green box. **(D)** 3D display of the particle. (E) derived Mn 2p spectrum, which is estimated to have been measured on 40,000 repeat units of MnO.

S6.7 Comparison of our results for MnO₂ to those of Gilbert [S5] and Toner [S6]

Figure S6.7 compares the Mn 2p and O 1s spectra of β-MnO₂ measured by STXM (curve a) with those from the literature reports by Gilbert et al. [S5] (curve b) and by Toner et al. [S6] (curve c).
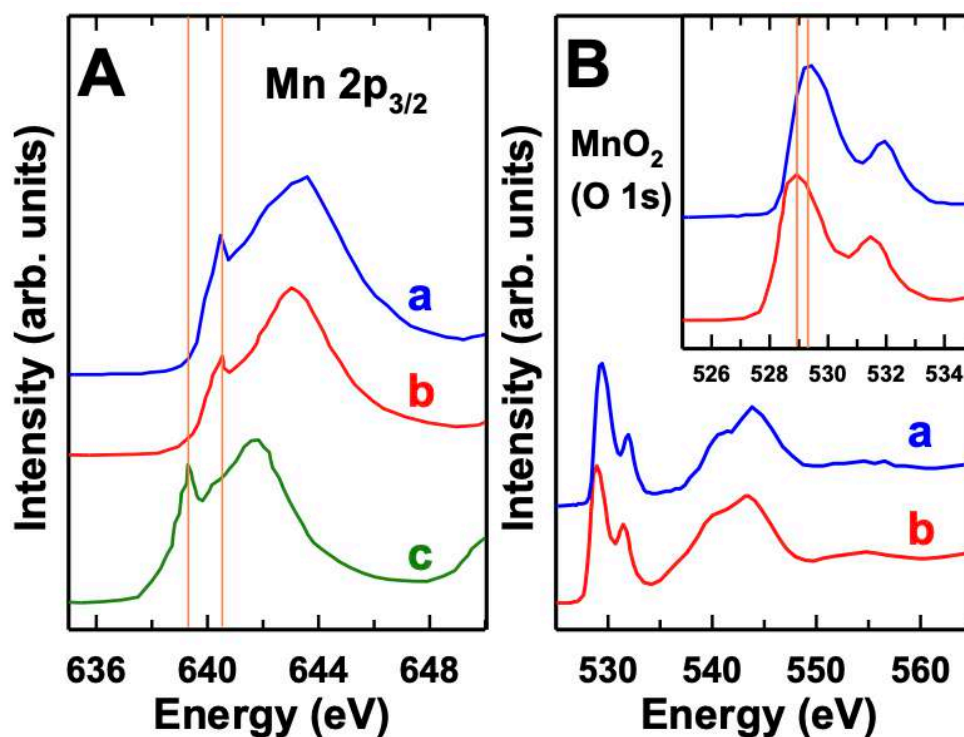
Figure S6.7 Plot of **(A)** Mn 2p spectra and **(B)** O 1s spectra of β-MnO₂ measured with STXM (this work) to that of β-MnO₂ reported by Gilbert et al. [S5] and that of δ-MnO₂Toner et al. [S6]. (a) this work. (b) Gilbert et al [S5]. (c) Toner et al. [S6]. The vertical lines highlight the discrepancies in peak positions.

S6.8 O 1s spectra of different compounds with different sulfur-oxygen bond lengths

Figure S6.8 presents the O 1s absorption spectra of MnO and MnO_2 in comparison with compounds contain SO_4^- and SO_3^- group (H_2SO_4 and perfluorosulfonic acid, which is dominated by C-O-C ether groups, with minor contribution from terminal sulfonate groups) showing the effect of the SO_x groups (as ligand) on the O 1s spectral features.
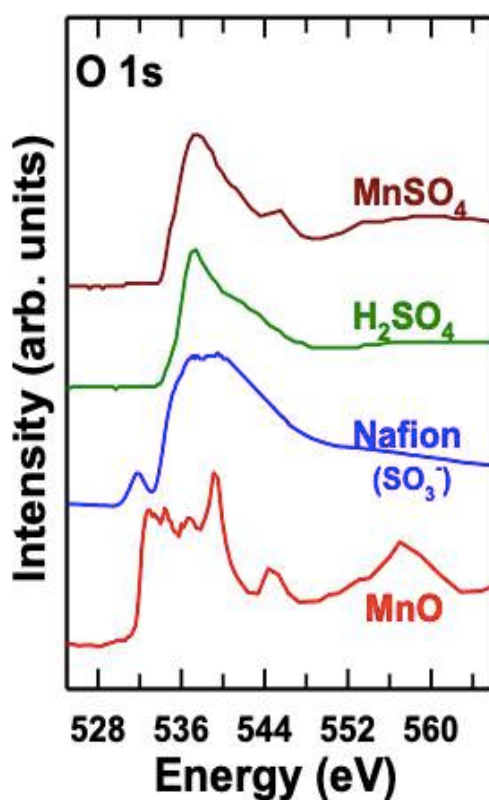
Figure S6.8 O 1s absorption spectra of MnO and MnO_2 (this work) in comparison with those of H_2SO_4 and perfluorosulfonic acid [S.7]

S6.9 O 1s spectra comparison of α-MnO₂ and β-MnO₂

Figure S6.9A presents O 1s spectra of α-MnO₂ and β-MnO₂ measured by STXM. **Figure S6.9A** presents expansion of O 1s → 3d "pre-edge" region (525 eV - 538 eV). Both α-MnO₂ and β-MnO₂ are similar in the O 1s → 3d spectral shape and peaks positions.
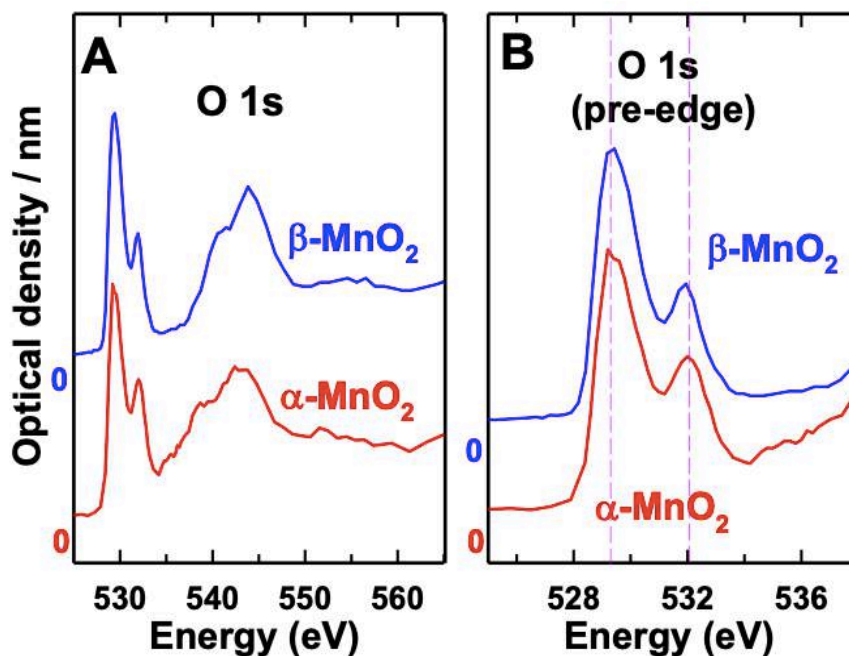
Figure S6.9 **(A)** Comparison of O 1s spectra of α-MnO₂ and β-MnO₂. **(B)** Expansion of O 1s → 3d features of α-MnO₂ and β-MnO₂ O 1s spectra.

References

S1   B.L. Henke, E.M. Gullikson, J.C. Davis, X-ray interactions: photoabsorption, scattering, transmission, and reflection at E= 50-30,000 eV, Z= 1-92, Atomic data and nuclear data tables 54 (1993) 181-342.

S2   Patnaik, P., *Handbook of inorganic chemicals* 529 (2003) McGraw-Hill New York.

S3   R.N. Sodhi, C. Brion, Reference energies for inner shell electron energy-loss spectroscopy, Journal of electron spectroscopy and related phenomena 34 (1984) 363-372.

S4   K. Prince, L. Avaldi, M. Coreno, R. Camilloni, M. De Simone, Vibrational structure of core to Rydberg state excitations of carbon dioxide and dinitrogen oxide, Journal of Physics B: Atomic, Molecular and Optical Physics 32 (1999) 2551.

S.5 B. Gilbert, B. Frazer, A. Belz, P. Conrad, K. Nealson, D. Haskel, J. Lang, G. Srajer, G. De Stasio, Multiple scattering calculations of bonding and X-ray absorption spectroscopy of manganese oxides, The Journal of Physical Chemistry A 107 (2003) 2839-2847.

S.6 B. Toner, S. Fakra, M. Villalobos, T. Warwick, G. Sposito, Spatially resolved characterization of biogenic manganese oxide production within a bacterial biofilm, Applied and environmental microbiology 71 (2005) 1300-1310.

S.7 R. Hayes, B.Sc. thesis McMaster University, 2014 (unpublished)

Appendix D

Supplemental Information for Chapter 7

Scanning transmission X-ray microscopy studies of electrochemical activation and capacitive behavior of Mn_3O_4 supercapacitor electrodes

Supplemental Information for

Scanning transmission X-ray microscopy studies of electrochemical activation and capacitive behavior of Mn_3O_4 supercapacitor electrodes

Wenjuan Yang,[1&] Haytham Eraky,[2&] Chunyang Zhang,[2,3] Adam P. Hitchcock[2] and Igor Zhitomirsky*
&these authors contributed equally
* corresponding author: zhitom@mcmaster.ca

CONTENTS

Section S1. Results of sedimentation tests
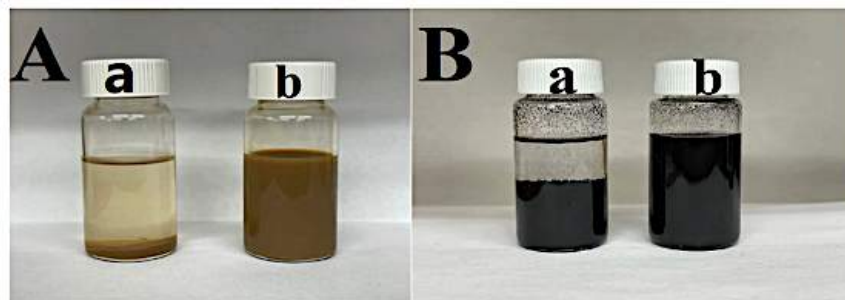
Figure S1. Suspensions of (A) Mn_3O_4 and (B) MWCNT, (a) without QC and (b) with QC as dispersants 7 days after preparation; mass ratio of QC:Mn_3O_4 and QC:MWCNT is 0.2.

Section S2. Schematic of STXM
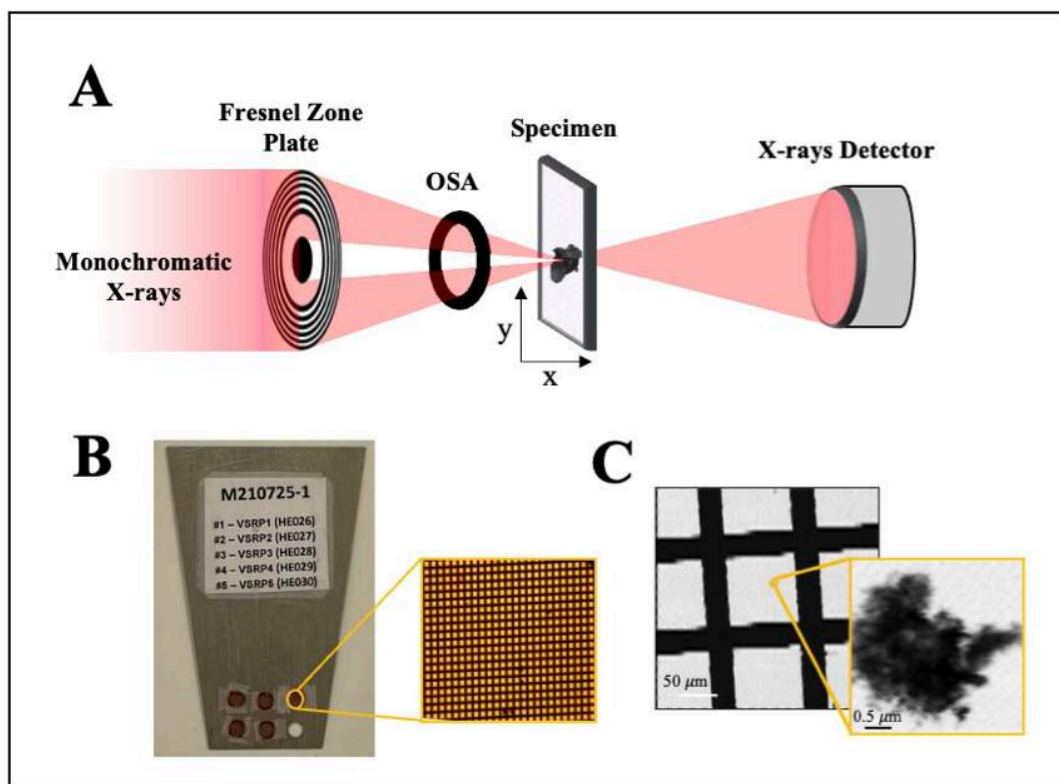
Figure S2. (A) Schematic diagram of scanning transmission x-ray microscopy (STXM), (B) samples on TEM grids mounted on STXM plate, (C) STXM image of the TEM grid square containing the measured region of the FSR1000 sample at 640 eV.

Figure S2A shows a schematic diagram of scanning transmission x-ray microscopy (STXM). Figure S2B shows VSRPs samples mounted on formvar coated TEM grids. Samples were prepared by attaching the TEM grid with a tape to the STXM plate, then drop-cast <1 mg powder on the support. This procedure was followed by tapping the edge of the STXM plate on a hard surface to detach weakly adhering particles. The TEM grid with remaining particles is then covered with a second TEM grid to avoid particles flying off the TEM grid due to sample charging when the X-ray beam hits the sample. Figure S-2C shows a STXM image of the TEM grid square containing the measured region of the FSR1000 sample.
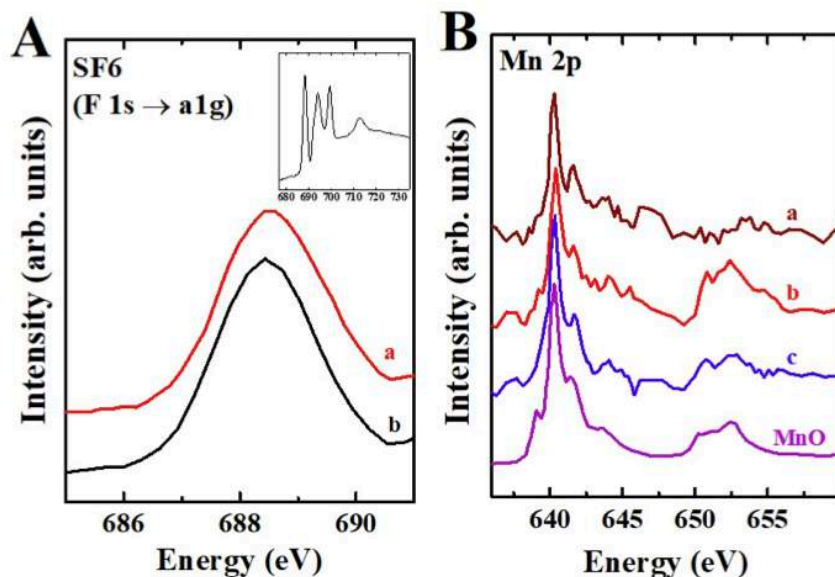
2

Section S3. Spectral energy calibration

Figure S3. (A) F 1s → a_{1g} absorption peak of sulfur hexafluoride (SF_6) gas measured I (a) the Io signal of a measurement of MnO_2 in the presence of SF_6 and, (b) at the hole (The inset shows the full F 1s spectrum of SF_6 gas [s1]. (B) Mn(II) signal present in the Io of Mn 2p spectra measured in STXM and used to confirm the energy scale. (a) as-prepared Mn_3O_4, (b) FSR 100 and (c) FSR1000 cycle samples, compared to the digitized spectrum of MnO [s2].

Table S1. Mn 2p and F 1s energy features of measured samples compared to reference spectra

Sample	edge	peak position (eV)	ΔE (eV)
MnO_2	F 1s (F 1s → a1g)	688.41	0.14
At the hole	F 1s (F 1s → a1g)	688.42	0.15
F 1s reference spectra[S1]	F 1s (F 1s → a1g)	688.27	-
As-prepared Mn_3O_4	Mn 2p (L_3)	640.10	-
FSR100 cycle sample	Mn 2p (L_3)	640.23	-
FSR1000 cycle sample	Mn 2p (L_3)	641.10	-
MnO digitized spectra[S2]	Mn 2p (L_3)	640.28	-

In order to calibrate the spectrum of MnO_2 and other species, sulfur hexafluoride (SF_6) gas (P = 5 mbar) was introduced into the STXM tank and its F 1s spectrum measured as part of Mn 2p stack measurements. The F 1s → a_{1g} peak (688.27 eV)[s1] is observed in the Io signal of the measured Mn 2p stacks. Shifts of up to 0.15 eV were observed in the position of the F 1s → a_{1g} absorption peak (see table S1) which were tracking some

3

irreproducibility of the beamline energy scale. These shifts were used to set the Mn 2p energy scale accurately. Additionally, during some measurements, Mn(II) signal was observed in the Io spectrum (see Figure S3B). This arises from contamination of the STXM zone plate or exit window. This signal was used to validate the Mn 2p energy scale of the as-prepared Mn_3O_4 and samples FSR 100 and 1000 cycle samples. The main L_3 peak Mn 2p spectrum of the Mn(II) contamination occurred at 640.4 eV, after calibration with the SF_6 signal measured at the same time.

Section S4 Analysis of impedance spectroscopy data using equivalent circuit

Figure S4(A) shows experimental EIS data presented in a Nyquist plot and simulation data obtained using (B) equivalent circuit.
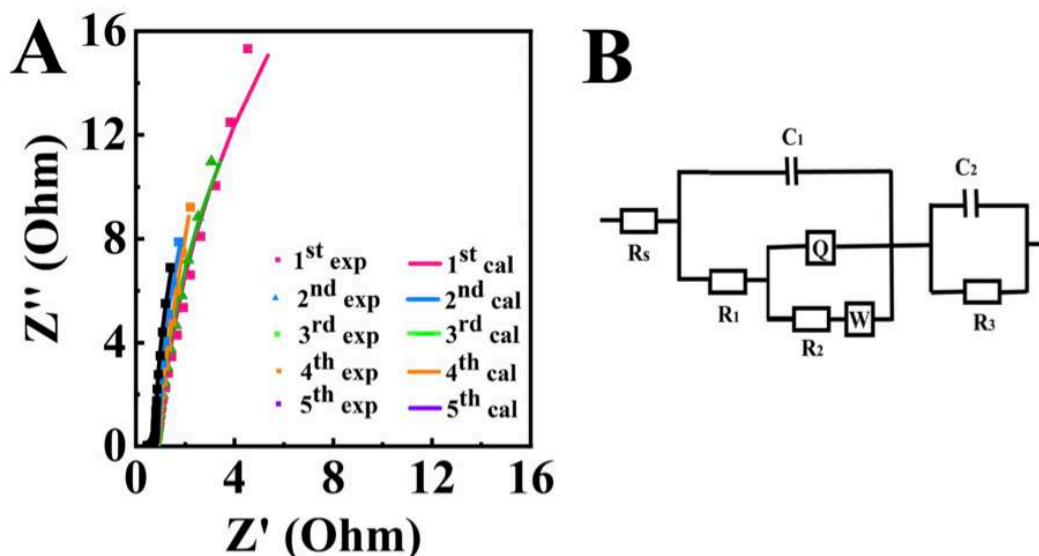
Figure S4. Nyquist plot of complex impedance for VSRPs 1-5: experimental data 1st exp-5th exp and simulation data 1st cal-5th cal, (B) equivalent circuit used for simulation.

The equivalent circuit was similar to that developed in a previous investigation (ref.[31] in manuscript) for the analysis of porous electrodes with high active mass. The equivalent circuit contains R–C(Q) transmission line, Warburg impedance (W) and solution resistance R_S. In this circuit, capacitance (C) and constant phase element (Q) represented

double-layer capacitance at the electrode material -electrolyte interface and pseudocapacitance of the active material, respectively. C_2 and R_3 represent capacitance at the current collector-active material interface and charge transfer resistance, respectively. Simulation results showed that reduction of imaginary component of capacitance can be mainly attributed to increase in pseudocapacitance Q. The decrease of the real component resulted from the reduction of resistance of the transmission line.

Section S5. Comparison of Mn 2p spectra of MnO_2 and Mn_3O_4 with literature

Figure S5 compares the Mn 2p spectrum of MnO_2 we measured by STXM, with the Mn 2p spectra of MnO_2 reported by Gilbert et al.,[s2] Toner et al.[s3] and Stuckey et al.[s4] The data plotted in figure S4 was digitized from the figures in these papers. Every effort was made to accurately reproduce the spectral shape and peak positions as reported in these papers. Gilbert et al. [s2] report the sharp low lying peak in MnO_2 at 640.5 eV, while Toner et al.[s3] report the corresponding peak at 639.3 eV, and Stuckey et al[s4] report the peak at 640.5 eV. Due to the presence of calibration signals above the Mn L signal (F 1s spectrum of SF_6), and exactly in the Mn L region (from the contaminant), we are confident our energy scale is accurate to within ±0.1 eV. Here we are pointing out the existence of significant discrepancies in the energies of the Mn 2p spectrum of MnO_2 reported in the literature, We are preparing a more detailed evaluation of the soft X-ray NEXAFS spectroscopy of manganese oxides, which will be presented elsewhere.
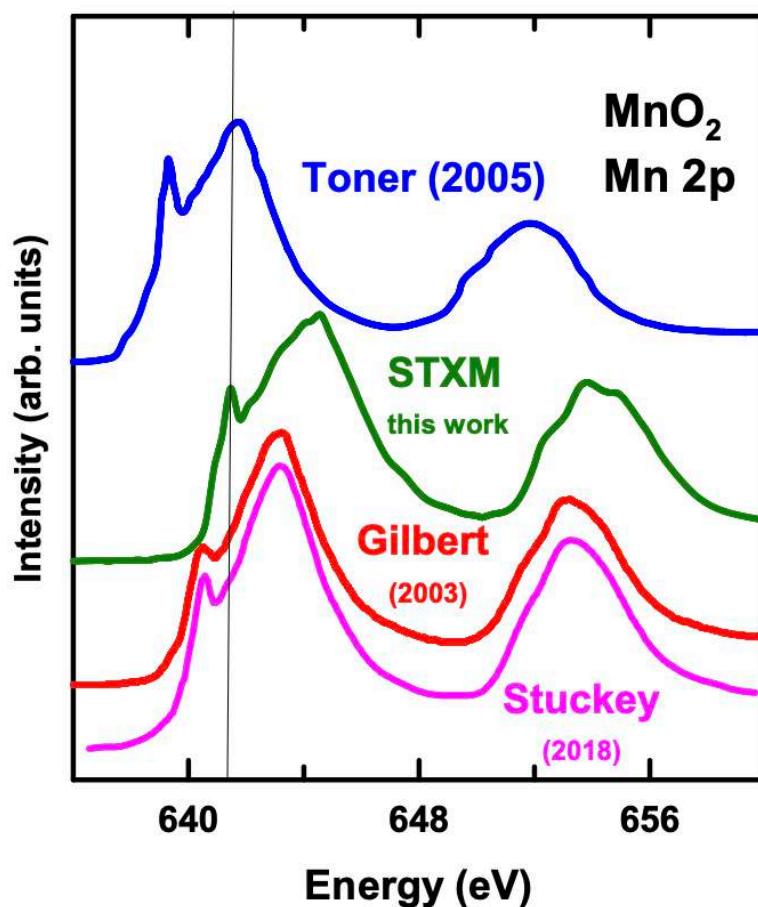
5

Figure S5 Comparison of the Mn 2p spectrum of MnO_2 from this work (STXM), with that reported in the literature by Gilbert et al.,[s2] Toner et al.[s3] and Stuckey et al.[s4]

Figure S6 compares the Mn 2p spectrum of Mn_3O_4 reported by Gilbert et al.[s2] and Stuckey et al.[s4] with spectra of a commercial Mn_3O_4 sample, and of the as-prepared Mn(II,III) sample, that we measured by STXM. For the comparison shown in Fig. S6, the energy scale of each spectrum was set by assigning the position of the first Mn L_3 peak to 639.9 eV, which is that observed in the spectrum of the as-prepared Mn_3O_4. The digitized reference spectrum[s2] and that of the as-prepared Mn_3O_4 previously measured showed the same Mn ($L_{2,3}$) features, indicating first L_3 sharp peak occurs at 639.9 eV. Although the main features of the Mn 2p spectrum of the commercial Mn_3O_4 sample

6

measured by TEY are present, the intensity of the first peak is considerably reduced, suggesting it is impure. For this reason we chose to use the spectra of the as-prepared material as the reference spectrum of Mn_3O_4 in the detailed analysis.
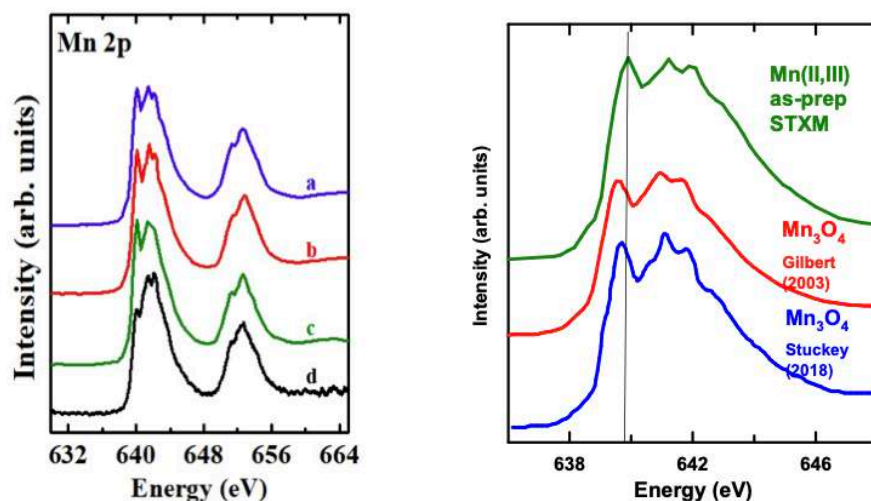

Figure S6. A. Mn_3O_4 (Mn 2p) absorption spectra of (a) as-prepared material, (b) digitized reference spectra from Gilbert et al.[s2], (c) previously measured Mn_3O_4 and (d) the SGM-TEY spectrum of commercial Mn_3O_4 (Sigma). B Expansion of the Mn L_3 region, comparing the spectrum of the as-prepared Mn(II,III) material with the spectra of Mn_3O_4 reported by Gilbert et al.,[s2] and Stuckey et al.[s4]

Section S6. Comparison of STXM and SGM spectra

Figure S7A and S6B present Mn $L_{2,3}$ and O 1s SGM spectra of the as-prepared Mn_3O_4 and MnO_2 reference spectra in comparison with measured spectra of VSRP1, VSRP3, VSRP5 and FSR1000 cycle samples. STXM and SGM spectra of the samples are presented in Figure S7C. The differences between SGM-TEY and STXM measurements might be related to the TEY spectra being dominated by the surface (sampling depth of ~5-10 nm) while STXM is representative of the bulk (100-150 nm).
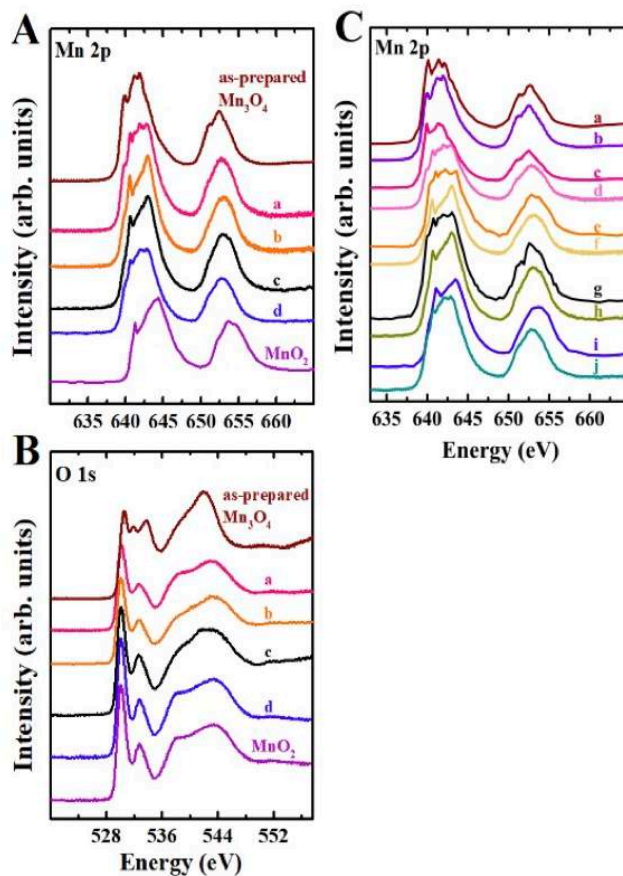
7

Figure S7. (A) Mn 2p, (B) O 1s SGM-TEY absorption spectra of (a) VSRP1, (b) VSRP3, (c) VSRP5 and (d) FSR1000 cycles, (C) shows comparison of STXM spectra (a), (c), (e), (g), (i) and SGM-TEY spectra, (b), (d), (f), (h), (j) of as-prepared Mn_3O_4, VSRP1, VSRP3, VSRP5 and FSR1000 cycles respectively.

References for SI

S1. R.N.S. Sodhi & C.E. Brion, *J. Electron Spectroscopy & Rel. Phenom* . **34** 363 (1984).

S2 B. Gilbert, B. Frazer, A. Belz, P. Conrad, K. Nealson, D. Haskel, J. Lang, G. Srajer and G. De Stasio, *The Journal of Physical Chemistry A* **107**, 2839 (2003)

S3 B. Toner, S. Fakra, M. Villalobos, T. Warwick and G. Sposito, *Applied and environmental microbiology* **71**, 1300 (2005)

S4 J. W. Stuckey, C. Goodwin, J. Wang, L.A. Kaplan, P. Vidal-Esquivel, T.P. Beebe Jr. and D.L. Sparks, *Geochem Trans* **19,** 6 (2018).

8

Appendix E

Supplemental Information for Chapter 8

Scanning Transmission X-ray Microscopy of MnO_2 and Mn_3O_4 for Supercapacitor Cathodes: Influence of Fabrication Method and Electrochemical Activation on Charge Storage

Table of Contents

Section S8.1   O 1s chemical mapping of different regions in Mn₃O₄-c sample after

FSRP

Figure S8.1 A shows average of STXM images measured at 64 energies in an O 1s stack measured on **Mn₃O₄-c** after FSRP. **Figure S8.1 B** presents a color-coded composite of the maps of the two spectra extracted from different region of the sample. **Figure S8.1 (B1-B2)** are the maps of each component. **Figure S8.1 C** presents the O 1s absorption spectra of the regions of each component, verifying the identity of these species.
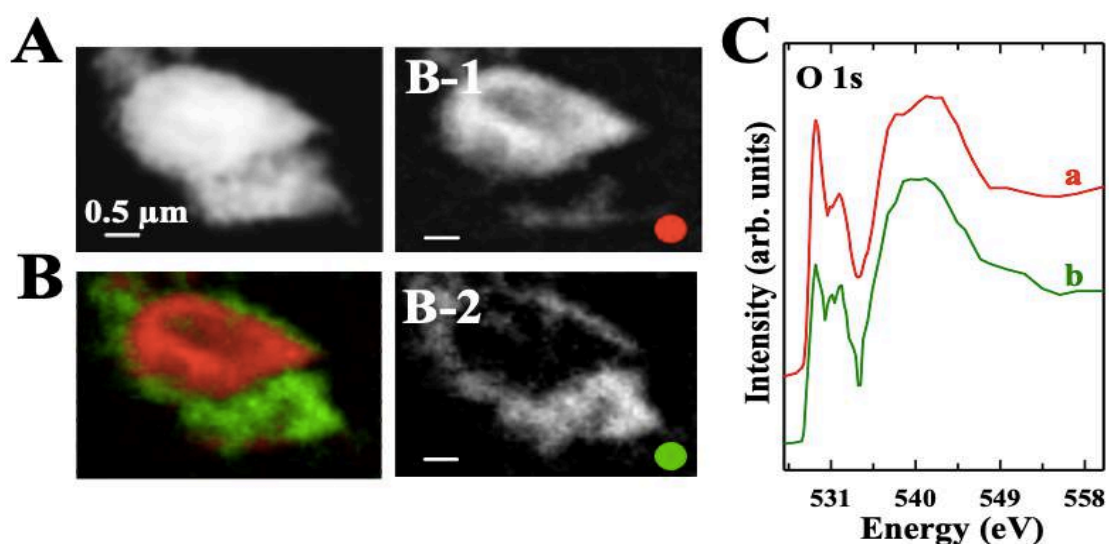

Figure S8.1 O 1s chemical mapping. (A) average of 64 images of O 1s stack of the **Mn₃O₄-c** after FSRP. **(B)** color coded composite of two different Mn oxides regions derived from a stack fit to the O 1s stack. **B-1** and **B-2** are the component maps of the two Mn oxides regions. **(C)** O 1s spectra extracted from different region of the sample. The color of each spectrum corresponds to the color-coding in **B.**

Section S8.2   O 1s chemical mapping of different regions in Mn₃O₄-b sample after

VSRP

Figure S8.2 A presents average of STXM images in an O 1s stack measured on **Mn₃O₄-b** after VSRP. **Figure S8.2 B** presents a color-coded composite of the maps of the two spectra extracted from different region of the sample. **Figure S8.2 (B1-B2)** are the maps of each component.   **Figure S8.2 C** presents the O 1s absorption spectra of the regions of each component, verifying the identity of these species.
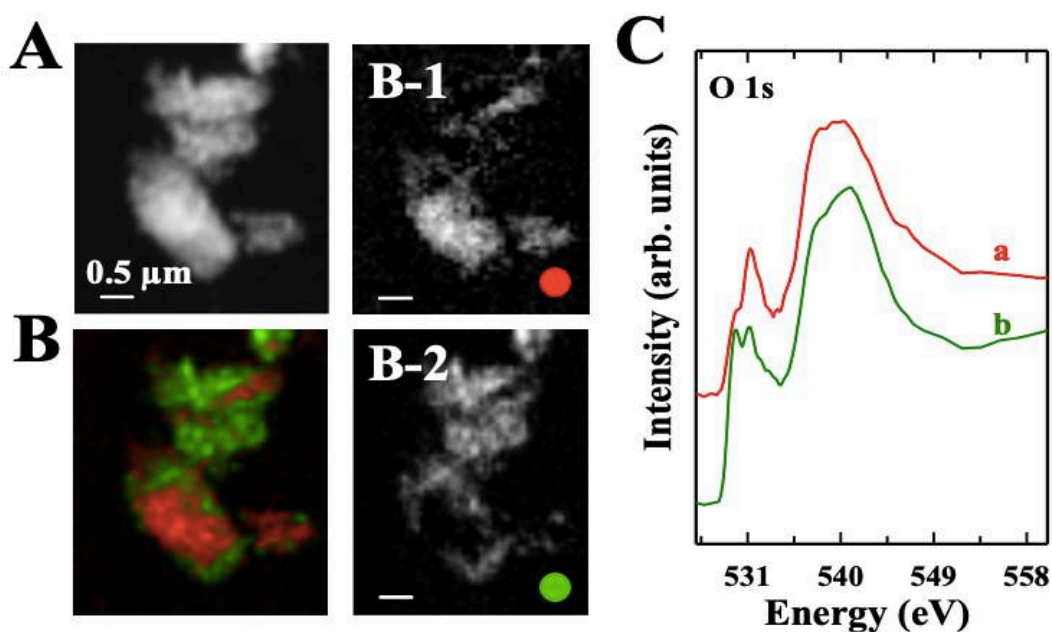

Figure S8.2 O 1s chemical mapping. (A) average of 64 images of O 1s stack of the **Mn₃O₄-b** after VSRP. **(B)** color coded composite of two different Mn oxides regions derived from a stack fit to the O 1s stack. **B-1** and **B-2** are the component maps of the two Mn oxides regions. **(C)** O 1s spectra extracted from different region of the sample. The color of each spectrum corresponds to the color-coding in **B.**

Section S8.3   O 1s chemical mapping of different regions in Mn₃O₄-b sample after FSRP

Figure S8.3 A presents average of STXM images in an O 1s stack measured on **Mn₃O₄-b** after FSRP. **Figure S8.3 B** presents a color-coded composite of the maps of the two spectra extracted from different region of the sample. **Figure S8.3 (B1-B2)** are the maps of each component. **Figure S8.3 C** presents the O 1s absorption spectra of the regions of each component, verifying the identity of these species.
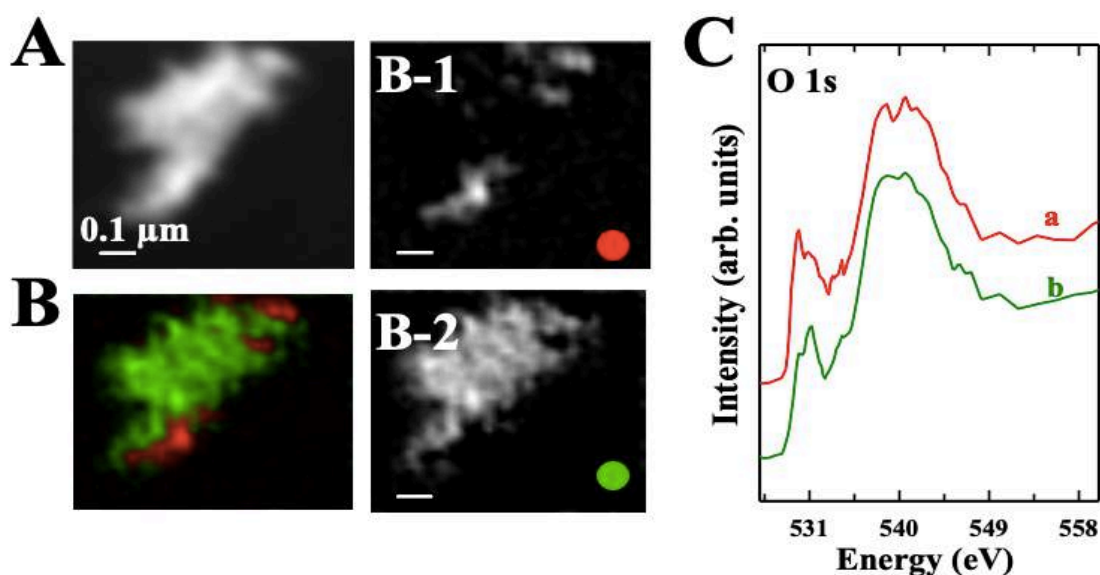

Figure S8.3 O 1s chemical mapping. (A) average of 64 images of O 1s stack of the **Mn₃O₄-b** after FSRP. **(B)** color coded composite of two different Mn oxides regions derived from a stack fit to the O 1s stack. **B-1** and **B-2** are the component maps of the two Mn oxides regions. **(C)** O 1s spectra extracted from different region of the sample. The color of each spectrum corresponds to the color-coding in **B.**

Section S8.4   Mn 2p chemical mapping of the as-prepared MnO₂-a and MnO₂-b samples

Figure S8.4 A and **B** present quantitative chemical maps of the MnO, Mn_3O_4 and MnO_2 species for **MnO₂-a** and **MnO₂-b**, derived by fitting Mn $2p_{3/2}$ stacks (70 energies from 630 – 650 eV) to the quantitative OD1 reference spectra of MnO, Mn_3O_4 and MnO_2 (**Figure 8.6**). **Figure S8.4 C** presents Mn $2p_{3/2}$ absorption spectra of the as-prepared **MnO₂-a** in comparison to that of **MnO₂-b.**
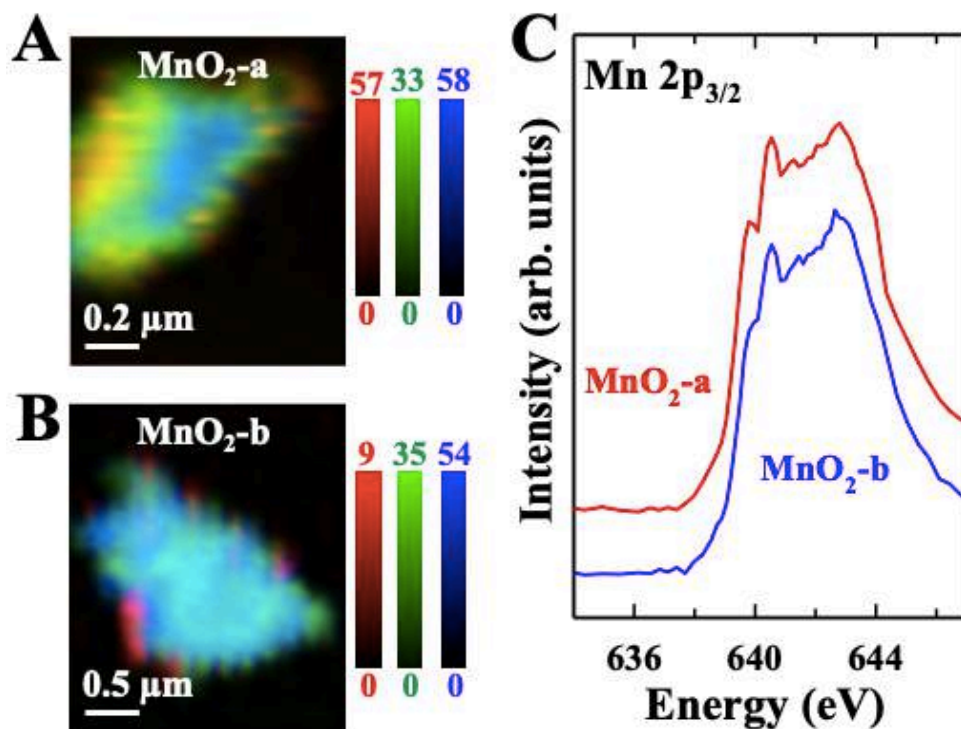

Figure S8.4   Color coded composites of MnO (red), Mn_3O_4 (green) and MnO_2 (blue) chemical maps derived by fitting Mn L_3 stacks. (A) MnO₂-a. (B) MnO₂-b. (C) Mn $2p_{3/2}$ absorption spectra of the as-prepared **MnO₂-a** in comparison to that of **MnO₂-b**

Section S8.5 O 1s chemical mapping of different regions in MnO$_2$-a and MnO$_2$-b samples

Figure S8.5 A presents a color-coded composite of the maps of the two spectra extracted from different region of **MnO$_2$-a** sample (A1 and A2). **Figure S8.5 B** presents the O 1s absorption spectra of the regions of each component, verifying the identity of these species. **Figure S8.5 C** presents a color-coded composite of the maps of the two spectra extracted from different region of **MnO$_2$-b** sample (C1 and C2). **Figure S8.5 D** presents the O 1s absorption spectra of the regions of each component, verifying the identity of these species.
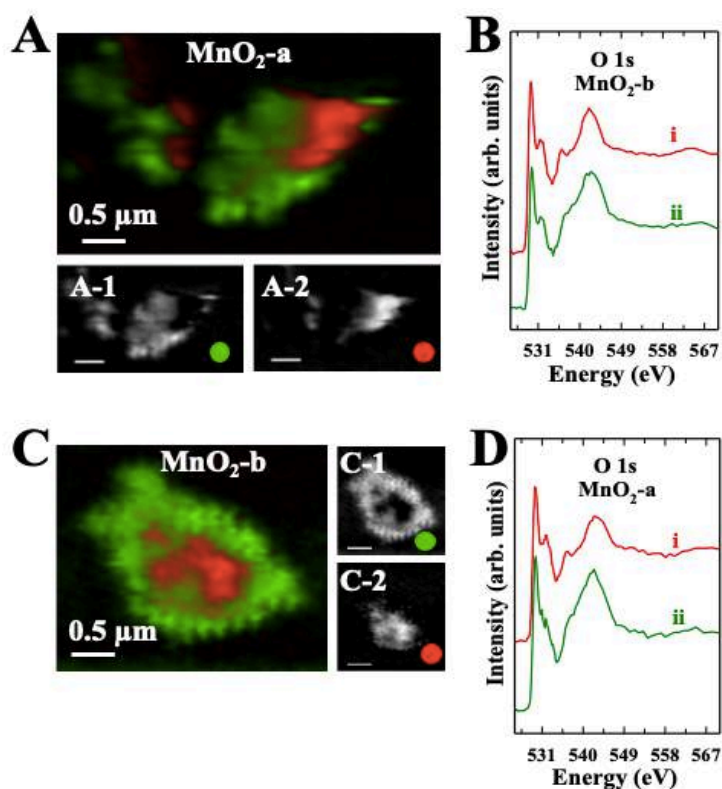

Figure S8.5 O 1s chemical mapping of MnO$_2$-a. (A) color coded composite of two different Mn oxides regions derived from a stack fit to the O 1s stack. **A-1** and **A-2** are the component maps of the two Mn oxides regions. **(B)** O 1s spectra extracted from different region of the sample. The color of each spectrum corresponds to the color-coded in (A). **O 1s chemical mapping of MnO$_2$-b. (C)** color coded composite of two different Mn oxides regions derived from a stack fit to the O 1s stack. **C-1** and **C-2** are the component maps of the two Mn oxides regions. **(D)** O 1s spectra extracted from different region of the sample. The color of each spectrum corresponds to the color-coding in **C**.

Section S8.6   FTIR testing results for MnO$_2$-a, MnO$_2$-b, Mn$_3$O$_4$-a, Mn$_3$O$_4$-b, Mn$_3$O$_4$-c
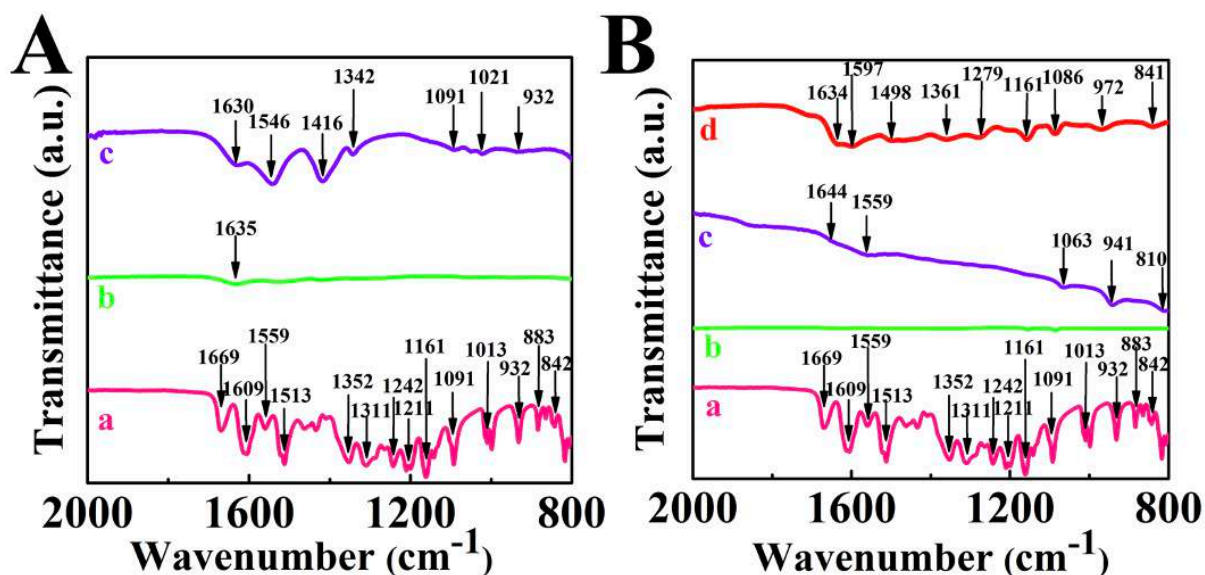
and QC.

Figure S8.6. FTIR spectra obtained using a Bruker Vertex 70 spectrometer for (A) (a) as-received QC, (b) **MnO$_2$-a**, (c) **MnO$_2$-b**, **(B)** (a) as-received QC, (b) **Mn$_3$O$_4$-a**, (c) **Mn$_3$O$_4$-b**, (d) **Mn$_3$O$_4$-c**.

The major peaks of QC [1-3] are related to C═O stretching at 1669 cm^{-1}, C─C stretching of aromatic rings in the range of 1400-1600 cm^{-1}, OH bending in the range of 1200-1400 cm^{-1}, C-H vibrations in the range of 1000-1100 cm^{-1}. Such absorptions were not observed in the spectra of **MnO$_2$-a** and **Mn$_3$O$_4$-a**. However, similar peaks were observed in the spectra of **MnO$_2$-b**, **Mn$_3$O$_4$-b**, and **Mn$_3$O$_4$-c** and confirmed QC absorption.

[1] A. Kumari, S.K. Yadav, Y.B. Pakade, B. Singh, S.C. Yadav, Development of biodegradable nanoparticles for delivery of quercetin, Colloids and Surfaces B: Biointerfaces 80(2) (2010) 184-192.
[2] S.N. Abd El-Rahmanand, S. Suhailah, Quercetin nanoparticles: Preparation and characterization, Indian Journal of Drugs 2(3) (2014) 96-103.
[3] Y. Wang, Y. Liu, I. Zhitomirsky, Surface modification of MnO 2 and carbon nanotubes using organic dyes for nanotechnology of electrochemical supercapacitors, Journal of Materials Chemistry A 1(40) (2013) 12519-12526.